

Cyclotron production and imaging properties of scandium-44

by

Denis Simon Ferguson

A thesis submitted in partial fulfillment of the requirements for the degree of

Doctor of Philosophy

in

Medical Physics

Department of Oncology  
University of Alberta

© Denis Simon Ferguson, 2022

## Abstract

Radioisotopes of scandium have been proposed as potential candidates for radiotheranostics, the combination of targeted imaging and therapy of cancer. Radiolabelling specific targeting vectors with positron emitting radioisotopes ( $^{43}\text{Sc}$ ,  $^{44}\text{Sc}$ ) provides a quantitative measure of the disease through molecular imaging; the information gained from the diagnostic study can be leveraged to improve treatment with an analogue of the same targeting vector with a therapeutic radionuclide ( $^{47}\text{Sc}$ ) to deliver dose to the disease. The development of a reliable supply of  $^{44}\text{Sc}$  was achieved for this thesis, and this has enabled preclinical research studies on its production and imaging.

Experimental surveys are often conducted to determine the viability of production routes for emerging radionuclides. Predictive tools for calculating radionuclidic yield can help curtail the cost of target materials and focus irradiations during experimental surveys. Improvements in Geant4 modelling of low energy proton-induced reactions has sparked interest in using simulations for radionuclide yield calculations. Simulations of thick target yields from the proton irradiation of natural calcium have been compared with calculations based on experimental cross-section data. Measurements of thick target yield were made at energies between 12 and 18 MeV, revealing that Geant4 could accurately predict the yield of several contaminants produced during irradiation within 10 %, including  $^{46}\text{Sc}$ ,  $^{47}\text{Sc}$  and  $^{48}\text{Sc}$ . With further validation, Geant4 could serve as a useful tool in target development.

The decay characteristics of radionuclides in PET studies can impact image reconstruction. The first measurements of standard performance metrics for  $^{44}\text{Sc}$  were made using the NEMA image quality phantom in the Siemens Inveon small-animal PET scanner. These measurements were compared with  $^{18}\text{F}$ ,  $^{64}\text{Cu}$  and  $^{68}\text{Ga}$ ; the recovery coefficients and the spill-over ratio in water were related to the mean positron emission energy, with the long-range positron emitter  $^{68}\text{Ga}$  having lower recovery coefficients and greater spill-over ratio than the short-range positron emitters  $^{64}\text{Cu}$  and  $^{18}\text{F}$ .  $^{44}\text{Sc}$  demonstrated

intermediate behaviour between  $^{18}\text{F}$  and  $^{68}\text{Ga}$ , with greater recovery coefficients than  $^{68}\text{Ga}$ . Derenzo and NEC phantoms were also used for comparisons, which revealed that the NEC rate for  $^{44}\text{Sc}$  increases at a lower rate than  $^{18}\text{F}$  and  $^{68}\text{Ga}$  as a function of activity in the field-of-view.

Radiolabeled peptides play a central role in nuclear medicine as radiotheranostics for targeted imaging and therapy of cancer; the gastrin-releasing peptide receptor has been demonstrated to be overexpressed in several cancers and a metabolically stabilized antagonist BBN2 has demonstrated potential for specific targeting.  $^{44}\text{Sc}$  and  $^{68}\text{Ga}$  were used to radiolabel DOTA complexes of BBN2 and the radiopeptides were prepared in high radiochemical yields. High GRPR binding affinity *in vitro* was found for both peptides, motivating *in vivo* biodistribution studies in MCF7 breast and PC3 prostate cancer models. PET imaging revealed low tumor uptake of both radiotracers in MCF7 xenografts, whereas high tumor uptake and retention was found for both radiopeptides in PC3 tumors.  $^{68}\text{Ga}$ - and  $^{44}\text{Sc}$ -radiolabelled peptides displayed comparable tumor uptake and retention, demonstrating the potential use of  $^{44}\text{Sc}$  as a diagnostic surrogate.

## Preface

The work presented in Chapter 3 was submitted for publication and is undergoing revisions.

The work presented in chapter 4 has been published as: Simon Ferguson, Hans-Sonke Jans, Melinda Wuest, Terence Riauka, and Frank Wuest, "Comparison of scandium-44 with other PET radionuclides in pre-clinical PET phantom imaging" *EJNMMI Physics* (2019) 6:23. The experimental design, experimental measurements, data analysis and writing of the manuscript was accomplished by SF. HSJ assisted with the phantom imaging, and data analysis. All authors assisted in the writing and review of the manuscript.

The work presented in Chapter 5 has been published as: Simon Ferguson, Melinda Wuest, Susan Richter, Cody Bergman, Jennifer Dufour, Daniel Kryszewski, Jennifer Simone, Hans-Sonke Jans, Terence Riauka, Frank Wuest, "A Comparative PET imaging study of  $^{44}\text{Sc}$ - and  $^{68}\text{Ga}$ -labeled bombesin antagonist BBN2 derivatives in breast and prostate cancer models" *Nuclear Medicine and Biology* 90-91 (2020) 74-83. The experimental design and writing of the manuscript was accomplished by SF and FW. Cyclotron irradiation of calcium, extraction and purification of  $^{44}\text{Sc}$  was done by SF, while elution of the  $^{68}\text{Ga}$  was done by SR. SF completed the radiolabelling and purifications, while initial peptide synthesis was completed by CB and JS, western blots were conducted by DK, JD performed the binding assays, and animal imaging was done by MW. All authors assisted in the writing and review of the manuscript.

The work presented in Appendix A has been published as: S. Ferguson, T. Riauka, H. Jans, and K. Gagnon "Radionuclide production calculations: A GUI to determine irradiation conditions" *AIP Conference Proceedings* 1845, 020008 (2017). It is based off a presentation that was given at the 16<sup>th</sup> Workshop on Targetry and Target Chemistry in Sante Fe, NM in August 2016. The GUI was entirely coded and verified by SF and is available for download [here](#). The abstract was edited by TR, HSJ and KG.

# Table of Contents

Chapter 1	Introduction .....	1
1.1	Nuclear medicine .....	1
1.1.1	PET imaging in Canada .....	2
1.2	PET Radionuclides .....	4
1.2.1	Immuno-PET.....	6
1.3	Theranostics .....	7
1.4	Radioscandium.....	9
1.4.1	Radioscandium production .....	11
1.4.2	Radioscandium labelling .....	13
1.4.3	Radioscandium imaging .....	13
1.4.4	Radioscandium therapy .....	15
1.5	Thesis overview.....	16
Chapter 2	Background .....	19
2.1	Radionuclides and the atom .....	19
2.1.1	Radioactivity.....	21
2.1.2	$\beta$ decay & detection .....	23
2.2	Particle interactions in matter .....	24
2.2.1	Photon interactions in matter.....	24
2.2.2	Charged-particle interactions in matter .....	27
2.2.3	Stopping power and range.....	29
2.2.4	Radiation detection.....	30
2.3	Radionuclide production.....	31
2.3.1	Cyclotron .....	32
2.3.2	Reaction kinematics .....	33
2.3.3	Radionuclide production.....	34
2.3.4	Beam monitoring .....	36
2.3.5	Yield quantification .....	38
2.4	PET imaging.....	40
2.4.1	Spatial Resolution .....	41
2.4.2	Photon Detection .....	42
2.4.3	Random coincidences & correction .....	45
2.4.4	Attenuation correction .....	46

2.4.5	Scatter coincidences & correction .....	48
2.4.6	Iterative reconstruction .....	49
2.5	Monte Carlo .....	50
2.5.1	Probability distributions and random sampling.....	52
2.6	Radiochemistry .....	54
Chapter 3	Experimental measurements and predictive analysis of the radionuclidic composition of radioscandium .....	57
3.1	Introduction .....	57
3.2	Materials and Methods.....	59
3.2.1	Target Preparation and Irradiation .....	59
3.2.2	Irradiation .....	60
3.2.3	Target processing.....	60
3.2.4	Yield comparison.....	61
3.2.5	Monte Carlo Simulations.....	63
3.3	Results and discussion .....	64
3.3.1	Geant4 Simulation .....	64
3.3.2	TTY of <sup>43</sup> Sc .....	66
3.3.3	TTY of <sup>44</sup> Sc .....	67
3.3.4	TTY of <sup>47</sup> Sc, <sup>48</sup> Sc, and <sup>47</sup> Ca .....	68
3.3.5	TTY of <sup>46</sup> Sc .....	70
3.3.6	Summary and comparison .....	71
3.4	Conclusion.....	72
3.5	References .....	72
Chapter 4	Comparison of scandium-44 with other PET radionuclides in pre-clinical PET phantom imaging   78	
4.1	Introduction .....	78
4.2	Materials and methods.....	79
4.2.1	Radionuclides .....	79
4.2.2	Image acquisition .....	80
4.2.3	Image noise, spill-over ratio and recovery coefficient.....	81
4.2.4	Contrast and feature size .....	83
4.2.5	Coincidence characteristics.....	84
4.3	Results.....	85
4.3.1	Image noise, spill-over ratio and recovery coefficient.....	85

4.3.2	Contrast and feature size .....	86
4.3.3	Coincidence characteristics.....	88
4.4	Discussion.....	89
4.5	Conclusions .....	92
4.6	References .....	92
Chapter 5 A comparative PET imaging study of <sup>44</sup> Sc- and <sup>68</sup> Ga-labeled bombesin antagonist derivatives in breast and prostate cancer models .....		97
5.1	Introduction .....	97
5.2	Materials and methods .....	99
5.2.1	Reagents and Radionuclides .....	99
5.2.2	Peptide syntheses .....	100
5.2.3	Radiolabelling of DOTA-Ava-BBN2 with <sup>44</sup> Sc and <sup>68</sup> Ga.....	101
5.2.4	Lipophilicity .....	101
5.2.5	Competitive binding assay .....	101
5.2.6	Gene expression microarray analysis.....	102
5.2.7	Protein expression .....	102
5.2.8	Immunohistochemistry .....	103
5.2.9	Dynamic PET Imaging Studies .....	103
5.3	Results.....	104
5.3.1	Radiosynthesis of <sup>68</sup> Ga- and <sup>44</sup> Sc-DOTA-Ava-BBN2 and lipophilicity determination .....	104
5.3.2	In vitro competitive binding assay .....	107
5.3.3	Gene expression microarray analysis.....	108
5.3.4	Protein expression of GRPR in breast cancer cell lines and human breast cancer tissue	109
5.3.5	Dynamic PET imaging studies in MCF7 and PC3 xenografts .....	111
5.4	Discussion.....	114
5.5	Conclusion.....	118
5.6	References .....	119
Chapter 6 Conclusion.....		123
Bibliography .....		130
Appendix A Radionuclide Production Calculations: A GUI to Determine Irradiation Conditions ....		152
A.1	Introduction .....	152
A.2	The “cross sections” tab.....	152
A.3	The “targets” tab.....	154

A.4	The “yield” tab .....	156
A.5	Conclusions .....	158
A.6	References .....	158

## List of Figures

Figure 1.1: Distribution of publicly funded PET scanners and cyclotrons in Canada. Data adapted from the CMII and the IAEA cyclotron directory (CADTH, 2021; IAEA, n.d.) .....	3
Figure 1.2 Simplified decay schemes for $^{43}\text{Sc}$ , $^{44}\text{Sc}$ , $^{47}\text{Sc}$ .....	9
Figure 1.3: Production pathways of positron-emitting radioscandium nuclides $^{43}\text{Sc}$ (right) and $^{44}\text{Sc}$ (left) .....	12
Figure 1.4: Production pathways of $\beta^-$ -emitting radioscandium nuclide $^{47}\text{Sc}$ .....	13
Figure 2.1: Half-lives of nuclides. ....	21
Figure 2.2: Energy spectrum of $\beta^+$ particles emitted during the decay of radionuclides for PET. ....	24
Figure 2.3: Dominant photon interaction in material of atomic number Z for each photon energy regime, where $\sigma$ denotes the Compton effect cross-section, $\tau$ denotes the photoelectric effect cross-section, and $\kappa$ denotes the pair production cross-section .....	24
Figure 2.4: Depiction of impact parameter b for a charged-particle interaction with an atom of radius a .....	28
Figure 2.5: Depiction of radionuclide yield production parameters .....	36
Figure 2.6: Spectrum of $^{137}\text{Cs}$ source measured in HPGe detector .....	39
Figure 2.7: True (left), scatter (center) and random (right) coincidences in PET. ....	44
Figure 2.8: Representation of 2D sinogram acquired from centered and offset source in PET scanner ...	45
Figure 2.9: Hybrid method and bilinear scaling of CT HU number to linear attenuation coefficient for 511 keV photons used in the calculation of attenuation correction. ....	47
Figure 3.1 Comparison of Geant4 thin target simulation results and TENDL-2014 cross-sections from simulation of 10 $\mu\text{m}$ foils. Notice the good agreement between the calculated cross-sections from the thin foil simulations and the TENDL-2014 inputs. ....	65
Figure 3.2: Thick target yield of $^{43}\text{Sc}$ in natural metallic calcium, displaying the contribution of both the $^{43}\text{Ca}(p,n)^{43}\text{Sc}$ and $^{44}\text{Ca}(p,2n)^{43}\text{Sc}$ reactions, as well as their sum (right). Yield predictions calculated from the cross-section measurements of Carzaniga et al., Levkovskij et al., and TENDL are compared to the Geant4 simulation and experimental measurements made in this study as well as by Sitarz et al. and Severin et al. Note that the Sitarz measurements were made in enriched calcium carbonate targets and were converted to equivalent yields in natural abundance metallic calcium. ....	67
Figure 3.3: Thick target yield of $^{44}\text{Sc}$ and $^{44\text{m}}\text{Sc}$ in natural metallic targets. Yields predictions calculated from the cross-section measurements of Carzaniga et al. and TENDL are compared to the results of the Geant4 simulation and experimental measurements made in this study as well as by Sitarz et al. and Severin et al. Note that the Sitarz et al. measurements were made in enriched calcium carbonate targets and were converted to equivalent yields in natural abundance metallic calcium. The Geant4 simulations was not able to predict yield of the $^{44\text{m}}\text{Sc}$ isomer. ....	68
Figure 3.4: Thick target yield of $^{47}\text{Sc}$ , $^{47}\text{Ca}$ , and $^{48}\text{Sc}$ in natural metallic targets. Yields predictions calculated from the cross-section measurements of Carzaniga et al. and TENDL are compared to the results of the Geant4 simulation and experimental measurements made in this study as well as by Sitarz et al., Misiak et al. and Severin et al. Note that the Sitarz et al. and Misiak et al. measurements were made in enriched calcium carbonate targets and were converted to equivalent yields in natural abundance metallic calcium. ....	70
Figure 3.5: Thick target yield of $^{46}\text{Sc}$ in natural metallic targets. Yields predictions calculated from TENDL are compared to the results of the Geant4 simulation and experimental measurements made in this	

study as well as by Misiak et al. Note that the Misiak et al. measurements were made in enriched calcium carbonate targets and were converted to equivalent yields in natural abundance metallic calcium. .... 71

Figure 4.1 Cross-sections of the NEMA image quality phantom with dimensions in mm. Left: Axial cross-section. Right: Transverse cross-sections of the three different regions. The grey area represents the PMMA phantom, the dark blue hashed region represents the volume filled with activity and the light blue represents the cold air and water volumes. .... 81

Figure 4.2 Phantom cross-sections with dimensions in mm. Left: Cross-section of the Derenzo phantom with the fillable rod diameters. Right: NEC phantom cross-section..... 83

Figure 4.3 Impact of radionuclide and reconstruction algorithm on %SD and SOR in air and water. All data were acquired with the same number of counts. Both the uncorrected and scatter corrected values are presented for comparison. .... 86

Figure 4.4 Impact of radionuclide and reconstruction strategy on measured recovery coefficients (RC). 86

Figure 4.5 Derenzo phantom image reconstructed with OSEM2D for different radionuclides ..... 87

Figure 4.6 Normalized contrast as a function of rod size ..... 88

Figure 4.7 Results from phantom imaging studies. The values reflect the FBP reconstruction for the NEMA Image quality phantom and Derenzo phantom studies. .... 88

Figure 5.1 Outline of the scandium extraction system. The irradiated calcium is dissolved in 10 mL of 10 M HCl in reaction vessel (1) and a peristaltic pump (3) is used to trap the scandium onto a UTEVA resin column (4). The column is washed with 3 mL of 10 M HCl prior to the elution of the scandium using DI water in 100  $\mu$ L fractions (2), which are collected separately (5) from the waste (6). The eluted fractions can then be used for radiolabelling. .... 105

Figure 5.2 Structure of DOTA-Ava-BBN2 and radiolabeling with  $^{68}\text{Ga}$  and  $^{44}\text{Sc}$ ..... 106

Figure 5.3 Radio-HPLC of [ $^{68}\text{Ga}$ ]-Ga-DOTA-BBN2 (left) and [ $^{44}\text{Sc}$ ]-Sc-DOTA-BBN2 (right) QC samples to be injected into animals..... 107

Figure 5.4 Dose-response curves for the competitive binding assay. Determination of  $\text{IC}_{50}$  values for  $^{\text{nat}}\text{Ga}$ -DOTA-Ava-BBN2,  $^{\text{nat}}\text{Sc}$ -DOTA-Ava-BBN2, Tyr<sup>4</sup>-BBN(1–14), and DOTA-Ava-BBN2 against  $^{125}\text{I}$ -Tyr<sup>4</sup>-BBN(1–14) to GRPR. Data as mean  $\pm$  SEM. .... 108

Figure 5.5 Total mRNA expression levels of GRPR in normal breast versus total breast cancer tissue, estrogen receptor (ER)-positive, and triple-negative breast cancer samples. Data are presented as mean  $\pm$  standard error of the mean of mRNA levels based on log-transformed values of the gene expression microarray signal intensity from analyzed patient samples. .... 109

Figure 5.6 Representative immunohistochemical staining of GRPR (top) in human ER-positive primary breast cancer tissue and corresponding lymph node metastases and Western blot analysis (bottom) of GRPR expression in MCF7 and MDA-MB231 cell lysates..... 110

Figure 5.7 Representative PET images (MIP) of MCF7 tumor-bearing mice at 20 min after injection of [ $^{68}\text{Ga}$ ]-Ga-DOTA-Ava-BBN2 (left) and [ $^{44}\text{Sc}$ ]-Sc-DOTA-Ava-BBN2 (right). Corresponding time-activity curves (middle) show the radioactivity levels in the tumor and muscle for both radiopeptides over time as SUV values (mean  $\pm$  SEM from n = 3 experiments). .... 111

Figure 5.8 Representative PET images (MIP) of PC3 tumor-bearing mice at 60 min after injection of [ $^{68}\text{Ga}$ ]-Ga-DOTA-Ava-BBN2 (top) and [ $^{44}\text{Sc}$ ]-Sc-DOTA-Ava-BBN2 (bottom) under control (right) and blocking conditions (left). Corresponding time-activity curves (middle) show the radioactivity levels in the tumor and muscle for both radiopeptides over time as SUV values (mean  $\pm$  SEM from n = 3 experiments)..... 113

Figure 5.9 Time-activity curves (TACs) for clearance kinetics from blood (heart = blood pool), kidneys, and liver after injection of [ <sup>68</sup> Ga]Ga-DOTA-Ava-BBN2 (blue) and [ <sup>44</sup> Sc]Sc-DOTA-Ava-BBN2 (green) into PC3 tumor bearing mice. ....	114
Figure 0.1 The cross-section tab allows the user to selectively import cross-sections and includes a table which summarizes all imported reaction channels which can be used to plot and compare various cross-sections. ....	153
Figure 0.2: Comparison of relevant (p,xn) reaction channels on naturally occurring isotopes of calcium from TENDL-2014.....	154
Figure 0.3: The target tab allows the user to import, add, modify, and save targets. It displays the target properties, including isotopic composition, density and molar mass. The stopping power of incident charged particles can be plotted along with the thickness of the target which will degrade an incident charged particle beam to the selected outgoing energy.....	155
Figure 0.4: Stopping power and thickness, assuming full density, of an incident proton beam degraded to 4.5 MeV in a natural.....	156
Figure 0.5: The yield tab includes a summary of the parameters used to calculate the saturated yields, including selected target and range of incident particle energies. The saturated yield can be used to calculate and plot activities as a function of time or beam energy, and these can be displayed for any radionuclide. The activity of the radionuclides is also compared in tabular format as a function of time. ....	157
Figure 0.6: (a) Activity of scandium-44g per μA of beam current for a 1-hour irradiation, as observed 30 min after end of beam in MBq. (b) Radioactivity fraction of scandium-44 at 30min after a 1-hour irradiation as a function of incident and exiting proton energy. The activity fraction is greatest for incident beam energies lower than 16 MeV as at higher energies, competing reaction channels begin to dominate.....	158

## List of Tables

Table 1.1: Radiotracers for clinical and research use in PET-CT units, adapted from the CMII (CADTH, 2021). .....	2
Table 1.2: Selection of radionuclides with applications for PET .....	5
Table 1.3: Properties of $\beta^-$ -emitting therapeutic radionuclides.....	10
Table 4: Trace metal analysis of calcium (Sigma-Aldrich, USA) .....	59
Table 5: Expected proton range in natural calcium target and corresponding areal density, as well as measured areal density of pressed calcium pellets. Note that the measured areal density is greater than the expected areal density to account for uncertainties in final target thickness and density. ....	59
Table 3.6: Radionuclides produced through proton-induced reactions in calcium target and associated $\gamma$ -emission energies and abundances used in assays to determine yields (National Nuclear Data Center, n.d.). The threshold energy was determined using atomic mass data (Wang et al., 2021). ....	61
Table 3.7: Physical thick target yield of nuclides of interest and yield ratio, which represents the average ratio across 4 energies of the yield of the radionuclide as calculated by TENDL or simulated in Geant4 to the measured experimental radionuclide yield.....	71
Table 4.1 Radioisotopic composition of radioscandium from irradiation of natural calcium target with 16 MeV protons .....	80
Table 4.2 Number of decays expected in standard scan conditions and time used to acquire an equal amount of positron decays for each radionuclide.....	82
Table 4.3 Results from phantom imaging studies. The values reflect the FBP reconstruction for the NEMA Image quality phantom and Derenzo phantom studies. ....	89

## List of Abbreviations

BBN	Bombesin
CADTH	Canadian Agency for Drugs and Technologies in Health
CDF	Cumulative Distribution Function
CMII	Canadian Medical Imaging Inventory
CRP	Coordinated Research Project
CT	Computed Tomography
DIPET	Dual-isotope positron emission tomography
DOTA	2,2',2'',2'''-(1,4,7,10-Tetraazacyclododecane-1,4,7,10-tetrayl)tetraacetic acid
EXFOR	Experimental Nuclear Reaction Data
FBP	Filtered back-projection
[ <sup>18</sup> F]FDG	2-deoxy-2-[ <sup>18</sup> F]fluoro-D-glucose
[ <sup>18</sup> F]FLT	Fluorothymidine
FOV	Field of view
FWHM	Full-width half-maximum
GATE	Geant4 application for emission tomography
GRPR	Gastrin-releasing peptide receptor
GUI	Graphical user interface
HPGe	High-purity germanium
HPLC	High performance liquid chromatography
IAEA	International Atomic Energy Agency
ITAP	Isotope Technology Acceleration Program
LOR	Line of response

LSO	Lutetium oxyorthosilicate doped with cerium $\text{Lu}_2\text{SiO}_5:\text{Ce}$
NECR	Noise equivalent count rate
NEMA	National Electrical Manufacturers Association
NETTER-1	Neuro-endocrine Tumors Therapy Trial
NISP	Non-reactor-based Isotope Supply Contribution Program
NNDC	National Nuclear Data Center
mAbs	Monoclonal antibodies
MAP	Maximum a posteriori
MIB	Medical isotope browser
MIBG	metaiodobenzylguanidine
MRI	Magnetic Resonance Imaging
OSEM	Ordered Subset Expectation Maximization
PDF	Probability Density Function
PET	Positron Emission Tomography
PFS	Progression-free survival
PMTs	Photo-multiplier tubes
RC	Recovery coefficient
RCY	Radiochemical yield
RNT	Radionuclide therapy
SOR	Spill-over ratio
SPECT	Single photon emission computed tomography
SRIM	Stopping and Range of Ions in Matter
TENDL	TALYS-based evaluated nuclear data library

TLC Thin layer chromatography

TTY Thick target yield

# Chapter 1

## Introduction

---

---

### 1.1 Nuclear medicine

Nuclear medicine consists of the use of unsealed radioactive sources for the diagnosis and treatment of disease. These radioactive sources, also referred to as radioactive tracers or radiopharmaceuticals, can be a simple compound like the diatomic salt [ $^{131}\text{I}$ ]NaI used to diagnose and treat thyroid cancer, or a larger molecule such as the norepinephrine analogue [ $^{131}\text{I}$ ]MIBG used to diagnose and treat neuroblastoma in neuroendocrine cancers. Common diagnostic procedures include bone scans, renal function scans, cardiac function scans, perfusion studies, and brain death studies. Some common therapeutic procedures are thyroid ablation with radioactive iodine and neuroendocrine cancer treatment with radioactive MIBG or radioactive DOTA-TATE.

Nuclear medicine plays a complementary role to other diagnostic radiology modalities; in contrast to computed tomography (CT) and magnetic resonance imaging (MRI) which provide excellent anatomical information, nuclear medicine imaging provides clinicians with functional information. Radionuclides introduced into the human body provide the signal for the image; the radionuclides' distribution in the body is based either on their chemical properties or on the properties of the molecule to which they are attached. Based on this approach, nuclear medicine imaging can reveal information about highly metabolic areas, hypoxic regions, tissues that overexpress protein receptors, and other functional processes. Positron emission tomography (PET) is of particular interest in molecular imaging as it provides improved resolution for tracer uptake, both in space and time, compared to other functional imaging techniques such as single photon emission computed tomograph (SPECT) and planar imaging.

The most widely used radiopharmaceutical in PET imaging is 2-deoxy-2- $^{18}\text{F}$ fluoro-D-glucose ( $^{18}\text{F}$ FDG).  $^{18}\text{F}$ FDG is a glucose analogue which is taken up into cells but cannot undergo glycolysis due to the missing hydroxyl group and as such accumulates within hyper-metabolic cells, such as many cancerous cell types that have accelerated glucose metabolism in the presence of oxygen (Bensinger and Christofk, 2012). As

the [<sup>18</sup>F]FDG uptake is proportional to the glucose accumulation in cells, regions of greater [<sup>18</sup>F]FDG build-up can identify malignant tumours in PET imaging (Martinuk and Meyer, 2013). PET imaging serves many purposes in oncologic imaging. It can be used in the initial diagnosis to differentiate between malignant and benign tumours, during staging to facilitate the implementation of a suitable treatment plan, as well as to monitor the patient response to therapy and assessing recurrence (Maisey, 2005).

### 1.1.1 PET imaging in Canada

There are many tracers available beyond [<sup>18</sup>F]FDG; in a recent survey of Canadian nuclear medicine departments, a number of tracers that are in current clinical or research use were identified with applications in oncology, cardiology and neurology; they are listed in Table 1.1 (CADTH, 2021). On average, respondents revealed that 93.9 % of the use of PET-CT was diagnostic, with 4.9 % research use and 0.1 % interventional use.

Table 1.1: Radiotracers for clinical and research use in PET-CT units, adapted from the CMII (CADTH, 2021).

Application	Radiotracer	Number of respondents reporting clinical use (23 respondents total)	Number of respondents reporting research use (14 respondents total)
Oncology	[ <sup>18</sup> F]FDG	22 (84.6 %)	10 (71.4 %)
	[ <sup>18</sup> F]NaF	6 (23.1 %)	2 (14.3 %)
	[ <sup>18</sup> F]F-Choline	1 (3.8 %)	2 (14.3 %)
	[ <sup>68</sup> Ga]Ga-DOTA-TATE	1 (3.8 %)	4 (28.6 %)
	[ <sup>18</sup> F]F-PSMA-1007	0 (0 %)	2 (14.3 %)
	[ <sup>18</sup> F]FLT	0 (0 %)	1 (7.1 %)
	[ <sup>68</sup> Ga]Ga-PSMA-HBED-CC	0 (0 %)	1 (7.1 %)
Cardiology	[ <sup>13</sup> N]ammonia	2 (7.7 %)	2 (14.3 %)
	[ <sup>82</sup> Rb]Rb-chloride	4 (15.4 %)	1 (7.1 %)
Neurology	[ <sup>18</sup> F]F-DOPA	1 (3.8 %)	1 (7.1 %)
	[ <sup>18</sup> F]Florbetaben	5 (19.2 %)	1 (7.1 %)
	[ <sup>18</sup> F]Flutemetamol	0 (0 %)	1 (7.1 %)

In addition to cataloguing the clinical and research use of tracers, the Canadian Medical Imaging Inventory (CMII) report assembled by the Canadian Agency for Drugs and Technologies in Health (CADTH) identified that a total of 125,775 PET-CT exams were conducted in Canada in the 2019-2020 year, at 46 sites with a total of 57 PET-CT scanners (CADTH, 2021). The distribution of the PET scanners across Canada is demonstrated in Figure 1.1, along with the distribution of cyclotrons; PET scanners are generally within a short distance of cyclotrons on which <sup>18</sup>F is produced, and the half-life of the tracer

used ultimately dictates how distant the scanner can be located from the radiopharmacy producing the compound.

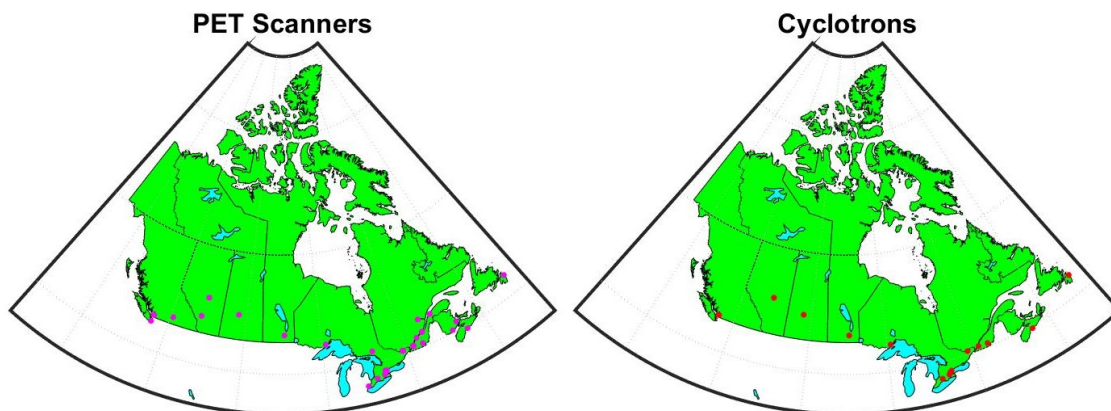


Figure 1.1: Distribution of publicly funded PET scanners and cyclotrons in Canada. Data adapted from the CMII and the IAEA cyclotron directory (CADTH, 2021; IAEA, n.d.)

In recent years, cyclotron production of radionuclides has been proposed as an alternate production strategy for radionuclides used in medicine due to global radionuclide supply shortages and increasing demand. The most abundantly used radionuclide in nuclear medicine is  $^{99m}\text{Tc}$ , with a well-established supply chain in which long-lived  $^{99}\text{Mo}$  is obtained either through fission reactions or neutron capture in a nuclear reactor. The  $^{99}\text{Mo}$  is placed in a portable generator, where it decays and provides a supply of high purity  $^{99m}\text{Tc}$  for use in local radiopharmacies. The ageing commercial nuclear reactor infrastructure used in the production of  $^{99}\text{Mo}$  led to pronounced, world-wide shortages of  $^{99m}\text{Tc}$  in 2007-2009 during scheduled maintenance and unanticipated interruptions of the National Research Universal (NRU) reactor in Chalk River, ON, which provided 31 % of the global market share of  $^{99}\text{Mo}$  (Benoit, 2010). As a result, the Canadian government made significant investments to research and install alternate production capabilities within Canada through the “Non-reactor-based Isotope Supply Contribution Program” (NISPC) and the “Isotope Technology Acceleration Program” (ITAP) (Jammal, 2017; Loughheed, 2012; Natural Resources Canada, 2013). This included investments into cyclotron infrastructure for the production of  $^{99m}\text{Tc}$ ; its 6-hour half-life allows delivery of  $^{99m}\text{Tc}$  to large areas surrounding a network of cyclotrons and radiochemistry facilities distributed throughout Canada, so that supply for the most populated areas of our country is ensured (Figure 1.1).

In addition to producing  $^{99m}\text{Tc}$ , this now-established cyclotron infrastructure can be leveraged to produce a variety of other popular or research radionuclides. For example,  $^{68}\text{Ga}$  radiolabeled tracers for diagnostic imaging have flourished due to the widespread availability of this radionuclide in a  $^{68}\text{Ge}/^{68}\text{Ga}$  generator system. However, rising costs on increased lead times for procurement of the  $^{68}\text{Ge}/^{68}\text{Ga}$  generator system have spurred interest in the cyclotron production of  $^{68}\text{Ga}$  (IAEA, 2019). Furthermore, while the use of generators proffers some advantages, including production of tracers in radiopharmacies that do not have access to a cyclotron, significant draw-backs are given by the limited daily eluted quantity of generator-produced  $^{68}\text{Ga}$  and the annually recurring cost of generator replacement and waste disposal (Kumar, 2020). A recent comprehensive report by the International Atomic Energy Agency (IAEA) on cyclotron production of  $^{68}\text{Ga}$  (IAEA, 2019) underlines its feasibility, and the excellent install base of cyclotrons in Canada provides the means for a greater abundance of  $^{68}\text{Ga}$  in clinical applications.

It is important to note that, while the tracers identified in Table 1.1 utilize the radionuclides  $^{18}\text{F}$ ,  $^{68}\text{Ga}$ ,  $^{13}\text{N}$  and  $^{82}\text{Rb}$ , research into the cyclotron-based production of a great number of other radionuclides with very promising properties for diagnostic, therapeutic and theranostic applications is on-going. Starting with pre-clinical research, such investigations pave the way for future clinical breakthroughs as has been previously observed with FDG or PSMA. Yet even pre-clinical research rests on the foundation of prior research into the production, imaging and dosimetric properties of each radionuclide in question.

## 1.2 PET Radionuclides

Many other cyclotron-produced radionuclides beyond  $^{18}\text{F}$  and  $^{68}\text{Ga}$  have PET imaging utility; these positron emitters can be produced by inelastic hadronic interactions with a variety of target materials. The proton beams produced in the majority of cyclotrons are amenable to the creation of proton-rich nuclei through (p,xn) reactions, which generally decay via  $\beta^+$  decay by emitting positrons. Similarly, deuteron and alpha particle beams production routes have been investigated for several radionuclides, although these are less widely applicable due to the beam energy limitations of conventional medical cyclotrons. Several radionuclides with application in PET are listed in Table 1.2, along with relevant decay properties. Note that typical production reactions are listed, but radionuclides may also be produced in several other nuclear reactions. Besides properties of the  $\beta^+$  emissions, Table 1.2 also lists other emissions with the greatest abundance (National Nuclear Data Center, n.d.; Schlyer, 2002).

Table 1.2: Selection of radionuclides with applications for PET

Radionuclide	Half-life	Mean (Max) positron energy	Positron branching ratio	Other emissions	Production
<sup>11</sup> C	20.4 min	386 (960) keV	99.8 %		<sup>14</sup> N(p,α) <sup>11</sup> C
<sup>13</sup> N	10.0 min	492 (1199) keV	99.8 %		<sup>16</sup> O(p, α) <sup>13</sup> N
<sup>15</sup> O	122 s	735 (1732) keV	99.9 %		<sup>14</sup> N(d,n) <sup>15</sup> O
<sup>18</sup> F	110 min	250 (633) keV	97 %		<sup>18</sup> O(p,n) <sup>18</sup> F
<sup>43</sup> Sc	3.89 h	476 (1199) keV	88.1 %	γ 373 keV (22.5 %)	<sup>43</sup> Ca(p,n) <sup>43</sup> Sc
<sup>44</sup> Sc	3.97 h	632 (1470) keV	94 %	γ 1157 keV (99.9 %)	<sup>44</sup> Ca(p,n) <sup>44</sup> Sc
<sup>64</sup> Cu	12.7 h	278 (653) keV	17 %	β <sup>+</sup> 190 (579) keV (39 %)	<sup>67</sup> Zn(p, α) <sup>64</sup> Cu
<sup>68</sup> Ga	68 min	836 (1899) keV	89 %	γ 1077 keV (3.2 %)	<sup>68</sup> Ge/ <sup>68</sup> Ga generator <sup>68</sup> Zn(p,n) <sup>68</sup> Ga
<sup>76</sup> Br	16.2 h	1180 (3941) keV	55.0 %	γ 559 keV (74 %) γ 657 keV (15.9 %) γ 1854 keV (14.7 %)	<sup>76</sup> Se(p,n) <sup>76</sup> Br
<sup>89</sup> Zr	78.4 h	396 (902) keV	23 %	γ 909 keV (99.0 %)	<sup>89</sup> Y(p,n) <sup>89</sup> Zr
<sup>124</sup> I	4.17 d	820 (2137) keV	22.7 %	γ 603 keV (63 %)	<sup>124</sup> Te(p,n) <sup>124</sup> I

These radionuclides may be categorized in several ways: organic radionuclides consist of <sup>11</sup>C, <sup>13</sup>N, and <sup>15</sup>O and are isotopes of elements commonly found in organic molecules; however, they tend to have shorter half-lives, i.e. on the order of seconds to minutes. Radiohalogens include <sup>18</sup>F, <sup>76</sup>Br and <sup>124</sup>I, which are highly reactive, can be readily incorporated into a variety of radiopharmaceuticals, and can lead to a greater binding affinity with receptors in vivo than their non-halogenated counterparts. Finally, radiometallic isotopes, such as <sup>68</sup>Ga, <sup>44</sup>Sc, <sup>64</sup>Cu and <sup>89</sup>Zr, can be labeled to peptides using chelators, among other uses.

<sup>18</sup>F has many desirable properties for PET imaging: the average energy of the positron emitted is low, leading to images with better spatial resolution. There are no prompt gammas emitted during decay and the half-life is short (i.e. 110 minutes), leading to a reduced radiation burden for the patient, yet long

enough to allow radiochemistry and transport. In addition, the decay product is oxygen, which is not toxic. With the emergence of small medical cyclotrons,  $^{18}\text{F}$  can be readily produced in many PET centres.  $^{68}\text{Ga}$  has emerged as a useful radionuclide for PET imaging due to its chelation chemistry, short half-life leading to low absorbed patient dose, and high positron branching ratio. However, some disadvantages include the high end-point energy of  $\beta^+$  decay resulting in decreased spatial resolution due to positron range, and the short half-life may lead to reduced yield in time-sensitive radiolabelling procedures.

As exemplified by  $^{18}\text{F}$  and  $^{68}\text{Ga}$ , both the physical and chemical properties of the radionuclide impact its utility in PET imaging: half-life will impact radiochemistry, patient dosimetry, optimal timing of imaging, and ability to transport the tracer to the PET imaging site. The positron emission energy will affect reconstructed image resolution and noise, as well as patient dosimetry. The chemical properties will determine the radiolabelling procedures and structure of the injected tracer, which in turn changes the tracer's biodistribution. Immuno-PET is an example of a recently developed application requiring radionuclides with half-lives specifically suited for the imaging task.

### 1.2.1 Immuno-PET

Immuno-PET is an emerging imaging technique that combines the specificity of monoclonal antibodies (mAbs) with the spatial resolution and sensitivity of PET imaging. While FDG is an excellent tracer for targeting accelerated glucose metabolism, it is non-tumour specific. mAbs are key molecules that can specifically target cellular processes such as cell proliferation and differentiation, as well as cell death and apoptosis (Dongen et al., 2007). In fact, mAbs can be used in disease-specific targeting for diagnostic imaging and therapy.

Four important considerations guide the choice of radionuclide for conducting immuno-PET studies. The first is the chemical properties of the radionuclide. It is desirable to maintain the in vivo binding & biodistribution of the unlabeled tracer, as this will allow the imaging to be indicative of the desired process. Radiohalogen labeling of mAbs, with  $^{76}\text{Br}$  and  $^{124}\text{I}$  for example, can lead to the degradation of the mAb and rapid clearance of the radiotracer from the target cells. Chelators or other groups are used to indirectly label radiometals such as  $^{68}\text{Ga}$ ,  $^{64}\text{Cu}$ ,  $^{86}\text{Y}$  and  $^{89}\text{Zr}$  to mAbs, which can lead to the radiotracers being trapped in cell lysosomes; the internalization of the mAb results in the maintenance of the tracer biodistribution.

A second consideration is the half-life of the nuclide used in the immuno-PET study. While the mAb is highly specific, its uptake in the targeted cells can vary significantly. It is important to match the half-life

of the radionuclide with the biological uptake characteristics of the tracer molecule, such that sufficient radionuclide concentration remains until the time it takes for the tracer to achieve maximum tumour-to-background (TBR) contrast. This length of this time is typically 2-4 days for mAbs, and 2-6 hours for mAb fragments. In their feasibility study with [<sup>89</sup>Zr]c-mAb U36 of a patient with head and neck squamous cell carcinoma, Dongen et al. found that the tumour contrast was superior at around 24 hours post-injection and beyond. Thus, radionuclides with significantly shorter half-lives would either provide inferior tumour contrast ratios (if imaged prior to maximum TBR), or images degraded by reduced signal-to-noise ratio (if imaged at optimum, later time points).

Thirdly, patient radiation dose generally increases for radionuclides with longer half-lives, such as the ones suited for labeling of mAbs. While long-lived radionuclides allow for imaging several days post-injection (when mAbs typically display optimal TBR contrast), radiation burden for patients also increases if similar activities are administered. This is somewhat mitigated by modern, high sensitivity PET scanners and 3D imaging protocols, which may allow smaller activities to be administered to the patient. All else being equal, a radionuclide with a shorter half-life would be preferable if feasible given the biodistribution of the tracer in question.

Finally, immuno-PET can be used as a diagnostic tool to identify patients who may be candidates for radioimmunotherapy. If the dosimetry profile found in the PET study is promising, the mAb can be labeled with a paired, therapeutic radionuclide with similar chemical properties. The mAb with the therapeutic nuclide will exhibit a biodistribution very similar to the diagnostic study. Commonly used PET radionuclides include <sup>64</sup>Cu, <sup>89</sup>Zr, <sup>86</sup>Y, <sup>124</sup>I, while their beta emitting, therapeutic counterparts for use in radioimmunotherapy (RIT) are <sup>67</sup>Cu, <sup>177</sup>Lu, <sup>90</sup>Y, and <sup>131</sup>I, respectively.

### 1.3 Theranostics

This combined approach to diagnostics and therapy has been dubbed theranostics (Rösch and Baum, 2011): the diagnostic study aims to achieve a quantitative measure of the disease through molecular imaging of the radionuclide directed by specific targeting vectors. The disease can then be treated with a therapeutic analogue of the same targeting vector using information gained from the diagnostic study to adjust treatment on an individual patient basis (precision medicine). Furthermore, treatment response and/or disease progression can be monitored through renewed use of the diagnostic molecular imaging vector. Ideally, the radionuclides used in the theranostic paradigm would be isotopes of the same element to ensure identical biodistribution. If this is not the case, additional biodistribution studies are

required prior to clinical use of a theranostic pair to establish sufficient similarity between the uptake patterns of the diagnostic and the therapeutic radiolabelled tracers.

The theranostic paradigm has flourished with the advent of specific targeting vectors such as DOTA-decorated peptides, which target G-protein coupled receptors such as octreotide or prostate specific membrane antigen (PSMA) derivatives (Baum et al., 2012; Chatalic et al., 2015). The advantage of these specific targeting vectors is the selective uptake of the tracer into target tissue with low non-specific uptake in other structures, which allows for the safe delivery of higher doses of radiation to eradicate disease. This condition is not typically fulfilled with tracers such as [<sup>18</sup>F]FDG; significant uptake in normal tissue, such as the brain, heart, kidneys and bladder limits their utility for a theragnostic approach.

Advances in radionuclide therapy (RNT) in recent years have demonstrated the importance of considering the impact of theranostics, including emerging evidence that RNT may be more effective than current standard of care for specific populations of oncology patients.

The Neuro-endocrine Tumors Therapy (NETTER-1) trial is a phase 3 multi-center clinical trial that was conducted at 41 centers in 8 countries to determine the effectiveness of [<sup>177</sup>Lu]Lu-DOTATATE treatment for midgut neuroendocrine tumors (Strosberg et al., 2017). The eligible patient population included adults with locally advanced or metastasized midgut neuroendocrine tumors which were inoperable, positive on somatostatin receptor imaging and showed progression during treatment with octreotide long-acting release (LAR). The progression-free survival (PFS), as well as the overall survival were important end-points that were examined when comparing the group of patients given [<sup>177</sup>Lu]Lu-DOTATATE in addition to best supportive care and the control group provided high-dose octreotide LAR, with tumor assessment on CT or MRI performed every 12 weeks. A significant difference at 20 months was demonstrated in a preliminary analysis, with a 65.2 % PFS for the [<sup>177</sup>Lu]Lu-DOTATATE intervention vs 10.8 % in the controls; the median PFS had not yet been reached at this time for the interventional arm but was determined to be 8.4 months for the controls. While the analysis is still on-going, these encouraging results demonstrate the efficacy of RNT, and the potential of these therapies for the effective treatment of disseminated disease.

In the case of neuroendocrine tumours, theranostics is accomplished by coupling the <sup>177</sup>Lu therapy with molecular imaging via [<sup>68</sup>Ga]Ga-DOTATOC (Baum et al., 2012; Baum and Kulkarni, 2012). This octreotide derivative helps establish an initial diagnosis by determining the tumours' somatostatin receptor status, enables staging of the disease, and helps monitor a patient's response to therapy. While standardized

doses of [ $^{177}\text{Lu}$ ]Lu-DOTATATE are currently provided to each patient, [ $^{68}\text{Ga}$ ]Ga-DOTATOC imaging may enable future clinicians to personalize dosing for their patients (Marco et al., 2019). Further research is also being conducted into other specific targeting vectors where RNT may show therapeutic advantages; one such emerging application consists of targeting prostate cancer with radiolabelled derivatives of prostate specific membrane antigen (PSMA) (Afshar-Oromieh et al., 2015). It is therefore obvious that the development of such matched pairs of radioisotopes for theranostic applications is advantageous and will enable further utilization of matched diagnostic and therapeutic targeting vectors.

## 1.4 Radioscandium

Scandium is a transition metal in the third row of the periodic table with an atomic number of 21, between calcium at 20 and titanium at 22. It has a single stable isotope with an atomic mass of 45, and several radioactive nuclides with half-lives greater than 1 hour, ranging from an atomic mass of 43 to 48.  $^{44}\text{Sc}$  is a positron emitter and is one of three isotopes of scandium of potential use in nuclear medicine:  $^{43}\text{Sc}$  is another positron emitter, while  $^{47}\text{Sc}$  is a beta emitter which could be of use in radionuclide therapy (RNT). The  $^{44}\text{Sc}/^{47}\text{Sc}$  and  $^{43}\text{Sc}/^{47}\text{Sc}$  theranostic pairs of scandium radioisotopes could serve as potential alternatives for current medical radionuclides; for example,  $^{177}\text{Lu}$  is commonly used for treatment of neuroendocrine tumours (Müller et al., 2013), often as a theranostic pair with  $^{68}\text{Ga}$ . Figure 1.2 presents the simplified decay schemes for the three radioisotopes of scandium of interest (National Nuclear Data Center, n.d.).

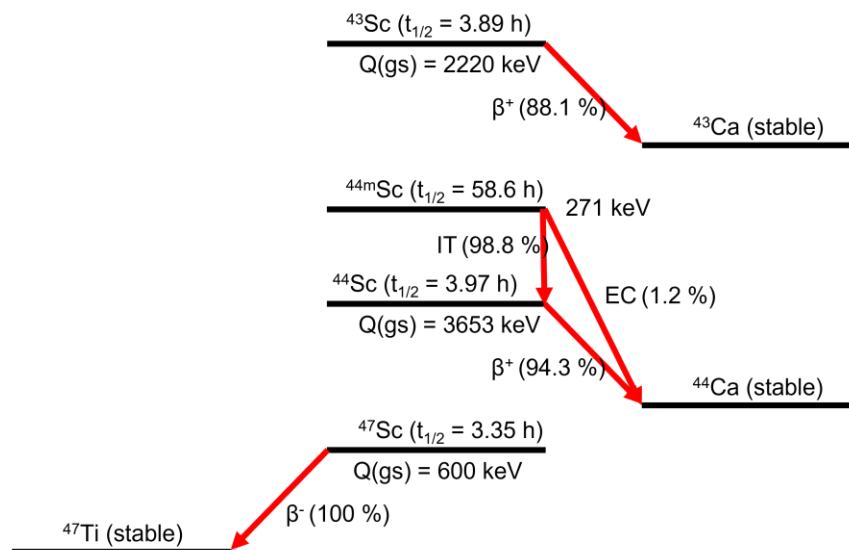


Figure 1.2 Simplified decay schemes for  $^{43}\text{Sc}$ ,  $^{44}\text{Sc}$ ,  $^{47}\text{Sc}$

Important properties of the positron emitters are presented in Table 1.2. The half-life of  $^{44}\text{Sc}$  and  $^{43}\text{Sc}$  are 3.97 hours and 3.89 hours respectively, which complements other radionuclides used in PET, such as  $^{68}\text{Ga}$ ,  $^{18}\text{F}$ ,  $^{64}\text{Cu}$  and  $^{89}\text{Zr}$  with half-lives of 68 min, 110 min, 12.7 hours and 78.4 hours, respectively. As previously discussed, the half-life of the radionuclide in PET studies should be balanced: sufficiently long to reach optimal biodistribution and target uptake, but short enough to limit the radiation burden to the patient. A longer half-life also allows for more complicated extraction chemistry and radiolabelling, as well as transportation to PET scanners at remote locations.  $^{44}\text{Sc}$  has a 94% positron branching ratio and chemical properties similar to other radionuclides currently in use, such as  $^{68}\text{Ga}$  and  $^{177}\text{Lu}$ , which makes it useful as a diagnostic imaging surrogate for existing therapies (McQuade et al., 2005). The mean positron emission energy of  $^{44}\text{Sc}$  and  $^{43}\text{Sc}$  are 632 keV and 476 keV, lower than their radiometallic counterpart  $^{68}\text{Ga}$  at 836 keV, which could improve reconstructed image quality.

Important properties of the radionuclides for use in therapeutics are presented in Table 1.3, along with one of many possible production routes (Gracheva et al., 2019; Loveless and Lapi, 2020; National Nuclear Data Center, n.d.; Smith et al., 2012). To deliver radiation during RNT, the therapeutic radionuclide must concentrate in the tumour. For therapy with a  $\beta^-$  emitter, this concentration must be high due to the low linear energy transfer (LET) of electrons, which only increases in the last few nm of their total path length of typically  $\sim 1$  cm (Kassis, 2008). Due to their short track length, the energy of the charged particles is typically absorbed locally while the x-rays and  $\gamma$ -rays contribute to the dose in a greater volume of the patient. When the goal is to irradiate local structures, it is therefore desirable for radionuclides to transfer a greater proportion of energy to charged particles, as is the case in RNT.  $^{47}\text{Sc}$  transfers a  $1.62 * 10^{-1} \text{ MeV}$  to charged particles per decay, which is similar to the commonly used therapeutic radionuclides  $^{131}\text{I}$  and  $^{177}\text{Lu}$ . While this total energy transfer is a useful measure of the therapeutic potential, further studies must be conducted to confirm the dose distribution of these radionuclides in tumours as the individual electron energies will dictate the range and dose drop-off.

Table 1.3: Properties of  $\beta^-$ -emitting therapeutic radionuclides.

Radionuclide	Half-life	X-ray, $\gamma$ -ray Radiation (MeV/Bq-s)	$\beta$ , ce, and Auger Radiations (MeV/Bq-s)	Production
$^{47}\text{Sc}$	3.349 d	$1.09 * 10^{-1}$	$1.62 * 10^{-1}$	$^{47}\text{Ti}(n,p)^{47}\text{Sc}$
$^{67}\text{Cu}$	61.83 h	$1.15 * 10^{-1}$	$1.55 * 10^{-1}$	$^{68}\text{Zn}(p,2p)^{67}\text{Cu}$
$^{90}\text{Y}$	64.05 h	-	$9.32 * 10^{-1}$	$^{89}\text{Y}(n,\gamma)^{90}\text{Y}$
$^{131}\text{I}$	8.025 d	$3.81 * 10^{-1}$	$1.90 * 10^{-1}$	$^{130}\text{Te}(n,\gamma)^{131}\text{Te} \rightarrow ^{131}\text{I}$

$^{161}\text{Tb}$	6.89 d	$0.34 * 10^{-1}$	$1.97 * 10^{-1}$	$^{160}\text{Gd}(n,\gamma)^{161}\text{Gd} \rightarrow ^{161}\text{Tb}$
$^{177}\text{Lu}$	6.647 d	$0.33 * 10^{-2}$	$1.47 * 10^{-1}$	$^{176}\text{Lu}(n,\gamma)^{177}\text{Lu}$

### 1.4.1 Radioscandium production

A robust supply of radionuclides is important for their use in pre-clinical research and clinical applications. There are several important factors to consider when investigating production routes, including (Synowiecki et al., 2018):

- *High yield and purity:* The nuclear reaction must have a sufficient cross-section in order to produce significant yields of the radionuclide, and detrimental radionuclidic contaminants must not be produced in significant amounts.
- *Target material:* The target nuclide must have sufficient natural abundance or, if needed, enriched materials must be available. This greatly affects the expense of the targetry and impact the yield and purity of the resulting product.
- *Extraction chemistry:* The radionuclide must be extracted from the target material and be able to be concentrated in a solution of sufficient quality for radiolabelling. This includes removing contaminants that would inhibit incorporation of the radionuclide, and may encompass the recovery of the target material as a cost-saving measure.
- *Half-life:* The production route must account for the half-life of the radionuclide of interest, as this will influence production rates and limit the time available for post-processing.

Several production schemes have been proposed for radioisotopes of scandium, and these are summarized in Figure 1.3 for  $^{43,44}\text{Sc}$ , the positron-emitting isotopes of scandium, and Figure 1.4 for  $^{47}\text{Sc}$ .

$^{44}\text{Sc}$  has been produced through the proton irradiation of natural abundance calcium targets (Severin et al., 2012; Valdovinos et al., 2015), enriched  $^{44}\text{Ca}$  targets (van der Meulen et al., 2015) as well as in liquid solution targets (Hoehr et al., 2014). An alternative production route is a  $^{44}\text{Ti}/^{44}\text{Sc}$  generator (Pruszyński et al., 2010; Roesch, 2012), which requires higher energy protons (25-30 MeV) and large integrated currents on target as the half-life of  $^{44}\text{Ti}$  is 60 years. Production has been proposed using alpha particle beams, such as the irradiation of  $^{42}\text{Ca}$  targets (Szkliniarz et al., 2016).

High yields of  $^{43}\text{Sc}$  have been accomplished using alpha particle beams via the  $^{nat}\text{Ca}(\alpha,p)^{43}\text{Sc}$  reaction using natural abundance calcium targets (Minegishi et al., 2016; Walczak et al., 2015), and more recently  $^{43}\text{Sc}$  has also been produced by proton irradiations via the  $^{46}\text{Ti}(p,\alpha)^{43}\text{Sc}$  and  $^{43}\text{Ca}(p,n)^{43}\text{Sc}$  nuclear reactions, resulting in radionuclidic purity of 98.2 % and 66.2 %, respectively (Domnanich et al., 2017a).

Proposed production pathways of  $^{47}\text{Sc}$  include the proton irradiation of  $^{48}\text{Ca}$  targets (Misiak et al., 2017), alpha irradiation of  $^{44}\text{Ca}$  (Minegishi et al., 2016), and gamma bombardment of  $^{48}\text{Ti}$  (Mamtimin et al., 2015; Rotsch et al., 2018; Yagi and Kondo, 1977), as well as indirect production schemes through the decay of  $^{47}\text{Ca}$  via the  $^{48}\text{Ca}(\gamma, n)^{47}\text{Ca}$  and  $^{46}\text{Ca}(n, \gamma)^{47}\text{Ca}$  nuclear reactions (Domnanich et al., 2017b; Rane et al., 2015; Starovoitova et al., 2015).

An important consideration in the production of these radioisotopes is the co-production of  $^{46}\text{Sc}$ , considered to be a contaminant; its considerably greater half-life ( $t_{1/2}=83.8$  d) is concerning for radionuclidic purity and patient dosimetry.

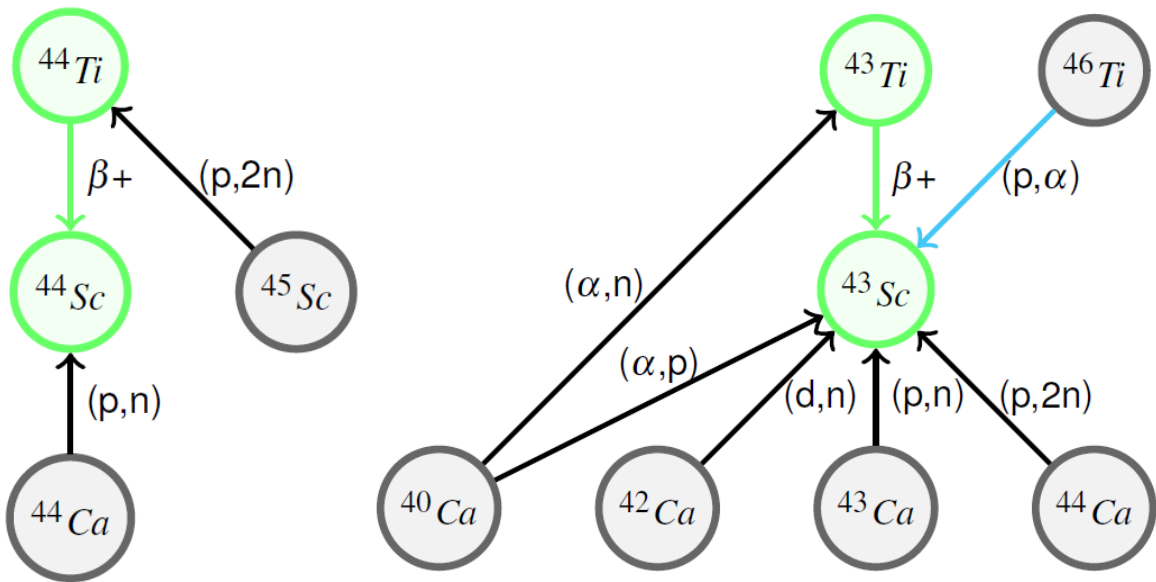


Figure 1.3: Production pathways of positron-emitting scandium nuclides  $^{43}\text{Sc}$  (right) and  $^{44}\text{Sc}$  (left)

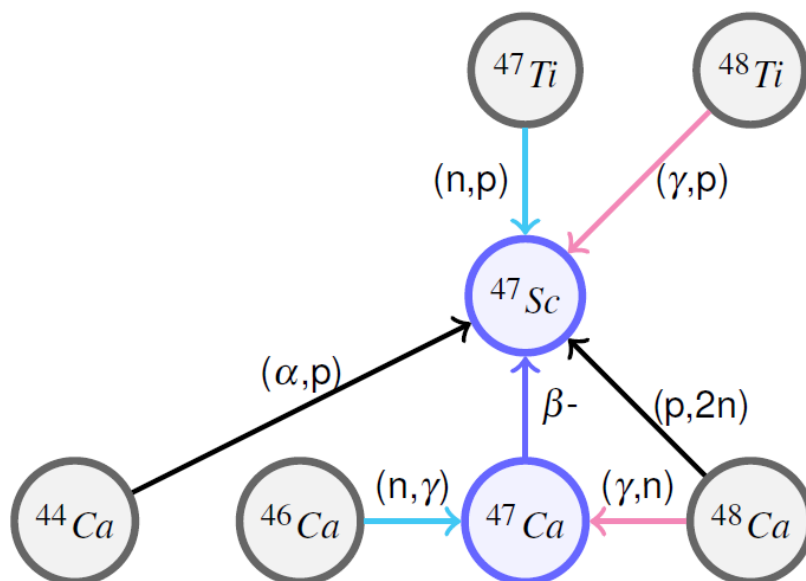


Figure 1.4: Production pathways of  $\beta^-$ -emitting radioscandium nuclide  $^{47}\text{Sc}$

### 1.4.2 Radioscandium labelling

Several review articles outline the radiolabelling and applications of radioscandium (Mikolajczak et al., 2021; Müller et al., 2018; W. Price et al., 2016). Bifunctional chelators are used in order to attach radiometals to targeting motifs; the chelators need to fulfill several requirements, including rapid complexation, mild complexation conditions, high *in vivo* stability and ready conjugation to targeting motifs (W. Price et al., 2016).

As radioscandium has become more readily available, several studies have described radiolabeling experiments, e.g. with DOTA and DTPA chelators (Alliot et al., 2015; Müller et al., 2014a; Severin et al., 2012; Valdovinos et al., 2015), with novel chelators such as AAZTA and H4pypa (Li et al., 2020; Nagy et al., 2017), and with DOTA-decorated peptides and other biomolecules, including  $[\text{}^{44}\text{Sc}]\text{Sc-DOTA-(cRGD)}_2$  (Hernandez et al., 2014),  $[\text{}^{44}\text{Sc}]\text{Sc-DOTA-TATE}$  (Huclier-Markai et al., 2014),  $[\text{}^{44}\text{Sc}]\text{Sc-DOTA-TOC}$  (Pruszyński et al., 2012),  $[\text{}^{44}\text{Sc}]\text{Sc-DOTA-NOC}$  (van der Meulen et al., 2015),  $[\text{}^{44}\text{Sc}]\text{Sc-DOTA-folate}$  (Müller et al., 2013), and  $[\text{}^{44}\text{Sc}]\text{Sc-PSMA-617}$  (Eppard et al., 2017; Umbricht et al., 2017). Other approaches include the radiolabelling of monoclonal antibodies (Chakravarty et al., 2014).

### 1.4.3 Radioscandium imaging

Several procedures exist to evaluate the performance of PET scanners (NEMA, 2018, 2008); these typically include measurements of standardized performance metrics in phantoms with measurement times and activities similar to those that will be used for *in vivo* scanning protocols. While these

measurements are usually performed for acceptance testing of scanners, they have also been used to compare the image quality for different positron emitters (Disselhorst et al., 2010).

In the first phantom imaging study with  $^{44}\text{Sc}$ , Bunka et al. compared the image resolution for several radionuclides in a Derenzo phantom and ranked the measured resolution for these radionuclides in pre-clinical imaging as  $^{68}\text{Ga} < ^{44}\text{Sc} < ^{89}\text{Zr} < ^{11}\text{C} < ^{64}\text{Cu} < ^{18}\text{F}$  (Bunka et al., 2016). This order, with  $^{18}\text{F}$  demonstrating the best resolution, is explained by the positron range of each radionuclide, which is smallest for  $^{18}\text{F}$ . Domnanich et al. subsequently compared three samples of scandium (sample 1: 99 %  $^{44}\text{Sc}$ , sample 2: 66.2%  $^{43}\text{Sc}$  and 33.3 %  $^{44}\text{Sc}$ , sample 3: 98.2 %  $^{43}\text{Sc}$  and 1.5 %  $^{44}\text{Sc}$ ) in the Derenzo phantom and found that increasing the proportion of  $^{43}\text{Sc}$  significantly decreased the measured FWHM, as expected by the lower end-point energy of the positron emitted by  $^{43}\text{Sc}$ .

The study presented in Chapter 4 of this thesis compares the standard imaging performance metrics for  $^{44}\text{Sc}$ ,  $^{18}\text{F}$ ,  $^{64}\text{Cu}$  and  $^{68}\text{Ga}$  using the NEMA image quality phantom, a Derenzo phantom and an NEC phantom in a preclinical PET scanner (Ferguson et al., 2019). Many of these measurements were repeated by Rosar et al. in their comparison of the phantom imaging of  $^{44}\text{Sc}$  and  $^{68}\text{Ga}$  in two preclinical PET scanners and confirmed our results (Rosar et al., 2020). Lima et al. assessed image quality of  $^{44}\text{Sc}$  in a commercial PET scanner to characterize signal recovery and investigate reconstruction protocols, including the available scatter corrections and prompt-gamma correction; they found that the recovery coefficients were greater than the previously recommended range (Lima et al., 2020). This indicates that corrections techniques require further optimization to improve quantitation of PET scans with  $^{44}\text{Sc}$ . Finally, Rosar et al. compared the activity recovery of  $^{44}\text{Sc}$  and  $^{18}\text{F}$  in preclinical and clinical scanners and concluded that while the reconstructed activity with  $^{44}\text{Sc}$  is underestimated, a single constant correction factor could be used to improve the quantitative accuracy (Rosar et al., 2021).

Several *in vivo* preclinical PET imaging studies have been conducted with a variety of radiolabelled tracers previously outlined. For example, Umbricht et al. investigated the *in vitro* and *in vivo* properties of [ $^{44}\text{Sc}$ ]Sc-PSMA-617, as a match for the therapeutic counterpart [ $^{177}\text{Lu}$ ]Lu-PSMA-617, in comparison with existing diagnostic tracers [ $^{68}\text{Ga}$ ]Ga-PSMA-617 and [ $^{68}\text{Ga}$ ]Ga-PSMA-11 (Umbricht et al., 2017); the authors demonstrated high tumour uptake in PC-3 tumour cells in mouse models with increasing tumor-to-background contrast up to 4 h post-injection, and found the *in vivo* kinetics of the  $^{44}\text{Sc}$  labeled analogue to be more similar to the  $^{177}\text{Lu}$  than either of the  $^{68}\text{Ga}$  radiolabeled ligands.

$^{47}\text{Sc}$  is a beta emitter well suited for radionuclide therapies. Like  $^{131}\text{I}$  and  $^{177}\text{Lu}$ ,  $^{47}\text{Sc}$  also emits a prompt photon with high abundance (68.3% at 159 keV) and therefore can be imaged using SPECT or SPECT/CT (Domnanich et al., 2017b); Domnanich et al. reported excellent visual agreement between [ $^{47}\text{Sc}$ ]Sc-DOTATOC SPECT scans and [ $^{44}\text{Sc}$ ]Sc-DOTATOC PET scans in a AR42J tumor-bearing mouse.

To date, clinical use of radioscandium for diagnostic imaging is limited and focuses on tracers that had their clinical utility first established when labeled with  $^{68}\text{Ga}$ : [ $^{44}\text{Sc}$ ]Sc-DOTATOC and [ $^{44}\text{Sc}$ ]Sc-PSMA-617 (Eppard et al., 2017; Khawar et al., 2018a, 2018b; Singh et al., 2017). Singh et al. imaged two patients following peptide receptor radionuclide therapy with [ $^{44}\text{Sc}$ ]Sc-DOTATOC, which allowed for the detection of small lesions with increasing tumor-to-background ratios for up to four hours post-injection (Singh et al., 2017). First-in-human studies with [ $^{44}\text{Sc}$ ]Sc-PSMA-617 have demonstrated an improved pre-therapeutic dosimetry compared to [ $^{68}\text{Ga}$ ]Ga-PSMA-617, for [ $^{177}\text{Lu}$ ]Lu-PSMA-617 radionuclide therapy of castrate-resistant prostate cancer (Eppard et al., 2017).

#### 1.4.4 Radioscandium therapy

While several investigations have demonstrated the feasibility of producing  $^{47}\text{Sc}$ , few studies have demonstrated its potential as a therapeutic radionuclide; this therapeutic potential is central to the application of radioscandium towards theranostics.

Champion et al. compared the efficacy of  $^{67}\text{Cu}$ ,  $^{47}\text{Sc}$ , and  $^{161}\text{Tb}$  for the irradiation of small tumors in simulations with the Monte Carlo code CELDOSE (Champion et al., 2016); these radionuclides were chosen because of their potential for use in theranostics with their diagnostic counterparts  $^{64}\text{Cu}$ ,  $^{43,44}\text{Sc}$ , and  $^{152,155}\text{Tb}$ . To compare the dose delivered to micrometastases or single cell tumours, the authors simulated the doses absorbed in spheres ranging from 5 mm to 10  $\mu\text{m}$ ; the dose from a single radioactive decay (S-values) and the absorbed dose normalized to total energy released by electrons for each radionuclide was compared. While Champion et al. conclude that  $^{161}\text{Tb}$  delivers a greater dose to the smaller diameter spheres, the doses delivered by the electrons emitted from all three radionuclides is nearly identical in the 5-mm metastases.

Müller et al. used a  $^{47}\text{Sc}$ -radiolabelled DOTA-folate conjugate (cm10) to investigate the therapeutic potential of  $^{47}\text{Sc}$  (Müller et al., 2014a). They determined the biodistribution of the [ $^{47}\text{Sc}$ ]Sc-cm10 in folate receptor-positive KB tumor-bearing mice, and compared the tumor growth and survival time of mice receiving 10 MBq of [ $^{47}\text{Sc}$ ]Sc-cm10 as compared to controls; they demonstrated that the treatment induced significant delays in tumor growth and increased the survival time by more than 50 %. In a

follow-up study, Nardo et al. used the biodistribution data from the murine models in the previous study to extrapolate the activity curves in human organs using relative mass scaling (Nardo et al., 2021).

In a related study, Siwowska et al. investigated the therapeutic potential of  $^{47}\text{Sc}$  as compared to the more established therapeutic radionuclides  $^{177}\text{Lu}$  and  $^{90}\text{Y}$  with the same DOTA-folate conjugate (Siwowska et al., 2019). In a study of ovarian tumour cells in a murine model, the authors determined that the tumor growth was similarly inhibited by each radiolabelled compound when the injected dose was controlled to obtain the same absorbed tumor dose of 21 Gy: 12.5 MBq [ $^{47}\text{Sc}$ ]Sc-folate, 10 MBq [ $^{177}\text{Lu}$ ]Lu-folate, and 5 MBq [ $^{90}\text{Y}$ ]Y-folate. Siwowska et al. also found that the intervention increased the median survival of the mice from 26 days in the controls to 39, 43 and 41 days respectively; they conclude that  $^{47}\text{Sc}$  is a promising radionuclide for therapeutic applications and likely comparable to  $^{177}\text{Lu}$ .

## 1.5 Thesis overview

Emerging radiometals may play an important role in the future of nuclear medicine, particularly with emphasis on theranostics. The purpose of this chapter was to provide some context on PET tracers used in nuclear medicine; the choice of radionuclide in a PET imaging study should be based on its physical and chemical properties and the desired application. Before adopting a radionuclide, it is important to study its production, properties and quantify how it will affect image quality. The work in this thesis details results of the development of a local production programme, including radiolabelling, which has enabled a steady supply of  $^{44}\text{Sc}$  for preclinical imaging studies. The production of  $^{44}\text{Sc}$  was investigated based on predictive calculations and imaging properties systematically compared with common PET radionuclides. The approach undertaken here can be adapted to evaluate other emerging radionuclides, to predict yields and investigate imaging characteristics. Peptide radiolabelling was performed to demonstrate the use of radioscandium in preclinical *in vivo* research studies of cancer models in mice.

An overview of the physics that serves as a basis for understanding the remaining work in this thesis is presented in Chapter 2. In particular, the physics of radioactivity and particle interactions with matter are relevant to radionuclide production and PET imaging.

Experimental surveys are often conducted to determine the viability of production routes for emerging radionuclides. Radionuclide yield calculations can facilitate this process by determining irradiation parameters and predicting yields prior to purchasing target material and performing irradiations, helping curtail the cost and narrow down the experimental scope. Chapter 3 investigates several predictive approaches and compares these with measurements of radionuclide yields of proton-induced reactions

on natural calcium targets. A common approach to radionuclide yield calculations utilizes experimental cross-section data, complemented with cross-sections determined from models for reactions that have not been investigated experimentally. Here, a tool has been developed to calculate radionuclide yield and production of contaminants over a range of energies and target thicknesses (Appendix A); it was one of the first general purpose graphical user interfaces to calculate radionuclide yield from charged particle beams using both experimental and semi-empirical cross-section data. Recent improvements in modelling proton cross-sections in the Monte Carlo simulation package Geant4 have sparked interest in using simulations for radionuclide yield calculations (Amin et al., 2018; Poignant et al., 2016).

Experimental measurements of the thick target yields of radioscandium isotopes ( $^{43}\text{Sc}$ ,  $^{44\text{g,m}}\text{Sc}$ ,  $^{46}\text{Sc}$ ,  $^{47}\text{Sc}$ , and  $^{48}\text{Sc}$ ) and  $^{47}\text{Ca}$  produced from natural calcium targets were made over the range of 12 and 18 MeV. Few yield measurements of these radionuclides have been performed in natural calcium targets. These measurements were compared with predictions based on calculations with cross-sections from experimental measurements and TENDL, as well as Monte Carlo simulations with Geant4, to determine the accuracy of predicting yields and contaminants.

The work presented Chapter 4 expands on the limited investigations of  $^{44}\text{Sc}$  in preclinical phantom imaging, which consists of  $^{44}\text{Sc}$  imaging studies in Derenzo phantoms. The decay characteristics of the radionuclide used in a PET study can impact image reconstruction and affect image quality. Previous Derenzo phantom measurements by Bunka et al. revealed differences in the resolution of reconstructed images which increased with decreasing mean positron energy (Bunka et al., 2016). To further quantify reconstructed image quality, phantom imaging experiments comparing  $^{44}\text{Sc}$ ,  $^{18}\text{F}$ ,  $^{68}\text{Ga}$  and  $^{64}\text{Cu}$  were carried out on the Siemens Inveon small-animal PET scanner at the CCI. The NEMA Image quality phantom was used to determine standard performance metrics under typical preclinical imaging conditions. A procedure first adapted by Disselhorst et al. was used to compare the recovery coefficients (RC), spill-over ratios (SOR), and noise (%SD) for the different radionuclides (Disselhorst et al., 2010). Additional measurements were completed in the Derenzo phantom and the NEC phantom to investigate contrast and coincidence characteristics of these radionuclides.

The focus of Chapter 5 is the application of  $^{44}\text{Sc}$  produced on a cyclotron from natural calcium targets for radiolabelling and preclinical *in vivo* imaging. Radiolabelled peptides can be used to specifically target protein receptors and have demonstrated great potential for the imaging and targeting of cancer. A metabolically stabilized gastrin-releasing peptide receptor (GRPR) antagonist was previously synthesized and was used here to evaluate the quality of the cyclotron produced  $^{44}\text{Sc}$ . Radiolabelling was performed

with both  $^{44}\text{Sc}$  and generator-derived  $^{68}\text{Ga}$ . The *in vitro* GRPR binding affinity of the bombesin complexes with scandium and gallium were compared, as well as the biodistribution of these tracers in breast and prostate cancer xenographs. Previous studies of bombesin derivatives by Koumarianou et al. have demonstrated that the choice of radionuclide may affect *in vitro* and *in vivo* properties of radiotracers (Koumarianou et al., 2012, 2009). This study builds on previous work to contrast the properties of  $^{44}\text{Sc}$  and  $^{68}\text{Ga}$  bombesin derivatives and explore differences and similarities between the two radiometal labeled radiotracers, as well as evaluate the radiotracer uptake in breast and prostate cancer models. Finally, Chapter 6 presents a summary of the work and highlights potential future applications and research areas of radios scandium.

## Chapter 2

### Background

---

---

#### 2.1 Radionuclides and the atom

Since early in its discovery, radiation has been used to form images, such as the famous radiograph of Mrs. Röntgen's hand, only a few months after the discovery of x-rays in 1895 (Goodman, 1995). Several models of the atom have been created to explain the various observed physical phenomena, and these models form the basis for the applications of radiation used in this thesis and explained in this chapter.

Atoms are composed of protons and neutrons, which together form a compact nucleus surrounded by electrons that are confined to energy levels while orbiting this nucleus. The distinct energy levels at which electrons are bound are unique for each atom; electrons can be excited to higher levels and can decay down to lower energy levels if these are not occupied. The nucleons can exist outside of atoms; their masses have been measured and the neutron is slightly more massive than the proton, with a mass of  $939.6 \text{ MeV}/c^2$  vs  $938.3 \text{ MeV}/c^2$ . The neutron is unstable outside of the atom, decaying into a proton accompanied by the emission of an electron and anti-neutrino with a mean lifetime of about 15 minutes, as described below in Section 2.1.2 about  $\beta$  decay.

The smallest nuclei are the hydrogen and deuterium atom, which are composed of a single proton and a proton bound to a neutron respectively. By the mass-energy equivalency Einstein described in his theory of special relativity, the energy contained in the atomic nucleus is enclosed in the mass of its nucleon constituents as well as the binding energy holding the nucleons together. The binding energy of a nucleus can be described as a function of its constituents:  $Z$  protons,  $N$  neutrons, and their sum  $A$  nucleons. It is well approximated by Eq. 2.1 (liquid drop model of the nucleus) where the coefficients are determined by fitting the equation to empirical data.

$$B(Z, A) = a_v A - a_s A^{\frac{2}{3}} - a_c Z(Z - 1)A^{-\frac{1}{3}} - a_{sym} \frac{(A - 2Z)^2}{A} + \delta \quad (2.1)$$

The first term,  $a_v A$ , has the binding energy increase proportional to the number of nucleons. This represents the attraction of nucleons to their closest neighbours, with each on average having the same number of neighbours (rather than an attraction to all other nucleons present in the nucleus which would result in an  $A^2$  proportionality). The second term,  $a_s A^{2/3}$ , represents a reduction in these binding forces in the nucleus due to the nucleons on the surface being surrounded by fewer neighbours and therefore being less tightly bound; this term, like a water droplet's surface, is proportional to the square of the radius of the nucleus, and thus is on the order of  $A^{2/3}$ . The third term,  $a_c Z(Z - 1)A^{-1/3}$ , represents the mutual Coulomb repulsion of the protons and thus reduce the binding energy; each proton repels all others present which gives the form of this term  $Z(Z - 1)$ , with the assumption of a uniformly charged sphere yielding the  $A^{-1/3}$  term (the 'radius' of the water droplet). The fourth term with the coefficient  $a_{sym}$  deals with the symmetry of nucleons: observation shows that in stable nuclei the number of protons is generally about half the total number of nucleons. Thus, when  $Z = A/2$ , this term is minimized. This applies more to light nuclei due to the greater effect of Coulomb repulsion in heavy nuclei which requires the addition of neutrons to increase stability. The last term,  $\delta$ , represents a quantum-mechanical pairing force of nucleons which tend to couple to form stable configurations: for even N and Z, it can be expressed as  $+a_p A^{-3/4}$ , for Z and N odd  $-a_p A^{-3/4}$ , and zero for odd A.

This binding energy is used in the semiempirical mass formula (Eq. 2.2), which can be used to calculate the mass  $M$  of an atom as a function of the number of its constituent protons and neutrons, where  $m({}_1^1H)$  represents the mass of an  ${}_1^1H$  atom,  $m_n$  the mass of a neutron, and  $c$  is the speed of light.

$$M(Z, A) = Zm({}_1^1H) + Nm_n - B(Z, A)/c^2 \quad (2.2)$$

Figure 2.1 shows the half-lives of known nuclei plotted as a function of their constituent number of protons and neutrons (National Nuclear Data Center, n.d.). An isotope is a nuclear species with the same number of protons but with varying numbers of neutrons, i.e. the nuclides within the same elemental species. An isotone is a nuclear species with the same number of neutrons but with varying numbers of protons. An isobar is a nuclear species with the same overall number of nucleons. An isomer consists of a nucleus with the same number of protons and neutrons but excited into a higher energy level than that of the ground state. This description of the binding energy is relevant to nuclear medicine as this will inform the modelling of unstable atoms decaying to nuclei with lower binding energies, as well as the projectile energy required to form an unstable atom during irradiation.

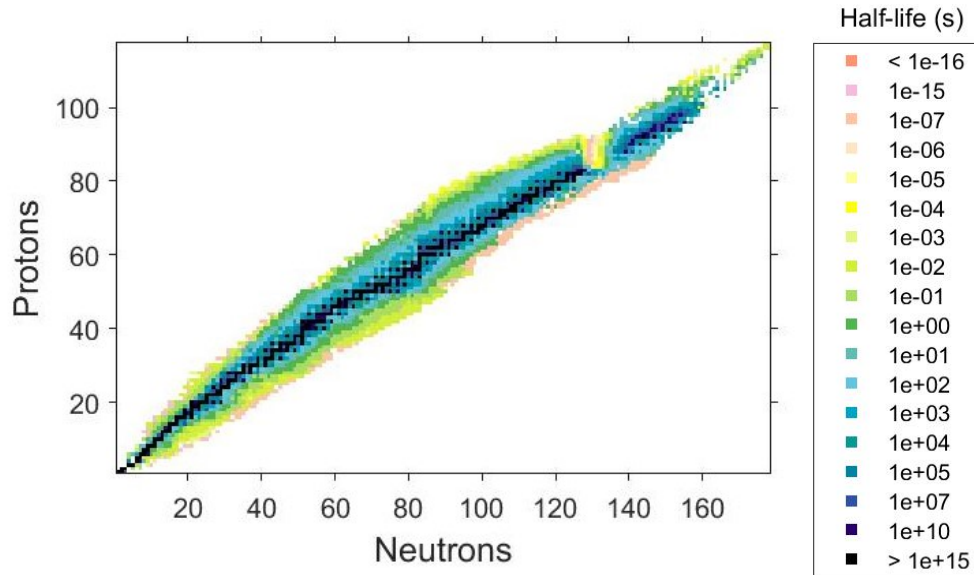


Figure 2.1: Half-lives of nuclides.

### 2.1.1 Radioactivity

Radioactive atoms can be found in naturally occurring materials, such as uranium ore and minerals containing thorium, or made artificially e.g. in nuclear reactors or particle accelerators. These unstable atoms decay with a constant mean lifetime; their decay is statistical in nature and can be described by a Poisson distribution. It is not possible to predict when an individual atom will decay, but the number of decays occurring on average in a large sample can be predicted. Eq. 2.3 describes the change in the number of unstable atoms as it relates to the total number of radionuclides in the sample  $N$ .

$$\frac{dN}{dt} = -\lambda N \quad (2.3)$$

In this equation, the proportionality factor  $\lambda$  is known as the decay constant, which represents the probability that an atom decays per unit time. Thus, the number un-decayed radionuclides present in a sample as a function of time  $t$  follows from integrating Eq. 2.3, where  $N_0$  is the number of unstable atoms at  $t = 0$ :

$$N(t) = N_0 e^{-\lambda t} \quad (2.4)$$

Carrying out the integrals to calculate the mean lifetime  $t_m$  of the parent nuclei reveals  $\lambda$  to be the inverse of their mean lifetime. More intuitively, the half-life  $t_{1/2}$  is the time required to reduce the number of parent nuclei by a factor of two. These values are related as follows in Eq. 2.5:

$$t_{1/2} = \log(2) t_m = \frac{\log(2)}{\lambda} \approx \frac{0.693}{\lambda} \quad (2.5)$$

The number of radioactive atoms present in a sample is difficult to determine directly, but the number of atoms undergoing decay can usually be measured by their emissions, which will be discussed later in this chapter. It is helpful to quantify the number of atoms undergoing decay per unit time, and this quantity is named the activity; it is related to the number of unstable nuclei in Eq. 2.6, where  $A_0$  is the activity at  $t = 0$ :

$$A(t) = \lambda N(t) = \lambda N_0 e^{-\lambda t} = A_0 e^{-\lambda t} \quad (2.6)$$

This is the instantaneous rate of decay of atoms in a sample. The number of decays  $D(t)$  over a finite time interval  $t$  is found by integrating the activity over the desired interval:

$$D(t) = \int_0^t A(\tau) d\tau = \int_0^t A_0 e^{-\lambda \tau} d\tau = \frac{A_0}{\lambda} (1 - e^{-\lambda t}) \quad (2.7)$$

In the limiting case where the half-life is much longer than the time interval used to observe the decay of the sample ( $t \ll t_{1/2}$ ), the number of decays  $D(t)$  can be approximated as the product of the activity and the time interval:

$$D(t) = \frac{A_0}{\lambda} (1 - e^{-\lambda t}) = \frac{A_0}{\lambda} (1 - [1 - \lambda t + O((\lambda t)^2)]) \approx A_0 t \quad (2.8)$$

Some unstable parent nuclei decay into daughter nuclei which are themselves unstable. The number of each nuclei present in a sample can be described by a pair of differential equations, where  $\lambda_i$  is the decay constant of nuclide  $N_i$ :

$$\begin{aligned} \frac{dN_1}{dt} &= -\lambda_1 N_1 \\ \frac{dN_2}{dt} &= \lambda_1 N_1 - \lambda_2 N_2 \end{aligned} \quad (2.9)$$

Solving these coupled equations reveals that  $N_1$  takes the form previously shown in Eq. 2.4 and  $N_2$  takes the form in equation 2.10, where  $N_{i0}$  represents the initial number of  $N_i$  atoms:

$$N_2(t) = \frac{\lambda_1}{\lambda_2 - \lambda_1} N_{10} (e^{-\lambda_1 t} - e^{-\lambda_2 t}) + N_{20} e^{-\lambda_2 t} \quad (2.10)$$

Bateman (Bateman, 1910) generalized this solution to a decay chain of arbitrary length (Eq. 2.11) in which each radionuclide  $i$  decays into another nuclide  $i + 1$  with decay constant  $\lambda_i$  in an extension of

the coupled differential equations 2.9; this Bateman equation, with the assumption that initially solely  $N_{10}$  atoms of the first nuclide are present, is:

$$N_n(t) = N_{10} \times \left( \prod_{i=1}^{n-1} \lambda_i \right) \times \left( \sum_{i=1}^n \frac{e^{-\lambda_i t}}{\prod_{j=1, j \neq i}^n (\lambda_j - \lambda_i)} \right) \quad (2.11)$$

### 2.1.2 $\beta$ decay & detection

Unstable nuclei can decay by emitting particulate radiation.  $\beta$  decay can be described as a proton in a nucleus being converted to a neutron or vice versa, allowing an unstable nucleus to approach a stable isobar; the total number of nucleons remains constant while the number of protons and neutrons will increase or decrease by one.

In  $\beta^-$  decay, a neutron decays to proton, emitting an electron ( $\beta^-$ ) and antineutrino ( $\bar{\nu}$ ):



On the other hand, in  $\beta^+$  decay, a proton will decay to a neutron, emitting a positron ( $\beta^+$ ) and a neutrino ( $\nu$ ) as per Eq. 2.13.



This conversion of the proton to a neutron in atomic nuclei can also occur through the capture of an orbital electron, in which case a positron will not be emitted, as per Eq. 2.14.



Unlike  $\alpha$  decay which is a two-body process, the  $\beta$  particles are emitted with a continuous energy spectrum because the kinetic energy of the produced particles is shared with the neutrino. Both particles take form during the decay process, and thus the masses must be accounted for in the calculation of the energetics of the reaction. The mass of the neutrino, on the other hand, is several orders of magnitude smaller than the mass of the electron and of the transition energy available from the change in atomic configuration.

Several factors affect the energy distribution (spectrum) of the emitted  $\beta$  particles, including a statistical factor accounting for the number of final states after decay (encompassing the nuclear, electron and neutrino wave functions), as well as the Fermi function accounting for the Coulomb attraction and repulsion of the nucleus. Figure 2.2 displays the positron energy spectrum of some radionuclides used in PET (Eckerman and Endo, 2008).

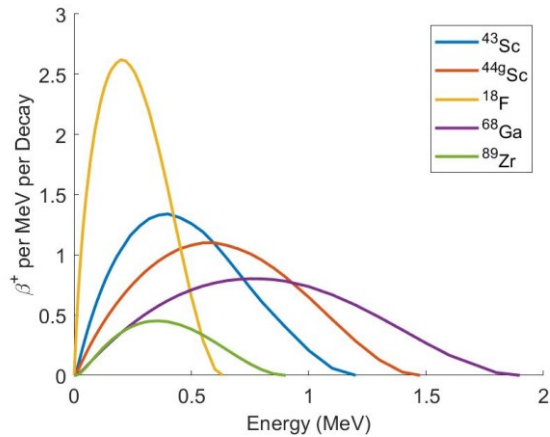


Figure 2.2: Energy spectrum of  $\beta^+$  particles emitted during the decay of radionuclides for PET.

## 2.2 Particle interactions in matter

### 2.2.1 Photon interactions in matter

It is important to consider photon interactions in matter because of their relevance for imaging, radiation detection and nuclear physics. Among the many possible interactions, the processes of greatest importance for this thesis will be explored: the photoelectric effect, Compton scattering and pair production. The relative importance of each process as a function of photon energy and atomic number is shown below in the Figure 2.3 (Berger et al., 2010).

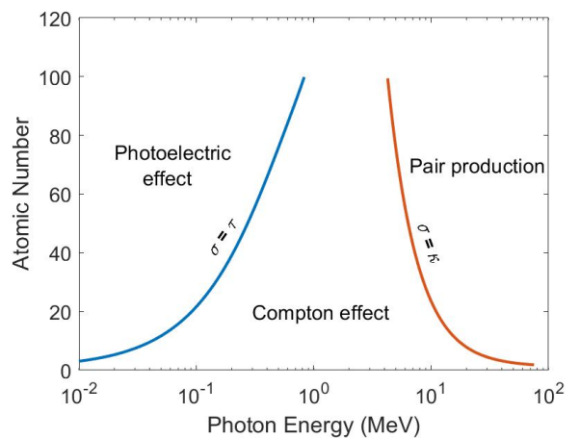


Figure 2.3: Dominant photon interaction in material of atomic number  $Z$  for each photon energy regime, where  $\sigma$  denotes the Compton effect cross-section,  $\tau$  denotes the photoelectric effect cross-section, and  $\kappa$  denotes the pair production cross-section.

The photoelectric effect describes the process in which a photon is absorbed by a bound electron, which is then excited and can be ejected from the atom. For this process to occur, the energy of the photon  $E_p$

must be greater than the atomic binding energy of the electron  $E_b$ . The kinetic energy,  $T$ , imparted to the electron is calculated as:

$$T = E_p - E_b - T_a \quad (2.15)$$

Conservation of energy and momentum is facilitated by the atom to which the electron is bound. The atom itself gains recoil energy  $T_a$ ; because the ratio of the energy imparted to the atom to the electron is inversely proportional to their mass ratio, this quantity is usually ignored in calculations. While the theoretical handling of the photoelectric cross-section is complicated, its dependence on  $Z$  and  $E_p$  can be approximated for energies less than 0.1 MeV by Eq. 2.16. As outlined in Figure 2.3, photoelectric absorption of photons is most important at lower energies and for materials with high atomic numbers.

$$\sigma_{PE} \propto \frac{Z^4}{E_p^3} \quad (2.16)$$

When an inner-shell electron is excited and ejected from the atom, it can create vacancies in the electron shells, which can be filled by relaxing electrons. These transitions will cause characteristic x-rays to be emitted during the relaxation of outer-shell electrons; they are termed characteristic because the photons' energy equals the difference between the inner-shell binding energy and the binding energy of the shell from which the electron relaxes. In an alternate process to the emission of a characteristic x-ray, an Auger electron can be released with this characteristic energy, minus their binding energy.

The Compton effect consists of inelastic photon scattering, which alters both the primary photon's energy and direction of travel. This process is important as a detrimental effect in imaging because of scattered photons affecting the distribution of photon counts used to reconstruct images. It is also important in radiation detection as the scattered photon will have a reduced energy with respect to the primary photon, and thus the expected number of photons contributing to the single energy peak (photo peak) will be decreased.

The energy of a photon  $E'$  scattered at a given angle  $\phi$  with a known starting energy  $E$  can be calculated using conservation of momentum and energy, resulting in Eq. 2.17, where  $E_0$  is the energy associated with the electron rest mass (511 keV).

$$E' = \frac{E}{1 - \frac{E}{E_0}(1 - \cos \phi)} \quad (2.17)$$

The energy imparted to the electron  $T$  is the difference between the photon energy prior and after being scattered:

$$T = E - E' \quad (2.18)$$

An expression for the differential cross-section of this process  $\frac{d\sigma_e}{d\Omega}$  was given by Klein and Nishina (Klein and Nishina, 1928):

$$\frac{d\sigma_e}{d\Omega} = \frac{r_0^2}{2} \left(\frac{E'}{E}\right)^2 \left(\frac{E}{E'} + \frac{E'}{E} - \sin^2 \phi\right) \quad (2.19)$$

Where  $r_0 = e^2/m_0c^2 = 2.818 * 10^{-13}cm$  is known as the classical electron radius. The total cross-section per electron ( $\sigma_e$ ) of this process is obtained by integrating this differential cross-section over all angles. The Compton mass attenuation coefficient in a material  $\frac{\sigma_C}{\rho}$  is thus dependent on the density of electrons,  $\sigma_e$ , present in the scattering material (calculated using Avogadro's number  $N_A$ ):

$$\frac{\sigma_C}{\rho} = \frac{N_A Z}{A} \sigma_e \quad (2.20)$$

Pair production consists of the absorption of a photon in an electric field leading to the production of an electron-positron pair. The photon must have energy greater than  $2m_0c^2 = 1.022 MeV$  as both an electron and positron arise from this interaction, and this is the sum of their resting mass. Consequently, the kinetic energy received by the electron ( $T^-$ ) and the positron ( $T^+$ ) follow the energy conservation Eq 2.21.

$$E = 2m_0c^2 + T^- + T^+ \quad (2.21)$$

An expression for the atomic differential cross-section of this process in the nuclear coulomb force field was derived by Bethe et al. (Bethe et al., 1934). If this expression is integrated over all possible values of kinetic energy imparted to the positron, it is found that the mass attenuation coefficient for nuclear pair-production  $\frac{\sigma_{PP}}{\rho}$  is proportional to the total atomic cross-section for pair production,  $\kappa_a$ , and can be approximated as in Eq. 2.22.

$$\frac{\sigma_{PP}}{\rho} = \kappa_a \frac{N_A}{A} \propto Z \quad (2.22)$$

Pair production can occur in the coulomb field of an electron; however, energy conservation dictates that the energy threshold for this process to occur is  $4m_0c^2 = 2.044 \text{ MeV}$ , which is greater than the photon energies considered in this thesis for activity quantification and imaging (c.f. Chapters 3-5).

The total photon attenuation in a material is dictated by the sum of the individual processes occurring; if both the source of the photons and the detector are collimated, attenuation of a photon beam follows an exponential law as in Eq. 2.23. It is dependent on the initial (source) photon intensity  $I_0$ , the linear attenuation coefficient  $\mu$  in the material, and the linear distance,  $x$ , travelled:

$$I = I_0 e^{-\mu x} \quad (2.23)$$

Where  $\mu$  encompasses all photon interactions considered here:

$$\mu = \sigma_{PE} + \sigma_C + \sigma_{PP} \quad (2.24)$$

### 2.2.2 Charged-particle interactions in matter

Charged-particle interactions are important to consider as they determine the positron range in PET imaging and the behaviour of protons during the irradiation of a target material in radionuclide production. In contrast to uncharged radiation, charged particles are surrounded by an electric field and interact with the constituent nuclei and electrons of a material. While travelling through a medium, charged particles undergo many interactions, each of which transfer varying amounts of their kinetic energy to secondary electrons or nuclei in the medium. Each interaction is stochastic: the energy loss and direction change cannot be predicted for an individual interaction as it is governed by a probability distribution. However, because the number of interactions is large ( $\sim 10^5$  interactions for a 1 MeV particle), the total path length before the particle of a given initial energy comes to rest is clustered about the mean that would be observed for a large number of such particles. This expected path length is called the range of the particle.

The relative size of the impact parameter  $b$  and the atomic radius  $a$ , depicted in Figure 2.4, is used to separate the different types of interactions.

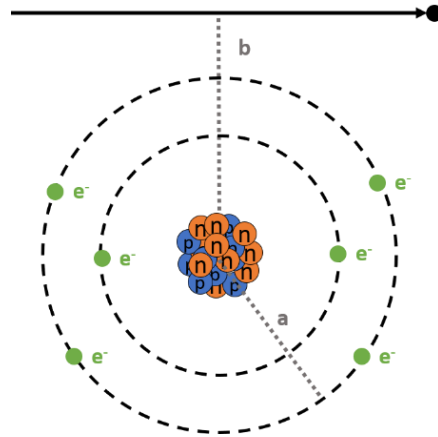


Figure 2.4: Depiction of impact parameter  $b$  for a charged-particle interaction with an atom of radius  $a$

The greatest number of interactions that charged particles undergo in a medium are “soft” collisions, in which charged particles are passing an atom at a large distance ( $b \gg a$ ). Such interactions can excite electrons to higher energy level or eject valence electrons. While individual interactions transfer small amounts of energy (on the order of a few eV) to the atom, the great number of these interactions account for about half of the energy transferred to the material.

In “hard” collisions, the charged particle interacts with a single charged constituent in the material, i.e. an electron or atomic nucleus. If interacting with an electron (i.e.  $b < a$ ), it is ejected from the atom. This electron is called a delta ( $\delta$ ) ray and has a significant amount of kinetic energy, which will be absorbed along the  $\delta$ -ray’s path while it undergoes coulomb-force interactions. Similar to the photoelectric effect, a characteristic x-ray or Auger electron can be emitted if an inner-shell electron is excited or ejected. The probability for these collisions to occur is dependent on the properties of the interacting particle, including their spin, and can vary greatly.

The charged particle can also interact with the nuclear Coulomb field when  $b \ll a$ . Electrons and positrons are more likely to undergo these interactions than heavier charged particles. In the majority of these interactions, the charged particle undergoes elastic scattering, in which minimal energy is lost and the particle is deflected. In 2-3% of cases, the charged particle interacts inelastically and emits an x-ray photon while being deflected. These are called bremsstrahlung x-rays, due to their slowing of the charged-particle (from the German word for breaking: “bremsen”); these x-rays can carry away a large portion of the kinetic energy of the particle. This is the main type of interaction utilized for the generation of x-rays in medical imaging; by accelerating electrons towards a tungsten anode, they interact with this high-Z material by emitting x-rays, which are collimated and used for imaging. Of note

is that the atomic cross-section of this process is proportional to the  $Z^2$  of the material, and thus it is not as important in tissue-like materials. Additionally, it has an inverse square dependence on the mass of the charged particle and as such is not important for protons.

A process of particular importance to PET is electron-positron annihilation. Particles can annihilate when they encounter their anti-particles; when a positron annihilates with an electron, two 511 keV photons are produced. In general, these are co-linear and travel in opposite directions,  $180^\circ$  apart. However, the interaction does not always occur at rest, and in-flight annihilation will cause the energy of one or both of the photons to increase slightly, as well as a slight deviation from the  $180^\circ$  distribution to conserve momentum.

### 2.2.3 Stopping power and range

As previously stated, individual interactions are stochastic but due to the large number of interactions, the behaviour of charged particles travelling through matter can be approximated by expectation values. The stopping power  $\left(\frac{dE}{dx}\right)$  is the energy loss per unit path length (in MeV/cm) of a charged particle, and is dependent on the type of particle, its energy and the characteristics of the material. The mass stopping power normalizes stopping power to the density of the material traversed. For dosimetric purposes, it can be useful to decompose the total stopping power into radiative and collisional components, but this is not the focus of the work in this thesis.

For heavy particles, the Bethe-Bloch equation (Eq. 2.25) describes the energy-dependent stopping power, where  $e$  is the elementary charge,  $z$  is the number of elementary charges of the charged particle,  $\beta$  is the particle's velocity relative to the speed of light  $c$ , and  $I$  is the mean excitation potential of the struck atom.

$$\left(\frac{dE}{dx}\right) = \frac{4\pi e^4}{m_0 c^2 \beta^2} \frac{N_A Z z^2}{A} \left[ \ln \left( \frac{2m_0 c^2 \beta^2}{I(1 - \beta^2)} \right) - \beta^2 \right] \quad (2.25)$$

For electrons and positrons, the soft-collision term derived by Bethe can be complemented by the Moller cross section for electrons  $F^-(\tau)$  and Bhabha cross section for positrons  $F^+(\tau)$  to derive a total stopping power in Eq. 2.26, where  $\tau = T/m_0 c^2$  is the charged particle energy scaled by its rest mass, and  $\delta$  is a correction term for polarization:

$$\left(\frac{dE}{\rho dx}\right)_c = \frac{2\pi e^4 N_A Z Z^2}{m_0 c^2 \beta^2 A} \left[ \ln \left( \frac{\tau^2 (\tau + 2)}{2 \left( \frac{I}{m_0 c^2} \right)^2} \right) + F^\pm(\tau) - \delta - \frac{2\pi N_A}{A} \left( \frac{e^2}{m_0 c^2} \right)^2 \right] \quad (2.26)$$

The total range  $r$  (cm) of a particle of energy  $E_0$  is estimated by the product of the material density  $\rho$  (g/cm<sup>3</sup>) and the integral of the mass stopping power (MeV · cm<sup>2</sup>/g) up to the incoming particle energy, as in Eq. 2.27. This range represents the distance the particle travels. However, collisions will cause non-zero scatter angles and lead to beam straggling, shortening the actual projected range of a particle. This effect is more pronounced for lighter particles such as electrons and positrons.

$$r = \frac{1}{\rho} \int_0^{E_0} \left( \frac{dE}{\rho dx} \right)^{-1} dE \quad (2.27)$$

Calculations for radionuclide production (c.f. 2.3.3) involve the use of the stopping power to determine energy loss of hadrons in targets. In practice, the SRIM software package is used to determine the stopping power of hadrons in targets (Ziegler et al., 2010). This package has been extensively used, with 700 citations per year. It provides data about mass stopping power that have been validated to be within 10 % of expected values for 85 % of data points for protons.

#### 2.2.4 Radiation detection

Three types of detectors are commonly used in radiation detection: gas-filled detectors, semi-conductor detectors and scintillators.

Gas-filled detectors are found in many areas in nuclear medicine, such as dose rate monitoring to ensure staff safety. As the name implies, an electric field is applied to a detector chamber containing a gas. In nuclear medicine, the chamber typically does not communicate with ambient air and the fill gas is usually inert, such as xenon. When ionizing radiation traverses the chamber, it interacts with the gas as previously discussed, ejecting electrons which are then accelerated by the electric field. At sufficiently high electric potential, these electrons interact with the neutral gas atoms to create cascades of electrons which are collected at the cathode of the detector. Gas-filled detectors operate in several regimes, depending on the strength of the applied electric field: in an ion chamber, chamber current is in fixed relation to the energy deposited in the gas volume; in a proportional counter, the amount of current generated is proportional to the energy deposited by the radiation that traverses the gas

chamber; in a Geiger-Mueller counter, the whole chamber gas gets ionized when only one interaction with the gas volume takes place.

Semi-conductor detectors such as high-purity germanium (HPGe) detectors provide an alternative method of detecting radiation. HPGe detectors consist of germanium crystals, where the constituent atoms have four valence atoms, which all participate in the covalent bonds filling the valence band. There is an energy gap on the order of 1 eV between the valence band and the empty conduction band, to which electrons can be thermally excited at room temperature, leaving a “hole” in the valence-band which can be filled by electrons from neighboring atoms. The spontaneous production of electron-hole pairs can be limited by cooling the detector with liquid nitrogen. Electrical conduction can be further controlled in semiconductor detectors by the addition of dopants; n-type detectors are made by adding atoms with 5-valence electron impurities such as P, As and Sb, while p-type detectors incorporate impurities with 3-valence electrons such as Li. By combining both these types of detectors and applying a reverse voltage bias, a depletion region is created at the junction of the two materials. This is caused by the migration of holes and electrons due to the electric field, which leaves behind fixed donor and acceptor sites. Radiation entering this zone releases electron-hole pairs. These migrate in the electric field to create an electronic signal that is amplified. Since the number of electron-hole pairs created depends on the amount of energy deposited in the p-n-junction, this energy is inferred from the amplitude of the signal.

Scintillation detectors are used in many applications, including in certain PET scanners and gamma cameras, and operate through a process known as luminescence. They consist of atoms in a crystal lattice, in which the energy levels have broadened such that the outermost electrons fill a valence band, and there is an energy gap of forbidden bands up to a higher energy conduction band; this gap is on the order of a few electron volts. When electrons in the valence band absorb energy, they are excited into the conduction band and de-excite with the emission of a scintillation photon to return to the ground state. To control the energy of the scintillation photon, impurities are added to the crystal to produce additional lower energy states and optical photons of longer wavelength. These optical photons can then be detected by a photodetector. The important properties of scintillation detectors used in PET imaging are described further below.

### 2.3 Radionuclide production

There are three common sources of radionuclides used in medicine: nuclear reactors, generators, and cyclotrons. Important considerations for radionuclide production include: the cost and availability of

target materials, the maximum yield of the production route and the radionuclidic purity of the resulting product, the processing of the target material and extraction of the product (with an emphasis on a procedure which can result in automation) and ensuring sufficient demand exists for the product to justify its production cost (Synowiecki et al., 2018).

High neutron flux is used to activate the target material in a nuclear reactor; this results in the high-efficiency production of neutron-rich radionuclides, generally for use in radionuclide therapy. While a single nuclear reactor can supply a large region, there is a high cost for the building and operation of such a facility, and it can result in long-lived radioactive waste. Nuclear reactors often serve to produce the long-lived parent nuclide for a radionuclide generator. Here, a short-lived daughter radionuclide of interest is eluted from a column onto which the parent radionuclide is adsorbed; as the long-lived parent decays, the activity of the daughter radionuclide increases to reach an equilibrium, and it can be regularly eluted for use in medical procedures. Radionuclide generators are convenient as they can be stored at the clinical site and eluted for several months (dependent on the parent-daughter nuclides in question); long-lived waste is returned to the manufacturer after use. However, the total number of doses eluted from the generator is limited by the decay characteristics of the radionuclides and suitable quality assurance procedures must be able to detect breakthrough of the parent radionuclide, which may occur after a large number of elutions.

Cyclotrons use charged particle beams (protons, deuterons, alpha particles, other ion beams) to activate targets. They generally produce proton rich elements, and are used for the majority of radionuclides used in PET. Cyclotrons are comparatively less expensive than nuclear reactors, produce less long-lived radioactive waste and can be installed at several suitable sites (i.e. population centres). While cyclotrons can produce radionuclides with high yields and radionuclidic purity, a network is usually required to accommodate the logistics of distributing short-lived radionuclides and the variety of radionuclides produced depends on the beam energies available.

### 2.3.1 Cyclotron

The cyclotron is a particle accelerator, first conceived by Lawrence in Berkeley in 1929, in which a charged particle is bent into an approximately circular path by a magnetic field and concurrently is repeatedly accelerated by an alternating electric field. This is accomplished by having a particle move inside a semi-circular metallic chamber named a “dee”, in which it experiences only a magnetic field and thus follows a circular orbit, before exiting the dee and being accelerated towards the other dee by an electric field caused by a voltage difference between the two dees. This voltage difference reverses

every time the particle exits a dee, creating many incremental accelerations as the particle repeatedly crosses the space between the dees.

A particle with charge  $q$  travelling with a velocity  $v$  in a magnetic field with strength  $B$  experiences a force perpendicular to both the direction of travel and the magnetic field, known as the Lorentz force. In the absence of other forces, a charged particle of mass  $m$  travelling at a velocity  $v$  in a magnetic field will follow a circular orbit of radius  $r$ , with the Lorentz force providing the centripetal acceleration, which is described by the balance of forces:

$$F = qvB = \frac{mv^2}{r} \quad (2.28)$$

The radius at which a particle travels is directly proportion to its momentum, and inversely proportional to the charge and magnitude of the magnetic field. By isolating the velocity, one finds an inverse relationship to these quantities:

$$v = \frac{qBr}{m} \quad (2.29)$$

The energy of the accelerated particle, which depends on its velocity, can be related to its charge, magnetic field strength and radius of curvature:

$$T = \frac{1}{2}mv^2 = \frac{q^2B^2r^2}{2m} \quad (2.30)$$

Thus, the energy of the particle extracted can be selected by adjusting the radius at which the particle is extracted. In cyclotron models where a hydrogen anion is accelerated, a carbon foil is placed at the appropriate radius. The foil strips the electrons from the travelling hydrogen anion which is then bent in the opposite direction by the magnetic field due to reversing the magnitude of the Lorentz force, and allows a proton beam to be extracted from the cyclotron. This proton beam is then directed onto a target material and produce radionuclides through inelastic hadronic interactions.

### 2.3.2 Reaction kinematics

Nuclear reactions can occur when a projectile  $x$  is accelerated towards a station target  $X$  to produce  $Y$  and  $y$  as the reaction products, where  $Y$  is usually a heavy product and  $y$  is a light particle, which can escape the target and can be detected or measured. This can be written as  $X(x, y)Y$ , or alternatively:



Nuclear reactions conserve the total energy and linear momentum, as well as the proton and neutron number separately for low energy processes. The energy balance, in which  $m_i$  represents the rest mass of each constituent  $i$  in the reaction, and  $T_i$  the kinetic energies, is:

$$m_X c^2 + T_X + m_x c^2 + T_x = m_Y c^2 + T_Y + m_y c^2 + T_y \quad (2.32)$$

The reaction Q value is defined as the initial mass energy minus the final mass energy, or the difference of the kinetic energy of the products and the reactants, as demonstrated in Eq. 2.33. In the case of a positive Q value, the reaction is exoergic and a portion of the binding energy of the reactants is converted to the kinetic energy of the final products. Conversely, a negative Q value indicates an endoergic reaction in which the kinetic energy of the projectile or target is converted in binding energy of the products.

$$Q = (m_X + m_x - (m_Y + m_y)) * c^2 = T_Y + T_y - T_X - T_x \quad (2.33)$$

A consequence of endoergic reactions is that a minimum threshold energy,  $T_{th}$ , exists for a projectile  $x$  to induce a nuclear reaction when impinging onto a stationary target atom  $X$ ; the projectile needs to possess a minimum kinetic energy of:

$$T_{th} = -Q \frac{(m_X + m_x)}{m_X} \quad (2.34)$$

### 2.3.3 Radionuclide production

Calculations of radionuclide production can be made using the reaction cross-section, which represents the probability that a nuclear reaction will occur and quantifies this probability in terms of a characteristics area. The rate of product formation  $R$  (reactions/s) is related to the cross-section  $\sigma$  (mb =  $10^{-27}$  cm), the number of target atoms per area  $N_a$  (atoms/cm<sup>2</sup>) and the proton fluence  $\Phi$  (protons/cm<sup>2</sup>/s) by:

$$R = N_a \sigma \Phi \quad (2.35)$$

While this is a convenient description for thin targets, the reaction cross-section depends on the energy of the projectile particle; this energy gradually decreases while the projectile traverses a thick target. Target thickness can be defined by its linear thickness  $r$  (cm), but a more useful quantity to quantify target thickness is areal density  $x$  (g/cm<sup>2</sup>) which is the product of the linear thickness and the density.

The areal density is a useful measure as pressed targets produced at different times may have varying densities and linear thicknesses.

$$x = r \cdot \rho \quad (2.36)$$

To estimate the rate of product formation for thick targets, the cross-section must therefore be integrated over the range of energies of the projectile throughout the target thickness. For a proton beam that is completely stopped in a thick target, the production rate  $R$  (reactions/s) in Eq. 2.37 is proportional to the number of target atoms per gram  $N_T$  (*atoms/g*) assuming constant density, and the integral of the ratio of the energy-dependent cross-section  $\sigma(E)$  (mb =  $10^{-27}$  cm<sup>2</sup>) and the mass stopping power of the protons  $\frac{dE}{\rho dx}$  (MeV · cm<sup>2</sup>/g) up to the incoming proton energy  $E_{in}$ . The production rate is also affected by the flux of protons in the target, which is controlled by the proton beam current  $I$  (μA), and the elementary charge of the proton  $e$  (C).

$$R = \frac{I}{e} N_t \int_0^{E_{in}} \frac{\sigma(E)}{\left(\frac{dE}{\rho dx}\right)} dE \quad (2.37)$$

The number of target atoms per gram  $N_t$  in a sample can be calculated with Eq. 2.38 using Avogadro's constant  $N_A$  (atoms/mol), the molar mass  $m$  (g/mol) of the target.

$$N_t = \frac{N_A}{m} \quad (2.38)$$

For a radioactive product nuclei with decay constant  $\lambda$  and with a rate of formation  $R$ , the number of nuclides  $N$  follows the differential Eq. 2.39. An important assumption of the calculation is that the formation of the nuclide  $N$  does not significantly decrease the number of target atoms, which is most generally the case for cyclotron target irradiation. The solution is presented in Eq. 2.40.

$$\frac{dN}{dt} = R - \lambda N \quad (2.39)$$

$$N(t) = \frac{R}{\lambda} (1 - e^{-\lambda t}) \quad (2.40)$$

The relationship between activity and number of radionuclides can be used to determine the activity produced as a function of time, as seen in Figure 2.5. As demonstrated, the activity produced with time increases but reaches a maximum when there is equilibrium between the formation rate and the decay

of the produced radionuclide. This quantity is named the saturation yield,  $a_{sat}$  (MBq/  $\mu$ A). The activity formed during an irradiation as a function of time  $A(t)$  (MBq) can be written as:

$$A(t) = a_{sat}I(1 - e^{-\lambda t}) \quad (2.41)$$

Another important property of radionuclide production is the physical target yield  $\alpha_{phys}$ , which represents the initial production rate at  $t = 0$ , and can be calculated from the saturation yield with Eq. 2.42.

$$\alpha_{phys} = a_{sat} * \lambda \quad (2.42)$$

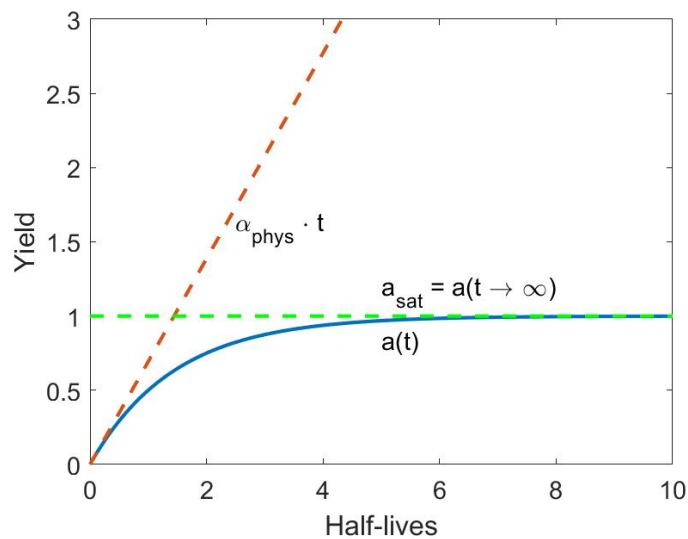


Figure 2.5: Depiction of radionuclide yield production parameters

Cross-section measurements for many reaction channels of interest have been measured and are compiled in the Experimental Nuclear Reaction Data (EXFOR) library (Otuka et al., 2014). These are often used in calculations for predicting radionuclide yield for specific irradiation parameters. Other libraries have been compiled from nuclear models to complement the experimental data and are useful for predictions of radionuclide yield when there is no experimental data available; in particular the TALYS-based evaluated nuclear data (TENDL) library is frequently used for these applications (Koning et al., 2019).

### 2.3.4 Beam monitoring

Monitor reactions consist of nuclear reactions that have been thoroughly studied and are well characterized over an energy range of interest. These are useful for characterizing charged particle

beams, such as for measurements of beam intensity and energy, since variations in these parameters can greatly affect radionuclide production. Several reviews of the available experimental data have been conducted and recommended numerical values of reaction cross-sections are tabulated for practical use as monitor reactions (IAEA, 2001).

Various techniques make use of monitor reactions to determine beam energy. The activity of a radionuclide produced in a thin foil will be proportional to the energy-dependent cross-section  $\sigma$  ( $10^{-27}$  cm<sup>2</sup>), target atoms per area  $N_a$  (atoms/cm<sup>2</sup>), beam current  $I$  ( $\mu$ A) and depends on the time of irradiation  $t_I$ , as per Eq. 2.43.

$$A = N_a I \sigma (1 - e^{-\lambda t_I}) \quad (2.43)$$

This relation can be used to determine the beam energy directly by irradiating a thin foil with a product radionuclide with a well-characterized energy-dependent cross-section; however, uncertainties in the activity measurement, as well as the target thickness, beam current and irradiation time can lead to errors in the energy. Another method of determining the beam energy involves measuring the activity ratio of two radionuclides produced within a single foil, thereby eliminating uncertainties in foil thickness and beam current (Eq. 2.44). The energy is deduced, with the help of the known monitor reactions, from the ratio of the cross-sections, which in turn is determined by the measured activity ratio of the two radionuclides produced in the single foil. This procedure still requires a well-calibrated detector to make precise measurements of activity.

$$\frac{A_1}{A_2} = \frac{\sigma_1 (1 - e^{-\lambda_1 t_I})}{\sigma_2 (1 - e^{-\lambda_2 t_I})} \quad (2.44)$$

An activity-calibration independent method of determining beam energy was proposed by using the activity ratio of the same radionuclide in two different foils, which are irradiated simultaneously interspersed by an energy degrader (Gagnon et al., 2011); for example, two copper foils producing Zn isotopes interspersed by an aluminum degrader, which changes the energy seen by each foil. The ratio of the activities of the same radionuclide in each foil is proportional to the ratio of the energy-dependent cross-section in each foil; through careful selection of the thickness of the energy degrader, this technique has demonstrated the ability to calculate the beam energy of a proton beam in a dose calibrator (Gagnon et al., 2011).

The intensity of a charged particle beam can be measured on cyclotrons through a current pick-up on electrically isolated targets. However, secondary electrons produced during irradiation can affect this

reading. One method to better characterize the total beam intensity during radionuclide production is to place a thin foil directly adjacent to the target material. The beam current  $I$  can then be deduced from equation 2.43 above. Other methods of monitoring beam intensity have been developed; for example, the UniBeam detector is built from doped silica ( $\text{Ce}^{3+}$  and  $\text{Sb}^{3+}$ ) and optical fibers have been used to monitor currents in the 1 pA to 20  $\mu\text{A}$  range (Auger et al., 2016).

### 2.3.5 Yield quantification

Gamma spectrometry is one technique used to quantify the activity of radionuclides produced in a cyclotron through the measurement of the gamma rays they emit. This non-destructive technique can be used to analyze multiple nuclides at once. The basic components for these measurements include a detector and a multichannel analyzer (MCA); HPGe detectors are commonly used for this application. As previously discussed, HPGe detectors produce a pulse for each gamma ray that interacts in the detector which is proportional to the energy deposited in the detector. The MCA receives the pulses, which are amplified and converted to discrete channels based on pulse height; the spectrum is formed by displaying the number of counts as a function of the channel number. Higher count rates will cause dead time losses in the detector, which should be kept below 10 % to decrease the error associated with the counts in each channel.

Ideally, a gamma ray is completely absorbed to produce a single peak in the spectrum, and the width of the peak is an indication of the resolution of the detector. The relationship between the channel number and the energy of the absorbed gamma ray can be determined through an energy calibration. This is accomplished through the measurement of sources that emit gamma rays of known energy and then fitting the gamma ray energy to the centroid channel number of its photopeak. Unknown radionuclides can be identified by comparing the detected photopeaks on the calibrated spectrum to the known decay characteristics of each radionuclide, which can be found in databases such as NUDAT(National Nuclear Data Center, n.d.). Ideally, the gamma rays used to identify the radionuclides have a high intensity and an energy that is different from other commonly produced radionuclides.

In practice, the ideal interaction of a gamma ray with the detector is through the photoelectric effect: the photoelectron receives all the photon's energy and ideally disperses all that energy in the detector material, resulting in a single peak. If the gamma ray interacts through Compton scattering and the scattered photon escapes the detector, the energy absorbed by the detector is dictated by the energy imparted to the recoil electron. The range of energies varies according to Eq. 2.17 and 2.18 from 0 eV, when the photon scatters with an angle  $\phi \cong 0$ , to a maximum value when the photon backscatters at an

angle  $\phi = 180^\circ$ . This will cause a Compton continuum and Compton edge at the energy  $E_{Compton}$ , which is dependent on the gamma ray energy  $E$  as outlined in Eq. 2.45. If the energy of the gamma ray is greater than 1.022 MeV, pair production can occur within the detector volume; if annihilation photons escape, single and double escape peaks can occur at energies of 0.511 MeV and 1.022 MeV below the energy of the photopeak.

$$E_{Compton} = E \left( 1 - \frac{1}{1 + \frac{2E}{E_0}} \right) \quad (2.45)$$

Figure 2.6 shows the spectrum acquired from a calibrated  $^{137}\text{Cs}$  NIST source.  $^{137}\text{Cs}$  undergoes  $\beta^-$  decay and emits a 661 keV photon with 85.1 % abundance. The photopeak can clearly be visualized in the spectrum, as can the Compton edge at 477 keV and the Compton continuum at energies below. Other notable features include signals from photons that have entered the detector after interacting with lead shielding surrounding the detector: x-ray peaks around 80 keV as well as backscattered photons, which form a backscatter peak from 184 keV.

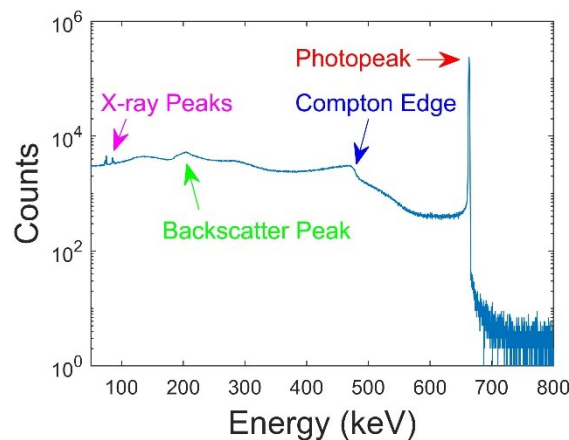


Figure 2.6: Spectrum of  $^{137}\text{Cs}$  source measured in HPGe detector

Not every gamma ray emitted by the sample and measured in the detector contributes to the signal in the photopeak; an efficiency calibration is required to convert the number of counts measured to the activity of the sample.

In practice, for a single energy and a fixed geometry, the efficiency can be calculated using calibrated sources of known activity; the efficiency is the ratio of the counts in the net peak area of the photopeak of the measured spectrum to the expected counts calculated from the decay-corrected activity of the calibration source at start of counting. The number of expected counts in the net peak area  $PA_E$  for a calibration source of activity  $A_{cal}$ , decay constant  $\lambda$ , time since calibration  $t_{cal}$ , gamma ray intensity  $I_\gamma$ , detector real time  $t_R$  and detector live time  $t_L$  is calculated using:

$$PA_E = A_{cal} \times e^{-\lambda t_{cal}} \times (1 - e^{-\lambda t_R}) \times I_\gamma \times \frac{t_L}{t_R} \quad (2.46)$$

Thus, if the measured net peak area of the photopeak for the calibration source has  $PA_M$  counts, then the efficiency  $\epsilon$  can be determined by:

$$\epsilon = \frac{PA_M}{PA_E} \quad (2.47)$$

The efficiency is energy dependent. Several calibrated sources which emit gamma rays over a wide range of energies should be used to determine the detector efficiency at these energies; this distribution can be fitted and interpolated to determine the efficiency at other energies of interest. The unknown activity of a radionuclide in a sample at the start of counting can then be calculated using:

$$A_{soc} = \frac{PA_M}{\epsilon(E_\gamma)I_\gamma} \times \frac{1}{(1 - e^{-\lambda t_R})} \times \frac{t_R}{t_L} \quad (2.48)$$

## 2.4 PET imaging

In contrast to CT, the signal that is used to reconstruct images in nuclear medicine originates from within the bore of the scanner, i.e. from inside a patient where the radionuclide is distributed and emits the radiation that is received by the detector. In the case of PET, the radionuclide emits a positron during  $\beta^+$  decay, which travels through the surrounding matter, interacting as previously outlined until it annihilates with an electron. This causes two 511 keV photons to be emitted at  $180^\circ$  (in the center of mass frame of reference) which will then interact with the PET detector. Electronic collimation is employed, in which the time difference between the detection of each photon is used to determine if these could have originated from the same positron annihilation, and the point of origin annihilation is assumed to be on the line intersecting the two points at which the photons were detected, called the line-of-response (LOR). To acquire images, a PET system must be able to detect 511 keV photons and digitize their signal, identify pairs of 511 keV photon originating from the same decays, and organize the data prior to reconstruction into images.

### 2.4.1 Spatial Resolution

There are many factors that affect the spatial resolution of PET system which is described by the FWHM and FWTM values of the PSF in the tomograph (Goertzen and Thiessen, 2017).

Discrete detectors limit the solid angle coverage of detector pairs, which causes the response profile of the two detectors to change as a function of the distance of the source between the two detectors. The coincidence response function is triangular with a FWHM that is half of the detector width and goes to zero at the detector edge when the source is equidistant from the two detectors, and changes to become trapezoidal then rectangular as the source distance to one of the detectors is decreased.

The annihilation photons travel through a thickness of the detector prior to being absorbed and can travel through discrete detector elements prior to interacting in the detector further from the surface. If the source of photons is not originating from the center of the field of view, the angle of incidence of the photon to the detector surface can be large leading to an increased uncertainty in the location of the photon interaction within the detector element. This depth of interaction will affect spatial resolution mainly in the radial direction as the uncertainty in the photon location increases as the source is further away from the center of the detector, leading to a decreased resolution  $R_{DOI}$  which is dependent on the source distance from the center of the detector ring  $r$ , the radius of the detector ring  $R$  and the mean depth of penetration of the photons in the detector  $L$ .

$$R_{DOI} = \frac{Lr}{\sqrt{r^2 + R^2}} \quad (2.49)$$

As the positron is emitted from the radionuclide nucleus with kinetic energy, it travels a distance prior to annihilating with an electron. The distribution of the total displacement of the positron has been characterized by a Lorentzian distribution and depends on the parent radionuclide (Levin and Hoffman, 1999). This displacement is called the positron range, and the contribution of the positron range to the blurring of the spatial resolution is often described by the root-mean-square value of the total displacement distribution. For example, the maximum positron energy of  $^{18}\text{F}$  is 634 keV and the effective positron range is 0.54 mm in human tissue (Lecomte, 2009).

The annihilation photons are not always emitted  $180^\circ$  apart as the positron may annihilate prior to coming at rest. To conserve energy and momentum, the photons are noncollinear which introduces

uncertainty in the line of response and degrades the spatial resolution in a way that is proportional to the diameter of the PET detector ring  $R$  according to equation 2.50 (Moses, 2011).

$$R_{noncollinearity} = 0.0044R \quad (2.50)$$

In addition to these effects, decoding errors and block effects can lead to a degradation of the spatial resolution as a smaller number of electronic channels are used to read out multiple detector elements, and nonuniform sampling of the field of view can lead to degradation of high-frequency components of the image signal. The image reconstruction algorithm can also degrade resolution as to compensate for noise smoothing filters are often used, such as Gaussian filters with FWHM kernels of 3-5 mm. Overall, when adding these factors in quadrature, the degradation of resolution  $R_{tot}$  in a PET system can be summarized by the following equation, where the positron range  $R_{\beta+}$  and the block decoding error are included  $R_b$ , as well as a 1.25 factor to describe the contribution of additional resolution degradation from image reconstruction (Moses, 2011):

$$R_{tot} = 1.25 * \sqrt{\left(\frac{d}{2}\right)^2 + R_{\beta+}^2 + (0.0044R)^2 + R_b^2 + \frac{(Lr)^2}{r^2 + R^2}} \quad (2.51)$$

## 2.4.2 Photon Detection

Photon detection is of primary importance to the PET imaging and therefore several important detector properties need to be considered. Detector rings are often made of scintillators crystals, in which the high-energy photons are absorbed and generate optical photons. The attenuation length of the scintillator, which depends on the atomic number of its constituent atoms and its density (see section 2.1.2), determines the efficiency in absorbing the annihilation photons arriving at the detector; a shorter attenuation length increases the efficiency as more photons are stopped in the detector. The light output describes the number of optical photons generated per annihilation photon; greater light output increases spatial and energy resolution. The energy resolution of the scintillator determines the distribution of the detector signal amplitude when a single photon of the same energy is detected. Greater energy discrimination reduces the photopeak width, thus allowing for greater energy discrimination, i.e. use of a smaller photopeak energy window. The luminescence decay constant governs the timing properties of the crystal and dictates the time it takes for the signal from a single photon interaction to decay; this becomes more important at high count rates, as a longer decay time may lead to a pulse pile-up and greater deadtime.

One common material used is lutetium oxyorthosilicate doped with cerium  $\text{Lu}_2\text{SiO}_5:\text{Ce}$  (LSO). This is a crystal with several desirable properties for PET: a high density ( $7.4 \text{ g/cm}^3$ ) and high effective atomic number (65.5) which results in a high attenuation coefficient ( $0.8658 \text{ cm}^{-1}$ ) and short attenuation length (1.16 cm); a light output of 29 photons/keV of energy deposited and an intrinsic FWHM energy resolution of 9.1 % at 511 keV; and a 40 ns decay constant which allows for high count rates. While LSO has many desirable properties for PET, one disadvantage is the inclusion of the radioactive isotope  $^{176}\text{Lu}$ , which has a natural abundance of 2.6 %, into the detector; it undergoes  $\beta$  decay and emits several photons (307 keV with 93.6 % abundance, 202 keV with 78.0 % abundance) with a half-life of  $3.8 \cdot 10^{10} \text{ y}$ , which contribute to intrinsic counts detected.

After being generated, optical photons are converted into an electrical signal, generally using photo-multiplier tubes (PMTs) or semiconductor-based photodiodes. The PMTs operate by detecting the optical photons and exciting photoelectrons in the photo-cathode; these electrons are accelerated by a series of increasing positive voltages to several dynodes, at which several electrons are additionally ejected from the increasing kinetic energy of each of the incident electrons, resulting in an amplified electric signal. This can then be further amplified and used to determine energy and timing of the detected photon.

If the generated signal surpasses an amplitude threshold, a timing window of predetermined length  $2\tau$  is opened. If the start of a second pulse indicating another photon detection arrives within this window, then these photons are deemed to have originated from the same positron annihilation event. The main factor that influences the width of the coincidence window is the detector's timing resolution; the timing resolution is determined by the amount of time and the consistency with which the signal threshold level is reached as a consequence of photoelectrons being created within the PET system. The timing resolution is affected by the physical properties of the detector such as the light output and the photodetection efficiency, as well as the properties of the electronics used in the pre-amplification of the detected signal. Another factor that influences the width of the timing window is the diameter of the ring detector because an off-axis annihilation event leads to different arrival times at opposite sides of the detector. This fact can be exploited in modern PET scanners by measuring this time-of-flight (TOF) difference extract additional information about the origin of the annihilation event on the LOR. Generally, the timing window is two to three times wider than the timing resolution of the PET system and a smaller timing window reduces the rate of random coincidences (c.f. 2.4.3).

It is therefore essential in PET to detect two photons within the coincidence timing window and determine whether each photon's energy measured by the detector crystal is encompassed within the energy window. An angle of acceptance is defined as an additional restriction, in which events with LOR is outside of this angle are rejected because they originate beyond the FOV of the reconstructed image. These restrictions help discriminate between true coincidences, in which both photons detected originate from the same positron annihilation event, random coincidences, and scatter coincidences. These three types of events are depicted in Figure 2.7. Multiple corrections must be applied to quantify the activity within the FOV in the reconstructed image. For example, variations in detector efficiency and solid angle can cause different sensitivities for different LORs. Normalization allows for the correction of these variations. A direct approach for normalization includes the measurement of a uniform positron source, and the normalization coefficients are proportional to the inverse of counts detected along each LOR. Other corrections are described in further detail below with some information about the procedure used for corrections. This discussion is necessarily limited as there has been much research conducted into these various corrections and many proposed solutions.

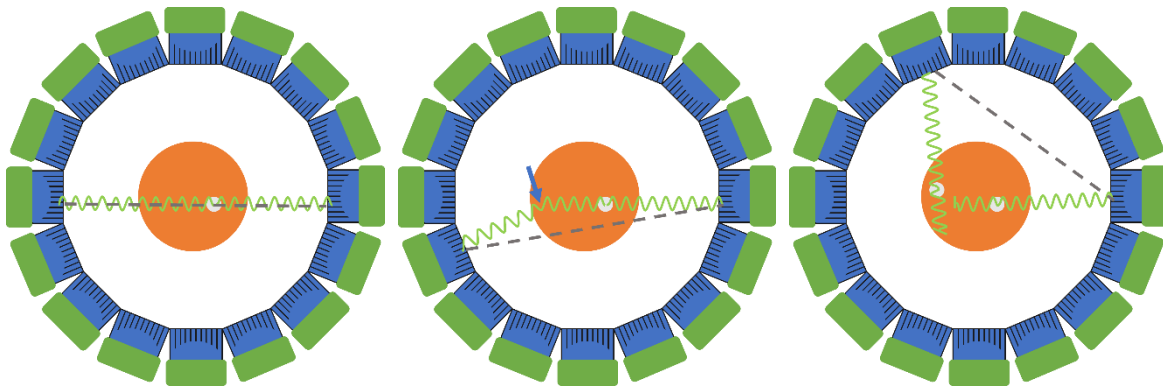


Figure 2.7: True (left), scatter (center) and random (right) coincidences in PET.

The PET detector is often configured in a series of parallel rings, which allows for both radial and axial sampling of photons; the convention for the three-dimensional coordinates is that the x-y axes form the transverse planes which are perpendicular to the z-axis along the center of the ring detectors. In the transverse planes, it is convenient to use polar coordinates to define the position of the LORs and group these into projection angles:  $\phi$  is the azimuthal angle of the projection, while  $s$  is the radial bin, representing the distance of the LOR from the center along that angle. If both photons interact within the same detector ring, the LOR will be within the transverse plane forming the 2D direct sinogram; the data acquired can be used to reconstruct the entire volume. However, LORs resulting from photon interactions in two different rings can also be formed; these are stored in oblique sinograms, where up

to  $n^2$  sinograms can be created with indices  $(i, j)$ , where  $i$  represents the ring number in which the first photon interacted and  $j$  the ring number of the second photon interaction. Using the data in oblique sinograms leads to increases in sensitivity and improvements in signal-to-noise ratios. Oblique sinograms can be used in 3D reconstruction algorithms or be recombined to form up to  $2n - 1$  2D planes, consisting of  $n$  direct planes and  $n - 1$  cross planes, with a spacing of  $z/2$  where  $z$  is the center-to-center ring width. Michelograms are a convenient graphical representation of how the data from oblique sinograms can be combined (Fahey, 2002). The span is a measure of the number of direct and oblique sinograms combined; it is the sum of the number of sinograms combined into odd-numbered planes and the number of sinograms combined into even-numbered planes.

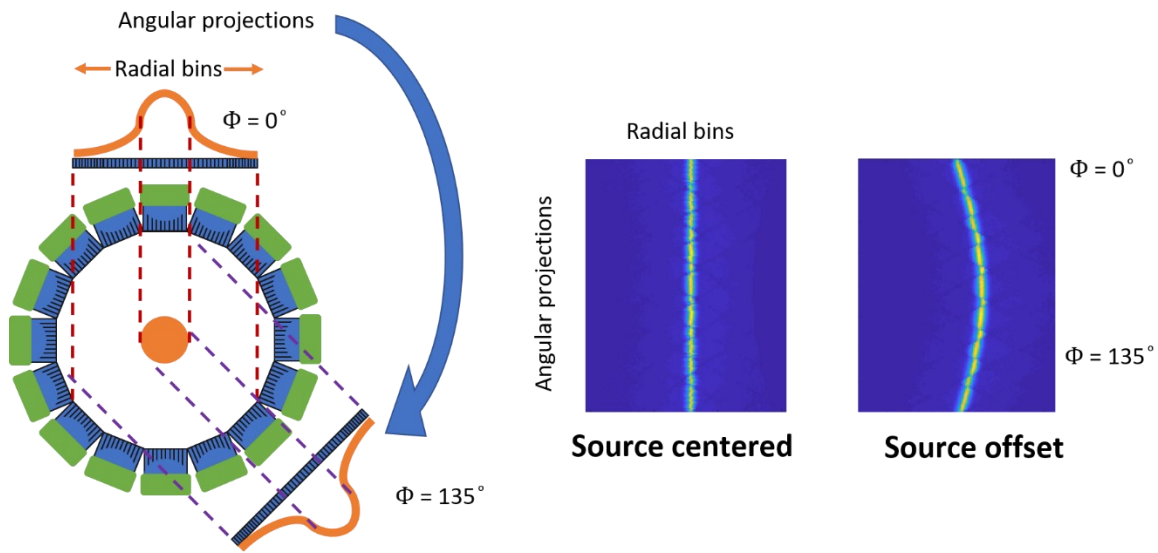


Figure 2.8: Representation of 2D sinogram acquired from centered and offset source in PET scanner

### 2.4.3 Random coincidences & correction

Random coincidences occur when two photons originating from different positron annihilations events are detected within the same coincidence timing window. The random rate  $C_{ab}$  in Eq. 2.52 is proportional to the product of the single event count rate  $r_i$  in each detector crystal and the coincidence timing window  $2\tau$ .

$$C_{ab} = 2\tau r_a r_b \quad (2.52)$$

One method of correcting random coincidences is to integrate the random rate over time to determine the number of coincidences in each element  $R_{ab}$ , as in Eq. 2.53. The single event count rate can be

approximated as the activity at the start of acquisition  $r_{i0}$  in element  $i$  multiplied by an exponential decay function  $f(t)$  for the radionuclide assuming the tracer distribution can be ignored.

$$R_{ab} = \int_0^T C_{ab}(t)dt = 2\tau \int_0^T r_a(t)r_b(t)dt = 2\tau r_{a0}r_{b0} \int_0^T (f(t))^2 dt \quad (2.53)$$

Tail fitting is another procedure that has been used to simultaneously correct for scatter and random coincidences; if the object being imaged does not cover the entire FOV, a function such as a gaussian can be fit to the tails of the sinogram outside of the imaged object. This function can then be used to estimate the distribution of random and scatter coincidences in the entire sinogram. Finally, a delayed coincidence channel estimation can be used, in which an additional timing window is opened after the coincidence timing window to remove the correlation between the single events occurring in each channel in order to estimate the randoms events.

#### 2.4.4 Attenuation correction

The annihilation photons will interact with material (e.g. patient) in the scanner's FOV, leading to a decrease in photons seen by the PET detector. This attenuation can be corrected for with knowledge of the matter along the LOR formed by the two points on the detector along which the photons interact. This attenuation will be constant and is not dependent on the position of the emission source along the LOR. An example of this is a photon source outside an object which has a thickness  $D$  along the LOR and a linear attenuation  $\mu$ . In this case, one photon pass through the entire thickness of the object and is attenuated, while the other photon does not interact along its path to the detector. Similarly, for a source a distance  $x$  along the LOR inside the object, the attenuated counts seen by the detector in which both photons arrive without being attenuated is:

$$C = C_0 e^{-\mu x} e^{-\mu(D-x)} = C_0 e^{-\mu D} \quad (2.54)$$

This relation between the attenuated counts and total counts is constant along an LOR as the sum of the distances each photon traverses through the object in the FOV is constant. Thus, a single correction is required for each LOR based on the distance through which the photons travel through matter along that LOR as well as the linear attenuation of the material.

The total attenuation along a LOR can be estimated in a few ways: first, an external source can be used, which is rotated around the interior casing of the scanner; the expected photon fluence along each LOR

when the FOV is empty is known (blank scan). When an object is inserted in the FOV, a transmission scan with this external source can be performed, such that the attenuation of the photons along each LOR can be recorded; the attenuation correction can then be calculated. The advantage of this method is that a source of the same energy as PET emissions (511 keV) can be used; a disadvantage is that the transmission scan can take a relatively long time, compromising patient comfort. A second option is to perform a sequential CT scan of the object in the FOV. The CT scan reconstruction allows determining a three-dimensional map of the Hounsfield units (HU) inside the scanner's FOV, and thus the total attenuation coefficient can be calculated along each LOR. Though fast and convenient, a potential pitfall can be a mismatch between the portion of the breathing cycle captured by the CT and the (slower, averaging) PET scan. The CT is also performed with a lower energy, polyenergetic photon spectrum. The attenuation values derived from the CT's Hounsfield units need to be converted to their values at 511 keV. A hybrid scaling/segmentation approach can be applied to the data, in which voxels which are a mix of bone and water ( $HU > 300$ ) are scaled with a different value than those that are a mix of water and tissue ( $HU < 300$ ) (Kinahan et al., 1998). Kinahan et al. demonstrated that this hybrid scaling can be used due to the similar ratio of the mass attenuation coefficients at the CT energy ( $\sim 70$  keV) and for 511 keV photons when materials are separated in this manner (Kinahan et al., 1998). The advantage of this method over older segmentation methods is that tissues such as lung which have variable density will be scaled continuously rather than to a single value (Carney et al., 2006).

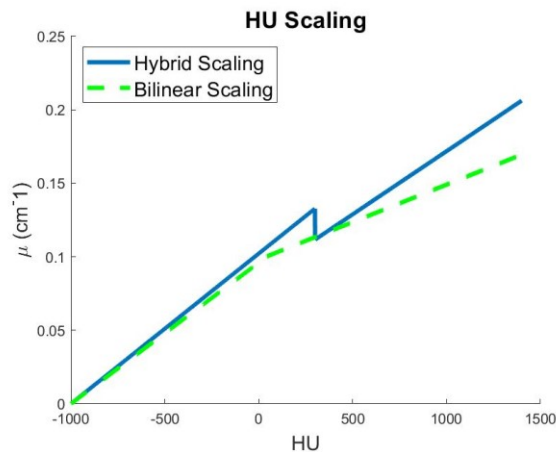


Figure 2.9: Hybrid method and bilinear scaling of CT HU number to linear attenuation coefficient for 511 keV photons used in the calculation of attenuation correction.

### 2.4.5 Scatter coincidences & correction

Once the positron annihilates, both photons must travel to the detector and be detected to assume a line of response along which the positron annihilated. However, as we have seen, the photons can interact with the material in the scanner and the most likely type of interaction is Compton scattering (Figure 2.3). If both photons are detected, but one (or both) have been scattered, the resulting LOR no longer is indicative of the site of positron annihilation; instead an erroneous scatter coincidence has been tallied. For example, if a 511 keV photon scatters at an angle of  $40^\circ$ , the resulting photon will have an energy of 414 keV. Assuming an energy acceptance window of 350 to 650 keV due to the poor energy resolution of commonly used scintillators in PET, this scattered photon would still be erroneously accepted as true coincidence. The scatter fraction is a quantity used to report the proportion of coincidences in which at least one photon has undergone Compton scattering prior to coincidence detection.

Some characteristics of scatter LORs can be used to estimate and correct measured data. As previously discussed with random coincidences, the distribution of coincidences outside the extent of the object is a result of scatter and random coincidences; by fitting the tails of the sinograms with a gaussian or a second order polynomial, the distribution within the object can be estimated.

Convolution approaches estimate the contribution of the scattered coincidences by integrating the product of the observed projections with  $h(s, x)$ , a function that models the contribution of a source position at  $x$  to the radial position  $s$  in the projection. This function can be determined using line source measurements throughout the field of view at regularly spaced points. The scatter projection  $P_{sc}$  can be estimated from the observed projection  $P_{obs}$  using Eq. 2.55. This estimate can then be subtracted from the observed projection, and this procedure can be repeated in an iterative manner to obtain a more accurate estimate.

$$P_{sc}(s) = \int_{-\infty}^{\infty} P_{obs}(t)h(s - t, t)dt \quad (2.55)$$

Finally, the contribution of scatter to projections can be estimated through analytical or Monte Carlo simulations modelling the photons interactions within the scanner FOV. An attenuation map of linear attenuation coefficients within the FOV is reconstructed along with an initial estimate of the activity distribution. The scatter contribution is then modeled through analytical calculations, for example by integrating the Klein-Nishina formula (Eq. 2.19) over the appropriate scattering angles, or through Monte Carlo simulations, transporting the photons from their source to the detector. This scatter

contribution for each projection is scaled such that the total estimated counts match the total observed counts.

#### 2.4.6 Iterative reconstruction

Measured projection data are used to reconstruct the unknown source distribution in the scanner. In model-based iterative reconstruction approaches, a linear transform known as the projection matrix  $\mathbf{P}$  is used to relate the unknown source distribution  $\mathbf{f}$  to the projection data  $\mathbf{y}$ . In these model-based approaches, the projection matrix incorporates the physics of photon propagation through the scanner geometry and their interactions in the detector, in contrast to older reconstruction strategies such as FBP which are based on the geometry of the scanner and projection data.

Uncorrected PET sinogram data are a collection of independent Poisson variables assuming detection of each event in the scanner is independent, and this lends itself to maximum likelihood methods and the use of statistically-based iterative reconstruction methods (Qi and Leahy, 2006). Thus, the mean of the projection data  $\bar{y}_i$  is related to the detector response function  $c(i, x)$  for the  $i$ th LOR in a tomographic system with a total of  $M$  detector bins, and  $r_i$  and  $s_i$  the expectations of the random events and scatter events along the LOR respectively:

$$\bar{y}_i = \int f(x)c(i, x)dx + r_i + s_i, \quad i = 1, \dots, M \quad (2.56)$$

While the tracer distribution can be represented by the continuous function  $f(x)$ , a voxel basis is a common representation of the tracer distribution, in which the count in the voxel is proportional to the radioactive nuclei encompassed within the volume of the voxel. The tracer distribution can be represented by  $N$  voxels, and  $\phi_j(x)$  represents the  $j$ th voxel basis function in which the tracer distribution is constant over its volume and zero elsewhere:

$$f_j = \int f(x)\phi_j(x)dx, \quad j = 1, \dots, N \quad (2.57)$$

The expected value of the measured data  $\bar{\mathbf{y}}$  can be expressed as the product of the projection matrix  $\mathbf{P}$  and source distribution  $\mathbf{f}$ , added to the random  $\mathbf{r}$  and scatter  $\mathbf{s}$  events, as in equation 2.58.

$$\bar{\mathbf{y}} = E[\mathbf{y}] = \mathbf{P}\mathbf{f} + \mathbf{r} + \mathbf{s} \quad (2.58)$$

The elements of the  $M$  by  $N$  projection matrix  $\mathbf{P}$  consist of elements which represent the probability that an emission from voxel  $j$  is detected along the LOR  $i$ :

$$p_{ij} = \int c(i, x) \phi_j(x) dx \quad (2.59)$$

The independent Poisson distribution is likelihood function which represents the conditional probability of the measured projections  $y$  given the tracer distribution  $f$ .

$$p(y|f) = \prod_i e^{-\bar{y}_i} \frac{\bar{y}_i^{y_i}}{y_i!} \quad (2.60)$$

The logarithm of this function can be taken as it is a monotonic function and can be maximized itself.

$$L(y|f) = \sum_i y_i \log(\bar{y}_i) - \bar{y}_i - \log(y_i!) \quad (2.61)$$

Maximizing the conditional expectation of the log likelihood of the complete data with respect to the image can be done through multiple methods, including substitution. In EM algorithm, the image estimate is updated based on the previous estimate and updated such as the conditional expectation of the log-likelihood is maximized in the following way, incorporating the random and scatter events into the formula for updating the next image value:

$$f^{(k+t)} = f_j^{(k)} e_j(f^{(k)}) / \sum_i p_{ij} \quad (2.62)$$

Where

$$e_j(f^{(k)}) = \sum_i \frac{p_{ij} f_j^{(k)}}{(\sum_l p_{il} f_l^{(k)} + r_i + s_i)} \quad (2.63)$$

Provided the initial image is composed of positive values, the EM algorithm converges monotonically towards to the global maximum of the likelihood function and maintains the non-negativity of the values within the image as it is updated. While it is known for slow convergence, many efforts have been made to modify algorithms for faster convergence, such as ordered subsets, in which the measured data is split into different sets and the EM algorithm is sequentially applied to each (Qi and Leahy, 2006).

## 2.5 Monte Carlo

Monte Carlo methods in medical physics are prominently used for modelling physical processes occurring in many applications, from detector design for high energy physics to absorbed dose modelling. Simulations of physical interactions of particles in matter are carried out by modelling

individual processes with probability distribution functions; the deterministic behaviour of a system is predicted through a series of statistical calculations. The previously discussed particle interactions in matter are important in Monte Carlo simulations as these are the processes modeled. Rigorous physics models for each of these processes are essential for the replication of the physical processes in these simulations. However, physics packages require validation; that is, prior to using such software to study further phenomena, a simple test case simulation should be set up and attempt to replicate known experimental results. Successful replication of measured values provides confidence that the underlying physics has been accurately modelled and will have bearing in a more complicated scenario.

Geant4 (GEometry ANd Tracking) is a well-established toolkit in physics which has been in continuous development since it was first released in 1998 (Agostinelli et al., 2003). The software package, coded in the C++ language, makes use of object-oriented programming to define classes which interact with each other in a well-established manner. The key modular components of the simulations relate to specific aspects of particles traversing matter: properties of materials and their geometry; physical processes modelling particle interactions; tracking particles along their trajectories; managing the particle interaction events; managing the counting and digitization of events; providing a framework to visualize results; and providing user interfaces. This modular approach to each component allows the software to be extended by the user for specific applications and for the re-use of components from one simulation to another. As previously outlined, an important feature of Monte Carlo simulations is rigorous modelling of the underlying physical processes involved in an experiment. The physics models used in Geant4 encompass the physics of photons, electrons, muons, hadrons, and ions for a large range of energies and processes, including electromagnetic, hadronic, transportation, decay and optical physics. The models are quite extensive and have been validated for several applications, including simulating DNA damage from low energy electrons (Lampe et al., 2018a, 2018b). Geant4 includes examples to help guide the user in developing a simulation related to their research: novice examples which focus on understanding the basic functionalities of the software such as particle tracking and summing particle interactions in a specific volume; extended examples which provide additional context for implementing simulations focused on specific fields such as simulating optical photons in a liquid xenon scintillator (LXe) or the radioactive dose deposition inside a cavity from an electron beam (FanoCavity2); and advanced examples which consist of fully developed programs for use in high-energy physics experiments and applications in medical physics, such as calculating the energy deposition in a water phantom produced by a brachytherapy source (brachytherapy) or simulating a Leksell Gama-knife unit (Gammaknife).

### 2.5.1 Probability distributions and random sampling

A probability density function (PDF)  $f(x)$  of a continuous random variable  $X$  is a non-negative function defined on a finite or infinite interval  $[a, b]$  which represents the probability that the random variable will assume a value between  $x_1$  and  $x_2$  within the interval  $[a, b]$ , where  $x_1 < x_2$ :

$$Prob\{x_1 \leq X \leq x_2\} = \int_{x_1}^{x_2} f(x)dx \quad (2.64)$$

As  $X$  is continuous and can assume any value within the interval, the probability of obtaining any single value (i.e.  $x_1 = x_2$ ) is zero. The PDF is normalized such that the integral over its interval  $[a, b]$  is equal to 1, i.e. the sum of the probability of observed values is 1.

$$\int_a^b f(\tau)d\tau = 1 \quad (2.65)$$

The cumulative distribution function (CDF)  $F(x)$  is defined as the integral of the PDF from the lower bound of the interval  $a$  to  $x$ :

$$F(x) = \int_a^x f(\tau)d\tau \quad (2.66)$$

This is the probability that the observed value of a continuous random variable  $X$  will lie between  $a$  and  $x$ . As the PDF is non-negative,  $F(x)$  is a monotonically increasing function where  $F(a) = 0$ , and  $F(b) = 1$ .

$$F(x) = Prob\{a \leq X \leq x\} \quad (2.67)$$

In a Monte Carlo simulation, these distributions are described for each physical process and are sampled to determine the interactions that each incoming particle undergoes, and the direction and energy of the outgoing particles. If the CDF is expressed as an analytical function, it can be directly sampled. An example for the use of this sampling is the transport of photons in an infinite medium. As previously expressed in Eq 2.23, the probability of photons interacting with a medium follows an exponential distribution and is governed by the total linear attenuation  $\mu$  in the medium. The probability  $p$  of a photon not interacting in a medium after travelling a distance  $x$  is:

$$p(x) = e^{-\mu x} \quad (2.68)$$

Normalizing this PDF to 1 on the interval  $[0, \infty]$  is straightforward:

$$p(x) = \frac{e^{-\mu x}}{\int_0^{\infty} e^{-\mu\tau} d\tau} = \mu e^{-\mu x} \quad (2.69)$$

An analytical CDF is found by directly integrating Eq. 2.69:

$$P(x) = \int_0^x \mu e^{-\mu\tau} d\tau = 1 - e^{-\mu x} \quad (2.70)$$

This CDF can be inverted to solve for the distance  $x$  a photon travels as a function of its CDF:

$$x = -\frac{1}{\mu} \log(1 - P(x)) \quad (2.71)$$

This relationship determines the distance at which the next photon interaction will occur in a Monte Carlo simulation: by generating a random number  $\eta$  with a uniform distribution between 0 and 1, the distance of the next photon interaction is found to be:

$$x = -\frac{1}{\mu} \log(1 - \eta) \quad (2.72)$$

The interaction process that occurred at this distance can be determined by selecting another random number. The relative probability of each process is determined as the ratio of the individual process cross-sections to the total cross-section of all processes. A uniform random number  $\eta$  where  $0 \leq \eta \leq 1$  is generated to select the process; for example, if there are two competing interactions, A and B, where A has a 60 % probability of occurring, then if  $\eta \leq 0.6$  the interaction process A is chosen and if  $\eta > 0.6$  the interaction process B is chosen.

The acceptance-rejection method first proposed by von Neumann is another procedure used to sample PDFs (Von Neumann, 1963). Among the many Monte Carlo methods able to compute the scattering angle and resulting energy of the scattered photon in Compton scattering, for example, the acceptance-rejection method stands out by its simplicity. Compton scatter probabilities are derived from the Klein-Nishina differential scattering cross-section (Eq. 2.19). In the acceptance-rejection method, a value  $\xi$  is chosen to be greater than the maximum of this cross-section:

$$\xi > \max \left\{ \frac{d\sigma_e}{d\Omega} \right\} \quad (2.73)$$

Two uniformly distributed random numbers  $\eta$  and  $\zeta$  are then generated such that  $0 \leq \eta \leq \pi$  and  $0 \leq \zeta \leq \xi$ . The first random number  $\eta$  is used to calculate the scattered photon energy (Eq. 2.17) when given a scattering angle  $\eta$ :

$$E_{\eta} = \frac{E}{1 - \frac{E}{E_0}(1 - \cos \eta)} \quad (2.74)$$

This scattered photon's angle  $\eta$  and energy  $E_{\eta}$  are then used to compute the value of the Klein-Nishina differential cross-section:

$$\left\{ \frac{d\sigma_e}{d\Omega} \right\}_{\eta} = \frac{r_0^2}{2} \left( \frac{E_{\eta}}{E} \right)^2 \left( \frac{E}{E_{\eta}} + \frac{E_{\eta}}{E} - \sin^2 \eta \right) \quad (2.75)$$

This value is now compared with the second random number  $\zeta$ ; the scattering angle  $\eta$  is accepted if  $\left\{ \frac{d\sigma_e}{d\Omega} \right\}_{\eta} \geq \zeta$  and rejected if  $\left\{ \frac{d\sigma_e}{d\Omega} \right\}_{\eta} < \zeta$ . The procedure is repeated until a scattering angle is accepted, which also determines the scattered photon energy  $E_{\eta}$ . Finally, a uniformly distributed random number  $\epsilon$  is generated such that  $0 \leq \epsilon < 2\pi$  to determine the azimuthal angle of the scattered photon. Both,  $\eta$  and  $\epsilon$  uniquely determine the direction of the scattered photon in three-dimensional space, and the next interaction distance is determined using 2.72 based on the modified attenuation coefficient  $\mu(E_{\eta})$  at the new (scattered) photon energy.

## 2.6 Radiochemistry

In nuclear medicine, a tracer is a general term for a compound that is injected prior to imaging or therapy in concentrations that do not disturb the molecules natural biodistribution. In it's simplest form, it can be an unbound radionuclide, such as  $^{82}\text{Rb}$  to assess myocardial blood flow (deKemp et al., 2016), or a radioactive atom can be incorporated into the structure of a compound with a useful *in vivo* distribution, such as the substitution of  $^{18}\text{F}$  for the hydroxyl group at the C-2 position in a glucose molecule to form the familiar [ $^{18}\text{F}$ ]-FDG compound. As previously discussed, this tracer is taken up in areas of increased glucose metabolism such as many cancers. Furthermore, a peptide can be decorated with a bifunctional chelator to which the radiometal will complex; the peptide is then able to interact specifically with the receptors it targets *in vivo*, while the radiometal provides the imaging signal.

The binding of a peptide to the receptor can cause different responses, which can be used to classify the peptides: agonists binding to a receptor stimulate its action, which can be downstream signalling or internalization; antagonists binding to a receptor do not induce an action and can block the receptor. Partial agonists may induce a partial action which is characterized by its efficacy (Rang, 2006). This concept of efficacy is separate from the binding affinity of the peptide, which represents the strength of the binding interaction between the receptor and the peptide. In practice, the binding affinity is

characterized through measurements of the  $IC_{50}$ , the concentration of peptide at which half-maximum inhibition occurs; it is desirable for the peptide to occupy receptors at low concentrations and have a high binding affinity. In radionuclide therapy, it can be desirable to perform treatments with antagonists to avoid unwanted side effects due to the activation of the receptor that would occur with a receptor agonist, as has been shown with  $^{177}\text{Lu}$ -labeled GRPR agonists. The lipophilicity of a tracer determines its distribution behaviour in a biphasic system which impacts the tracer's pharmacokinetic and pharmacodynamic actions such as solubility, reactivity and degradation (Rutkowska et al., 2013). The partition coefficient  $P$  is a measure of the distribution of a tracer at equilibrium in a non-polar phase (organic phase such as n-octanol) and polar phase (aqueous phase such as water).

To characterize a radiolabelling process, it is helpful to define relevant terms (Coenen et al., 2017). Radiochemical yield (RCY) is the ratio of the activity of the product to the starting activity used in a process (radiolabelling, extraction) and decay corrected to the same point in time, often expressed as a percentage. Radiochemical purity quantifies the absence of other radiochemical compounds. Molar activity is the measured radioactivity per mole of compound, often expressed in  $\text{GBq}/\mu\text{mol}$ ; in practice, the term apparent molar activity can be used to describe a process in which precursor molecules are not fully removed during purification and the measured molar activity is lower than the true value. Thin-layer chromatography (TLC) is a technique used to separate components of a mixture and is used as an analytical tool to separate radiolabelled tracer and unlabelled radiometals after a chemical reaction and can be used to calculate the RCY (*Thin Layer Chromatography*, 2019). TLCs can be used to monitor the progress of a reaction by placing a small amount of the reaction solution on a silica gel plate which acts as a stationary phase, and allowing a solvent as the mobile phase to migrate up the plate and create a separation of the compounds based on their relative affinities for the mobile and stationary phases. The retention factor is the ratio of the distance the compound travelled to the total distance travelled by the solvent. In the case of radioactive compounds, a radiation detector can be used to determine the linear distribution of counts along the plate and calculate the radiochemical purity by integrating the relative counts observed at the retention factor of the labelled compound, and comparing the number of counts observed for the unlabelled radiometal. Similar to TLC, high performance liquid chromatography (HPLC) uses a pump to force a solvent phase (e.g. water, methanol) at pressures up to 400 atmospheres through a column packed with a solid phase (e.g. silica) to obtain separation (*C. High Performance Liquid Chromatography (HPLC)*, 2020). The retention time of a compound is the time it takes from injection to travel through the column and be detected, and is dependent on the pressure, flow rate, stationary

phase, composition of the solvent, the temperature of the column; this time will differ for various compounds, allowing for the detection and separation of product and precursor materials.

## Chapter 3

# Experimental measurements and predictive analysis of the radionuclidic composition of radioscandium

---

---

### 3.1 Introduction

Pairs of radionuclides have been proposed for labelling molecular tracers to combine diagnostic imaging ( $\beta^+$  and  $\gamma$  emitters) and targeted therapy ( $\beta^-$  and  $\alpha$  emitters); three radioisotopes of scandium have been proposed for such theragnostic applications:  $^{43}\text{Sc}$  ( $\beta^+$ ),  $^{44}\text{Sc}$  ( $\beta^+$ ) and  $^{47}\text{Sc}$  ( $\beta^-$ ) (Huclier-Markai et al., 2018; Müller et al., 2018, 2013). The production of these radionuclides has been the subject of many recent investigations.  $^{44}\text{Sc}$  has been produced through the proton irradiation of natural abundance calcium targets (Severin et al., 2012; Valdovinos et al., 2015), enriched  $^{44}\text{Ca}$  targets (van der Meulen et al., 2015) as well as in liquid solution targets (Hoehr et al., 2014). An alternative production route is a  $^{44}\text{Ti}/^{44}\text{Sc}$  generator (Pruszyński et al., 2010; Roesch, 2012), which requires higher energy protons (25-30 MeV) and large integrated currents on target as the half-life of  $^{44}\text{Ti}$  is 60 years. High yields of  $^{43}\text{Sc}$  have been accomplished using alpha particle beams via the  $^{nat}\text{Ca}(\alpha, p)^{43}\text{Sc}$  reaction using natural abundance calcium targets (Minegishi et al., 2016; Walczak et al., 2015), and more recently  $^{43}\text{Sc}$  has also been produced by proton irradiations via the  $^{46}\text{Ti}(p, \alpha)^{43}\text{Sc}$  and  $^{43}\text{Ca}(p, n)^{43}\text{Sc}$  nuclear reactions, resulting in radionuclidic purity of 98.2 % and 66.2 %, respectively (Domnanich et al., 2017a). Proposed production pathways of  $^{47}\text{Sc}$  include the proton irradiation of  $^{48}\text{Ca}$  targets (Misiak et al., 2017), alpha irradiation of  $^{44}\text{Ca}$  (Minegishi et al., 2016), and gamma bombardment of  $^{48}\text{Ti}$  (Mamtimin et al., 2015; Rotsch et al., 2018; Yagi and Kondo, 1977), as well as indirect production schemes through the decay of  $^{47}\text{Ca}$  via the  $^{48}\text{Ca}(\gamma, n)^{47}\text{Ca}$  and  $^{46}\text{Ca}(n, \gamma)^{47}\text{Ca}$  nuclear reactions (Domnanich et al., 2017b; Rane et al., 2015; Starovoitova et al., 2015).

The production of these radionuclides remains under investigation; the chosen irradiation conditions, target composition and thickness affect radionuclide yield and purity, which are important to assess to

determine the viability of the production pathway. Predictive tools for determining radionuclide yields in cyclotrons are important as they inform experiments to help curtail costs which can be quite high, especially when surveying enriched materials. Radionuclide yields can be predicted using experimental cross-section data, such as that available in the Experimental Nuclear Reaction Data (EXFOR) database; however, these data are often limited and may not cover all reactions of interest and projectile energies. The TALYS-Evaluated Nuclear Data Library (TENDL) provides data for every nuclear reaction process expected to take place by relying on nuclear modeling and where available adjusting parameters to match experimental data (Koning et al., 2019). These nuclear data libraries can be used to calculate theoretical radionuclide yields and contaminants produced during irradiations. Some novel tools such as the IAEA medical isotope browser (MIB) take advantage of both TENDL and recommended production cross-sections for these calculations (Koning and Verpelli, 2020).

Monte Carlo (MC) simulations play an important role in medicine, with applications in radiation therapy, diagnostic imaging and radionuclide production (Infantino et al., 2011; Ljungberg et al., 2012; Rogers, 2006; Seco and Verhaegen, 2013). A variety of MC packages have been used to model the cyclotron production of radionuclides, including MCNP, FLUKA and Geant4, which has been enabled by the implementation of physics packages to model low-energy inelastic hadronic interactions (Amin et al., 2018; Fassbender et al., 2007; Ratcliffe et al., 2013). In the Geant4 MC package, the incorporation of the EXFOR and TENDL nuclear reaction cross-sections to model low-energy hadronic interactions in the QGSP\_BIC\_AllHP model has allowed for more accurate calculations of radionuclidic yield in the setting of medical radionuclide production (Amin et al., 2018; Poignant et al., 2016). Further validation is required as the simulated radionuclide yield is highly reliant on the physics model and cross-sections used; for targets in which multiple radionuclides can be produced, it is important to determine whether simulations can not only predict the yield of the radionuclide of interest but also the radionuclidic purity by quantifying contaminants.

In this study, the production of radioscandium isotopes from natural calcium targets is evaluated. Proton irradiations of thick natural calcium targets will be performed on the variable energy ACSI TR19 cyclotron at the Cross Cancer Institute (CCI) to quantify the yield of radioscandium isotopes. These yields will be used to assess the accuracy of theoretical calculations using the EXFOR and TENDL nuclear data libraries, as well as results from simulations with the MC package Geant4.

## 3.2 Materials and Methods

### 3.2.1 Target Preparation and Irradiation

Thick targets were prepared by pressing dendritic chunks of metallic natural abundance calcium (99.99% metals basis, Sigma-Aldrich, USA; 96.94 %  $^{40}\text{Ca}$ , 0.647 %  $^{42}\text{Ca}$ , 0.135 %  $^{43}\text{Ca}$ , 2.086 %  $^{44}\text{Ca}$ , 0.004 %  $^{46}\text{Ca}$ , 0.187 %  $^{48}\text{Ca}$ ). The analysis of the trace metal in the calcium is given in Table 4 as provided by the target materials supplier. Calcium pellets were first made by pressing the dendritic chunks of metallic calcium using a 10 mm diameter pressing die for 45 seconds at 30 MPa (Across International, USA). These calcium pellets were then pressed into an indentation in a silver backing plate. The backing plate was included into a target assembly which was installed on the cyclotron, where water cooling was applied to the back face of the silver plate while the front face was open to vacuum.

Table 4: Trace metal analysis of calcium (Sigma-Aldrich, USA)

Element	Ag	Al	Ba	Co	Cu	Fe	K	Mg	Mn	Ni	Sr	Ti	Zn
Content (ppm)	0.1	0.2	33.6	1.1	0.6	1.2	3.4	1.7	22.8	<22.3	24.7	0.6	3.3

This expected range and the corresponding areal density of the 10 mm diameter calcium pellet at natural density ( $1.54 \text{ g/cm}^3$ ) for each energy is given in Table 1, as well as the measured areal density of the pressed pellets used for irradiation. The measured areal density was chosen to be greater than the expected areal density to ensure protons were fully stopped in the calcium target material in order to account for uncertainties in thickness and density of the pellets. Three calcium pellets were irradiated at each beam energy.

Table 5: Expected proton range in natural calcium target and corresponding areal density, as well as measured areal density of pressed calcium pellets. Note that the measured areal density is greater than the expected areal density to account for uncertainties in final target thickness and density.

Beam Energy (MeV)	Expected proton range (mm)	Expected Areal Density ( $\text{g/cm}^2$ )	Measured Areal Density ( $\text{g/cm}^2$ )
12	1.52	0.2341	$0.3352 \pm 0.0001$
14	1.99	0.3065	$0.3727 \pm 0.0038$
16	2.51	0.3865	$0.4538 \pm 0.0013$
18	3.09	0.4759	$0.5399 \pm 0.0013$

### 3.2.2 Irradiation

Irradiations were performed on the ACSI TR19 cyclotron at the Cross Cancer Institute (CCI) in Edmonton, Alberta, Canada. The targets were irradiated with nominal proton energies of 12, 14, 16 and 18 MeV and 2  $\mu\text{A}$  of current for 7.5 min, for a total integrated current of 15  $\mu\text{Amin}$ . To confirm the beam energy, the dual-copper foil irradiation method was employed (Gagnon et al., 2011). Copper foils with a thickness of 25  $\mu\text{m}$  were irradiated at each energy using aluminum foil spacers to degrade the energy between the first and second copper foil: 250  $\mu\text{m}$ , 750  $\mu\text{m}$ , 1000  $\mu\text{m}$  and 1250  $\mu\text{m}$  Al foil degraders were used for 12 MeV, 14 MeV, 16 MeV and 18 MeV respectively. The foil stacks were irradiated with 1  $\mu\text{A}$  of current for 5 min, resulting in a total integrated current of 5  $\mu\text{Amin}$ . Repeat measurements of the copper foil activity were conducted from 30 min post-irradiation until 3 hours post irradiation in intervals varying from 5 min to 30 min using an Atomlab 400 dose calibrator (Biodex Medical Systems, NY, USA). The decay curve was fit with a multi-exponential distribution to describe the decay of the three radionuclides produced in the foil:  $^{62}\text{Zn}$  (9.186 h),  $^{63}\text{Zn}$  (38.47 min), and  $^{63}\text{Cu}$  (9.67 min). The ratio of the  $^{63}\text{Zn}$  in each foil was used to determine the ratio of the cross-sections at the different energies; the monitor reaction cross-sections and fitting procedure to determine the energy from this ratio are described in more detail by Gagnon et al. It was found through repeat measurements that uncertainty associated with these measurements was on the order of 0.1 MeV.

### 3.2.3 Target processing

After experimental irradiations, the calcium was removed and dissolved using 1 M hydrochloric acid and placed in a scintillation flask. The irradiated samples were placed 25 cm from the top of a high purity germanium (HPGe) detector (Ortec model GEM35P4-S) to measure the gamma ray spectra. Deadtime of the detector was maintained below 10% for sample counting. NIST traceable sources ( $^{133}\text{Ba}$ ,  $^{109}\text{Cd}$ ,  $^{22}\text{Na}$ ,  $^{54}\text{Mn}$ ,  $^{60}\text{Co}$  and  $^{137}\text{Cs}$ ) were used to determine the energy calibrations and absolute efficiencies of the HPGe detectors. To assess the thick target yield of the radionuclides of interest in Table 3.6, the peaks in the series of gamma-ray spectra measurements were fit using the GammaVision v.6.01 software and the counts were used to determine the activity at the end of irradiation for each radionuclide after energy, geometry and decay corrections. The physical thick target yield  $\alpha_{phys}$  (MBq/ $\mu\text{A}\cdot\text{h}$ ) was calculated from the measured activity at end of irradiation  $A_{end}$  (MBq), the beam current  $I$  ( $\mu\text{A}$ ) and irradiation time  $t$  (h) for each radionuclide with decay constant  $\lambda$  ( $\text{h}^{-1}$ ) using Eq. 2 (Otuka and Takács, 2015).

$$\alpha_{phys} = \frac{A_{end}}{I} \cdot \frac{\lambda}{(1 - e^{-\lambda t})} \quad (3.1)$$

Table 3.6: Radionuclides produced through proton-induced reactions in calcium target and associated  $\gamma$ -emission energies and abundances used in assays to determine yields (National Nuclear Data Center, n.d.). The threshold energy was determined using atomic mass data (Wang et al., 2021).

Radionuclide	Half-life	Emission (keV)	Intensity	Reaction	Threshold
$^{43}\text{Sc}$	3.891 h	372.9	22.5 %	$^{43}\text{Ca}(p,n)^{43}\text{Sc}$	3.1 MeV
				$^{44}\text{Ca}(p,2n)^{43}\text{Sc}$	14.5 MeV
$^{44}\text{Sc}$	3.97 h	1157.020	99.9 %	$^{44}\text{Ca}(p,n)^{44}\text{Sc}$	4.5 MeV
$^{44\text{m}}\text{Sc}$	58.61 h	271.241	86.7 %	$^{44}\text{Ca}(p,n)^{44\text{m}}\text{Sc}$	4.8 MeV
$^{46}\text{Sc}$	83.79 d	889.277	99.9840 %	$^{46}\text{Ca}(p,n)^{46}\text{Sc}$	2.2 MeV
		1120.545	99.9870 %		
$^{47}\text{Sc}$	3.3492 d	159.381	68.3 %	$^{48}\text{Ca}(p,2n)^{47}\text{Sc}$	8.9 MeV
$^{48}\text{Sc}$	43.67 h	983.526	100.1 %	$^{48}\text{Ca}(p,n)^{48}\text{Sc}$	0.51 MeV
		1037.522	97.6 %		
		1312.120	100.1 %		
$^{47}\text{Ca}$	4.536 d	1297.09	67 %	$^{48}\text{Ca}(p,pn)^{47}\text{Sc}$	10.2 MeV
				$^{48}\text{Ca}(p,d)^{47}\text{Sc}$	7.9 MeV

### 3.2.4 Yield comparison

For comparison, a theoretical calculation of the physical target yields was completed. Eq. 3.3 was used to estimate the saturation yield  $a_{sat}$  (MBq/  $\mu\text{A}$ ) of each nuclide of interest (Krasnov, 1974):

$$a_{sat} = 10^{-6} \frac{1}{e} N_t \int_{E_{out}}^{E_{in}} \frac{\sigma(E)}{\left(\frac{dE}{\rho dx}\right)} dE = 6.24 * 10^{12} N_t \int_{E_{out}}^{E_{in}} \frac{\sigma(E)}{\left(\frac{dE}{\rho dx}\right)} dE \quad (3.2)$$

where  $10^6$  is a conversion factor from Bq to MBq,  $e$  (C) is the elementary charge and its inverse represents the number of protons per second per  $\mu\text{A}$ ,  $N_t$  is the number of target atoms per gram (atoms/g),  $\sigma(E)$  is the energy dependent cross-section (mb =  $10^{-27}$  cm), and  $\frac{dE}{\rho dx}$  is the energy-dependent mass stopping power (MeV  $\text{cm}^2 \text{g}^{-1}$ ) of protons in calcium. The energy-dependent mass stopping power was determined using SRIM-2013 (Ziegler et al., 2008).

The saturation yield was then used to compute the thick target yield  $\alpha_{phys}$  (MBq/ $\mu\text{A}\cdot\text{h}$ ), which relates to the saturation yield through as demonstrated in Eq. 3.4.

$$\alpha_{phys} = a_{sat} * \lambda \quad (3.3)$$

To calculate the thick target yield (TTY) of specific nuclear reactions, the cross-section measurements used must cover the excitation function up to the incident proton energy. The EXFOR library contains numerous measurements of the cross-sections of proton-induced nuclear reaction on calcium; however, several measurements have limited data points and do not cover the full range of energies of interest. The cross-section measurements by Carzaniga et al. were used for predictions of the measured thick target yields with experimental data as these were the most complete for the proton-induced reactions on calcium up to 20 MeV (Carzaniga et al., 2017; Carzaniga and Braccini, 2019). The TENDL-2014 output provides a complete dataset for these reactions and can provide a useful comparison for measurements based on predictions from nuclear models (Koning et al., 2019). The accuracy of predictions made using the TENDL-2014 outputs is interesting as it can be used to estimate the yields of all nuclides produced in a target, including contaminants which may not have been directly evaluated in experimental measurements. The 2014 version of the TENDL library was chosen over newer iterations as it used in the G4TENDL1.3.2 data files. The IAEA medical isotope browser (MIB), a novel tool published by the IAEA to predict radionuclide production yields, combines the newer iterations of the TENDL library with recommended cross-sections from the IAEA for radionuclide production and was also used to predict TTY (Koning and Verpelli, 2020).

In addition to cross-section measurements, the EXFOR library contains measurements of thick target yield. These measurements are limited in natural calcium targets, and have largely been completed using natural abundance and enriched calcium carbonate targets; a single measurement of thick target yield in natural calcium targets is included for certain radionuclides at 16 MeV, but these were previously found to underestimate the thick target yield due to decreased beam intensity on target from the target geometry (Misiak et al., 2017; Severin et al., 2012; Sitarz, 2019; Sitarz et al., 2018). In order to compare the thick target yields with the values found in studies using calcium carbonate targets, the yields  $\alpha_i$  (MBq/ $\mu$ A·h) in natural calcium can be estimated by correcting for isotopic abundance  $f_i$  (%) (in the case of targets with enriched isotopic levels of calcium), molar mass  $m_i$  (g/mol) to account for proportion of calcium atoms in the targets, and the energy-dependent mass stopping power  $\left(\frac{dE}{\rho dx}(E_{in})\right)_i$  (MeV cm<sup>2</sup> g<sup>-1</sup>) at the incident proton energy  $T_{in}$  (MeV) to account for energy deposition in each target, using Eq. 3.4.

$$\alpha_2 = \alpha_1 * \frac{f_2}{f_1} * \frac{m_1}{m_2} * \frac{\left(\frac{dE}{\rho dx}(E_{in})\right)_1}{\left(\frac{dE}{\rho dx}(E_{in})\right)_2} \quad (3.4)$$

This approximation has been previously used for comparisons of yields in different target materials and is based on the formula for calculating the saturated yield, as previously stated in Eq. 3.3 (Sitarz et al., 2018). For conversions of yields of radionuclides with a known cross-section  $\sigma(E)$  (mb), a more exact approximation would be represented by Eq. 3.5.

$$\alpha_2 = a_1 * \frac{f_2}{f_1} * \frac{m_1}{m_2} * \int_{E_{out}}^{E_{in}} \frac{\sigma(E)}{\left(\frac{dE}{\rho dx}\right)_2} dE / \int_{T_{out}}^{T_{in}} \frac{\sigma(E)}{\left(\frac{dE}{\rho dx}\right)_1} dE \quad (3.5)$$

### 3.2.5 Monte Carlo Simulations

The MC simulations were carried out in Geant4 v10.04.p01 on a Dell XPS-8930 with a Intel Core i7-9700 CPU at 3 GHz with 8 cores on the Ubuntu 18.04.6 LTS operating system. The physics lists used for the simulations included radioactive decay physics (G4RadioactiveDecayPhysics), electromagnetic physics (G4EMStandard\_opt3), hadron elastic interaction physics (G4HadronElasticPhysicsHP) and the hadron inelastic interaction physics (G4HadronPhysicsQGSP\_BIC\_AllHP). As the intent of the simulations was to verify the yield of radionuclides in a target from an incident proton beam, the choice of hadron inelastic physics package to use was important. This QGSP\_BIC\_AllHP was chosen as it combines data from the EXFOR and TENDL-2014 libraries to simulate inelastic interactions between 0 MeV and 200 MeV, and in a previous study was found to provide the best approximation of yields (Amin et al., 2018). A uniform flat proton beam with diameter 1 cm incident on a 1 cm diameter cylinder target of different thicknesses (10  $\mu\text{m}$ , 5 mm) was used for the simulations, with monoenergetic protons varied between 1 MeV and 20 MeV in separate simulations. Computational times varied between simulations, from 3 hours to 30 hours for a 5 mm thick target and  $10^9$  monoenergetic primary protons (1 MeV and 20 MeV respectively). Secondary electrons and neutrons were not simulated, and range cuts of 0.05 mm for protons and 0.001 mm for ions were used. Interactions leading to the production of nuclides were recorded in a root Tree file, which was processed in Root v6.19/01 such that the total number of interactions leading to each nuclide was ascertained and output into a text file for each simulation. These results from multiple simulations were then processed in Matlab v2020a to calculate the physical thick target yields for each nuclide as a function of proton energy and plotted for comparison with cross-section-based calculations.

To verify the Geant4 inelastic proton interactions, thin target simulations were performed. The geometry consisted of 10  $\mu\text{m}$  thick cylinders of 1 cm diameter, with a uniform flat proton beam incident on the circular surface. The energy of the protons was varied between 1 MeV and 20 MeV in 1 MeV

increments, and  $10^9$  primary events were generated. To study the cross-section channels of interest, different simulations were performed with target materials consisting of  $^{43}\text{Ca}$ ,  $^{44}\text{Ca}$ ,  $^{46}\text{Ca}$  and  $^{48}\text{Ca}$ . The radionuclides created through the inelastic proton interactions in the target were recorded and used to determine the cross-section using the following formula:

$$r_x = \Phi * \sigma_x * \rho_A \quad (3.6)$$

Where  $r_x$  is the amount of reactions per unit volume,  $\phi$  is the flux of protons per unit area,  $\sigma_x$  is the energy dependent cross-section, and  $\rho_A$  is the density of the atoms in the target per unit volume.

After the cross-section verifications, thick target simulations were performed for comparison with measured yields. A thickness of 5mm was chosen to ensure targets were thick over the range of proton energies, and  $10^9$  primary events were generated. The radionuclides created through inelastic proton interactions in the target were recorded and used to determine the TTY.

### 3.3 Results and discussion

#### 3.3.1 Geant4 Simulation

The comparison of the TENDL-2014 cross-sections and the cross-sections computed from the result of the Geant4 simulation of thin targets is depicted in Figure 3.1(Koning et al., 2019). The Geant4 simulated cross-section is calculated using Eq. 3.6 from the total number of primary protons generated, the density of scattering target atoms, and the number of each radionuclide produced in each thin foil during simulation. The results of the 10  $\mu\text{m}$  thin foil simulation allows for the validation of the hadron physics models and verification of the scoring of radionuclides in the target volume by demonstrating that basic cross-sections could be accurately replicated.

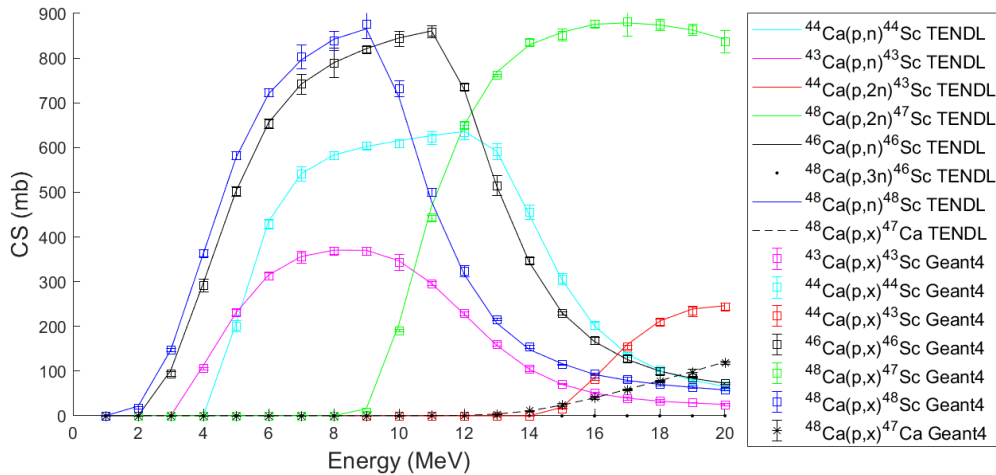


Figure 3.1 Comparison of Geant4 thin target simulation results and TENDL-2014 cross-sections from simulation of 10  $\mu\text{m}$  foils. Notice the good agreement between the calculated cross-sections from the thin foil simulations and the TENDL-2014 inputs.

For the thick target yield measurements, the geometry chosen for the Geant4 simulations is a target modeled as a 5mm cylinder of calcium in a vacuum with a proton beam that is uniform over the surface of the 1 cm diameter target and incident perpendicular to the surface. While this geometry is simple and does not account for beam shape or the specific cyclotron target station geometry, the simulations provides a good estimate of the production of radionuclides in the target material. This demonstrates that detailed cyclotron modelling in Monte Carlo simulations is not necessary to get an estimate of production parameters. To simulate a full target station, information about beam shape and intensity profile would be required; this would significantly increase the complexity and validation required of the simulation. A more detailed model of a GE PETtrace cyclotron solid target station created by Poignant et al. is available as an advanced example with Geant4 (AdvancedExampleSTCyclotron) (Poignant et al., 2016). A potential advantage of modelling the cyclotron target station includes predicting target heating and shielding of target station areas.

Limited benchmarking of Geant4 applications for the cyclotron production of radionuclides has been conducted. Some studies have been restricted to the comparison of simulated cross-sections to experimental data or the production of a single radionuclide in a target (Poignant et al., 2016; Ratcliffe and Edgecock, 2017). Amin et al. compared different Geant4 models for low energy physics applications in the calculation of medically relevant radionuclides and found that the QGSP\_BIC\_AllHP represented the best approximation of resulting radionuclide activity (Amin et al., 2018). This study comprehensively compares the production of all relevant radionuclides produced upon irradiation of natural calcium and provides a comparison to Geant4 results, which allows for a better benchmarking of the Monte Carlo

package's ability to provide predictions relevant for yield and radionuclidic purity. One major limitation of the QGSP\_BIC\_AllHP physics model in Geant4 is the lack of ability to calculate the yield of isomeric states, as previously reported by Chiappara (Chiappara, 2019). While the cross-sections relevant to the production of isomeric states of radionuclides is available in the G4TENDL1.3.2 data files used as input to the QGSP\_BIC\_AllHP physics model, the *isomerFlag* that is set in reading the data is not currently used in the simulation of inelastic hadronic interactions. This is particularly relevant for the proton irradiation of  $^{44}\text{Ca}$  as  $^{44\text{m}}\text{Sc}$  is co-produced with  $^{44}\text{Sc}$ , and the ratio of these radionuclides is of interest for production calculations.

Thick target yields of a radionuclide in a given target can be calculated from the relevant reaction cross-sections using Eq. 3 and 4. This requires knowledge of the cross-sections, which must be accompanied by regular measurements at all relevant energies below the incident proton energy; reported cross-sections can often be incomplete and not cover the entire energy range of interest. For example, Levkovskij's measurement of the  $^{44}\text{Ca}(p,n)^{44}\text{Sc}$  reaction cross-section start at 7.7 MeV and are thus insufficient for predicting the thick target yield  $^{44}\text{Sc}$  as the reaction threshold is 4.5 MeV (Levkovskij and Levkovskij, 1991). Therein lies the advantage of a nuclear data library such as TENDL which predicts the reaction cross-section at all energies below 100 MeV at regular intervals for all possible reaction channels; this enables the prediction of the yield of all potential radionuclides produced in a target. There are many emerging tools that use nuclear data libraries such as these for yield and radionuclidic purity calculations, including the IAEA MIB (Ferguson et al., 2017; Hou et al., 2014; Koning and Verpelli, 2020; Sitarz et al., 2019). However, the calculations made with these nuclear data libraries must be validated. The advantage in using a deterministic equation to calculate the yield as opposed to a Monte Carlo simulation is that it is significantly less computationally intensive and does not require validation or benchmarking of the underlying physics models.

### 3.3.2 TTY of $^{43}\text{Sc}$

The best prediction of  $^{43}\text{Sc}$  yield was the calculation based on the Carzaniga et al. cross-section measurements, which did not demonstrate any significant differences with the thick target yield measurements. On the other hand, both GEANT4 and the IAEA MIB predictions demonstrated an overestimation of production yield. The  $^{43}\text{Sc}$  yield significantly increases above 16 MeV due to the  $^{44}\text{Ca}(p,2n)^{43}\text{Sc}$  reaction and the higher abundance of  $^{44}\text{Ca}$  in natural calcium. While production routes of  $^{43}\text{Sc}$  with alpha bombardment of  $^{40}\text{Ca}$  or  $^{nat}\text{Ca}$  targets have been proposed, this may not be widely feasible due to the limited number of cyclotrons with alpha particle beams (Minegishi et al., 2016;

Walczak et al., 2015). Proton bombardment of  $^{46}\text{Ti}$  and  $^{43}\text{Ca}$  enriched targets at energies of 15 MeV and 12 MeV have been shown to produce  $^{43}\text{Sc}$  with radionuclidic purities of 99 % and 66 % respectively (Domnanich et al., 2017a). The data presented in this study suggest that an additional production route that would be of interest to investigate includes the bombardment of thin targets of enriched  $^{44}\text{Ca}$  at energies above 16 MeV, as this results in greater increases in  $^{43}\text{Sc}$  while  $^{44}\text{Sc}$  does not significantly increase. This could potentially make use of already existing  $^{44}\text{Ca}$  enriched materials that have been used to produce  $^{44}\text{Sc}$ .

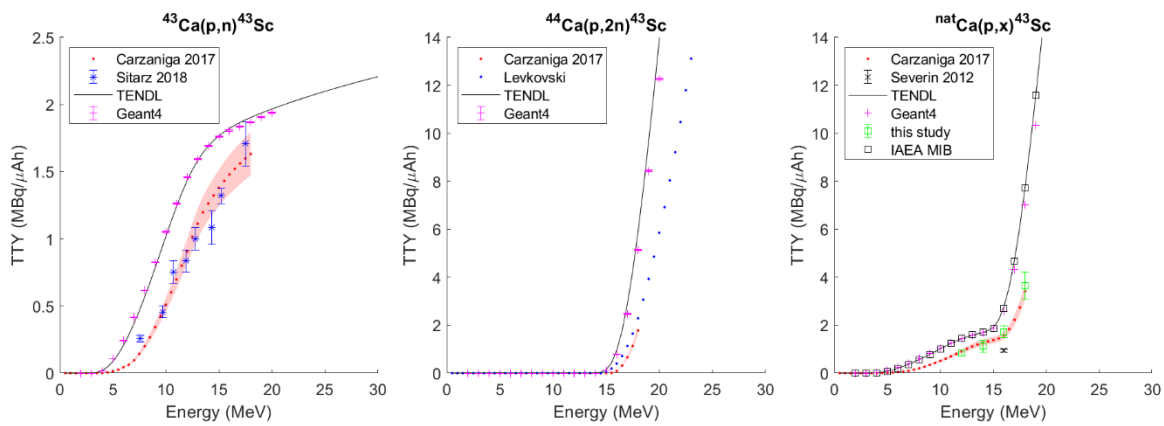


Figure 3.2: Thick target yield of  $^{43}\text{Sc}$  in natural metallic calcium, displaying the contribution of both the  $^{43}\text{Ca}(p,n)^{43}\text{Sc}$  and  $^{44}\text{Ca}(p,2n)^{43}\text{Sc}$  reactions, as well as their sum (right). Yield predictions calculated from the cross-section measurements of Carzaniga et al., Levkovskij et al., and TENDL are compared to the Geant4 simulation and experimental measurements made in this study as well as by Sitarz et al. and Severin et al. Note that the Sitarz measurements were made in enriched calcium carbonate targets and were converted to equivalent yields in natural abundance metallic calcium.

### 3.3.3 TTY of $^{44}\text{Sc}$

The production of  $^{44}\text{Sc}$  has been widely investigated, including cross-section measurements by Carzaniga et al. that span the energy range of the  $^{44}\text{Ca}(p,n)^{44}\text{Sc}$  reaction up to 18 MeV enabling thick target yield calculations based on experimental measurements (Carzaniga et al., 2017; Carzaniga and Braccini, 2019). As previously noted, the yield of the isomer  $^{44m}\text{Sc}$  cannot be predicted by Geant4, even if the data necessary for calculation is available. From our thin foil simulation, we have further evidence that this is the case as the simulations of  $^{44}\text{Sc}$  are comparable to the total cross-section. However, it was found that this total cross-section approximates the production of  $^{44}\text{Sc}$  quite accurately within the target. On the other hand, while it was not possible to determine the yield of  $^{44m}\text{Sc}$  using the Geant4 simulation, it was found that the measured thick target yields agree with previous measurements by Sitarz et al. and the

IAEA MIB predictions. There have been previous simulations of  $^{44}\text{Sc}$  in a liquid target, where Amin et al. reported an overestimation of the predicted yield in liquid targets by a factor of 2.35 and 2.1 for FLUKA and Geant4 respectively (Amin et al., 2018); although as the authors stated in their study the simulations were conducted in a liquid target and thus a greater uncertainty was expected due to fluid and thermal dynamics of the liquid target, this study represents an improvement in the prediction of the yield of  $^{44}\text{Sc}$  with Geant4.

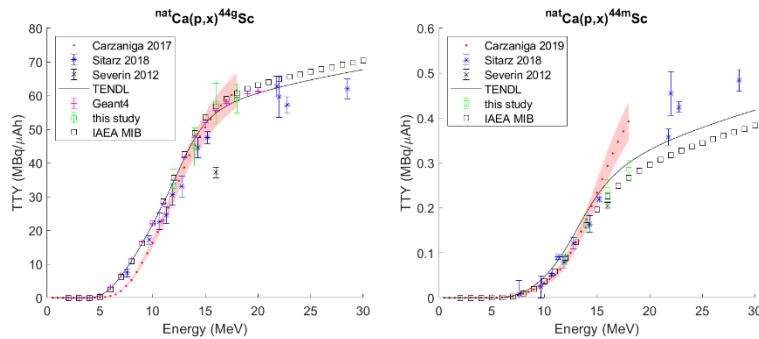


Figure 3.3: Thick target yield of  $^{44}\text{Sc}$  and  $^{44m}\text{Sc}$  in natural metallic targets. Yields predictions calculated from the cross-section measurements of Carzaniga et al. and TENDL are compared to the results of the Geant4 simulation and experimental measurements made in this study as well as by Sitarz et al. and Severin et al. Note that the Sitarz et al. measurements were made in enriched calcium carbonate targets and were converted to equivalent yields in natural abundance metallic calcium. The Geant4 simulations was not able to predict yield of the  $^{44m}\text{Sc}$  isomer.

### 3.3.4 TTY of $^{47}\text{Sc}$ , $^{48}\text{Sc}$ , and $^{47}\text{Ca}$

The production of  $^{47}\text{Sc}$  has been the focus of many recent studies due to its potential as a therapeutic radionuclide (Müller et al., 2014a). In this study, there is excellent agreement between the measured thick target yields and Geant4 simulations. Existing thick target yield measurements by Sitarz et al. and Misiak et al. follow the same trend as the Geant4 results and exhibit a lower rate of increase than predicted with the IAEA MIB (Misiak et al., 2017; Sitarz et al., 2018). Higher proton energies would increase the yield of  $^{47}\text{Sc}$  while limiting target thickness to ensure protons exit the target around the threshold energy of the  $^{48}\text{Ca}(p,2n)^{47}\text{Sc}$  reaction at 8.9 MeV would minimize the contribution of  $^{48}\text{Sc}$ .

The production of  $^{47}\text{Ca}$  has been investigated as an indirect method to produce  $^{47}\text{Sc}$  via the  $^{46}\text{Ca}(n,\gamma)^{47}\text{Ca}$  reaction and recently in an isotope harvesting system with a  $^{48}\text{Ca}$  beam (Abel et al., 2020; Domnanich et al., 2017b). While this is a promising avenue for the creation of a pseudo-generator system that can be eluted to generate radionuclidically pure  $^{47}\text{Sc}$ , the  $^{48}\text{Ca}(p,x)^{47}\text{Ca}$  reaction does not have a significant yield.

The Geant4 simulations and the IAEA MIB predictions do not demonstrate significant differences in predictions up to 20 MeV, but underestimate the experimental measurements in this study, which are in turn overestimated by the calculation using the Carzaniga cross-section measurements. While the proton bombardment of  $^{48}\text{Ca}$  is not a significant source of  $^{47}\text{Ca}$  compared to  $^{47}\text{Sc}$  and  $^{48}\text{Sc}$ , the low levels produced could be used to enhance the radionuclidic purity by delaying purification of the resulting solution. This delay enables  $^{47}\text{Ca}$  to decay to the desired  $^{47}\text{Sc}$  product and for the  $^{48}\text{Sc}$  activity to decrease to a greater extent due to the shorter half-life compared to  $^{47}\text{Ca}$  and  $^{47}\text{Sc}$ .

$^{48}\text{Sc}$  is an important radioisotope to characterize because the production of the therapeutic  $^{47}\text{Sc}$  isotope from calcium targets is based on the presence of the same target nuclide  $^{48}\text{Ca}$ , and thus differences in target enrichment will not lead to increases of one over the other. Accurate measurements of thick target yield can allow for the determination of beam energy and target thickness to optimize the radioisotopic ratio. Geant4 simulations more closely predict the experimental measurements in this study, while the IAEA MIB predictions tend to overestimate the yield. A previous discrepancy was noted by Sitarz et al. between their measured thick target yields of  $^{48}\text{Sc}$  and the measurements of Misiak et al., which suggested production was lower by a factor of 1.4 (Misiak et al., 2017; Sitarz et al., 2018). Our measurements suggest closer agreement with the thick target yields measured by Sitarz et al., suggesting that significant yields of  $^{48}\text{Sc}$  may be coproduced with  $^{47}\text{Sc}$ , especially for thick targets and lower beam energies. This is detrimental as  $^{48}\text{Sc}$  emits three high energy gammas with high yield, which would greatly increase the dose to non-target organs if co-administered with  $^{47}\text{Sc}$ . Of note are the predictions based off the Carzaniga measurements of the cross-section; the estimates of thick target yield greatly diverge from the predicted trends for energies greater than 10 MeV.

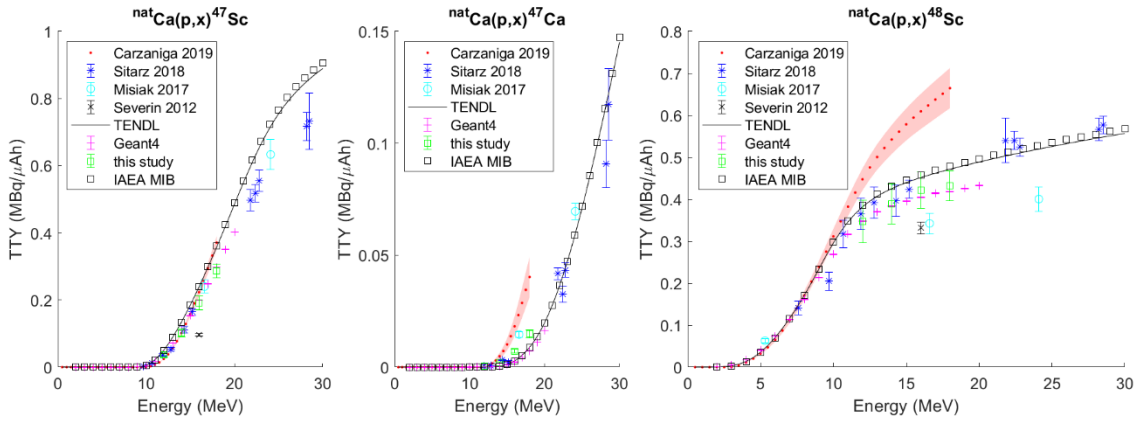


Figure 3.4: Thick target yield of  $^{47}\text{Sc}$ ,  $^{47}\text{Ca}$ , and  $^{48}\text{Sc}$  in natural metallic targets. Yields predictions calculated from the cross-section measurements of Carzaniga et al. and TENDL are compared to the results of the Geant4 simulation and experimental measurements made in this study as well as by Sitarz et al., Misiak et al. and Severin et al. Note that the Sitarz et al. and Misiak et al. measurements were made in enriched calcium carbonate targets and were converted to equivalent yields in natural abundance metallic calcium.

### 3.3.5 TTY of $^{46}\text{Sc}$

Very few experimental measurements relating to the production of  $^{46}\text{Sc}$  from proton-induced reactions are available in literature. This is likely due to the low natural abundance of the target atom  $^{46}\text{Ca}$  in natural calcium (0.004 %), as well as the significantly lower proportion of this target nuclide in enriched materials used to determine cross-sections and thick target yield measurements. While the natural enrichment leads to low levels of  $^{46}\text{Sc}$  produced in targets with respect to other nuclides, this is an important impurity to quantify as it has the longest half-life of the radioscaandium isotopes produced at 83.8 days, which is important from a radiation safety and contamination standpoint. The Geant4 simulations and IAEA MIB predictions closely agree with the experimental measurements. While limited experimental measurements are available for comparison, Misiak et al.'s measurement of the production of  $^{46}\text{Sc}$  at 16.6 MeV is consistent with the predictions; the increase of their measurement at 24.1 MeV from the predicted trend calculated using the  $^{46}\text{Ca}(p,n)^{46}\text{Sc}$  cross-section from TENDL is due to the contribution from the  $^{48}\text{Ca}(p,3n)^{46}\text{Sc}$  reaction which has an energy threshold of 19.8 MeV, as the abundance of  $^{48}\text{Ca}$  atoms in natural calcium is significantly greater than the abundance of  $^{46}\text{Ca}$  (Misiak et al., 2017).

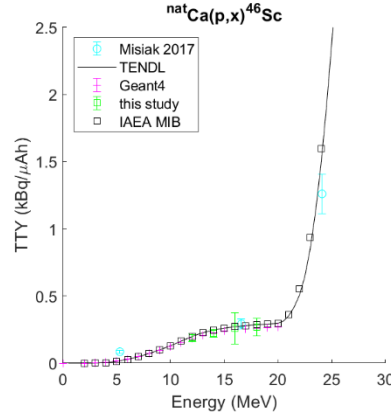


Figure 3.5: Thick target yield of  $^{46}\text{Sc}$  in natural metallic targets. Yields predictions calculated from TENDL are compared to the results of the Geant4 simulation and experimental measurements made in this study as well as by Misiak et al. Note that the Misiak et al. measurements were made in enriched calcium carbonate targets and were converted to equivalent yields in natural abundance metallic calcium.

### 3.3.6 Summary and comparison

The summary of the calculated thick target yields can be found in Table 3.7.

Table 3.7: Physical thick target yield of nuclides of interest and yield ratio, which represents the average ratio across 4 energies of the yield of the radionuclide as calculated by TENDL or simulated in Geant4 to the measured experimental radionuclide yield.

Proton Energy	Measured Thick Target Yield						
	$^{43}\text{Sc}$ MBq/μAh	$^{44}\text{Sc}$ MBq/μAh	$^{44\text{m}}\text{Sc}$ MBq/μAh	$^{46}\text{Sc}$ kBq/μAh	$^{47}\text{Sc}$ MBq/μAh	$^{48}\text{Sc}$ MBq/μAh	$^{47}\text{Ca}$ kBq/μAh
$12.1 \pm 0.2$	$0.84 \pm 0.13$	$33.3 \pm 4.9$	$0.087 \pm 0.013$	$0.19 \pm 0.03$	$0.036 \pm 0.006$	$0.347 \pm 0.051$	$0.34 \pm 0.05$
$14.1 \pm 0.1$	$1.13 \pm 0.24$	$44.8 \pm 5.5$	$0.165 \pm 0.020$	$0.22 \pm 0.03$	$0.102 \pm 0.013$	$0.389 \pm 0.048$	$2.10 \pm 0.32$
$16.0 \pm 0.1$	$1.72 \pm 0.24$	$57.6 \pm 6.0$	$0.239 \pm 0.024$	$0.26 \pm 0.12$	$0.191 \pm 0.020$	$0.421 \pm 0.043$	$7.10 \pm 0.85$
$18.0 \pm 0.1$	$3.65 \pm 0.58$	$59.2 \pm 4.4$	$0.285 \pm 0.021$	$0.27 \pm 0.07$	$0.287 \pm 0.021$	$0.432 \pm 0.036$	$14.89 \pm 1.79$
Yield Ratio							
IAEA MIB	1.73	1.04	0.97	1.07	1.3	1.10	0.32
Geant4	1.66	1.02	-	0.98	1.07	0.98	0.27

In this work, it was generally found that the values calculated with Eq. 3.3 and 3.4 were comparable to the Geant4 results which both use the same underlying cross-sections as inputs for calculations, with Geant4 predicting lower yields for some radionuclides. Additionally, when using measured reaction cross-sections to calculate thick target yield, it was found that these predictions diverged for certain radionuclides at higher energies ( $^{48}\text{Sc}$ ,  $^{44\text{m}}\text{Sc}$ ,  $^{47}\text{Ca}$ ), which is likely due to integrating over a larger range of measurements each associated with their own uncertainties. As seen from Table 3.7, Geant4 was

generally more accurate for yield prediction compared to IAEA MIB, with yield ratios closer to 1. Geant4 predicted the yield of  $^{46}\text{Sc}$ ,  $^{47}\text{Sc}$  and  $^{48}\text{Sc}$  within 10%, but both the calculations and simulations of the yields of  $^{43}\text{Sc}$  and  $^{47}\text{Ca}$  were not accurate. For  $^{43}\text{Sc}$ , the yields calculated with the Carzaniga et al. cross-sections demonstrated an average yield ratio of 1.01 across measured energies, which represents a significant improvement over the Geant4 or IAEA MIB. However, with  $^{47}\text{Ca}$ , neither the simulations nor the predictions based off the IAEA MIB or Carzaniga et al. could accurately represent the experimental data, and further measurements are needed in the range of 15-20MeV to quantify the radionuclidic yield.

### 3.4 Conclusion

Investigation of simulated and theoretical yield predictions using Geant4 and the IAEA MIB revealed that greater accuracy was generally obtained through Monte Carlo simulations when compared with experimental measurements in natural calcium targets and scaled measurements in enriched calcium carbonate materials. However, this greater accuracy was not consistent across all radionuclide yields measured; higher levels of accuracy using Geant4 were obtained for  $^{46}\text{Sc}$ ,  $^{47}\text{Sc}$ , and  $^{48}\text{Sc}$ , whereas the IAEA MIB allowed for the accurate calculation of the yield of the isomeric states of  $^{44}\text{Sc}$ . This demonstrates the need for careful validation of simulation results with measurements. Further validation of the low-energy inelastic hadron physics models in Geant4 is required prior to use for radionuclide yield production calculations as the accuracy of simulations varies based on the cross-sections used as the input data. However, these results indicate that Geant4 simulations could prove a valuable tool for predicting yield and purity for different irradiation conditions and target compositions.

### 3.5 References

- Abel, E.P., Domnanich, K., Clause, H.K., Kalman, C., Walker, W., Shusterman, J.A., Greene, J., Gott, M., Severin, G.W., 2020. Production, Collection, and Purification of  $^{47}\text{Ca}$  for the Generation of  $^{47}\text{Sc}$  through Isotope Harvesting at the National Superconducting Cyclotron Laboratory. *ACS Omega* 5, 27864–27872. <https://doi.org/10.1021/acsomega.0c03020>
- Amin, T., Infantino, A., Barlow, R., Hoehr, C., 2018. Validating production of PET radionuclides in solid and liquid targets: Comparing Geant4 predictions with FLUKA and measurements. *Appl. Radiat. Isot.* 133, 61–67. <https://doi.org/10.1016/j.apradiso.2017.12.009>
- Carzaniga, T.S., Auger, M., Braccini, S., Bunka, M., Ereditato, A., Nesteruk, K.P., Scampoli, P., Türler, A., van der Meulen, N., 2017. Measurement of  $^{43}\text{Sc}$  and  $^{44}\text{Sc}$  production cross-section with an

- 18MeV medical PET cyclotron. *Appl. Radiat. Isot.* 129, 96–102.  
<https://doi.org/10.1016/j.apradiso.2017.08.013>
- Carzaniga, T.S., Braccini, S., 2019. Cross-section measurement of  $^{44m}\text{Sc}$ ,  $^{47}\text{Sc}$ ,  $^{48}\text{Sc}$  and  $^{47}\text{Ca}$  for an optimized  $^{47}\text{Sc}$  production with an 18 MeV medical PET cyclotron. *Appl. Radiat. Isot.* 143, 18–23. <https://doi.org/10.1016/j.apradiso.2018.10.015>
- Chiappara, D., 2019. Preliminary modelling for the Proton Boron Capture Therapy (PBCT) [WWW Document]. URL <http://tesi.cab.unipd.it/62579/> (accessed 11.8.20).
- Domnanich, K.A., Eichler, R., Müller, C., Jordi, S., Yakusheva, V., Braccini, S., Behe, M., Schibli, R., Türler, A., van der Meulen, N.P., 2017a. Production and separation of  $^{43}\text{Sc}$  for radiopharmaceutical purposes. *EJNMMI Radiopharm. Chem.* 2, 14. <https://doi.org/10.1186/s41181-017-0033-9>
- Domnanich, K.A., Müller, C., Benešová, M., Dressler, R., Haller, S., Köster, U., Ponsard, B., Schibli, R., Türler, A., van der Meulen, N.P., 2017b.  $^{47}\text{Sc}$  as useful  $\beta^-$ -emitter for the radiotheragnostic paradigm: a comparative study of feasible production routes. *EJNMMI Radiopharm. Chem.* 2, 5. <https://doi.org/10.1186/s41181-017-0024-x>
- Fassbender, M., Arzumanov, A., Jamriska, D.J., Lyssukhin, S.N., Trelle, H., Waters, L.S., 2007. Proton beam simulation with MCNPX: Gallium metal activation estimates below 30MeV relevant to the bulk production of  $^{68}\text{Ge}$  and  $^{65}\text{Zn}$ . *Nucl. Instrum. Methods Phys. Res. Sect. B Beam Interact. Mater. At., The Application of Accelerators in Research and Industry* 261, 742–746.  
<https://doi.org/10.1016/j.nimb.2007.03.099>
- Ferguson, S., Riauka, T., Jans, H., Gagnon, K., Engle, J.W., Barnhart, T.E., Nortier, F.M., O’Neil, J.P., Birnbaum, E.R., Gangon, K.M., 2017. Radionuclide production calculations: A GUI to determine irradiation conditions. *AIP Conf. Proc.* 1845, 020008. <https://doi.org/10.1063/1.4983539>
- Gagnon, K., Jensen, M., Thisgaard, H., Publicover, J., Lapi, S., McQuarrie, S.A., Ruth, T.J., 2011. A new and simple calibration-independent method for measuring the beam energy of a cyclotron. *Appl. Radiat. Isot.* 69, 247–253. <https://doi.org/10.1016/j.apradiso.2010.09.012>
- Hoehr, C., Oehlke, E., Benard, F., Lee, C.J., Hou, X., Badesso, B., Ferguson, S., Miao, Q., Yang, H., Buckley, K., Hanemaayer, V., Zeisler, S., Ruth, T., Celler, A., Schaffer, P., 2014.  $^{44g}\text{Sc}$  production using a water target on a 13 MeV cyclotron. *Nucl. Med. Biol.* 41, 401–406.  
<https://doi.org/10.1016/j.nucmedbio.2013.12.016>
- Hou, X., Vuckovic, M., Buckley, K., Bénard, F., Schaffer, P., Ruth, T., Celler, A., 2014. Graphical user interface for yield and dose estimations for cyclotron-produced technetium. *Phys. Med. Biol.* 59, 3337. <https://doi.org/10.1088/0031-9155/59/13/3337>

- Huclier-Markai, S., Alliot, C., Kerdjoudj, R., Mougin-Degraef, M., Chouin, N., Haddad, F., 2018. Promising Scandium Radionuclides for Nuclear Medicine: A Review on the Production and Chemistry up to *In Vivo* Proofs of Concept. *Cancer Biother. Radiopharm.* 33, 316–329.  
<https://doi.org/10.1089/cbr.2018.2485>
- Infantino, A., Cicoria, G., Pancaldi, D., Ciarmatori, A., Boschi, S., Fanti, S., Marengo, M., Mostacci, D., 2011. Prediction of <sup>89</sup>Zr production using the Monte Carlo code FLUKA. *Appl. Radiat. Isot., Proceedings of the 6th CHERNE Workshop* 69, 1134–1137.  
<https://doi.org/10.1016/j.apradiso.2010.11.027>
- Koning, A.J., Rochman, D., Sublet, J.-Ch., Dzysiuk, N., Fleming, M., van der Marck, S., 2019. TENDL: Complete Nuclear Data Library for Innovative Nuclear Science and Technology. *Nucl. Data Sheets, Special Issue on Nuclear Reaction Data* 155, 1–55.  
<https://doi.org/10.1016/j.nds.2019.01.002>
- Krasnov, N.N., 1974. Thick target yield. *Int. J. Appl. Radiat. Isot.* 25, 223–227.  
[https://doi.org/10.1016/0020-708X\(74\)90031-3](https://doi.org/10.1016/0020-708X(74)90031-3)
- Levkovskij, V.N., Levkovskij, A., 1991. Activation cross section nuclides of average masses (A= 40-100) by protons and alpha-particles with average energies (E= 10-50 MeV). *Cs Protons Alphas Mosc.*
- Ljungberg, M., Strand, S.-E., King, M.A., 2012. *Monte Carlo Calculations in Nuclear Medicine, Second Edition: Applications in Diagnostic Imaging.* CRC Press.
- Mamtimin, M., Harmon, F., Starovoitova, V.N., 2015. Sc-47 production from titanium targets using electron linacs. *Appl. Radiat. Isot.* 102, 1–4. <https://doi.org/10.1016/j.apradiso.2015.04.012>
- Minegishi, K., Nagatsu, K., Fukada, M., Suzuki, H., Ohya, T., Zhang, M.-R., 2016. Production of scandium-43 and -47 from a powdery calcium oxide target via the nat/<sup>44</sup>Ca( $\alpha$ ,x)-channel. *Appl. Radiat. Isot.* 116, 8–12. <https://doi.org/10.1016/j.apradiso.2016.07.017>
- Misiak, R., Walczak, R., Waś, B., Bartyzel, M., Mietelski, J.W., Bilewicz, A., 2017. <sup>47</sup>Sc production development by cyclotron irradiation of <sup>48</sup>Ca. *J. Radioanal. Nucl. Chem.* 313, 429–434.  
<https://doi.org/10.1007/s10967-017-5321-z>
- Müller, C., Bunka, M., Haller, S., Köster, U., Groehn, V., Bernhardt, P., Meulen, N. van der, Türler, A., Schibli, R., 2014. Promising Prospects for <sup>44</sup>Sc-/<sup>47</sup>Sc-Based Theragnostics: Application of <sup>47</sup>Sc for Radionuclide Tumor Therapy in Mice. *J. Nucl. Med.* 55, 1658–1664.  
<https://doi.org/10.2967/jnumed.114.141614>
- Müller, C., Bunka, M., Reber, J., Fischer, C., Zhernosekov, K., Türler, A., Schibli, R., 2013. Promises of Cyclotron-Produced <sup>44</sup>Sc as a Diagnostic Match for Trivalent  $\beta^-$ -Emitters: In Vitro and In Vivo

- Study of a  $^{44}\text{Sc}$ -DOTA-Folate Conjugate. *J. Nucl. Med.* 54, 2168–2174.  
<https://doi.org/10.2967/jnumed.113.123810>
- Müller, C., Domnanich, K.A., Umbricht, C.A., van der Meulen, N.P., 2018. Scandium and terbium radionuclides for radiotheranostics: current state of development towards clinical application. *Br. J. Radiol.* 20180074. <https://doi.org/10.1259/bjr.20180074>
- National Nuclear Data Center, n.d. Nudat 2 database v.2.8 [WWW Document]. URL <https://www.nndc.bnl.gov/nudat2/> (accessed 6.1.20).
- Otuka, N., Takács, S., 2015. Definitions of radioisotope thick target yields. *Radiochim. Acta* 103, 1–6.  
<https://doi.org/10.1515/ract-2013-2234>
- Poignant, F., Penfold, S., Asp, J., Takhar, P., Jackson, P., 2016. GEANT4 simulation of cyclotron radioisotope production in a solid target. *Phys. Med.* 32, 728–734.  
<https://doi.org/10.1016/j.ejmp.2016.04.006>
- Pruszyński, M., Loktionova, N.S., Filosofov, D.V., Rösch, F., 2010. Post-elution processing of  $^{44}\text{Ti}/^{44}\text{Sc}$  generator-derived  $^{44}\text{Sc}$  for clinical application. *Appl. Radiat. Isot.* 68, 1636–1641.  
<https://doi.org/10.1016/j.apradiso.2010.04.003>
- Rane, S., Harris, J.T., Starovoitova, V.N., 2015.  $^{47}\text{Ca}$  production for  $^{47}\text{Ca}/^{47}\text{Sc}$  generator system using electron linacs. *Appl. Radiat. Isot.* 97, 188–192. <https://doi.org/10.1016/j.apradiso.2014.12.020>
- Ratcliffe, N., Barlow, R., Bungau, A., Bungau, C., Cywinski, R., 2013. GEANT4 Target Simulations for Low Energy Medical Applications, in: *Proceedings of the 4th International Particle Accelerator Conference*. JACoW, Shanghai, China, pp. 3717–3719.
- Ratcliffe, N., Edgecock, T.R., 2017. A Study of Potential Accelerator Production of Radioisotopes for Both Diagnostics and Therapy 3.
- Roesch, F., 2012. Scandium-44: Benefits of a Long-Lived PET Radionuclide Available from the  $^{44}\text{Ti}/^{44}\text{Sc}$  Generator System. *Curr. Radiopharm.* 5, 187–201.
- Rogers, D.W.O., 2006. Fifty years of Monte Carlo simulations for medical physics\*. *Phys. Med. Biol.* 51, R287. <https://doi.org/10.1088/0031-9155/51/13/R17>
- Rotsch, D.A., Brown, M.A., Nolen, J.A., Brossard, T., Henning, W.F., Chemerisov, S.D., Gromov, R.G., Greene, J., 2018. Electron linear accelerator production and purification of scandium-47 from titanium dioxide targets. *Appl. Radiat. Isot.* 131, 77–82.  
<https://doi.org/10.1016/j.apradiso.2017.11.007>
- Seco, J., Verhaegen, F., 2013. *Monte Carlo Techniques in Radiation Therapy*. CRC Press.

- Severin, G.W., Engle, J.W., Valdovinos, H.F., Barnhart, T.E., Nickles, R.J., 2012. Cyclotron produced  $^{44}\text{gSc}$  from natural calcium. *Appl. Radiat. Isot.* 70, 1526–1530.  
<https://doi.org/10.1016/j.apradiso.2012.04.030>
- Sitarz, M., 2019. Research on production of new medical radioisotopes with cyclotron.
- Sitarz, M., Nigron, E., Guertin, A., Haddad, F., Matulewicz, T., 2019. New Cross-Sections for  $\text{natMo}(\alpha, x)$  Reactions and Medical  $^{97}\text{Ru}$  Production Estimations with Radionuclide Yield Calculator. *Instruments* 3, 7. <https://doi.org/10.3390/instruments3010007>
- Sitarz, M., Szkliniarz, K., Jastrzębski, J., Choiński, J., Guertin, A., Haddad, F., Jakubowski, A., Kapinos, K., Kisieliński, M., Majkowska, A., Nigron, E., Rostampour, M., Stolarz, A., Trzcińska, A., Walczak, R., Wojtkowska, J., Zipper, W., Bilewicz, A., 2018. Production of Sc medical radioisotopes with proton and deuteron beams. *Appl. Radiat. Isot.* 142, 104–112.  
<https://doi.org/10.1016/j.apradiso.2018.09.025>
- Starovoitova, V.N., Cole, P.L., Grimm, T.L., 2015. Accelerator-based photoproduction of promising beta-emitters  $^{67}\text{Cu}$  and  $^{47}\text{Sc}$ . *J. Radioanal. Nucl. Chem.* 305, 127–132.  
<https://doi.org/10.1007/s10967-015-4039-z>
- Valdovinos, H.F., Hernandez, R., Barnhart, T.E., Graves, S., Cai, W., Nickles, R.J., 2015. Separation of cyclotron-produced  $^{44}\text{Sc}$  from a natural calcium target using a dipentyl pentylphosphonate functionalized extraction resin. *Appl. Radiat. Isot.* 95, 23–29.  
<https://doi.org/10.1016/j.apradiso.2014.09.020>
- van der Meulen, N.P., Bunka, M., Domnanich, K.A., Müller, C., Haller, S., Vermeulen, C., Türler, A., Schibli, R., 2015. Cyclotron production of  $^{44}\text{Sc}$ : From bench to bedside. *Nucl. Med. Biol.* 42, 745–751. <https://doi.org/10.1016/j.nucmedbio.2015.05.005>
- Walczak, R., Krajewski, S., Szkliniarz, K., Sitarz, M., Abbas, K., Choiński, J., Jakubowski, A., Jastrzębski, J., Majkowska, A., Simonelli, F., Stolarz, A., Trzcińska, A., Zipper, W., Bilewicz, A., 2015. Cyclotron production of  $^{43}\text{Sc}$  for PET imaging. *EJNMMI Phys.* 2, 33. <https://doi.org/10.1186/s40658-015-0136-x>
- Wang, M., Huang, W.J., Kondev, F.G., Audi, G., Naimi, S., 2021. The AME 2020 atomic mass evaluation (II). Tables, graphs and references\*. *Chin. Phys. C* 45, 030003. <https://doi.org/10.1088/1674-1137/abddaf>
- Yagi, M., Kondo, K., 1977. Preparation of carrier-free  $^{47}\text{Sc}$  by the  $^{48}\text{Ti}(\gamma, p)$  reaction. *Int. J. Appl. Radiat. Isot.* 28, 463–468. [https://doi.org/10.1016/0020-708X\(77\)90178-8](https://doi.org/10.1016/0020-708X(77)90178-8)

Ziegler, J., Littmark, U., Biersack, J., 2008. Calculation using the stopping and range of ions in matter (SRIM) code.

## Chapter 4

# Comparison of scandium-44 with other PET radionuclides in pre-clinical PET phantom imaging

---

---

### 4.1 Introduction

The physical properties of the radionuclide used in a PET study affect the quality of the reconstructed image and the quantification of reconstructed activity. The positron energy spectrum of the radionuclide determines the positron range. The positron range is one of the dominant factors affecting resolution, and this is especially pronounced in pre-clinical scanners with smaller crystal sizes (Laforest et al., 2002; Levin and Hoffman, 1999) There have been many experimental and Monte Carlo studies investigating the positron range of radionuclides in various media (Alva-Sánchez et al., 2016; Cal-González et al., 2013; Champion and Loirec, 2007, 2006; Lehnert et al., 2011). Techniques for correcting the blurring caused by the positron range have been proposed (Jørdal et al., 2012; Laforest and Liu, 2009).

Some newly proposed radionuclides possess high-energy co-emitted gammas (i.e. prompt gammas) which negatively interfere with the detection of positron annihilation photon pairs (Conti and Eriksson, 2016); added image noise, owing to the increased the rate of spurious coincidences, has been reported (Martin et al., 1995; Schueller et al., 2003) and is not directly accounted for in conventional PET corrections. The prompt gammas are often of different energy and therefore possess different scatter and detection kernels. Prompt gamma corrections have been proposed to increase the accuracy of quantitative imaging, but are often radionuclide specific and require further investigation before being applied to novel radionuclides (Anizan et al., 2012; Braad et al., 2015; Buchholz et al., 2003; Eigner et al., 2013; Esteves et al., 2010; Robinson et al., 2004; Walrand et al., 2003).

$^{44}\text{Sc}$  is of particular interest in PET imaging, and more broadly for theranostic applications in conjunction with  $^{47}\text{Sc}$  (Huclier-Markai et al., 2018; Loveless et al., 2019; Müller et al., 2018, 2014b).  $^{44}\text{Sc}$  can be cheaply produced in high yields on low energy cyclotrons through the proton irradiation of natural

calcium or enriched  $^{44}\text{Ca}$  targets (Severin et al., 2012; Valdovinos et al., 2015).  $^{44}\text{Sc}$  can also be obtained through the decay of  $^{44}\text{Ti}$ ; there have been initial developments into  $^{44}\text{Ti}/^{44}\text{Sc}$  generator systems (Pruszyński et al., 2010; Radchenko et al., 2017; Roesch, 2012). Wider availability of the radionuclide has led to more radiolabelling and imaging studies (Domnanich et al., 2016; Koumarianou et al., 2012; Pruszyński et al., 2012; van der Meulen et al., 2015; W. Price et al., 2016). However, the image quality and quantitative accuracy of  $^{44}\text{Sc}$  needs to be investigated rigorously to determine its clinical relevancy with respect to other potential radiometals used for PET imaging.

Phantom imaging is a useful tool for comparing radionuclide performance under similar imaging conditions (Soderlund et al., 2015). Thus far, phantom imaging with  $^{44}\text{Sc}$  has been mainly limited to Derenzo phantoms. A radionuclide comparison in a Derenzo phantom was first reported by Bunka et al. comparing the relative spatial resolution of  $^{68}\text{Ga}$ ,  $^{44}\text{Sc}$ ,  $^{89}\text{Zr}$ ,  $^{11}\text{C}$ ,  $^{64}\text{Cu}$  and  $^{18}\text{F}$  (Bunka et al., 2016). Domnanich et al. later expanded on this study by comparing the resolution of Derenzo phantom images for  $^{44}\text{Sc}$  and  $^{43}\text{Sc}$  obtained in different ratios through different production routes, such as the proton irradiation of enriched  $^{46}\text{Ti}$  and  $^{43}\text{Ca}$  (Domnanich et al., 2017a).

While spatial resolution as a function radionuclide is of interest, other performance metrics also necessitate quantification when evaluating new imaging radionuclides (Williams et al., 2005). The NEMA guidelines have provided a standardized procedure for evaluating the performance of small-animal PET scanners (NEMA NU4-2008). These same procedures might be used to compare image parameters between different radionuclides on the same scanner; this was done by Disselhorst et al. to compare the recovery coefficients and spill-over ratios for  $^{18}\text{F}$ ,  $^{68}\text{Ga}$ ,  $^{124}\text{I}$  and  $^{89}\text{Zr}$  (Disselhorst et al., 2010).

In this study, the imaging properties of  $^{44}\text{Sc}$  are further assessed through phantom imaging in the Siemens Inveon small-animal PET scanner; this includes measurements of noise (%SD) and activity quantification (RC, SOR) that were not previously determined. Three different phantoms are used to acquire relevant measurements. In addition, all quantitative parameters evaluated for  $^{44}\text{Sc}$  were also measured for  $^{18}\text{F}$ , the most common PET radionuclide, as well as the two widely used PET radiometals  $^{68}\text{Ga}$  and  $^{64}\text{Cu}$  to allow intercomparison of all radionuclides.

## 4.2 Materials and methods

### 4.2.1 Radionuclides

Four radionuclides were used in this comparison study:  $^{18}\text{F}$ , the most commonly used PET radionuclide, and three radiometals,  $^{68}\text{Ga}$ ,  $^{44}\text{Sc}$ , and  $^{64}\text{Cu}$ .

*Fluorine-18:* The radiofluorine was produced locally at the Cross Cancer Institute (CCI) from enriched  $^{18}\text{O}$  water. With a half-life of 109.8 minutes,  $^{18}\text{F}$  is a pure, low-energy positron emitter, with an average and maximum energy of emission of 249.8 keV and 633.5 keV respectively (96.7 % abundance).

*Copper-64:* Radiocopper was produced at Washington University in St. Louis, USA and shipped to the University of Alberta in Edmonton, Canada.  $^{64}\text{Cu}$  has a 12.7 h half-life and decays through both  $\beta^-$  (38.5 %) and  $\beta^+$  (17.6 %) decay. The positron is emitted with an average and endpoint energy of 278.2 and 653.0 keV respectively.

*Gallium-68:* Radiogallium was obtained from a  $^{68}\text{Ge}/^{68}\text{Ga}$  generator (iThemba Laboratories, Sommerset West, South Africa).  $^{68}\text{Ga}$  decays with the shortest half-life of the radionuclides in this study, at 67.71 minutes. On the other hand, it emits the positron with the greatest average and endpoint energies, at 836.0 and 1890 keV respectively with 87.7 % abundance and a total positron branching ratio of 88.8 %. An additional 1077 keV gamma is emitted with 3.22 % of decays.

*Scandium-44:*  $^{44}\text{Sc}$  has a 3.97 hour half-life and emits a 1157 keV gamma (99.9 % abundance) in addition to a positron (94.27 % abundance) with an average and maximum energy of 632.0 and 1474 keV respectively. The radioscandium was produced locally at the CCI through the irradiation of natural calcium with 16 MeV protons. The radionuclidic purity is reported in Table 4.1.

*Table 4.1 Radioisotopic composition of radioscandium from irradiation of natural calcium target with 16 MeV protons*

Isotope	Half-life	Percent activity at EOB	Percent activity at 9.5 h post EOB
$^{44}\text{Sc}$	3.97 h	94.9	90.1
$^{43}\text{Sc}$	3.89 h	3.6	3.2
$^{44\text{m}}\text{Sc}$	58.61 h	0.5	2.1
$^{47}\text{Sc}$	3.35 d	0.4	1.8
$^{48}\text{Sc}$	43.67 h	0.6	2.7

#### 4.2.2 Image acquisition

The Siemens Inveon PET platform was used to perform imaging experiments. Its detector consists of lutetium oxyorthosilicate (LSO) crystals coupled through a light-guide to position sensitive photo-multiplier tubes. The LSO crystals are arranged in 16 detector blocks, each with 4 detectors axially which are divided into a 20x20 crystal arrays. The ring diameter is 16.1 cm and the axial length 12.7 cm, with

individual crystal sizes of  $1.5 \times 1.5 \times 10 \text{ mm}^3$ . For the acquisitions, an energy window of 350-650 keV and a coincidence timing window of  $3.432 \mu\text{s}$  was used.

Prior to injection into the phantoms, the radionuclide activity was measured in an Atomlab 400 dose calibrator (Biodex Medical Systems, NY, USA). Emission data was acquired in list-mode and the Inveon Acquisition Workplace (v. 1.5.0.28) was used to bin the data into sinograms and reconstruct the images. Images were reconstructed with three image reconstruction procedures available, using the default parameters. The reconstruction procedures were 2D FBP (Fourier rebinning, Nyquist cut-off 0.5), OSEM3D-MAP (2 OSEM3D iterations, 18 MAP iterations, 1.5mm requested resolution), and OSEM2D (4 iterations).

#### 4.2.3 Image noise, spill-over ratio and recovery coefficient

As the quality of reconstructed images can vary under different imaging situations, the National Electrical Manufacturers Association (NEMA) have provided a standard for acquiring and evaluating the data equivalent to a full body scan of a rodent with cold and hot regions (NEMA NU 4-2008). A NEMA image quality phantom consists of a polymethylmethacrylate (PMMA) cylinder with three distinct sections, as outlined in Figure 4.1, with the fillable activity hashed in blue.

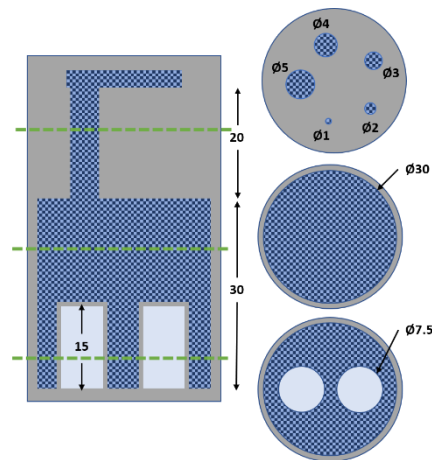


*Figure 4.1 Cross-sections of the NEMA image quality phantom with dimensions in mm. Left: Axial cross-section. Right: Transverse cross-sections of the three different regions. The grey area represents the PMMA phantom, the dark blue hashed region represents the volume filled with activity and the light blue represents the cold air and water volumes.*

The NEMA guidelines state that measurements should be performed with a total activity of  $3.7 \text{ MBq} \pm 5\%$  of  $^{18}\text{F}$  and counts acquired over 1200 s. To compare standard metrics for different radionuclides, modifications to this procedure must be made. The number of positron decays for a given activity and time is affected by the radionuclide's half-life and positron branching ratio. The approach taken in this

study is to keep the starting activity 3.7 MBq and modify the acquisition time in order to achieve the same number of positron decays as  $^{18}\text{F}$  in 1200 seconds. Table 4.2 lists the number of positron decays for a 3.7 MBq source of each different radionuclide, as well as the acquisition time used to obtain the same number of counts as  $^{18}\text{F}$  in the guideline conditions.

Table 4.2 Number of decays expected in standard scan conditions and time used to acquire an equal amount of positron decays for each radionuclide.

Nuclide	Positron annihilations in 1200s for 3.7 MBq	Time to acquire same number of positron annihilations as $^{18}\text{F}$ (s)
$^{18}\text{F}$	$4.03 \cdot 10^9$	1200
$^{68}\text{Ga}$	$3.57 \cdot 10^9$	1376
$^{64}\text{Cu}$	$0.774 \cdot 10^9$	6506
$^{44}\text{Sc}$	$4.07 \cdot 10^9$	1190

After the emission acquisition, a 30 min transmission scan was acquired with a  $^{57}\text{Co}$  point source and used for attenuation correction. The reconstructed transmission image was segmented into five materials: background ( $0.00 \text{ cm}^{-1}$ ), animal bed ( $0.0150 \text{ cm}^{-1}$ ), water ( $0.095 \text{ cm}^{-1}$ ), bone ( $0.1780 \text{ cm}^{-1}$ ) and aluminum ( $0.22 \text{ cm}^{-1}$ ).

To measure uniformity, the central uniform region of the phantom was contoured. A 22.5 mm diameter (75% of active diameter) and 10 mm long cylindrical VOI was drawn, and the mean ( $C_{uniform}$ ), maximum, and minimum values were recorded, while the percent standard deviation ( $\sigma_{uniform}$ ) was calculated.

The hot rod region was used to measure the recovery coefficient. The central 10 mm length of the rods were averaged, circular ROIs twice the size of each rod drawn and the pixel with the maximum value in each ROI was found. This transverse pixel was used in an axial profile over the 10 mm to determine for each rod the mean ( $C_{rod}$ ) and standard deviation ( $\sigma_{rod}$ ). The recovery coefficient ( $RC$ ) is the ratio of the mean value of the rods to that of the uniform region, while the uncertainty ( $\sigma_{RC}$ ) is calculated using the standard deviation.

$$RC = \frac{C_{rod}}{C_{uniform}} \quad \text{and} \quad \sigma_{RC} = 100 * \sqrt{\left(\frac{STD_{rod}}{C_{rod}}\right)^2 + \left(\frac{STD_{uniform}}{C_{uniform}}\right)^2} \quad (4.1)$$

Finally, the spill-over ratio (SOR) in air and water was measured using a 4mm diameter (50 % of cylinder diameter) and 7.5mm long cylindrical volume for interest in the water- and air-filled inserts. The mean

activity ( $C_{cold}$ ) and standard deviation ( $STD_{cold}$ ) was calculated in each ROI; the SOR is the ratio of the mean value in the inserts to the mean value of the uniform region, while the uncertainty ( $\sigma_{SOR}$ ) is calculated using the standard deviation.

$$SOR = \frac{C_{cold}}{C_{uniform}} \quad \text{and} \quad \sigma_{SOR} = 100 * \sqrt{\left(\frac{STD_{cold}}{C_{cold}}\right)^2 + \left(\frac{STD_{uniform}}{C_{uniform}}\right)^2} \quad (4.2)$$

#### 4.2.4 Contrast and feature size

Regions of interest in pre-clinical scans can vary in size; many image quality models relate contrast to feature size and signal-to-noise ratio. It is important to understand the relationship between contrast and feature size because radionuclide properties, such as the positron energy spectrum, can affect lesion visibility and quantification. The Derenzo phantom, depicted in Figure 4.2, is commonly used to quantify the trade-off between image contrast and visibility of small features. It is constructed from PMMA and contains triangular arrangements of hollow rods which can be filled with radioactivity. Each of the six sections contains rods of a given diameter (2.5, 2.0, 1.5, 1.25, 1.0 and 0.8 mm) and each rod is separated from its nearest neighbours by twice its diameter (center-to-center distance).

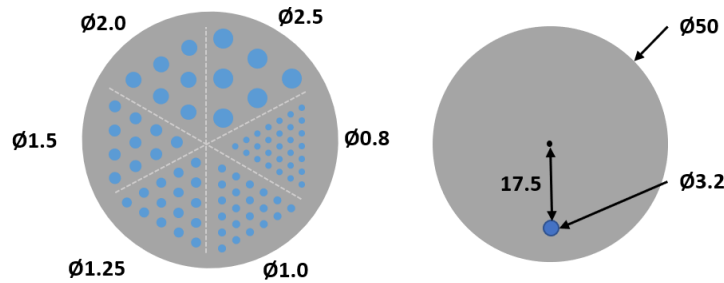


Figure 4.2 Phantom cross-sections with dimensions in mm. Left: Cross-section of the Derenzo phantom with the fillable rod diameters. Right: NEC phantom cross-section.

A large number of coincidences (greater than  $5 \times 10^7$ ) was acquired for each radionuclide in the Derenzo phantom and the images were reconstructed with attenuation correction and a final reconstructed pixel size of 0.388 mm (zoom 2). A transverse slice was used to determine the contrast in each triangular region. A profile was drawn between the central pixels of the center-most rod and an outer rod. The peak ( $C_{max}$ ) and minimum ( $C_{min}$ ) value of this profile were utilized to calculate image contrast ( $C$ ):

$$C = \frac{C_{max} - C_{min}}{C_{max} + C_{min}} \quad (4.3)$$

#### 4.2.5 Coincidence characteristics

Scanner performance is affected by the amount of radioactivity and geometry of the object in the scanner's field of view. Count losses occur as a result of camera dead time, decreasing the scanner's counting rate capability. Additionally, some scanners manifest a difference in sensitivity to scattered and primary radiation (Goertzen et al., 2012). In this study, following NEMA NU 4-2008, these effects are investigated for each radionuclide using a "rat"-sized phantom made of high-density polyethylene (density  $0.96 \pm 0.1 \text{ g/cm}^3$ ) with  $50 \pm 0.5 \text{ mm}$  diameter and a length of  $150 \pm 0.5 \text{ mm}$ . A 3.2 mm diameter hole 17.5 mm from the center extends through the length of the phantom, depicted in Figure 4.2, through which a 140 mm line source containing the radionuclide of interest is inserted.

For this study, sources of  $^{18}\text{F}$ ,  $^{44}\text{Sc}$ , and  $^{68}\text{Ga}$  with activities greater than 100 MBq were placed in the phantom which was centered in the field of view, and counts were acquired over several half-lives as the radionuclides decayed. This study was not performed with  $^{64}\text{Cu}$  due to the low branching ratio and long half-life; the activity required to observe count rates similar to the other radionuclides would be significantly larger (5.5 times the activity of  $^{18}\text{F}$  to achieve the same amount of emitted positrons) and the acquisition time would greatly increase (greater than 3 days to decay from 100 MBq to 1.5 MBq). Prior to binning into sinograms, the list mode data was separated into 15 minute time frames for  $^{18}\text{F}$  and  $^{68}\text{Ga}$ , and 30 minute time frames for  $^{44}\text{Sc}$ . These durations were chosen to be less than a quarter of each radionuclide's half-life.

Single-slice rebinning was used to collapse oblique sinograms into single sinograms for each slice, with a span of 79 and ring difference of 39. No corrections were applied to the acquired counts, and the random coincidences were estimated in a separate sinogram. True ( $R_T$ ), random ( $R_R$ ) and scatter ( $R_S$ ) event rates, as prescribed by NEMA NU-4, were used to calculate the noise equivalent count rate, NECR, using:

$$NECR = \frac{R_T^2}{R_T + R_S + R_R} \quad (4.4)$$

The NECR is the true count rate that would lead to the same amount of noise due to counting statistics in the absence of scattered and random coincidences

## 4.3 Results

Measured results for each parameter are discussed below; summary of key numeric values for each parameter is provided in table 3 at the end of this section.

### 4.3.1 Image noise, spill-over ratio and recovery coefficient

The percentage standard deviation (%SD) is a measure for noise in the reconstructed image, and the measured values are shown in Figure 4.3 (rightmost chart). It's variation is similar for all radionuclides with FBP and OSEM2D reconstruction algorithms; however, OSEM3D-MAP with scatter correction increases noise for  $^{68}\text{Ga}$  and  $^{44}\text{Sc}$  while decreasing it for  $^{18}\text{F}$  and  $^{64}\text{Cu}$ . While  $^{18}\text{F}$  and  $^{64}\text{Cu}$  exhibit similar values, %SD for  $^{68}\text{Ga}$  and  $^{44}\text{Sc}$  is slightly increased. Note that the same number of counts were acquired for each radionuclide; an increase in %SD therefore indicates a relative decrease in the signal-to-noise ratio in the resulting image.

The spill-over ratio (SOR) is a measure for activity falsely assigned to regions in the reconstructed image in which no radioactivity was present during image acquisition. The SOR in air and in water are also found in Figure 4.3 as a function of reconstruction algorithm and radionuclide. As expected, the scatter correction decreases the SOR because of the decrease of accepted scattered photons. The reconstruction strategy is the main determinant of the SOR in air which is largely independent of the radionuclide species, as demonstrated in Figure 4.3.

The SOR in water has two distinct groupings: the SOR in water for short-range positron emitters ( $^{18}\text{F}$  and  $^{64}\text{Cu}$ ) is significantly smaller than for the long-range positron emitters  $^{44}\text{Sc}$  and  $^{68}\text{Ga}$ . Contrary to air, the SOR in water is determined less by the scatter correction strategy than the positron range. Overall, SOR in water scales with positron range, with  $^{44}\text{Sc}$  exhibiting intermediate values between  $^{64}\text{Cu}$  and  $^{68}\text{Ga}$ .

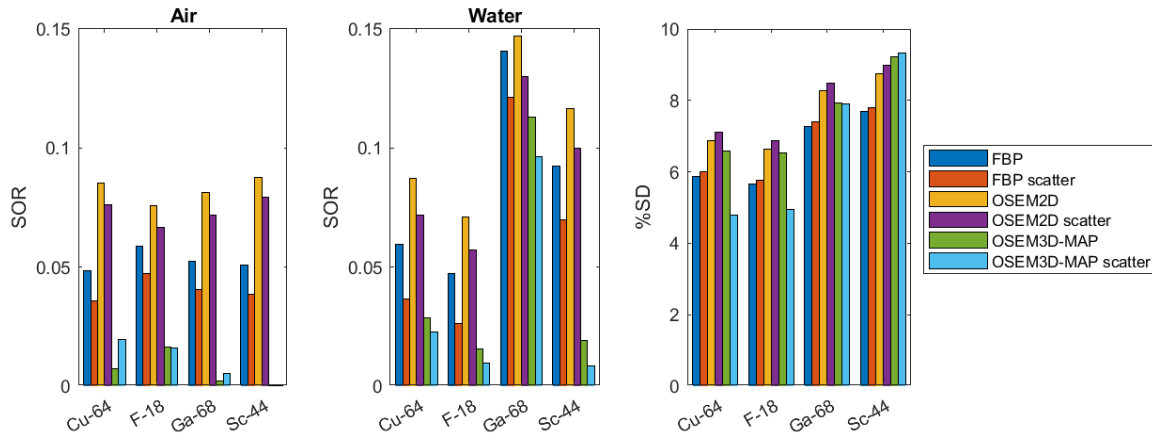


Figure 4.3 Impact of radionuclide and reconstruction algorithm on %SD and SOR in air and water. All data were acquired with the same number of counts. Both the uncorrected and scatter corrected values are presented for comparison.

The recovery coefficient (RC) is a measure of the fraction of activity reconstructed in a small region. RCs are plotted in Figure 4.4 as a function of rod size for the different radionuclides and reconstruction strategies. The same overall trend is observed in all graphs: the RC increases towards unity with increasing rod diameter. The RC for  $^{64}\text{Cu}$  remains almost constant down to rod sizes of 2 mm before sharply dropping for the 1 mm rod. Among all isotopes, the RC for  $^{68}\text{Ga}$  is smallest for all rod sizes, while the RC for  $^{44}\text{Sc}$  is only slightly below  $^{18}\text{F}$ , with a gradual decrease as a function of rod diameter.

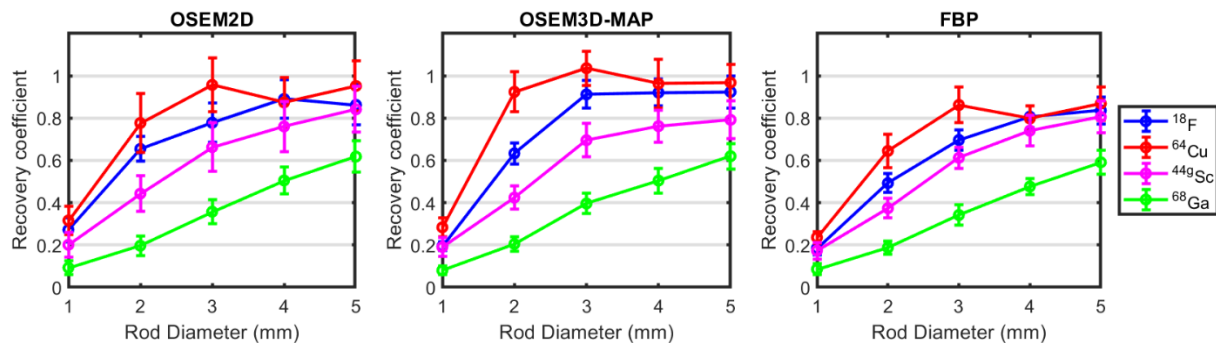


Figure 4.4 Impact of radionuclide and reconstruction strategy on measured recovery coefficients (RC)

### 4.3.2 Contrast and feature size

A comparison of the reconstructed images acquired in the Derenzo phantom is shown in Figure 4.5. The transverse cross-section of the hot rods demonstrates a clear difference in appearance between the short-range positron emitters  $^{18}\text{F}$  and  $^{64}\text{Cu}$  and the long-range positron emitters  $^{68}\text{Ga}$  and  $^{44}\text{Sc}$ . For the

latter two, the ability to distinguish smaller rods and separate them in the reconstructed images was impaired due to significant blurring.

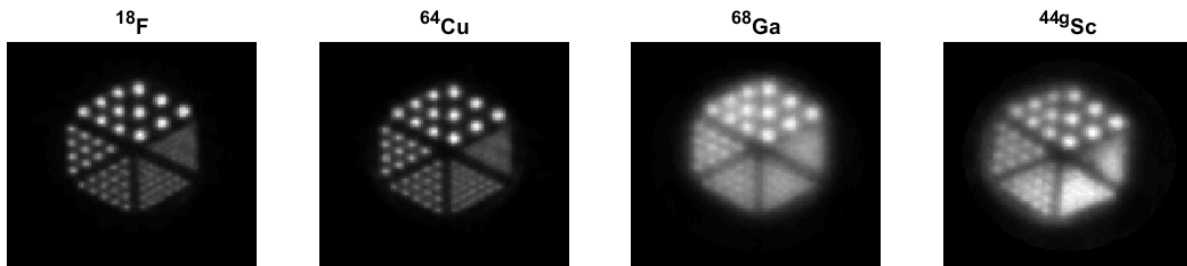


Figure 4.5 Derenzo phantom image reconstructed with OSEM2D for different radionuclides

The contrast between the rods and background in each of the six triangular segments was calculated (Equation 2) and is shown in Figure 4.6. There is clear separation between short-range positron emitters  $^{18}\text{F}$  and  $^{64}\text{Cu}$ , which demonstrate a contrast greater than 0.5 for feature sizes of 1.5 mm and above. While contrast of  $^{44}\text{gSc}$  is superior to  $^{68}\text{Ga}$  for the larger rod diameters, both radionuclides show the same contrast for rod diameters of 1.5 mm and below, leading to significant blurring of smaller features (Figure 4.5). The rods can no longer be distinguished when their diameters shrink below 1 mm for the long-range positron emitters and 0.8 mm for the short-range positron emitters. This blurring is due to the extrinsic scanner resolution, which is significantly impacted by positron range. While the contrast is expected to reach zero, measurements for the smallest rod diameters show non-zero values, owing to image noise. As there is a constant activity concentration, less counts are originating from the smaller rods, leading to increased noise; this increased noise can affect contrast measurements, as is apparent in OSEM3D measurements of contrast with respect to  $^{64}\text{Cu}$  and  $^{18}\text{F}$  in the 1.25 mm rod, in which  $^{64}\text{Cu}$  has a lower value. The 1.25 mm rod is in the regime in which the contrast is decreasing at the greatest rate for OSEM3D, and increased noise from the smaller diameter rod can affect measurements.

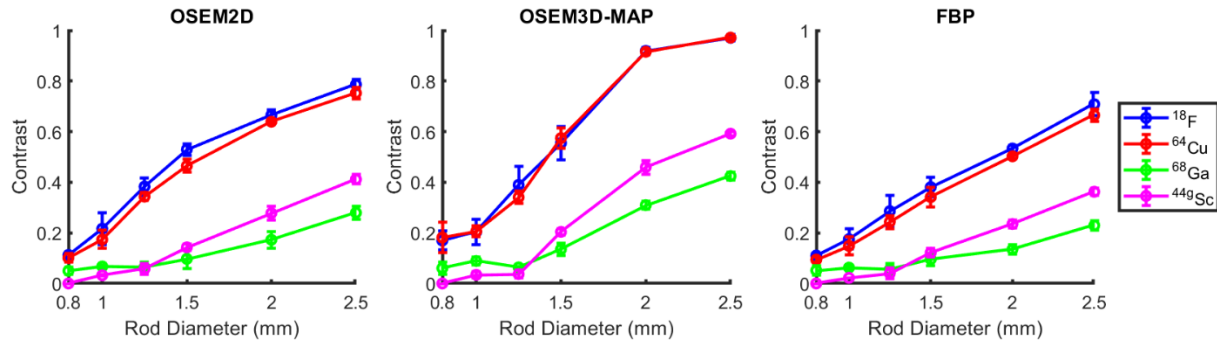


Figure 4.6 Normalized contrast as a function of rod size

### 4.3.3 Coincidence characteristics

The true, scatter and random event rates measured using the NEC phantom are plotted in Figure 4.7, along with the calculated NEC rate (equation 3). The random coincidence rate is expected to increase with the square of the single photon rate, represented by the x-axis (activity); it was found that a second order polynomial fits the random rate data for all isotopes in the range up to 100 MBq with an R-squared value of 0.999 as expected. The scatter contribution measured for  $^{44}\text{Sc}$  is increased relative to  $^{18}\text{F}$  and  $^{68}\text{Ga}$ , while the true event count rate is decreased.

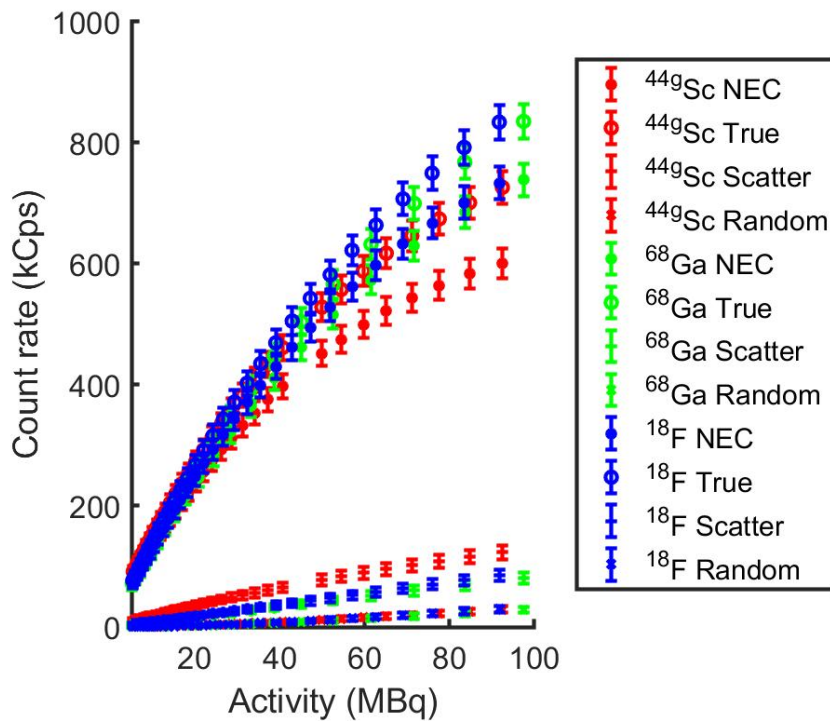


Figure 4.7 Results from phantom imaging studies. The values reflect the FBP reconstruction for the NEMA Image quality phantom and Derenzo phantom studies.

Table 4.3 Results from phantom imaging studies. The values reflect the FBP reconstruction for the NEMA Image quality phantom and Derenzo phantom studies.

Nuclide	Half-life	Mean (Max) positron emission energy (keV)	RC (5 mm)	% SD	SOR water	SOR air	Contrast	NECR at 10 MBq (kcps)
<sup>18</sup> F	109.8 m	249.8 (633.5)	0.849	5.65	0.0473	0.0589	0.674	132
<sup>64</sup> Cu	12.7 h	278.2 (654.0)	1.01	5.88	0.0595	0.0484	0.637	-
<sup>44</sup> Sc	3.97 h	632.0 (1474)	0.825	7.70	0.0923	0.0509	0.347	127
<sup>68</sup> Ga	67.7 m	836.0 (1890)	0.615	7.28	0.141	0.0525	0.196	131

#### 4.4 Discussion

Imaging of the four radionuclides in the NEMA image quality phantom allowed for a comparison of <sup>18</sup>F and the three radiometals <sup>64</sup>Cu, <sup>44</sup>Sc, and <sup>68</sup>Ga, in order of descending half-life and increasing positron range. The %SD measurements revealed a slight noise increase in images acquired with <sup>68</sup>Ga and <sup>44</sup>Sc, although still within 2-3% of the <sup>18</sup>F and <sup>64</sup>Cu measurements.

The SOR measurements in water were largely affected by positrons annihilating in the cold volume, as previously observed by Disselhorst et al. in their comparison of the short-range positron emitters <sup>18</sup>F and <sup>89</sup>Zr in contrast with the long-range positron emitters <sup>68</sup>Ga and <sup>124</sup>I (Disselhorst et al., 2010). <sup>44</sup>Sc showed intermediate behaviour as expected from a radionuclide with a mean positron emission energy of 632 keV, compared to <sup>18</sup>F (250 keV) and <sup>68</sup>Ga (836 keV). Overall, SOR in air is markedly decreased for the long-range positron emitters compared to water due to the greatly reduced electron density. However, the radius of the cold region would ideally exceed the maximum positron range of the radionuclide being investigated. Therefore, to obtain a true measure of the contribution of scatter and random coincidences to reconstructed activity of cold regions, a different phantom design with a larger cold volume would be required for accurate measurements with long-range positron emitters; such a phantom, however, is not currently part of the NEMA test protocol.

The RC measurements revealed that activity recovery in 1 mm diameter structures is at 25% or less for all radionuclides and reconstruction algorithms and increases for larger structures. Once again <sup>44</sup>Sc exhibits intermediate behaviour between <sup>18</sup>F (short-range) and <sup>68</sup>Ga (long-range). This indicates that a distinction beyond long-range and short-range positron emitters must be made when dealing with radionuclides with medium positron emission energies, and that general trends can be predicted using positron emission energies.

Generally, the RC measurements for  $^{18}\text{F}$  and  $^{64}\text{Cu}$  agreed within the bounds of uncertainty. However, certain measurements show deviations, which are due to distinct image artifacts in which the activity in the center of the hot rods were underestimated and the edges were overestimated; this artifact, known as the Gibbs phenomenon (Snyder et al., 1987), lead to noisier measurements of RC and caused values to exceeded the theoretical maximum of 1. The RC measurements are prone to large uncertainty as a single pixel per transverse cross-section is averaged over an axial profile, and the Gibb's phenomenon will affect the central rod pixel value for different rod sizes; another challenge affecting the measurements is the alignment of the rods with the reconstructed voxel positions. As seen in Figure 4.4, this phenomenon leads to noisier measurements for  $^{64}\text{Cu}$  and  $^{18}\text{F}$ ; the RC of the 4 mm rod with  $^{64}\text{Cu}$  is measured as decreased compared to 3 mm and 5 mm but remains within the bounds of uncertainty, while the same applies to the RC of the 5 mm rod with  $^{18}\text{F}$  reconstructed with OSEM2D demonstrates a decrease with respect to the 4 mm rod. The Gibbs effect should be carefully considered when considering quantification in images reconstructed from activity distributions with sharp transitions, as is the case with hot rods and the short-range positron emitters  $^{64}\text{Cu}$  and  $^{18}\text{F}$ .

The measurements in the Derenzo phantom allow us to rank the relative contrast in the reconstructed images with the four radionuclides. We find similar measurements for the short-range positron emitters  $^{18}\text{F}$  and  $^{64}\text{Cu}$ , while the contrast is degraded with  $^{44}\text{Sc}$  and to a greater extent with  $^{68}\text{Ga}$  for all reconstruction methods. The decreasing contrast can be predicted by the increasing positron energies as well as positron range, and follows the same trend as the relative resolution as determined Bunka et al. to be  $^{18}\text{F} > ^{64}\text{Cu} > ^{44}\text{Sc} > ^{68}\text{Ga}$  (Bunka et al., 2016).

The NEMA image quality study was conducted at activity levels commonly used for pre-clinical research; however, from the count rate curves acquired in the NEC phantom, the NECR curve for  $^{44}\text{Sc}$  increases at a lesser rate than that of  $^{18}\text{F}$ . This indicates that with increasing activity, the noise is expected to increase at a greater rate for  $^{44}\text{Sc}$  than  $^{18}\text{F}$ , which is likely due to spurious coincidences caused by the co-emitted 1.157 MeV gamma with 99% abundance. While this noise scaling is a not a practical concern for pre-clinical investigations, it suggests that radionuclide specific image quality assessments could be beneficial when larger activities are present in the PET field-of-view. The total activity used in our studies with the NEMA image quality phantom was 3.7 MBq, which is representative of typical activities used for mice imaging; the %SD is expected to decrease and the RC is expected to improve if the activity is increased because more counts are acquired with higher activities (assuming similar imaging times),

while the SOR should remain constant or decrease as the count rates are in the linear regime at least for activities less than 20 MBq.

The NEMA NU 4-2008 standard for calculating event count rates does not address the case of spurious coincidences caused by the co-emission of prompt gammas during the radionuclide decay. Scattered and random events, which result from two annihilation photons detected in the energy window around 511 keV, cannot be distinguished from spurious coincidences, which involve the detection of at least one prompt gamma. At the current time, the impact of the contribution of spurious coincidences to the event counts for a radionuclide emitting prompt gammas must be assumed via a comparison with a pure positron emitter such as  $^{18}\text{F}$ .

Various methods to produce  $^{44}\text{Sc}$  exist, each leading to a different radioisotopic composition of the scandium used for imaging. The radios scandium used in this study was produced from natural calcium targets with a radioisotopic purity of 95%  $^{44}\text{Sc}$  at end of beam and it remains at greater than 90% for 9.5 hours afterwards (Table 4.1). Our most abundant co-produced isotope is  $^{43}\text{Sc}$ , which is a positron emitter as well and has a 3.89 hour half-life. It is also considered a good candidate for PET imaging, and has the favourable property that the most energetic and abundant positron emission has a mean and maximum energy of 508 and 1199 keV respectively, which is lower than for  $^{44}\text{Sc}$ . Consequently, it's smaller positron range provides improved resolution compared to  $^{44}\text{Sc}$  and  $^{68}\text{Ga}$ , as demonstrated by Domnanich et al. (Domnanich et al., 2017a).  $^{43}\text{Sc}$  may also be a more favourable choice for clinical studies from a radiation safety perspective because high energy photon emissions, such as the 1157 keV prompt gamma (99.9% yield) emitted by  $^{44}\text{Sc}$ , do not occur. Shielding for the high energy photons emitted by  $^{44}\text{Sc}$  does not pose significant challenge in pre-clinical studies (such as this one) because of the relatively low amounts of activity handled and the spatially confined nature of the experiments. When transitioning to patients, however, radiation safety aspects need to be carefully considered in order to ensure adequate protection of personnel and the public.  $^{43}\text{Sc}$  might then be preferable despite the somewhat more costly production process which utilizes an enriched Calcium target. Initial *in vivo* human patient studies are underway to compare the dosimetric impact of  $^{44}\text{Sc}$  to the patient (Eppard et al., 2017). Other co-produced radioisotopes with a total abundance of less than 1%, are  $^{44\text{m}}\text{Sc}$  ( $t_{1/2}=58.61$  h) which decays to  $^{44}\text{Sc}$  and therefore also contributes to the total number of positrons available for imaging, as well as the two long-lived  $\beta^-$  contaminants  $^{47}\text{Sc}$  ( $t_{1/2}=3.35$  d) and  $^{48}\text{Sc}$  ( $t_{1/2}=43.67$  h). These isotopes are not expected to significantly impact the imaging performance but may contribute to a small error in the absolute measurements of source activity. However, as they make up less than 1% of the

total activity at end-of-beam (EOB), their impact is neither noticeable in images nor measurable within the uncertainties inherent in activity measurement with a radionuclide dose calibrator.

## 4.5 Conclusions

The performance of the Siemens Inveon PET scanner was evaluated for  $^{18}\text{F}$  and the radiometals  $^{44}\text{Sc}$ ,  $^{64}\text{Cu}$ , and  $^{68}\text{Ga}$ . The most significant differences observed in our measurements can be attributed to the radionuclides' positron emission energy: the short-range positron emitters  $^{18}\text{F}$  and  $^{64}\text{Cu}$  displayed greater recovery coefficients and contrast, as well as lower spill-over ratios than the long-range positron emitters  $^{68}\text{Ga}$  and  $^{44}\text{Sc}$ . For a given radionuclide, the OSEM3D-MAP reconstruction provided the best contrast in the reconstructed images.

In conclusion,  $^{44}\text{Sc}$  is a promising radionuclide for further study, as its intermediate positron emission energy provides increase contrast compared to  $^{68}\text{Ga}$ , another popular radiometal. The contribution of the high-energy gamma emission to image noise should be further studied because of its potential impact on image reconstruction when higher activity levels are present in the scanner's field-of-view.

## 4.6 References

- Alva-Sánchez, H., Quintana-Bautista, C., Martínez-Dávalos, A., Ávila-Rodríguez, M.A., Rodríguez-Villafuerte, M., 2016. Positron range in tissue-equivalent materials: experimental microPET studies. *Phys. Med. Biol.* 61, 6307. <https://doi.org/10.1088/0031-9155/61/17/6307>
- Anizan, N., Carlier, T., Hindorf, C., Barbet, J., Bardiès, M., 2012. dAcquisition setting optimization and quantitative imaging for  $^{124}\text{I}$  studies with the Inveon microPET-CT system. *EJNMMI Res.* 2, 7. <https://doi.org/10.1186/2191-219X-2-7>
- Braad, P.E.N., Hansen, S.B., Thisgaard, H., Høilund-Carlsen, P.F., 2015. PET imaging with the non-pure positron emitters:  $^{55}\text{Co}$ ,  $^{86}\text{Y}$  and  $^{124}\text{I}$ . *Phys. Med. Biol.* 60, 3479. <https://doi.org/10.1088/0031-9155/60/9/3479>
- Buchholz, H.G., Herzog, H., Förster, G.J., Reber, H., Nickel, O., Rösch, F., Bartenstein, P., 2003. PET imaging with yttrium-86: comparison of phantom measurements acquired with different PET scanners before and after applying background subtraction. *Eur. J. Nucl. Med. Mol. Imaging* 30, 716–720. <https://doi.org/10.1007/s00259-002-1112-y>
- Bunka, M., Müller, C., Vermeulen, C., Haller, S., Türlér, A., Schibli, R., van der Meulen, N.P., 2016. Imaging quality of  $^{44}\text{Sc}$  in comparison with five other PET radionuclides using Derenzo

- phantoms and preclinical PET. *Appl. Radiat. Isot.* 110, 129–133.  
<https://doi.org/10.1016/j.apradiso.2016.01.006>
- Cal-González, J., Herraiz, J.L., España, S., Corzo, P.M.G., Vaquero, J.J., Desco, M., Udias, J.M., 2013. Positron range estimations with PeneloPET. *Phys. Med. Biol.* 58, 5127.  
<https://doi.org/10.1088/0031-9155/58/15/5127>
- Champion, C., Loirec, C.L., 2007. Positron follow-up in liquid water: II. Spatial and energetic study for the most important radioisotopes used in PET. *Phys. Med. Biol.* 52, 6605.  
<https://doi.org/10.1088/0031-9155/52/22/004>
- Champion, C., Loirec, C.L., 2006. Positron follow-up in liquid water: I. A new Monte Carlo track-structure code. *Phys. Med. Biol.* 51, 1707. <https://doi.org/10.1088/0031-9155/51/7/005>
- Conti, M., Eriksson, L., 2016. Physics of pure and non-pure positron emitters for PET: a review and a discussion. *EJNMMI Phys.* 3, 8. <https://doi.org/10.1186/s40658-016-0144-5>
- Disselhorst, J.A., Brom, M., Laverman, P., Slump, C.H., Boerman, O.C., Oyen, W.J.G., Gotthardt, M., Visser, E.P., 2010. Image-Quality Assessment for Several Positron Emitters Using the NEMA NU 4-2008 Standards in the Siemens Inveon Small-Animal PET Scanner. *J. Nucl. Med.* 51, 610–617.  
<https://doi.org/10.2967/jnumed.109.068858>
- Domnanich, K.A., Eichler, R., Müller, C., Jordi, S., Yakusheva, V., Braccini, S., Behe, M., Schibli, R., Türler, A., van der Meulen, N.P., 2017. Production and separation of <sup>43</sup>Sc for radiopharmaceutical purposes. *EJNMMI Radiopharm. Chem.* 2, 14. <https://doi.org/10.1186/s41181-017-0033-9>
- Domnanich, K.A., Müller, C., Farkas, R., Schmid, R.M., Ponsard, B., Schibli, R., Türler, A., van der Meulen, N.P., 2016. <sup>44</sup>Sc for labeling of DOTA- and NODAGA-functionalized peptides: preclinical in vitro and in vivo investigations. *EJNMMI Radiopharm. Chem.* 1, 8. <https://doi.org/10.1186/s41181-016-0013-5>
- Eigner, S., Vera, D.R.B., Fellner, M., Loktionova, N.S., Piel, M., Lebeda, O., Rösch, F., Roß, T.L., Henke, K.E., 2013. Imaging of Protein Synthesis: In Vitro and In Vivo Evaluation of <sup>44</sup>Sc-DOTA-Puromycin. *Mol. Imaging Biol.* 15, 79–86. <https://doi.org/10.1007/s11307-012-0561-3>
- Eppard, E., de la Fuente, A., Benešová, M., Khawar, A., Bundschuh, R.A., Gärtner, F.C., Kreppel, B., Kopka, K., Essler, M., Rösch, F., 2017. Clinical Translation and First In-Human Use of [<sup>44</sup>Sc]Sc-PSMA-617 for PET Imaging of Metastasized Castrate-Resistant Prostate Cancer. *Theranostics* 7, 4359–4369. <https://doi.org/10.7150/thno.20586>

- Esteves, F.P., Nye, J.A., Khan, A., Folks, R.D., Halkar, R.K., Garcia, E.V., Schuster, D.M., Lerakis, S., Raggi, P., Votaw, J.R., 2010. Prompt-gamma compensation in Rb-82 myocardial perfusion 3D PET/CT. *J. Nucl. Cardiol.* 17, 247–253. <https://doi.org/10.1007/s12350-009-9170-1>
- Goertzen, A.L., Bao, Q., Bergeron, M., Blankemeyer, E., Blinder, S., Cañadas, M., Chatziioannou, A.F., Dinelle, K., Elhami, E., Jans, H.-S., Lage, E., Lecomte, R., Sossi, V., Surti, S., Tai, Y.-C., Vaquero, J.J., Vicente, E., Williams, D.A., Laforest, R., 2012. NEMA NU 4-2008 Comparison of Preclinical PET Imaging Systems. *J. Nucl. Med.* 53, 1300–1309. <https://doi.org/10.2967/jnumed.111.099382>
- Huclier-Markai, S., Alliot, C., Kerdjoudj, R., Mouglin-Degraef, M., Chouin, N., Haddad, F., 2018. Promising Scandium Radionuclides for Nuclear Medicine: A Review on the Production and Chemistry up to *In Vivo* Proofs of Concept. *Cancer Biother. Radiopharm.* 33, 316–329. <https://doi.org/10.1089/cbr.2018.2485>
- Jødal, L., Loirec, C.L., Champion, C., 2012. Positron range in PET imaging: an alternative approach for assessing and correcting the blurring. *Phys. Med. Biol.* 57, 3931. <https://doi.org/10.1088/0031-9155/57/12/3931>
- Koumarianou, E., Loktionova, N.S., Fellner, M., Roesch, F., Thews, O., Pawlak, D., Archimandritis, S.C., Mikolajczak, R., 2012. <sup>44</sup>Sc-DOTA-BN[2-14]NH<sub>2</sub> in comparison to <sup>68</sup>Ga-DOTA-BN[2-14]NH<sub>2</sub> in pre-clinical investigation. Is <sup>44</sup>Sc a potential radionuclide for PET? *Appl. Radiat. Isot.* 70, 2669–2676. <https://doi.org/10.1016/j.apradiso.2012.08.004>
- Laforest, R., Liu, X., 2009. Cascade removal and microPET imaging with <sup>76</sup>Br. *Phys. Med. Biol.* 54, 1503. <https://doi.org/10.1088/0031-9155/54/6/008>
- Laforest, R., Rowland, D.J., Welch, M.J., 2002. MicroPET imaging with nonconventional isotopes. *IEEE Trans. Nucl. Sci.* 49, 2119–2126. <https://doi.org/10.1109/TNS.2002.803685>
- Lehnert, W., Gregoire, M.-C., Reilhac, A., Meikle, S.R., 2011. Analytical positron range modelling in heterogeneous media for PET Monte Carlo simulation. *Phys. Med. Biol.* 56, 3313. <https://doi.org/10.1088/0031-9155/56/11/009>
- Levin, C.S., Hoffman, E.J., 1999. Calculation of positron range and its effect on the fundamental limit of positron emission tomography system spatial resolution. *Phys. Med. Biol.* 44, 781. <https://doi.org/10.1088/0031-9155/44/3/019>
- Loveless, C.S., Radford, L.L., Ferran, S.J., Queern, S.L., Shepherd, M.R., Lapi, S.E., 2019. Photonuclear production, chemistry, and in vitro evaluation of the theranostic radionuclide <sup>47</sup>Sc. *EJNMMI Res.* 9, 42. <https://doi.org/10.1186/s13550-019-0515-8>

- Martin, C.C., Christian, B.T., Satter, M.R., Nickerson, L.D.H., Nickles, R.J., 1995. Quantitative PET with positron emitters that emit prompt gamma rays. *IEEE Trans. Med. Imaging* 14, 681–687.  
<https://doi.org/10.1109/42.476109>
- Müller, C., Bunka, M., Haller, S., Köster, U., Groehn, V., Bernhardt, P., Meulen, N. van der, Türler, A., Schibli, R., 2014. Promising Prospects for 44Sc-/47Sc-Based Theragnostics: Application of 47Sc for Radionuclide Tumor Therapy in Mice. *J. Nucl. Med.* 55, 1658–1664.  
<https://doi.org/10.2967/jnumed.114.141614>
- Müller, C., Domnanich, K.A., Umbricht, C.A., van der Meulen, N.P., 2018. Scandium and terbium radionuclides for radiotheragnostics: current state of development towards clinical application. *Br. J. Radiol.* 20180074. <https://doi.org/10.1259/bjr.20180074>
- Pruszyński, M., Laktionova, N.S., Filosofov, D.V., Rösch, F., 2010. Post-elution processing of 44Ti/44Sc generator-derived 44Sc for clinical application. *Appl. Radiat. Isot.* 68, 1636–1641.  
<https://doi.org/10.1016/j.apradiso.2010.04.003>
- Pruszyński, M., Majkowska-Pilip, A., Laktionova, N.S., Eppard, E., Roesch, F., 2012. Radiolabeling of DOTATOC with the long-lived positron emitter 44Sc. *Appl. Radiat. Isot.* 70, 974–979.  
<https://doi.org/10.1016/j.apradiso.2012.03.005>
- Radchenko, V., Engle, J.W., Medvedev, D.G., Maassen, J.M., Naranjo, C.M., Unc, G.A., Meyer, C.A.L., Mastren, T., Brugh, M., Mausner, L., Cutler, C.S., Birnbaum, E.R., John, K.D., Nortier, F.M., Fassbender, M.E., 2017. Proton-induced production and radiochemical isolation of 44Ti from scandium metal targets for 44Ti/44Sc generator development. *Nucl. Med. Biol.* 50, 25–32.  
<https://doi.org/10.1016/j.nucmedbio.2017.03.006>
- Robinson, S., Julyan, P.J., Hastings, D.L., Zweit, J., 2004. Performance of a block detector PET scanner in imaging non-pure positron emitters—modelling and experimental validation with 124 I. *Phys. Med. Biol.* 49, 5505. <https://doi.org/10.1088/0031-9155/49/24/008>
- Roesch, F., 2012. Scandium-44: Benefits of a Long-Lived PET Radionuclide Available from the 44Ti/44Sc Generator System. *Curr. Radiopharm.* 5, 187–201.
- Schueller, M.J., Mulnix, T.L., Christian, B.T., Jensen, M., Holm, S., Oakes, T.R., Roberts, A.D., Dick, D.W., Martin, C.C., Nickles, R.J., 2003. Addressing the third gamma problem in PET. *IEEE Trans. Nucl. Sci.* 50, 50–52. <https://doi.org/10.1109/TNS.2002.807868>
- Severin, G.W., Engle, J.W., Valdovinos, H.F., Barnhart, T.E., Nickles, R.J., 2012. Cyclotron produced 44gSc from natural calcium. *Appl. Radiat. Isot.* 70, 1526–1530.  
<https://doi.org/10.1016/j.apradiso.2012.04.030>

- Snyder, D.L., Miller, M.I., Thomas, L.J., Politte, D.G., 1987. Noise and Edge Artifacts in Maximum-Likelihood Reconstructions for Emission Tomography. *IEEE Trans. Med. Imaging* 6, 228–238. <https://doi.org/10.1109/TMI.1987.4307831>
- Soderlund, A.T., Chaal, J., Tjio, G., Totman, J.J., Conti, M., Townsend, D.W., 2015. Beyond 18F-FDG: Characterization of PET/CT and PET/MR Scanners for a Comprehensive Set of Positron Emitters of Growing Application—18F, 11C, 89Zr, 124I, 68Ga, and 90Y. *J. Nucl. Med.* 56, 1285–1291. <https://doi.org/10.2967/jnumed.115.156711>
- Valdovinos, H.F., Hernandez, R., Barnhart, T.E., Graves, S., Cai, W., Nickles, R.J., 2015. Separation of cyclotron-produced 44Sc from a natural calcium target using a dipentyl pentylphosphonate functionalized extraction resin. *Appl. Radiat. Isot.* 95, 23–29. <https://doi.org/10.1016/j.apradiso.2014.09.020>
- van der Meulen, N.P., Bunka, M., Domnanich, K.A., Müller, C., Haller, S., Vermeulen, C., Türler, A., Schibli, R., 2015. Cyclotron production of 44Sc: From bench to bedside. *Nucl. Med. Biol.* 42, 745–751. <https://doi.org/10.1016/j.nucmedbio.2015.05.005>
- Walrand, S., Jamar, F., Mathieu, I., Camps, J.D., Lonneux, M., Sibomana, M., Labar, D., Michel, C., Pauwels, S., 2003. Quantitation in PET using isotopes emitting prompt single gammas: application to yttrium-86. *Eur. J. Nucl. Med. Mol. Imaging* 30, 354–361. <https://doi.org/10.1007/s00259-002-1068-y>
- Williams, H.A., Robinson, S., Julyan, P., Zweit, J., Hastings, D., 2005. A comparison of PET imaging characteristics of various copper radioisotopes. *Eur. J. Nucl. Med. Mol. Imaging* 32, 1473–1480. <https://doi.org/10.1007/s00259-005-1906-9>
- W. Price, T., Greenman, J., J. Stasiuk, G., 2016. Current advances in ligand design for inorganic positron emission tomography tracers 68 Ga, 64 Cu, 89 Zr and 44 Sc. *Dalton Trans.* 45, 15702–15724. <https://doi.org/10.1039/C5DT04706D>

## Chapter 5

# A comparative PET imaging study of $^{44}\text{Sc}$ - and $^{68}\text{Ga}$ -labeled bombesin antagonist derivatives in breast and prostate cancer models

---

---

### 5.1 Introduction

Radiolabeled peptides play a central role in nuclear medicine as radiotheranostics for targeted imaging and therapy of cancer (Chatalic et al., 2015; Fani et al., 2012; Opalinska et al., 2017; Tornesello et al., 2017). The success of using radiolabeled peptides for the accurate detection and effective treatment of cancer stems particularly from the well-documented overexpression of various regulatory peptide receptors on the surface of certain cancer cells. The majority of these peptide receptors belong to the large family of G protein-coupled receptors, which bind with high affinity and specificity small regulatory peptides such as somatostatin, bombesin, neurotensin, VIP, gastrin, and GLP-1. Many radiopeptides originate from natural regulatory peptides, which have been optimized to improve metabolic stability and pharmaco-kinetics to close the gap between their promise for targeted imaging and therapy of diseases and their clinical implementation. Prominent clinical examples of using small regulatory peptides as radiotheranostics comprise various radiolabeled somatostatin analogs for targeted visualization (i.e. [ $^{68}\text{Ga}$ ]Ga-DOTATATE ) and treatment (i.e. [ $^{177}\text{Lu}$ ]Lu-DOTATATE ) of differentiated neuroendocrine tumors (Baum et al., 2012; Baum and Kulkarni, 2012; Kelkar and Reineke, 2011). Radiolabeled somatostatin analogs exert their diagnostic and therapeutic potential upon specific binding to somatostatin receptors (SSTRs), which are notably overexpressed in neuroendocrine tumors. SSTR-targeted peptide receptor radionuclide therapy (PRRT) with [ $^{177}\text{Lu}$ ]Lu-DOTATATE resulted in impressive clinical results in patients with neuroendocrine tumors by optimizing medical care for individual patients and their disease characteristics (Baum and Kulkarni, 2012; Cives and Strosberg, 2017).

Gastrin-releasing peptide receptors (GRPRs) bind with high-affinity amphibian tetradecapeptide bombesin (BBN). The mammalian counterpart to the amphibian BBN is called gastrin-releasing

polypeptide (GRP). The expression and mechanism of action of GRP and GRPRs have extensively been studied in many tumor types pointing to GRPR as an autocrine growth factor receptor for tumor cell proliferation and/or morphogen factor for tumor cell differentiation (Baratto et al., 2020; Gugger and Reubi, 1999; Hohla and Schally, 2010; Patel et al., 2006). Thus, GRPRs represent promising molecular targets for targeted radiopeptide-based imaging and therapy of cancer with particular emphasis on prostate and breast cancer. Various BBN derivatives with high GRPR affinity have been synthesized and labeled with multiple radionuclides, including  $^{18}\text{F}$ ,  $^{64}\text{Cu}$ , and  $^{68}\text{Ga}$  for PET imaging (Rogers et al., 2003; Schroeder et al., 2011; Yang et al., 2006),  $^{99\text{m}}\text{Tc}$ , and  $^{111}\text{In}$  for SPECT imaging (Abiraj et al., 2010; García Garayoa et al., 2007; Pujatti et al., 2012), and  $^{90}\text{Y}$  and  $^{177}\text{Lu}$  for radiotherapy (Koumarianou et al., 2009; Thomas et al., 2008). The impact of the radionuclide on the biodistribution and tumor uptake profile of BBN radiopeptides was the subject of several studies.

Koumarianou *et al.* found small but noticeable differences in the *in vitro* receptor affinity for BBN agonist DOTA-BN[2-14] $\text{NH}_2$  labeled with chemically alike radiolanthanides  $^{177}\text{Lu}$  ( $\text{IC}_{50} = 1.34 \text{ nM}$ ) and  $^{90}\text{Y}$  ( $\text{IC}_{50} = 1.99 \text{ nM}$ ) (Koumarianou et al., 2009). Despite the only minor differences in their *in vitro* receptor affinity, the authors observed significant differences in the biodistribution experiments with both radiopeptides. This led to the conclusion that the choice of the radionuclide also influences the *in vivo* GRPR binding of the radiopeptide and, therefore, their biodistribution profile. In contrast to the study by Koumarianou *et al.*, comparable biodistribution and tumor uptake profiles were recently observed with  $^{68}\text{Ga}$ - and  $^{44}\text{Sc}$ -labeled BBN agonist DOTA-BN[2-14] $\text{NH}_2$  in rats bearing Dunning prostate R3327-AT1 tumors despite their more drastic *in vitro* binding affinity differences ( $\text{IC}_{50} = 0.85 \text{ nM}$  versus  $6.49 \text{ nM}$ , respectively) (Koumarianou et al., 2012).

Current clinical PET imaging of GRPRs is dominated by  $^{68}\text{Ga}$ -labeled BBN analogs (Gnesin et al., 2017; Gruber et al., 2020; Maina et al., 2016; Zhang et al., 2018). Several studies confirmed the trend and preference of using GRPR antagonists over GRPR agonists. Antagonists often show higher binding and more favorable pharmacokinetics when compared with GRPR agonists. Moreover, clinical studies with GRPR agonists resulted in unwanted side effects caused by the activation of the GRPR upon binding of the agonist ligand (Bodei et al., 2007). Thus, the majority of clinical GRPR PET imaging studies use  $^{68}\text{Ga}$ -labeled GRPR antagonist such as [ $^{68}\text{Ga}$ ]Ga-NODAGA-MJ9, [ $^{68}\text{Ga}$ ]Ga-RM26, [ $^{68}\text{Ga}$ ]Ga-SB3, [ $^{68}\text{Ga}$ ]Ga-NeoBOMB1, and more recently, [ $^{68}\text{Ga}$ ]Ga-RM2 (Bodei et al., 2007; Gnesin et al., 2017; Gruber et al., 2020; Maina et al., 2016; Zhang et al., 2018).

PET imaging with generator-produced  $^{68}\text{Ga}$  ( $t_{1/2} = 67.71$  min) was recently challenged with cyclotron-produced scandium radioisotopes  $^{44}\text{Sc}$  ( $t_{1/2} = 3.97$  h) and  $^{43}\text{Sc}$  ( $t_{1/2} = 3.89$  h). As  $^{44}\text{Sc}$  has become more readily available, several studies described radiolabeling experiments with DOTA and DTPA chelators (Alliot et al., 2015; Müller et al., 2014a; Severin et al., 2012; Valdovinos et al., 2015) as well as with DOTA-decorated peptides and other biomolecules, including [ $^{44}\text{Sc}$ ]Sc-DOTA-(cRGD) $_2$  (Hernandez et al., 2014), [ $^{44}\text{Sc}$ ]Sc-DOTA-TATE (Huclier-Markai et al., 2014), [ $^{44}\text{Sc}$ ]Sc-DOTA-TOC (Pruszyński et al., 2012), [ $^{44}\text{Sc}$ ]Sc-DOTA-NOC (van der Meulen et al., 2015), [ $^{44}\text{Sc}$ ]Sc-DOTA-folate (Müller et al., 2013), and [ $^{44}\text{Sc}$ ]Sc-PSMA-617 (Eppard et al., 2017; Umbricht et al., 2017). First-in-human studies with [ $^{44}\text{Sc}$ ]Sc-PSMA-617 demonstrated an improved pre-therapeutic dosimetry for radiotherapy with [ $^{177}\text{Lu}$ ]Lu-PSMA-617 when compared with the corresponding [ $^{68}\text{Ga}$ ]Ga-PSMA-617 (Eppard et al., 2017).

Our research group has recently proposed the use of metabolically stabilized GRPR antagonist BBN2 for radiolabeling with  $^{18}\text{F}$  and  $^{68}\text{Ga}$  and subsequent PET imaging of GRPRs in prostate cancer resulting in favorable tumor uptake and biodistribution profiles (Richter et al., 2016, 2013).

In addition to recent studies describing the impact of radiometals on the biodistribution and tumor uptake profile of BBN agonist DOTA-BN[2-14]NH $_2$ , our work was aimed at a comparative study on the impact of  $^{44}\text{Sc}$ - and  $^{68}\text{Ga}$ -labeled DOTA complexes attached to GRPR antagonist BBN2 on the *in vitro* GRPR binding affinity, and their biodistribution and tumor uptake profiles in MCF7 breast and PC3 prostate cancer models.

## 5.2 Materials and methods

### 5.2.1 Reagents and Radionuclides

All chemicals were obtained from Sigma-Aldrich (St. Louis, MO, USA). Reagents for peptide synthesis were purchased from NovaBioChem (Millipore Ltd., ON, Canada). Peptides were synthesized using a combination of manual coupling procedures and automated solid-phase peptide synthesis (SPPS) with a Syro I peptide synthesizer (MultiSynTech/Biotage, Charlotte, NC, USA).  $^{68}\text{Ga}$  was eluted from an iThemba LABS 50 mCi  $^{68}\text{Ge}/^{68}\text{Ga}$  generator (isoSolutions Inc., BC, Canada). Mass spectra were recorded on a AB Sciex Voyager Elite matrix-assisted laser desorption ionization mass spectrometer time-of-flight (MALDI-MA TOF, AB Sciex, Forster City, CA, USA).  $^{44}\text{Sc}$  was produced on the ACSI TR19/9 variable energy cyclotron at the Cross Cancer Institute (Edmonton, AB, Canada) via the  $^{44}\text{Ca}(p,n)^{44}\text{Sc}$  nuclear reaction. The irradiations were conducted with natural Ca metal at a proton energy of 16 MeV, with beam currents up to 4  $\mu\text{A}$ . The radiochemical separation proceeded using a modified version of the procedure

developed by Valdovinos et al., and the activity was eluted in several 100  $\mu$ L fractions of water (Valdovinos et al., 2015). The fraction with the largest activity was used to perform radiolabelling. The Atomlab 400 dose calibrator (Biodex Medical Systems, NY, USA) was used for determining the activity during the radiochemical separation, during labelling experiments and prior to imaging.

### 5.2.2 Peptide syntheses

The metabolically stabilized bombesin peptide Ava-Gln<sup>7</sup>-Trp<sup>8</sup>-Ala<sup>9</sup>-Val<sup>10</sup>-Sar<sup>11</sup>-His<sup>12</sup>-FA01010<sup>13</sup>-Tle<sup>14</sup>-NH<sub>2</sub> (Ava-BBN2) was synthesized as previously described [39,40]. The peptide synthesis was performed using the Fmoc-orthogonal solid-phase peptide synthesis on an automated Syro I peptide synthesizer. HPLC purification of peptides were performed using a Phenomenex Jupiter 4u Proteo 90A, 250x10mm, 4  $\mu$ m C12 column at a flow rate of 2 mL/min using gradient elution. Solvent A: water/0.2% TFA. Solvent B: acetonitrile.

DOTA-Ava-Gln<sup>7</sup>-Trp<sup>8</sup>-Ala<sup>9</sup>-Val<sup>10</sup>-Sar<sup>11</sup>-His<sup>12</sup>-FA01010<sup>13</sup>-Tle<sup>14</sup>-NH<sub>2</sub> (DOTA-Ava-BBN2). 5.0 mg (4.7  $\mu$ mol) of Ava-BBN2 was dissolved in 100  $\mu$ L of DMF in a 1.5 mL LoBind Eppendorf, and 3.3 mg (6  $\mu$ mol) of pSCN-Bn-DOTA (1.3 equiv.) was added, as well as 10  $\mu$ L of triethylamine (TEA). The reaction mixture was incubated at 37 °C for 16 h prior to HPLC purification (2 mL/min, 0-10 min 10% B, 25 min 50%B, 30-40 min 80%B, 40-45 min 90% B ( $t_R$  = 29.9 min)).

The HPLC solvent was reduced under vacuum using a rotary evaporator, and lyophilisation afforded DOTA-Ava-BBN2 as a white powder (6.5 mg, 4.0  $\mu$ mol, 85% isolated yield). MW C<sub>76</sub>H<sub>115</sub>N<sub>19</sub>O<sub>18</sub>S 1613.8, measured MALDI-MS (positive) m/z 1614.8 [M+H]<sup>+</sup>.

<sup>nat</sup>Ga-DOTA-Ava-BBN2. 2.0 mg (1.24  $\mu$ mol) of DOTA-Ava-BBN2 and 3.5 mg Ga(NO<sub>3</sub>)<sub>3</sub> dissolved in 200  $\mu$ L of 10% CH<sub>3</sub>CN in 1 M NaOAc buffer (pH = 4.5) were reacted at 90 °C overnight in a 1.5 mL LoBind Eppendorf vial. The reaction mixture was purified with HPLC (0-10 min 20% B, 25 min 50%B, 30-40 min 80%B;  $t_R$  = 17.6 min) at a flow rate of 2 mL/min. The HPLC solvent was reduced under vacuum using a rotary evaporator, and lyophilization afforded <sup>nat</sup>Ga-DOTA-Ava-BBN2 as a powder (1.6 mg, 4.0  $\mu$ mol, 85% isolated yield). MW C<sub>76</sub>H<sub>112</sub>GaN<sub>19</sub>O<sub>18</sub>S 1679.8, measured MALDI-MS (positive) m/z 1680.7 [M+H]<sup>+</sup>.

<sup>nat</sup>Sc-DOTA-Ava-BBN2. 2.0 mg (1.24  $\mu$ mol) of DOTA-Ava-BBN2 and 3.0 mg Sc(OTf)<sub>3</sub> dissolved in 200  $\mu$ L of 10% CH<sub>3</sub>CN in 1 M NaOAc buffer (pH = 4.5) were reacted at 90 °C overnight in a 1.5 mL LoBind Eppendorf vial. The reaction mixture was purified with HPLC (0-10 min 20% B, 25 min 50%B, 30-40 min 80%B;  $t_R$  = 17.4 min) at a flow rate of 2 mL/min. The HPLC solvent was reduced under vacuum using a

rotary evaporator, and lyophilisation afforded <sup>nat</sup>Sc-DOTA-Ava-BBN2 as a powder (1.5 mg, 0.9 μmol, 89% isolated yield). MW C<sub>76</sub>H<sub>112</sub>N<sub>19</sub>O<sub>18</sub>SSc 1655.8, measured MALDI-MS (positive) m/z 1679.4 [M+Na]<sup>+</sup>.

### 5.2.3 Radiolabelling of DOTA-Ava-BBN2 with <sup>44</sup>Sc and <sup>68</sup>Ga

For the radiolabelling of the DOTA-Ava-BBN2 with <sup>44</sup>Sc, 90 μL of the third eluted fraction was buffered to a pH of 4.5 using 140 μL of 4 M NaOAc (pH 9.3) and was reacted with 50 μg of DOTA-BBN2 in 30 μL deionized water in a 1.5 mL LoBind Eppendorf tube at 99 °C for 20 min at 750 rpm. The <sup>68</sup>Ga was eluted from the <sup>68</sup>Ge/<sup>68</sup>Ga generator with an average activity of 577 MBq in 2.3 mL 0.6 M HCl. A 1 mL fraction of the eluate was diluted with 250 μL of 4 M NaOAc (pH 9.3) to adjust the pH to 4.5 and reacted with 50 μg of the DOTA-Ava-BBN2 in 30 μL deionized water at 99 °C for 20 min at 750 rpm.

The reaction mixtures were collected and diluted with 9 mL of deionized water before purification via solid-phase extraction (SPE) using a Sep-Pak tC18 Plus cartridge (Waters Corporation, Milford, MA, USA). The cartridge was preconditioned with 5 mL of acetonitrile and 10 mL of deionized water. The cartridge trapped the radiolabeled peptide, which was eluted using 1.1 mL of EtOH.

The EtOH was reduced under vacuum using a rotary evaporator and subsequently re-dissolved in 200 μL of 8% ethanol in saline (0.9 % w/v of NaCl). Isolated radiochemical yields were in the range of 70-80 % (decay-corrected). The radiochemical purity exceeded 97% as assessed by radio-TLC on RP18 plates using 0.1 M citric acid as eluent (R<sub>f</sub> = 0.0). The identity of radiopeptides was confirmed by their retention times on radio-HPLC when compared to the respective reference compounds.

### 5.2.4 Lipophilicity

The shake-flask method was used to determine the partition coefficients of the <sup>68</sup>Ga- and <sup>44</sup>Sc-radiolabelled peptides in n-octanol as the organic solvent and PBS buffer (pH 7.4) as the aqueous phase (Wilson et al., 2001). 250 μL of each layer was added to approximately 150 kBq of the radiopeptide (<sup>68</sup>Ga/<sup>44</sup>Sc-DOTA-Ava-BBN2) in a LoBind Eppendorf tube, which was vigorously mixed for 3 min. The layers were allowed to separate by centrifugation at 2000 rpm for 5 min. Aliquots of 50 μL were taken from each layer and measured in a Wizard gamma counter (Wallac 1480 Wizard-3, PerkinElmer, Woodbridge, ON, Canada). The logD<sub>7.4</sub> values were calculated as the logarithm of the activity in each phase and expressed as mean ± SD from three experiments each performed in triplicate.

### 5.2.5 Competitive binding assay

A competitive displacement cell-binding assay was performed to assess the in vitro gastrin-releasing peptide receptor binding affinity and specificity of the <sup>nat</sup>Ga-DOTA-BBN2 and <sup>nat</sup>Sc-DOTA-BBN2

compounds. The assay was performed using PC-3 cells and concentrations for the half-maximum inhibition ( $IC_{50}$  values) were determined using  $^{125}I$ -Tyr<sup>4</sup>-bombesin (Perkin Elmer; Waltham, MA, USA) with increasing concentrations of nonradioactive reference peptide structures DOTA-BBN2,  $^{nat}Ga$ -DOTA-BBN2 and  $^{nat}Sc$ -DOTA-BBN2 from  $10^{-12}$  M to  $10^{-6}$  M. After incubation for 1 h at 37 °C and two consecutive washing steps, cells were harvested and counted in a Wizard gamma counter (Perkin Elmer; Waltham, MA, USA). Data were analyzed as % control uptake of  $^{125}I$ -Tyr<sup>4</sup>-bombesin and plotted versus the log of peptide concentration to generate sigmoidal dose-response curves using GraphPad Prism 5.04 (GraphPad Software, La Jolla, CA, USA).

### 5.2.6 Gene expression microarray analysis

Gene-expression microarray analysis was performed as described previously using primary samples from 176 treatment-naive patients with BC and 10 healthy breast-tissue samples collected from reduction mammoplasties through the Canadian Breast Cancer Foundation Tumor Bank (Northern Alberta Study Center, Cross Cancer Institute, Edmonton, AB, Canada). Patient information was collected under Research Ethics Board Protocol ETH-02-86-17.

### 5.2.7 Protein expression

For analysis of GRPR and  $\beta$ -actin, MCF10A, MCF7, and MDA-MB231 cells were seeded in 60 mm dishes (Nunc™ Cell Culture/Petri Dishes, ThermoFisher Scientific) and had their media changed 24 h prior to collection. Cells in the dishes were washed with PBS, then suspended in lysis buffer (50mM Tris, 150 mM NaCl, 0.1% SDS, 0.5% sodium deoxycholate, 0.5% Triton X) containing protease inhibitor cocktail (ab65621, abcam, 1:500). The extracts were sonicated (10% amplitude, 10 s) on ice and centrifuged at 14,500 g for 10 min at 4°C to remove debris. Protein determination in supernatants was conducted, using a BCA based protein assay (Pierce/Thermo Scientific, Rockford, IL, USA). Aliquots of supernatants were mixed with 1/2 volume of 2x Laemmli buffer (2x Laemmli Sample Buffer #1610737, Bio-Rad) and heated for 5 min at 95°C. Protein extracts were loaded onto SDS-polyacrylamide gels and separated by electrophoresis. Proteins were transferred to nitrocellulose membranes by electroblotting and blocked for 1 h at room temperature in 5% (w/v) non-fat dry milk in Tris-buffered saline containing 0.05% (v/v) of Tween-20 (TBST). Membranes were incubated overnight at 4°C with the mouse monoclonal anti-GRPR IgG<sub>2 $\alpha$</sub>  (sc-377316, F-6, Santa Cruz Biotechnology, 1:100), and rabbit polyclonal anti- $\beta$ -actin (A5060, Sigma-Aldrich, 1:5000) followed by incubation for 1 h at 21°C with a peroxidase-conjugated goat anti-mouse IgG<sub>2 $\alpha$</sub>  secondary antibody (sc-2061, Santa Cruz Biotechnology) in 1:5000 dilution or peroxidase-conjugated goat anti-rabbit IgG secondary antibody 1:5000 dilution ( $\beta$ -actin). Housekeeping protein was

chosen based on its utility and minimal interference it had with the proteins of interest. Prior to the addition of anti- $\beta$ -actin for blot already stained with anti-GRPR a stripping procedure was performed due to the close proximity of the staining between both of the antibodies. Stripping buffer (1 L: 15 g glycine, 1 g SDS, 1% Tween20, pH 2.2) was used to wash the membranes twice for 5-10 minutes each, followed by two washes with PBS each for 10 minutes and two washes with TBST for 5 minutes each.

After incubation with secondary antibodies, membranes were washed in TBST and incubated with Clarity ECL Western blotting substrate (Bio-Rad Laboratories, Hercules, CA, USA). Luminescence signals were captured using Fuji Medical X-ray Films (Fujifilm Canada, Mississauga, ON, Canada). Films were scanned, and analysis was done using the ImageJ program (National Institutes of Health, Bethesda, MD, USA). Density of each band was determined, and individual lane backgrounds were subtracted. Values for GRPR were divided by values for the housekeeping protein  $\beta$ -actin. Received values were compared to each other, with the individual values of the cell lines being calculated as such:  $((\text{GRPR band density} - \text{lane background density}) / (\beta\text{-actin band density} - \text{lane background density}))$ .

### 5.2.8 Immunohistochemistry

For immunohistochemistry staining on tissue microarrays, 4-mm-thick paraffin-embedded tissue sections were mounted on slides. The staining procedure was conducted using the Ventana Benchmark-ultra automated staining system with primary anti-GRPR antibody (Acris Antibody GmbH, SP4337P) at a 1:1400 dilution following a recently published procedure [42]. The staining was generally cytoplasmic with no evidence of nuclear presentation. GRPR expressions were assessed under light microscope and expressed as an immunoreactive score [43].

### 5.2.9 Dynamic PET Imaging Studies

The INVEON<sup>®</sup> PET/CT scanner (Siemens Preclinical Solutions, Knoxville TN, U.S.A) was used for the in vivo PET imaging of the radiolabelled peptides. The guidelines outlined by the Canadian Council on Animal Care (CCAC) were used to carry out the animal studies, along with the approval of the local Cross Cancer Institute Animal-Care Committee.

The prostate cancer studies were conducted using NU/NU nude male mice and PC3 cells, while the breast cancer studies were done using NIH-III female mice with MCF7 cell. About  $3\text{-}5 \times 10^6$  PC3 or MCF7 cells in 200  $\mu\text{L}$  of PBS or PBS/matrigel (50/50) were injected subcutaneously into the upper left flank of the mice to generate tumour xenografts. In case of mammary MCF7 cells a 0.72 mg/pellet containing estrogen in a 60-day release preparation (Innovative Research of America, Sarasota, FL, USA) was

implanted subcutaneously into the upper right flank of the NIH-III mice to allow for a constant estrogen level needed for the estrogen-dependent MCF7 cells.

After 3-5 weeks, the tumours reached sizes of ~300-500 mm<sup>3</sup> and were used for the in vivo imaging studies. Prior to the injection of the radiopeptides, the mice were anesthetized through inhalation of isoflurane in 40% O<sub>2</sub> 60% N<sub>2</sub>.

Mice were injected with 3- 5 MBq of <sup>68</sup>Ga-DOTA-Ava-BBN2 or <sup>44</sup>Sc-DOTA-Ava-BBN2 in 100 to 150 µL of saline through a tail vein catheter. The dynamic PET acquisition was performed over 60 min, and 3D list mode data were recorded. The data were sorted into sinograms with 54 time frames (10 × 2, 8 × 5, 6 × 10, 6 × 20, 8 × 60, 10 × 120, 6 × 300 s), and each frame was reconstructed using maximum a priori (MAP) reconstruction. For blocking studies, 300 µg of BBN2 [38,39] in 50 µL of saline was injected ~5 min prior to radiotracer injection.

Tracer uptake in the tumour was analyzed using the ROVER v2.0.51 software (ABX GmbH, Radeberg, Germany). Regions of interest (ROI) covered the entire visible tumour mass, and thresholds of 50 % of the maximum radioactivity uptake level were defined. A mean standardized uptake value [SUV<sub>mean</sub> = (activity/mL tissue)/(injected activity/body weight), mL/g] was calculated and time-activity curves (TACs) were generated using GraphPad Prism 5.04 (GraphPad Software, La Jolla, CA, USA). The plotted TACs are presented as mean ± SEM from n experiments.

## 5.3 Results

### 5.3.1 Radiosynthesis of <sup>68</sup>Ga- and <sup>44</sup>Sc-DOTA-Ava-BBN2 and lipophilicity determination

Metabolically stabilized bombesin derivative Ava-BBN2 (Gln-Trp-Ala-Val-Sar-His-FA01010-Tle-CONH<sub>2</sub>) [38,39] was decorated with bifunctional chelator p-NCS-Bn-DOTA using thiourea conjugation chemistry in solution. Peptide DOTA-Ava-BBN2 was obtained in isolated chemical yield of 85% and high chemical purity (>99%) after HPLC purification and lyophilization suitable for radiolabeling with <sup>68</sup>Ga and <sup>44</sup>Sc. <sup>68</sup>Ga was obtained from a 50 mCi <sup>68</sup>Ge/<sup>68</sup>Ga generator connected to a Scintomics GRP automated synthesis module for remotely controlled elution of radioactivity. <sup>44</sup>Sc was obtained via the <sup>44</sup>Ca(p,n)<sup>44</sup>Sc nuclear reaction using natural Ca metal as the target material on a ACSI TR19/9 cyclotron. Target processing and purification of <sup>44</sup>Sc was performed using a modified version of the original procedure reported by Valdovinos *et al.*, outlined in Figure 5.1 (Valdovinos *et al.*, 2015).

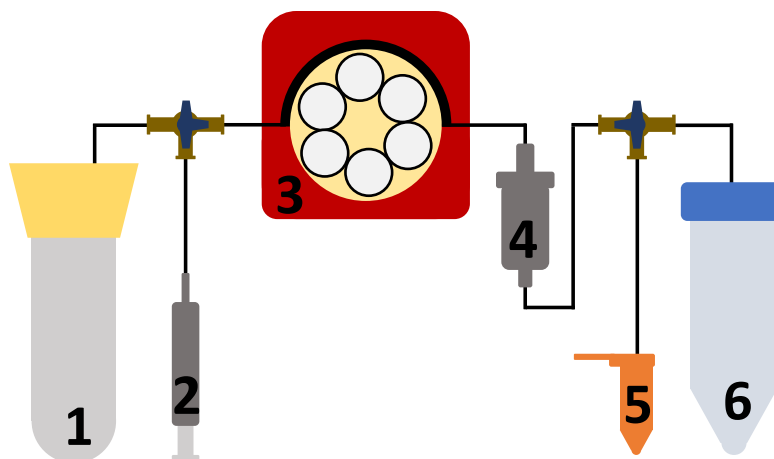
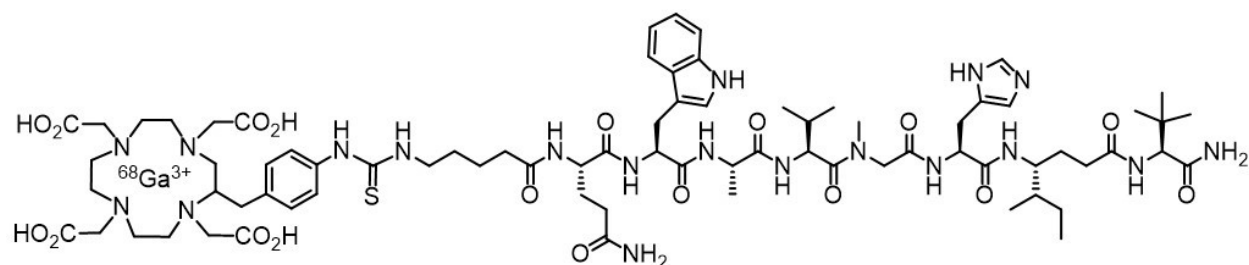


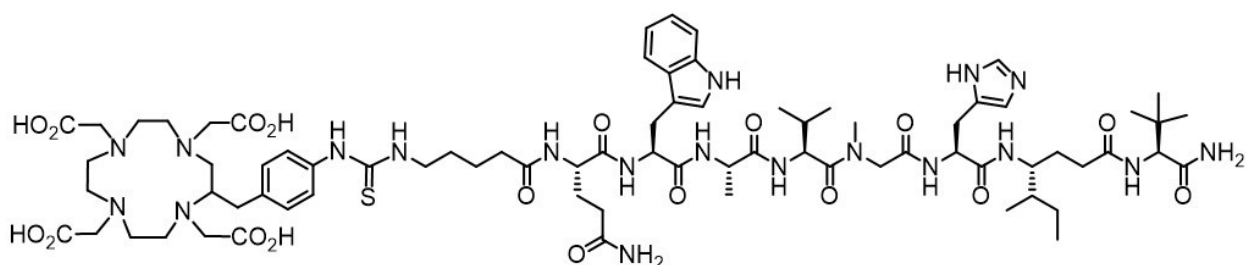
Figure 5.1 Outline of the scandium extraction system. The irradiated calcium is dissolved in 10 mL of 10 M HCl in reaction vessel (1) and a peristaltic pump (3) is used to trap the scandium onto a UTEVA resin column (4). The column is washed with 3 mL of 10 M HCl prior to the elution of the scandium using DI water in 100  $\mu$ L fractions (2), which are collected separately (5) from the waste (6). The eluted fractions can then be used for radiolabelling.

Radiolabelling of DOTA-Ava-BBN2 with  $^{68}\text{Ga}$  and  $^{44}\text{Sc}$  was conducted manually, and the radiolabelling process is given in Figure 5.2.



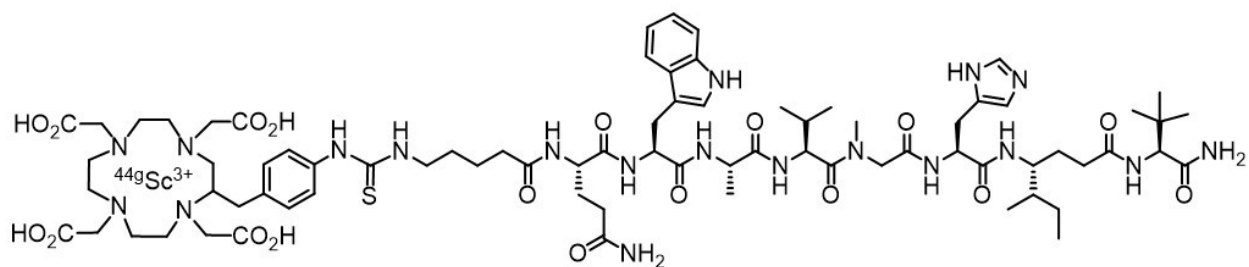
**[<sup>68</sup>Ga]Ga-DOTA-Ava-BBN2**

- 1.) [<sup>68</sup>Ga]GaCl<sub>3</sub>
- 2.) NaOAc buffer (pH 9.3), 20 min, 95 °C
- 3.) SPE purification



DOTA-Ava-Gln-Trp-Ala-Val-Sar-His-FA01010-Tle-CONH<sub>2</sub> (DOTA-Ava-BBN2 (50 µg))

- 1.) [<sup>44</sup>Sc]ScCl<sub>3</sub>
- 2.) NaOAc buffer (pH 9.3), 20 min, 95 °C
- 3.) SPE purification



**[<sup>44</sup>Sc]Sc-DOTA-Ava-BBN2**

Figure 5.2 Structure of DOTA-Ava-BBN2 and radiolabeling with <sup>68</sup>Ga and <sup>44</sup>Sc.

Peptide DOTA-Ava-BBN2 (50 µg) was labeled with <sup>68</sup>Ga and <sup>44</sup>Sc at pH 4.5 using 4 M NaOAc buffer (pH 9.3) at 95 °C for 20 min. Radiolabeling was quantitative, and the radiolabeled peptides were purified via solid-phase extraction (SPE) using a tC18 Plus cartridge. Radiolabeled peptides were eluted from the cartridge with EtOH and isolated by evaporation of EtOH under reduced pressure. The residue was re-dissolved in saline for subsequent radiopharmacological studies. <sup>68</sup>Ga- and <sup>44</sup>Sc-DOTA-Ava-BBN2 were

obtained in 70-80% decay-corrected radiochemical yields at high radiochemical purity greater than 97%. Effective molar activities were in the range of 3-8 GBq/ $\mu\text{mol}$  using starting activities of 100-400 MBq for  $^{68}\text{Ga}$  and  $^{44}\text{Sc}$ .

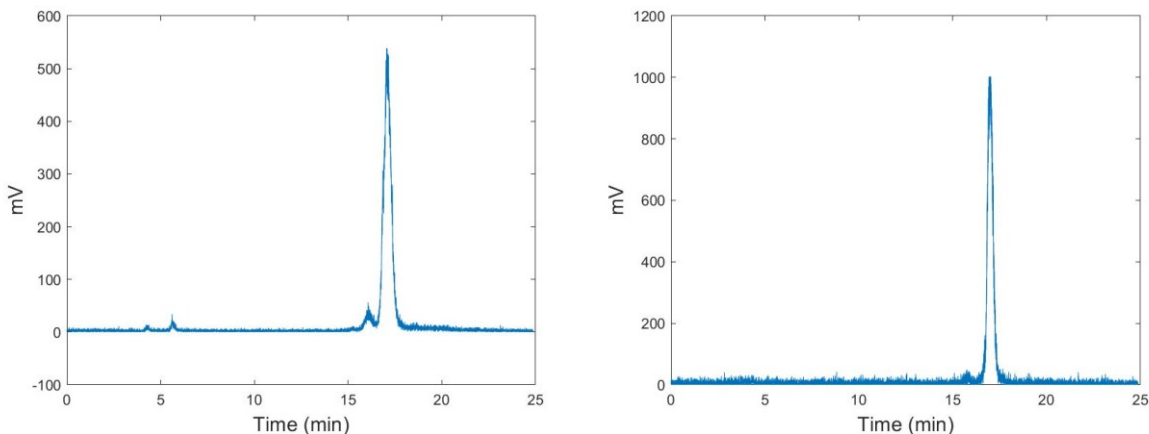


Figure 5.3 Radio-HPLC of  $[^{68}\text{Ga}]\text{-Ga-DOTA-BBN2}$  (left) and  $[^{44}\text{Sc}]\text{-Sc-DOTA-BBN2}$  (right) QC samples to be injected into animals.

Partition coefficients for both radiopeptides were determined as  $\log D_{7.4}$  values ( $-2.50 \pm 0.02$  for  $[^{44}\text{Sc}]\text{Sc-DOTA-Ava-BBN2}$  and  $-2.57 \pm 0.02$  for  $[^{68}\text{Ga}]\text{Ga-DOTA-Ava-BBN2}$ ) using the shake-flask method in *n*-octanol and PBS at pH 7.4, which represent the lipophilicity of the radiopeptides.

### 5.3.2 In vitro competitive binding assay

A radiometric competitive binding assay was performed to determine the inhibitory potency of  $^{nat}\text{Ga-DOTA-Ava-BBN2}$ ,  $^{nat}\text{Sc-DOTA-Ava-BBN2}$ , and  $\text{DOTA-Ava-BBN2}$  in GRPR-expressing PC3 prostate cancer cells. All three peptides competed for binding to GRPRs in a concentration-dependent manner using commercially available  $^{125}\text{I-Tyr}^4\text{-BBN(1-14)}$  as a radiotracer. GRPR-binding peptide  $\text{Tyr}^4\text{-BBN(1-14)}$  was used as an internal reference compound in the binding assay. Figure 5.4 displays the measured concentration-dependent dose-response curves of all tested peptides and their calculated respective  $\text{IC}_{50}$  values.

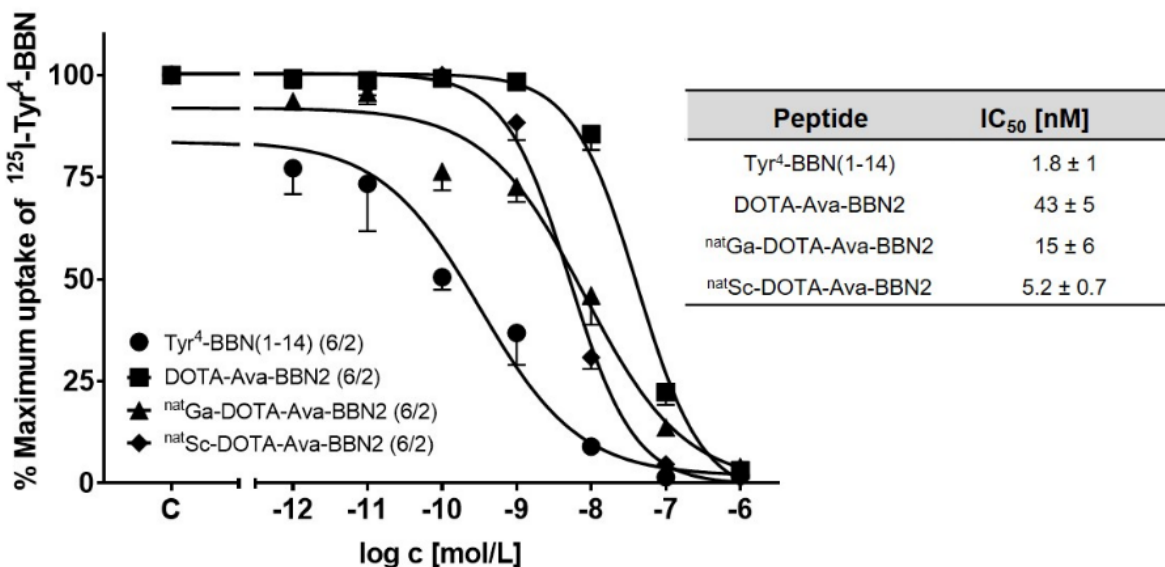


Figure 5.4 Dose-response curves for the competitive binding assay. Determination of IC<sub>50</sub> values for <sup>nat</sup>Ga-DOTA-Ava-BBN2, <sup>nat</sup>Sc-DOTA-Ava-BBN2, Tyr<sup>4</sup>-BBN(1-14), and DOTA-Ava-BBN2 against <sup>125</sup>I-Tyr<sup>4</sup>-BBN(1-14) to GRPR. Data as mean ± SEM.

Metal-containing peptides <sup>nat</sup>Ga-DOTA-Ava-BBN2 and <sup>nat</sup>Sc-DOTA-Ava-BBN2 retained high binding affinity to the GRPR with IC<sub>50</sub> values 15±6 nM and 5.2±0.7 nM, respectively. The measured IC<sub>50</sub> value for <sup>nat</sup>Sc-DOTA-Ava-BBN2 was in the same order of magnitude as endogenous-derived reference compound Tyr-BBN(1-14), which had an IC<sub>50</sub> value of 1.8±1 nM in the cell-based binding assay. <sup>nat</sup>Ga-DOTA-Ava-BBN2 bound with a somewhat lower affinity to the GRPR, and the lowest binding affinity was found for DOTA-Ava-BBN2 peptide (IC<sub>50</sub> = 43±5 nM).

### 5.3.3 Gene expression microarray analysis

The retrospective GRPR mRNA expression levels based on tissue microarray analysis in breast cancer tissue biopsy samples from 176 breast cancer patients and 10 control healthy human breast tissue samples are summarized in Figure 5.5.

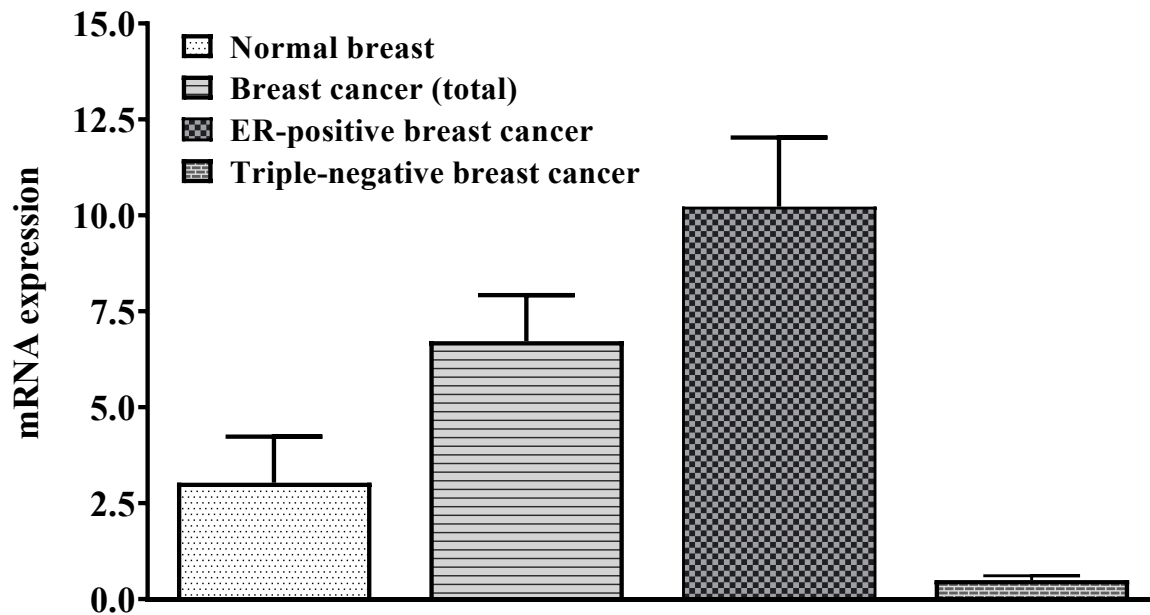


Figure 5.5 Total mRNA expression levels of GRPR in normal breast versus total breast cancer tissue, estrogen receptor (ER)-positive, and triple-negative breast cancer samples. Data are presented as mean  $\pm$  standard error of the mean of mRNA levels based on log-transformed values of the gene expression microarray signal intensity from analyzed patient samples.

The mean GRPR mRNA levels are upregulated in breast cancer samples ( $6.72 \pm 1.21$ ) compared to normal breast tissue ( $3.04 \pm 1.20$ ). Analysis of 56 triple-negative breast cancer ( $0.49 \pm 0.11$ ) versus 112 estrogen receptor (ER)-positive breast cancer ( $10.23 \pm 1.82$ ) revealed much higher GRPR mRNA transcript levels in ER-positive breast cancer.

#### 5.3.4 Protein expression of GRPR in breast cancer cell lines and human breast cancer tissue

Representative immunohistochemistry analysis of ER-positive primary breast cancer tissue and corresponding lymph node metastasis and Western blot analysis of MCF7 (ER-positive) and MDA-MB231 (triple-negative) breast cancer cells are given in Figure 5.6.

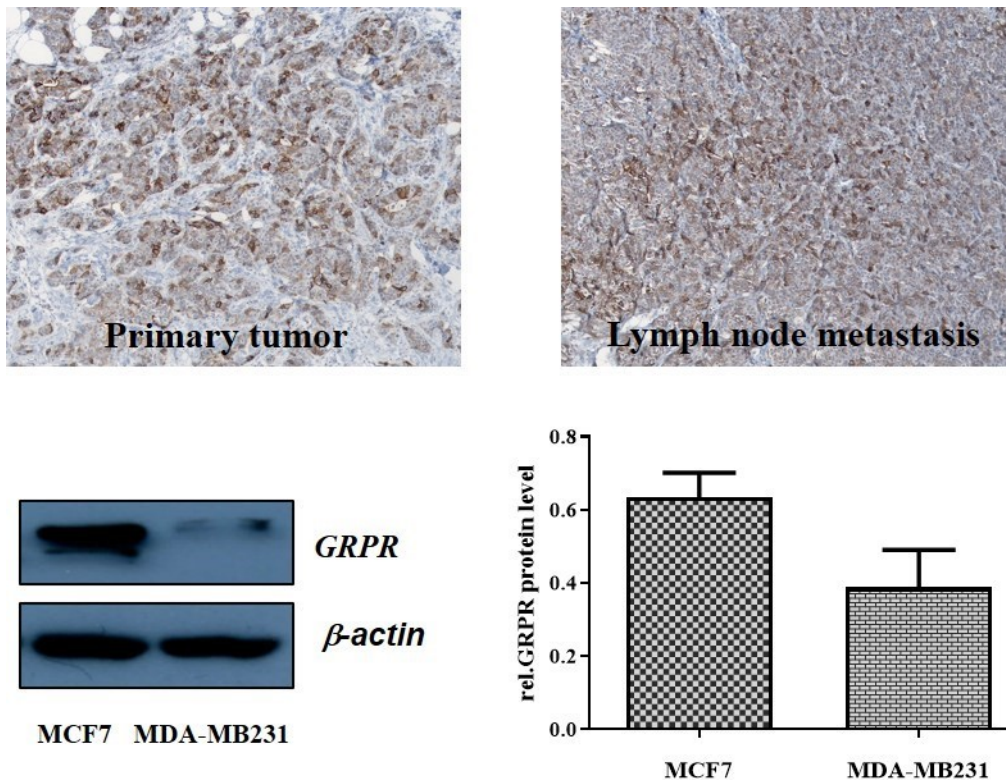


Figure 5.6 Representative immunohistochemical staining of GRPR (top) in human ER-positive primary breast cancer tissue and corresponding lymph node metastases and Western blot analysis (bottom) of GRPR expression in MCF7 and MDA-MB231 cell lysates.

Immunohistochemical analysis revealed GRPR protein expression levels in ER-positive human breast cancer tissue representing primary tumor and lymph node metastases.

We studied nine invasive ER-positive breast cancer tissues (primary tumor and respective lymph node metastasis). We found 3 samples with strong staining, 3 with moderate staining and 3 with weak staining in the case of primary tumor samples. Analysis of respective lymph node metastases revealed 6 samples with strong, 2 samples with moderate and 1 sample with weak staining.

High GRPR protein expression was also confirmed in ER-positive MCF7 cells, whereas only low expression levels were found in triple-negative MDA-MB231 breast cancer cells. The detected high GRPR mRNA and protein expression levels correspond with literature reports describing the upregulation of GRPR in ER-positive breast cancer and low GRPR expression levels in triple-negative breast cancers [44,45].

### 5.3.5 Dynamic PET imaging studies in MCF7 and PC3 xenografts

Tumor-targeting properties of [ $^{68}\text{Ga}$ ]Ga-DOTA-Ava-BBN2 and [ $^{44}\text{Sc}$ ]Sc-DOTA-Ava-BBN2 were studied in ER-receptor positive breast cancer xenografts (MCF7) and hormone-independent prostate cancer PC3 xenografts with dynamic PET imaging.

In the first set of experiments, we studied both radiopeptides in MCF7 xenograft. Figure 5.7 illustrates PET images as maximum intensity projections (MIPs) of MCF7 tumor-bearing mice at 20 min after the injection of both radiopeptides as well as corresponding time-activity curves (TACs) representing the time course of radioactivity accumulation and retention in the tumor and muscle tissue over time.

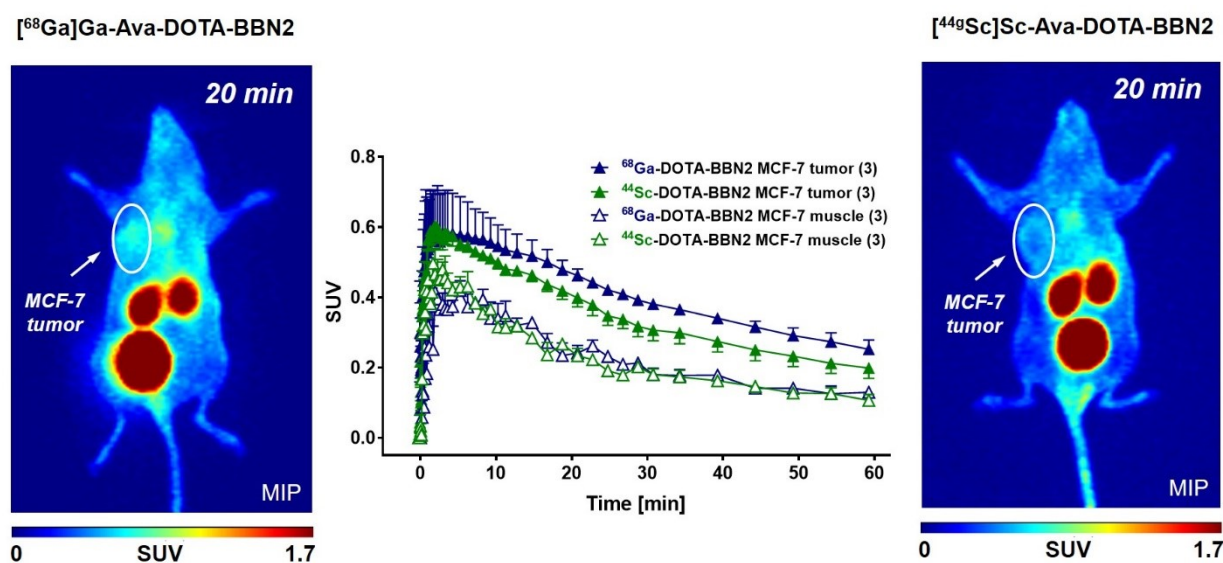


Figure 5.7 Representative PET images (MIP) of MCF7 tumor-bearing mice at 20 min after injection of [ $^{68}\text{Ga}$ ]Ga-DOTA-Ava-BBN2 (left) and [ $^{44}\text{Sc}$ ]Sc-DOTA-Ava-BBN2 (right). Corresponding time-activity curves (middle) show the radioactivity levels in the tumor and muscle for both radiopeptides over time as SUV values (mean  $\pm$  SEM from  $n = 3$  experiments).

Radioactivity of both radiopeptides in MCF7 tumors followed a comparable accumulation and retention profile over the 60 min time course of the PET study. Radioactivity accumulation in the MCF7 tumor reached a maximum within 5 min after the injection of the radiopeptides resulting in a  $\text{SUV}_{\text{mean}}$  of  $0.61 \pm 0.04$  for [ $^{44}\text{Sc}$ ]Sc-DOTA-Ava-BBN2 and  $0.58 \pm 0.11$  for [ $^{68}\text{Ga}$ ]Ga-DOTA-Ava-BBN2. Radioactivity in the tumor washed out over time, reaching a  $\text{SUV}_{\text{mean}}$  of  $0.20 \pm 0.03$  for [ $^{44}\text{Sc}$ ]Sc-DOTA-Ava-BBN2 and  $0.25 \pm 0.03$  for [ $^{68}\text{Ga}$ ]Ga-DOTA-Ava-BBN2 at 60 min post-injection (p.i.). Over the 60 min time course of the PET study, radiopeptide [ $^{68}\text{Ga}$ ]Ga-DOTA-Ava-BBN2 displayed a slightly higher tumor uptake than  $^{44}\text{Sc}$ -labeled radiopeptide [ $^{44}\text{Sc}$ ]Sc-DOTA-Ava-BBN2. This can presumably be attributed to the higher effective molar

activities obtained during the radiosynthesis of radiopeptide [ $^{68}\text{Ga}$ ]Ga-Ava-DOTA-BBN2 as higher starting activities of  $^{68}\text{Ga}$  (~600 MBq) were used compared to  $^{44}\text{Sc}$  (~150 MBq).

Radioactivity levels in muscle as reference tissue were always lower as tumor radioactivity levels during the time course of the PET imaging study. Both radiopeptides showed only low muscle uptake and retention, reaching a  $\text{SUV}_{\text{mean}}$  of 0.11 and 0.12, respectively, after 60 min p.i.. The elimination pathway of both radiopeptides was via kidneys towards final radioactivity accumulation in the bladder, which was consistent with previous studies using bombesin derivatives as radiopeptides for imaging of GRPRs [39,40,44,45]. However, the observed overall uptake in MCF7 tumors was unexpectedly low for both radiopeptides, and no blocking studies were performed to demonstrate the specific binding of both radiopeptides to GRPRs in the tumor tissue.

The majority of radiolabeled bombesin derivatives have been used for PET and SPECT imaging in prostate cancer models. PC3 tumors have been demonstrated as a suitable prostate cancer model with high expression levels of GRPRs

Figure 5.8 displays PET images of PC3 tumor-bearing BALB/c mice at 60 min after the injection of radiopeptides [ $^{68}\text{Ga}$ ]Ga-DOTA-Ava-BBN2 and [ $^{44}\text{Sc}$ ]Sc-DOTA-Ava-BBN2 in the absence (control) and presence of 300  $\mu\text{g}$  BBN2 as blocking agent, as well as corresponding time-activity curves (TACs) for radioactivity levels in PC3 tumors and muscle tissue.

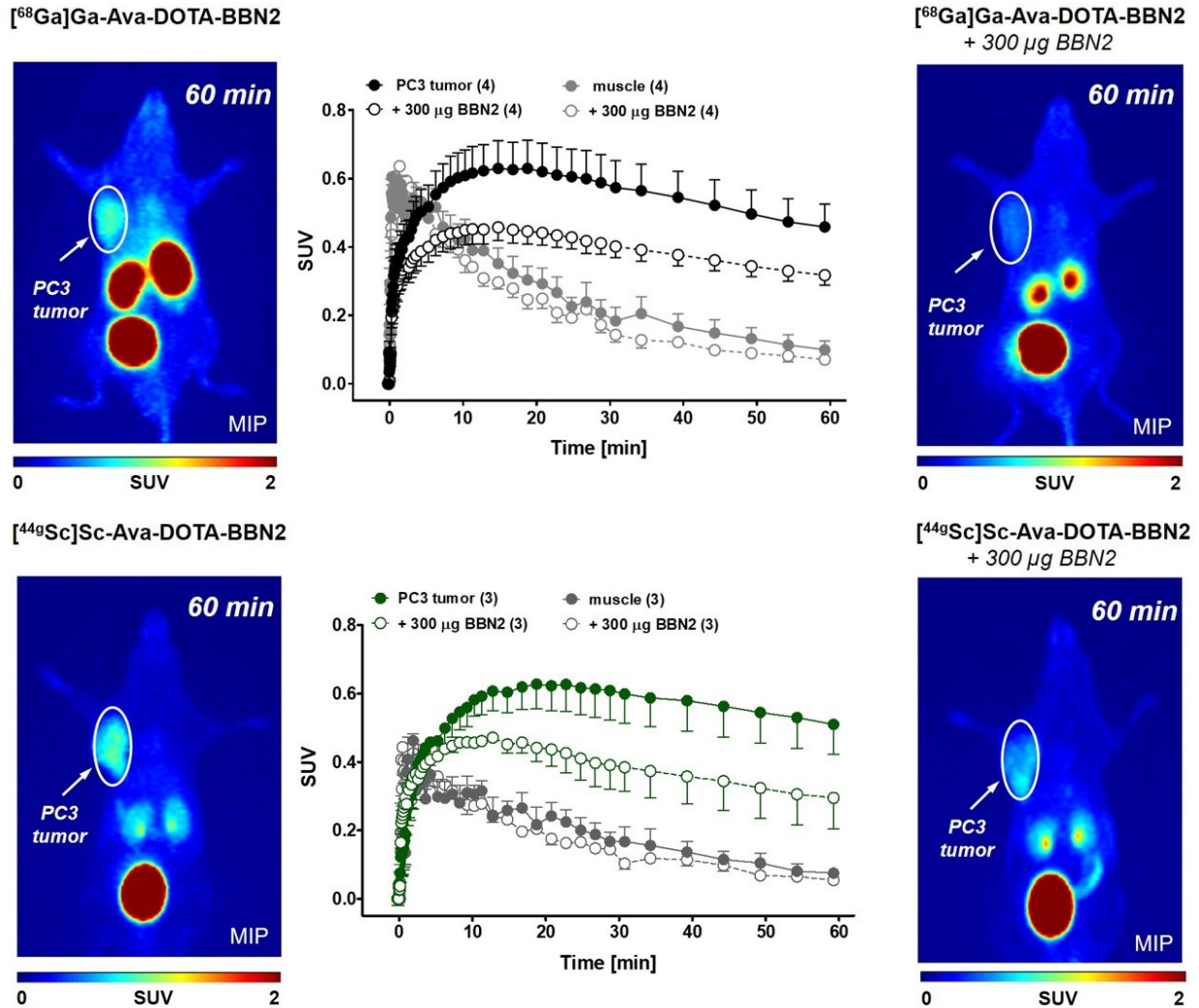


Figure 5.8 Representative PET images (MIP) of PC3 tumor-bearing mice at 60 min after injection of  $[^{68}\text{Ga}]\text{Ga-DOTA-Ava-BBN2}$  (top) and  $[^{44}\text{Sc}]\text{Sc-DOTA-Ava-BBN2}$  (bottom) under control (right) and blocking conditions (left). Corresponding time-activity curves (middle) show the radioactivity levels in the tumor and muscle for both radiopeptides over time as SUV values (mean  $\pm$  SEM from  $n = 3$  experiments).

Radiotracer uptake in PC3 tumors was clearly visible for both radiopeptides. Overall, radiotracer accumulation and retention profiles were comparable for both radiopeptides. Radioactivity accumulation in PC3 tumor tissues resulted in a  $\text{SUV}_{\text{mean}}$  of  $0.46 \pm 0.07$  for  $[^{68}\text{Ga}]\text{Ga-DOTA-Ava-BBN2}$  and a slightly higher  $\text{SUV}_{\text{mean}}$  of  $0.51 \pm 0.09$  for  $[^{44}\text{Sc}]\text{Sc-DOTA-Ava-BBN2}$  60 min after radiotracer injection.

Tumor-to muscle ratio at 60 min p.i. was somewhat higher for  $[^{44}\text{Sc}]\text{Sc-DOTA-Ava-BBN2}$  (6.4) compared to  $[^{68}\text{Ga}]\text{Ga-DOTA-Ava-BBN2}$  (4.6). Blocking studies with 300  $\mu\text{g}$  of BBN2 confirmed the specific binding of both radiopeptides to the GRPR. Tumor uptake at 60 min p.i. under blocking conditions could be

reduced by 31% ( $[^{68}\text{Ga}]\text{Ga-DOTA-Ava-BBN2}$ ) and 43% ( $[^{44}\text{Sc}]\text{Sc-DOTA-Ava-BBN2}$ ), respectively. Significantly reduced tumor uptake was clearly visible in the PET images and the respective TACs. Muscle uptake was not effected under blocking conditions, which resulted in reduced tumor to muscle ratios of 3.3 ( $[^{68}\text{Ga}]\text{Ga-DOTA-Ava-BBN2}$ ) and 3.5 ( $[^{44}\text{Sc}]\text{Sc-DOTA-Ava-BBN2}$ ), respectively.

Radioactivity cleared rapidly from the blood with comparable clearance profiles after the injection of both radiopeptides. Both radiopeptides also showed predominant renal clearance patterns via kidneys and subsequent radioactivity accumulation in the bladder. No noticeable radioactivity was detected in hepatobiliary organs like the liver and intestines. Both radiopeptides displayed a comparable clearance pattern from the liver and kidneys over time. Clearance kinetics for both radiopeptides from blood, kidneys, and liver is given in Figure 5.9.

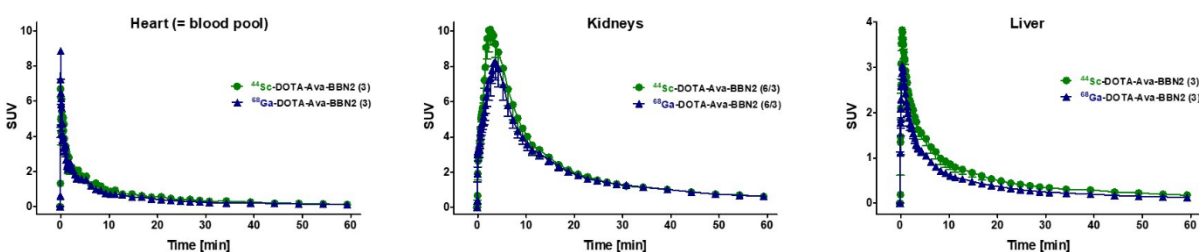


Figure 5.9 Time-activity curves (TACs) for clearance kinetics from blood (heart = blood pool), kidneys, and liver after injection of  $[^{68}\text{Ga}]\text{Ga-DOTA-Ava-BBN2}$  (blue) and  $[^{44}\text{Sc}]\text{Sc-DOTA-Ava-BBN2}$  (green) into PC3 tumor bearing mice.

## 5.4 Discussion

Radiopeptides are versatile radiopharmaceuticals for diagnostic imaging and radionuclide therapy of diseases with particular emphasis on cancer. Over the last decade, numerous radiolabeled bombesin derivatives have been developed and tested for targeting GRPRs in cancer. GRPR expression has been widely studied in many different tumor types (Baratto et al., 2020), including prostate, breast, lung, colon, renal, and head and neck cancer. However, breast and prostate cancers dominate clinical studies with radiolabeled bombesin derivatives for diagnostic imaging and radionuclide therapy. The role of GRPRs in cancer has been described as autocrine growth factor receptors promoting cancer cell proliferation or as morphogen factors to trigger cancer cell differentiation (Carroll et al., 2000). Recent studies have shown a preference for radiolabeled GRPR antagonists compared with GRPR agonists (Baratto et al., 2020; Dalm et al., 2017, 2015). Antagonist often displayed higher GRPR binding and more favorable pharmacokinetics. Moreover, clinical studies with  $^{177}\text{Lu}$ -labeled GRPR agonists for radionuclide therapy reported unwanted side effects due to the activation of the GRPR (Bodei et al., 2007).

Our present work described the synthesis and evaluation of metabolically stabilized bombesin derivative DOTA-Ava-BBN2 labeled with  $^{68}\text{Ga}$  and  $^{44}\text{Sc}$  as radiopeptide antagonists for PET imaging of GRPRs in breast and prostate cancer. The study discussed the influence of  $^{68}\text{Ga}$ - and  $^{44}\text{Sc}$ -labeled DOTA complexes attached to Ava-BBN2 on the *in vitro* GRPR binding affinity and the biodistribution profile in GRPR-expressing estrogen receptor (ER)-positive breast (MCF7) and prostate (PC3) cancer models.

Both radiopeptides were prepared in isolated radiochemical yields of 70-80% (d.c.) after incubating the radiometals with DOTA-Ava-BBN2 (50  $\mu\text{g}$ ) at 95 °C for 20 min followed by solid-phase extraction for purification. The obtained radiochemical yields were comparable to that of previously reported  $^{68}\text{Ga}$ - and  $^{44}\text{Sc}$ -DOTA complexes attached to bombesin BN[2-14] (Koumariou et al., 2012). The fast, robust, and high-yielding radiosynthesis with DOTA-Ava-BBN2 as labeling precursor underlines the suitability of the DOTA chelator for the efficient incorporation of radiometals  $^{68}\text{Ga}^{3+}$  and  $^{44}\text{Sc}^{3+}$ . Several studies also showed that DOTA complexes with  $^{68}\text{Ga}^{3+}$  and  $^{44}\text{Sc}^{3+}$  display high thermodynamic stability and kinetic inertness with higher thermodynamic stability constants ( $\log K_{\text{ML}}$ ) for scandium ( $\log K_{\text{ML}} = 27.0$ ) over gallium ( $\log K_{\text{ML}} = 21.3$ ) (W. Price and Orvig, 2014). Moreover, our group confirmed high metabolic stability *in vivo* of the GRPR-binding motif BBN2 in various studies involving  $^{18}\text{F}$ - and  $^{68}\text{Ga}$ -labeled BBN2 radiopeptides (Richter et al., 2016, 2013).

The high metabolic stability of the GRPR-binding motif BBN2 combined with the high thermodynamic and kinetic stability of DOTA complexes with  $^{68}\text{Ga}^{3+}$  and  $^{44}\text{Sc}^{3+}$  make radiopeptides [ $^{68}\text{Ga}$ ]Ga-DOTA-Ava-BBN2 and [ $^{44}\text{Sc}$ ]Sc-DOTA-Ava-BBN2 suitable for subsequent radiopharmacological studies *in vivo*. Incorporation of radiometals  $^{68}\text{Ga}^{3+}$  and  $^{44}\text{Sc}^{3+}$  into DOTA-Ava-BBN2 resulted in the formation of negatively charged complexes with comparable lipophilicities ( $\log D_{7.4}$  values of -2.50 for [ $^{68}\text{Ga}$ ]Ga-DOTA-Ava-BBN2 and -2.57 for [ $^{44}\text{Sc}$ ]Sc-DOTA-Ava-BBN2). Thus, the use of  $^{68}\text{Ga}$  or  $^{44}\text{Sc}$  has no effect on the lipophilicity of the resulting radiopeptides. The determined hydrophilic character of both radiopeptides is in line with related PEGylated bombesin derivatives labeled with  $^{68}\text{Ga}$  (Liolios et al., 2018; Schuhmacher et al., 2005). The influence of the radiometal was more pronounced in the binding affinities of both radiopeptides to the GRPR as determined in the *in vitro* binding assay. [ $^{nat}\text{Sc}$ ]Sc-DOTA-Ava-BBN2 displayed a three-fold higher binding affinity ( $\text{IC}_{50} = 5.2 \pm 0.7$  nM) than [ $^{68}\text{Ga}$ ]Ga-DOTA-Ava-BBN2 ( $\text{IC}_{50} = 15 \pm 6$  nM). This finding is in contrast to a recent study discussing a higher binding affinity of the  $^{nat}\text{Ga}$ -DOTA bombesin BN[2-14] peptide compared to the corresponding  $^{nat}\text{Sc}$ -DOTA peptide (Koumariou et al., 2012). Regardless of using an Ava linker connecting the GRPR-binding peptide to the DOTA chelator in our peptides, the main difference in the previous study was the use of the BN[2-

14] bombesin motif, which acts as a GRPR agonist rather than an antagonist as with our BBN2 motif (Richter et al., 2016, 2013).

The majority of reported studies with radiolabeled bombesin derivatives describe molecular targeting of GRPRs in prostate cancer. However, several reports in the literature also demonstrated a significant correlation between GRPR expression and estrogen receptor (ER) status in breast cancer. ER-positive breast cancers are associated with higher GRPR levels suggesting that especially ER-positive breast cancer patients would benefit from GRPR-targeting radiopeptides for imaging and therapy (Dalm et al., 2017; Parry et al., 2007). Moreover, also lymph node metastases derived from primary tumors expressing GRPRs were GRPR positive (Dalm et al., 2017; Gugger and Reubi, 1999; Reubi et al., 2002). In the present study, we also confirmed high GRPR expression levels in ER-positive breast cancer at both mRNA and protein levels. Gene expression microarray analysis on 176 primary, treatment-naive breast cancer samples, and 10 healthy breast tissue samples revealed higher expression levels of GRPR mRNA in ER-positive breast cancer. In contrast, significantly lower GRPR mRNA levels were detected in triple-negative breast cancer. We also screened GRPR protein expression levels in ER-positive breast cancer cell line MCF-7 and ER-negative breast cancer cell line MDA-MB-231 using Western blot analysis.

ER-positive MCF-7 cell line showed high GRPR expression, whereas low GRPR expression levels were found in ER-negative MDA-MB-231 cells. This finding corresponds with the gene expression microarray analysis data.

Immunohistochemistry experiments further confirmed high GRPR expression levels in ER-positive primary human breast cancer samples and corresponding lymph node metastases. These results also confirmed the recently reported positive correlation between ER status and the extent of GRPR expression levels in breast cancer (Dalm et al., 2017; Morgat et al., 2017).

The obtained GRPR expression data prompted us to study the biodistribution and the tumor accumulation and retention profiles of both radiopeptides in ER-positive MCF7 breast cancer xenografts. To our surprise and disappointment, however, both radiopeptides showed only low uptake and retention in the MCF7 tumors. SUVs were 0.20-0.25 at 60 min p.i.. Radioactivity accumulation peaked at 5 min p.i. but radioactivity was washed out continuously from the tumor tissue over time afterward. This resulted in SUVs only slightly higher than that of the muscle as reference tissue at 60 min p.i.. Moreover, uptake of radioactivity was predominantly observed in the tumor periphery, which can be explained by recently postulated the differences in the tumor microenvironment and differential expression of GRPRs

in the MCF7 tumor tissue (Koumarianou et al., 2012). Over the entire 60 min time course of the PET study, radiopeptide [ $^{68}\text{Ga}$ ]Ga-DOTA-Ava-BBN2 showed somewhat higher tumor uptake and retention compared to [ $^{44}\text{Sc}$ ]Sc-DOTA-Ava-BBN2. A recent PET study using  $^{64}\text{Cu}$ -DOTA labeled bombesin BN(7-14) in ER-positive T-47D tumor xenografts as breast cancer model also resulted in comparable low SUVs ( $\sim 0.3$ ) at 60 min p.i. (Parry et al., 2007). MCF-7 cells have previously been reported to have lower uptake of radiolabeled GRPR ligands in comparison with T-47D cancer cells (Parry et al., 2007). To the best of our knowledge, no other preclinical studies have been reported using radiolabeled bombesin derivatives for PET imaging in breast cancer xenografts. The overall rather low tumor uptake (SUV 0.2-0.25 at 60 min p.i.) of both radiopeptides in the MCF7 tumors did not warrant blocking studies to confirm GRPR-mediated uptake of both radiopeptides in the MCF7 breast cancer model.

Further validation of both radiopeptides was performed in the well-established and studied PC3 prostate cancer model. Dynamic PET studies with both radiopeptides revealed promising radioactivity uptake and retention in the PC3 tumors. Moreover, both radiopeptides showed a more homogeneous uptake in the PC3 tumor tissue, which was different from the more distinct peripheral uptake in the MCF7 tumors. PC3 tumors were clearly visible in the PET images.

The small size and the hydrophilic nature of both radiopeptides enabled fast clearance of radioactivity from the blood and non-target tissues resulting in favorable image contrast and high tumor-to muscle ratios of 6.4 for [ $^{44}\text{Sc}$ ]Sc-DOTA-Ava-BBN2 and 4.6 for [ $^{68}\text{Ga}$ ]Ga-DOTA-Ava-BBN2, respectively. Blood and muscle clearance was almost identical for both radiopeptides. The observed slightly higher tumor uptake and retention of [ $^{44}\text{Sc}$ ]Sc-DOTA-Ava-BBN2 correlated with the higher GRPR binding affinity compared to [ $^{68}\text{Ga}$ ]Ga-DOTA-Ava-BBN2. However, PET imaging experiments did not reveal a measurable effect of the radiometal on tumor uptake and retention. The obtained time-activity curves representing radioactivity levels in PC3 tumors and muscle tissue over time after the injection of both radiopeptides are comparable with data from recently studied and structurally related radiopeptide [ $^{68}\text{Ga}$ ]Ga-NOTA-Ava-BBN2 (Richter et al., 2016). The use of DOTA as a radiometal chelator resulted in the formation of negatively charged radiometal complexes, which led in a renal clearance profile as the predominant clearance pathway for both radiopeptides. However, recently reported  $^{68}\text{Ga}$ -labeled NOTA-Ava-BBN2 as a presumably neutral radiometal complex also displayed some radioactivity retention in the liver and intestines.

Renal clearance was similar for [ $^{68}\text{Ga}$ ]Ga-DOTA-Ava-BBN2 and [ $^{44}\text{Sc}$ ]Sc-DOTA-Ava-BBN2 in our study further confirming that the radiometal has no measurable effect on the biodistribution profile of both

radiopeptides. A related study, however, comparing various  $^{68}\text{Ga}$ - and  $^{44}\text{Sc}$ - labeled DOTA- and NODAGA-functionalized peptides (RGD and NOC-based peptides) found a somewhat slower renal clearance and higher liver uptake in the case of  $^{68}\text{Ga}$ -DOTA-labeled peptides (Domnanich et al., 2016). Analysis of all recently performed PET studies with radiolabeled BBN2-based GRPR antagonists in PC3 prostate cancer models confirmed higher tumor uptake and retention for radiometal-labeled BBN2 peptides compared to  $^{18}\text{F}$ -labeled BBN2 derivatives (Richter et al., 2013). A direct comparison of  $^{44}\text{Sc}$ -labeled BBN2 over  $^{68}\text{Ga}$ -labeled BBN2 revealed no measurable biological differences which would favor  $^{44}\text{Sc}$  or  $^{68}\text{Ga}$  for PET imaging of GRPRs in the PC3 prostate cancer model. Both radiopeptides displayed high tumor uptake and retention while exhibiting a favorable renal clearance profile. The specificity of radiopeptide uptake in PC3 tumors through binding to GRPRs was confirmed by blocking studies with DOTA-Ava-BBN2 (300  $\mu\text{g}$  dose per animal). The observed reduced tumor uptake was more distinct for [ $^{44}\text{Sc}$ ]Sc-DOTA-Ava-BBN2, which resulted in a 43% reduction in comparison to the control experiments. The reduction of radioactivity uptake in PC3 tumors for both radiopeptides under blocking conditions were comparable to results obtained with [ $^{68}\text{Ga}$ ]Ga-NOTA-Ava-BBN2 (Richter et al., 2016).

## 5.5 Conclusion

Our present study confirms the excellent GRPR-targeting properties of metabolically stabilized bombesin antagonists like BBN2 peptides for PET imaging of prostate cancer. A direct comparison of  $^{68}\text{Ga}$ - and  $^{44}\text{Sc}$ -labeled DOTA-Ava-BBN2 peptides revealed subtle but noticeable differences of the radiometal, which impacted on the *in vitro* GRPR receptor binding properties in PC3 cells. No differences were observed in the biodistribution profiles in PC3 xenografts. [ $^{68}\text{Ga}$ ]Ga-DOTA-Ava-BBN2 and [ $^{44}\text{Sc}$ ]Sc-DOTA-Ava-BBN2 displayed comparable tumor uptake and retention with rapid blood and renal clearance profiles. The improved availability, the convenient 4.04 h half-life, and the favorable PET imaging performance of  $^{44}\text{Sc}$  make  $^{44}\text{Sc}$ -labeled radiotracers highly attractive alternatives to current  $^{68}\text{Ga}$ -labeled radiopharmaceuticals, especially for preclinical PET studies. The excellent PET imaging performance of [ $^{44}\text{Sc}$ ]Sc-DOTA-Ava-BBN2 should warrant the development of an [ $^{43}\text{Sc}$ ]Sc-DOTA-Ava-BBN2 analog as a potential radiopeptide for clinical translation since the clinical application of  $^{44}\text{Sc}$ -labeled radiopharmaceuticals may be limited by the high dose to the high energy 1157 keV gamma emission (99.9% intensity).  $^{43}\text{Sc}$  embraces comparable physical characteristics while lacking a high energy gamma emission.  $^{43}\text{Sc}$  emits a main gamma line at 372 keV which is much more suitable for clinical applications. Thus, radiopeptide [ $^{43}\text{Sc}$ ]Sc-DOTA-Ava-BBN2 should be tested as a novel radiolabeled GRPR antagonist for clinical PET imaging of prostate cancer.

## 5.6 References

- Abiraj K, Mansi R, Tamma M-L, Forrer F, Cescato R, Reubi JC, et al. Tetraamine-Derived Bifunctional Chelators for Technetium-99m Labelling: Synthesis, Bioconjugation and Evaluation as Targeted SPECT Imaging Probes for GRP-Receptor-Positive Tumours. *Chem – Eur J* 2010; 16:2115–24.
- Alliot C, Kerdjoudj R, Michel N, Haddad F, Huclier-Markai S. Cyclotron production of high purity  $^{44m}\text{Sc}$  with deuterons from  $^{44}\text{CaCO}_3$  targets. *Nucl Med Biol* 2015; 42:524-529.
- Baratto L, Duan H, Mäcke H, Iagaru A. Imaging the Distribution of Gastrin-Releasing Peptide Receptors in Cancer. *J Nucl Med*. 2020; 61:792-798.
- Baum RP, Kulkarni HR, Carreras C. Peptides and Receptors in Image-Guided Therapy: Theranostics for Neuroendocrine Neoplasms. *Semin Nucl Med* 2012; 42:190–207.
- Baum RP, Kulkarni HR. THERANOSTICS: From Molecular Imaging Using Ga-68 Labeled Tracers and PET/CT to Personalized Radionuclide Therapy - The Bad Berka Experience. *Theranostics* 2012; 2:437–47.
- Bodei L, Ferrari M, Nunn AD, et al.  $^{177}\text{Lu}$ -AMBA bombesin analogue in hormone refractory prostate cancer patients: a phase I escalation study with single-cycle administrations [abstract]. *Eur J Nucl Med Mol Imaging*. 2007; 34:S221.
- Carroll RE, Matkowskyj KA, Tretiakova MS, Battey JF, Benya RV. Gastrin-releasing peptide is a mitogen and a morphogen in murine colon cancer. *Cell Growth Differ*. 2000; 11:385-393.
- Chatalic KL, Kwekkeboom DJ, de Jong M. Radiopeptides for Imaging and Therapy: A Radiant Future. *J Nucl Med*. 2015; 56:1809-1812.
- Cives M, Strosberg J. Radionuclide Therapy for Neuroendocrine Tumors. *Curr Oncol Rep*. 2017; 19:9.
- Dalm SU, Bakker IL, de Blois E, et al.  $^{68}\text{Ga}/^{177}\text{Lu}$ -NeOBOMB1, a Novel Radiolabeled GRPR Antagonist for Theranostic Use in Oncology. *J Nucl Med*. 2017; 58:293-299.
- Dalm SU, Martens JW, Sieuwerts AM, et al. In vitro and in vivo application of radiolabeled gastrin-releasing peptide receptor ligands in breast cancer. *J Nucl Med*. 2015; 56:752-757.
- Domnanich KA, Müller C, Farkas R, Schmid RM, Ponsard B, Schibli R, et al.  $^{44}\text{Sc}$  for labeling of DOTA- and NODAGA-functionalized peptides: preclinical in vitro and in vivo investigations. *EJNMMI Radiopharm Chem* 2016; 1:8.
- Eppard E, de la Fuente A, Benešová M, Khawar A, Bundschuh RA, Gärtner FC, et al. Clinical Translation and First In-Human Use of  $^{44}\text{Sc}$ Sc-PSMA-617 for PET Imaging of Metastasized Castrate-Resistant Prostate Cancer. *Theranostics* 2017; 7:4359-43269.

Fani M, Maecke HR, Okarvi SM. Radiolabeled peptides: valuable tools for the detection and treatment of cancer. *Theranostics*. 2012; 2:481-501.

García Garayoa E, Rüegg D, Bläuenstein P, Zwimpfer M, Khan IU, Maes V, et al. Chemical and biological characterization of new  $\text{Re}(\text{CO})_3/[^{99\text{m}}\text{Tc}](\text{CO})_3$  bombesin analogues. *Nucl Med Biol* 2007; 34:17–28.

Gnesin S, Cicone F, Mitsakis P, et al. First in-human radiation dosimetry of the gastrin-releasing peptide (GRP) receptor antagonist  $^{68}\text{Ga}$ -NODAGA-MJ9. *EJNMMI Res*. 2018; 8:108.

Gruber L, Jimenez-Franco LD, Decristoforo C, et al. MITIGATE-NeoBOMB1, a Phase I/IIa Study to Evaluate Safety, Pharmacokinetics and Preliminary Imaging of  $^{68}\text{Ga}$ -NeoBOMB1, a Gastrin-releasing Peptide Receptor Antagonist, in GIST Patients. *J Nucl Med*. 2020; jnumed.119.238808.

Gugger M, Reubi JC. Gastrin-Releasing Peptide Receptors in Non-Neoplastic and Neoplastic Human Breast. *Am J Pathol* 1999; 155:2067–76.

Hernandez R, Valdovinos HF, Yang Y, Chakravarty R, Hong H, Barnhart TE, et al.  $^{44}\text{Sc}$ : An Attractive Isotope for Peptide-Based PET Imaging. *Mol Pharm* 2014; 11:2954-2961.

Hohla F, Schally AV. Targeting gastrin releasing peptide receptors: New options for the therapy and diagnosis of cancer. *Cell Cycle* 2010; 9:1738–41.

Huclier-Markai S, Kerdjoudj R, Alliot C, Bonraisin AC, Michel N, Haddad F, et al. Optimization of reaction conditions for the radiolabeling of DOTA and DOTA-peptide with  $^{44}\text{m}/^{44}\text{Sc}$  and experimental evidence of the feasibility of an in vivo PET generator. *Nucl Med Biol* 2014; 41, Suppl:e36-43.

Kelkar SS, Reineke TM. Theranostics: Combining Imaging and Therapy. *Bioconjug Chem* 2011; 22:1879–903.

Koumarianou E, Loktionova NS, Fellner M, Roesch F, Thews O, Pawlak D, et al.  $^{44}\text{Sc}$ -DOTA-BN[2-14]NH<sub>2</sub> in comparison to  $^{68}\text{Ga}$ -DOTA-BN[2-14]NH<sub>2</sub> in pre-clinical investigation. Is  $^{44}\text{Sc}$  a potential radionuclide for PET? *Appl Radiat Isot* 2012; 70:2669–76.

Koumarianou E, Mikołajczak R, Pawlak D, Zikos X, Bouziotis P, Garnuszek P, et al. Comparative study on DOTA-derivatized bombesin analog labeled with  $^{90}\text{Y}$  and  $^{177}\text{Lu}$ : in vitro and in vivo evaluation. *Nucl Med Biol* 2009; 36:591–603.

Liolios C, Buchmuller B, Bauder-Wüst U, et al. Monomeric and Dimeric  $^{68}\text{Ga}$ -Labeled Bombesin Analogues for Positron Emission Tomography (PET) Imaging of Tumors Expressing Gastrin-Releasing Peptide Receptors (GRPrs). *J Med Chem*. 2018; 61:2062-2074.

- Maina T, Bergsma H, Kulkarni HR, et al. Preclinical and first clinical experience with the gastrin-releasing peptide receptor-antagonist [<sup>68</sup>Ga]SB3 and PET/CT. *Eur J Nucl Med Mol Imaging*. 2016; 43:964-973.
- Müller C, Bunka M, Haller S, Köster U, Groehn V, Bernhardt P, et al. Promising Prospects for <sup>44</sup>Sc-/<sup>47</sup>Sc-Based Theragnostics: Application of <sup>47</sup>Sc for Radionuclide Tumor Therapy in Mice. *J Nucl Med* 2014; 55:1658-1664.
- Müller C, Bunka M, Reber J, Fischer C, Zhernosekov K, Türler A, et al. Promises of Cyclotron-Produced <sup>44</sup>Sc as a Diagnostic Match for Trivalent β--Emitters: In Vitro and In Vivo Study of a <sup>44</sup>Sc-DOTA-Folate Conjugate. *J Nucl Med* 2013; 54:2168-2174.
- Opalinska M, Hubalewska-Dydejczyk A, Sowa-Staszczak A. Radiolabeled peptides: current and new perspectives. *Q J Nucl Med Mol Imaging*. 2017; 61:153-167.
- Pruszyński M, Majkowska-Pilip A, Loktionova NS, Eppard E, Roesch F. Radiolabeling of DOTATOC with the long-lived positron emitter <sup>44</sup>Sc. *Appl Radiat Isot* 2012; 70:974-979.
- Parry JJ, Andrews R, Rogers BE. MicroPET imaging of breast cancer using radiolabeled bombesin analogs targeting the gastrin-releasing peptide receptor. *Breast Cancer Res Treat*. 2007; 101:175-183.
- Patel O, Shulkes A, Baldwin GS. Gastrin-releasing peptide and cancer. *Biochim Biophys Acta BBA - Rev Cancer* 2006; 1766:23-41.
- Price EW, Orvig C. Matching chelators to radiometals for radiopharmaceuticals. *Chem Soc Rev*. 2014; 43:260-290.
- Pujatti PB, Massicano AVF, Mengatti J, de Araújo EB. Preparation of [<sup>111</sup>In]-labeled-DTPA-bombesin conjugates at high specific activity and stability: Evaluation of labeling parameters and potential stabilizers. *Appl Radiat Isot* 2012; 70:856-63.
- Reubi C, Gugger M, Waser B. Co-expressed peptide receptors in breast cancer as a molecular basis for in vivo multireceptor tumour targeting. *Eur J Nucl Med Mol Imaging*. 2002; 29:855-862.
- Richter S, Wuest M, Krieger SS, Rogers BE, Friebe M, Bergmann R, et al. Synthesis and radiopharmacological evaluation of a high-affinity and metabolically stabilized <sup>18</sup>F-labeled bombesin analogue for molecular imaging of gastrin-releasing peptide receptor-expressing prostate cancer. *Nucl Med Biol* 2013; 40:1025-1034.
- Richter S, Wuest M, Bergman CN, Krieger S, Rogers BE, Wuest F. Metabolically Stabilized <sup>68</sup>Ga-NOTA-Bombesin for PET Imaging of Prostate Cancer and Influence of Protease Inhibitor Phosphoramidon. *Mol Pharm* 2016; 13:1347-1357.

Rogers BE, Bigott HM, McCarthy DW, Manna DD, Kim J, Sharp TL, et al. MicroPET Imaging of a Gastrin-Releasing Peptide Receptor-Positive Tumor in a Mouse Model of Human Prostate Cancer Using a  $^{64}\text{Cu}$ -Labeled Bombesin Analogue. *Bioconjug Chem* 2003; 14:756–63.

Severin GW, Engle JW, Valdovinos HF, Barnhart TE, Nickles RJ. Cyclotron produced  $^{44}\text{Sc}$  from natural calcium. *Appl Radiat Isot* 2012; 70:1526-1530.

Schroeder RPJ, van Weerden WM, Krenning EP, Bangma CH, Berndsen S, Grievink-de Ligt CH, et al. Gastrin-releasing peptide receptor-based targeting using bombesin analogues is superior to metabolism-based targeting using choline for in vivo imaging of human prostate cancer xenografts. *Eur J Nucl Med Mol Imaging* 2011; 38:1257–66.

Schuhmacher J, Zhang H, Doll J, et al. GRP receptor-targeted PET of a rat pancreas carcinoma xenograft in nude mice with a  $^{68}\text{Ga}$ -labeled bombesin(6-14) analog. *J Nucl Med*. 2005; 46:691-699.

Thomas R, Chen J, Roudier MM, Vessella RL, Lantry LE, Nunn AD. In vitro binding evaluation of  $^{177}\text{Lu}$ -AMBA, a novel  $^{177}\text{Lu}$ -labeled GRP-R agonist for systemic radiotherapy in human tissues. *Clin Exp Metastasis* 2008; 26:105.

Tornesello AL, Tornesello ML, Buonaguro FM. An Overview of Bioactive Peptides for in vivo Imaging and Therapy in Human Diseases. *Mini Rev Med Chem*. 2017; 17:758-770.

Umbricht CA, Benešová M, Schmid RM, Türler A, Schibli R, Meulen NP van der, et al.  $^{44}\text{Sc}$ -PSMA-617 for radiotheragnostics in tandem with  $^{177}\text{Lu}$ -PSMA-617-preclinical investigations in comparison with  $^{68}\text{Ga}$ -PSMA-11 and  $^{68}\text{Ga}$ -PSMA-617. *EJNMMI Res* 2017; 7:9.

Valdovinos HF, Hernandez R, Barnhart TE, Graves S, Cai W, Nickles RJ. Separation of cyclotron-produced  $^{44}\text{Sc}$  from a natural calcium target using a dipentyl pentylphosphonate functionalized extraction resin. *Appl Radiat Isot* 2015; 95:23-29.

van der Meulen NP, Bunka M, Domnanich KA, Müller C, Haller S, Vermeulen C, et al. Cyclotron production of  $^{44}\text{Sc}$ : From bench to bedside. *Nucl Med Biol* 2015; 42:745-751.

Wilson AA, Jin L, Garcia A, Dasilva JN, Houle S. An Admonition When Measuring the Lipophilicity of Radiotracers Using Counting Techniques. *Appl Radiat Isot* 2001; 54:203-208.

Yang Y-S, Zhang X, Xiong Z, Chen X. Comparative in vitro and in vivo evaluation of two  $^{64}\text{Cu}$ -labeled bombesin analogs in a mouse model of human prostate adenocarcinoma. *Nucl Med Biol* 2006; 33:371–80.

Zhang J, Niu G, Fan X, et al. PET Using a GRPR Antagonist  $^{68}\text{Ga}$ -RM26 in Healthy Volunteers and Prostate Cancer Patients. *J Nucl Med*. 2018; 59:922-928.

## Chapter 6

### Conclusion

---

Radioisotopes of scandium present a great opportunity for the development and future applications of radionuclides in theranostics. Two IAEA coordinated research projects (CRP) reports released in 2021 demonstrate the large interest in emerging radioisotopes of scandium for diagnostic and therapeutic medicine (IAEA, 2021a, 2021b). These reports detail several direct and indirect production routes, provide details on radionuclide extraction, and explore initial radiolabelling experiments with chelators, in order to facilitate the development of international expertise in the production of these radionuclides and their use in nuclear medicine. The work in this thesis focuses on the radionuclide  $^{44}\text{Sc}$  and expands on earlier work by detailing the production and evaluation of this radionuclide for preclinical PET. A local production programme for  $^{44}\text{Sc}$  was developed to ensure reliable supply of this radionuclide for preclinical research activities, including phantom and *in vivo* imaging. Radionuclide production was achieved through proton irradiation of natural calcium targets and measured radionuclide yields were compared with several strategies for radionuclide yield prediction. Phantom imaging studies were the first measurements of  $^{44}\text{Sc}$  carried out in standardized NEMA image quality phantoms to quantify imaging performance of this radionuclide. Furthermore, the production and extraction process employed for  $^{44}\text{Sc}$  demonstrated sufficient quality to enable peptide radiolabelling and *in vivo* imaging studies of cancer models in mice. This, in turn allowed for the comparison of the image quality of  $^{44}\text{Sc}$  with the more widespread, and chemically similar, PET radionuclide  $^{68}\text{Ga}$ . The approach taken in this thesis can be generalized and applied to other emerging radionuclides when evaluating their production and imaging applications.

A conventional approach for predicting thick target radionuclide yield for a variety of production routes uses calculations based on experimental cross-section data from EXFOR complemented with semi-empirical cross-section data derived from models such as TENDL; several codes have been written to facilitate these calculations, including GUIs such as the one presented Appendix A and the recent IAEA MIB (Ferguson et al., 2017; Koning and Verpelli, 2020; Sitarz et al., 2019). In Chapter 3, this approach is compared with yield predictions using the Monte Carlo simulation package Geant4 and yield measurements from proton irradiation of thick calcium metal targets to quantify radionuclide yield and

radionuclidic purity. Recent developments in the modelling of low energy hadronic interactions through the incorporation of TENDL cross-sections below 200 MeV has sparked interest in using Monte Carlo simulations for radionuclide yield predictions (Amin et al., 2018; Poignant et al., 2016; Ratcliffe and Edgecock, 2017). It is desirable to determine if Monte Carlo codes such as Geant4 can accurately predict radionuclide yield as this would promote confidence in modelling capabilities for applications with low energy proton beams, such as the online monitoring of proton beam therapy through detection of radionuclide production which has been the topic of recent research (Ferrero et al., 2018; Kraan et al., 2015; Paganetti and El Fakhri, 2015). Experimental measurements of thick target yields for radioisotopes of scandium ( $^{43}\text{Sc}$ ,  $^{44\text{g,m}}\text{Sc}$ ,  $^{46}\text{Sc}$ ,  $^{47}\text{Sc}$ , and  $^{48}\text{Sc}$ ) as well as  $^{47}\text{Ca}$  were made over the range of 12 MeV to 18 MeV to enable comparisons with predictive yield calculation approaches; while several measurements of radionuclide yield have been made in enriched calcium carbonate target, this data presents some of the first data for certain radionuclides (i.e.  $^{46}\text{Sc}$ ) in metallic calcium targets. Overall, Geant4 was found to predict the yield of several nuclides within 10 %, including  $^{46}\text{Sc}$ ,  $^{47}\text{Sc}$  and  $^{48}\text{Sc}$ ;  $^{46}\text{Sc}$  is a contaminant of particular interest due to its 83.8 day half-life. Some limitations of Geant4 were exposed, such as the inability to calculate the yield of radionuclides with isomeric states; this will have to be addressed in future code developments for simulations to be of use for yield calculations. The IAEA MIB, which combines recommended cross-section data and TENDL-2017 data, provides very similar predictions, demonstrating significant improvements in the recent Geant4 modelling developments of low energy proton interactions. Finally, while the production of  $^{44}\text{Sc}$  from the proton-induced reaction on enriched  $^{44}\text{Ca}$  targets provides a well validated approach to high yields and radionuclidic purity, the many production routes of  $^{43}\text{Sc}$  and  $^{47}\text{Sc}$  continue to be investigated (Misiak et al., 2017; Sitarz et al., 2018; Szkliniarz et al., 2016; Walczak et al., 2015).

Reconstructed image quality is affected by the choice of radionuclide used in the PET study and imaging performance must be quantified for novel radionuclides. The work presented in Chapter 4 builds on the previous work by Bunka et al., who imaged a Derenzo phantom in a preclinical PET scanner and subsequently ranked radionuclides in terms of increasing resolution based on the FWHM measurement of the 1.3mm hot rod:  $^{68}\text{Ga} < ^{44}\text{Sc} < ^{89}\text{Zr} < ^{11}\text{C} < ^{64}\text{Cu} < ^{18}\text{F}$  (Bunka et al., 2016). This present work employed three different phantoms to quantify imaging performance on the Siemens Inveon small-animal PET scanner, including the first published measurements in the NEMA image quality phantom. The NEMA NU-4 2008 phantom procedure was adapted to quantify the recovery coefficients (RC) of the radionuclides in rods of diameter varying from 1 to 5 mm, as well as the spill-over ratio (SOR) in air and water (NEMA, 2008). The RC and SORs in water were correlated to the end-point energy of the positron

emitters, and a similar relation to Bunka et al. was determined: the long-range positron emitter  $^{68}\text{Ga}$  was found to have lower RC and greater SORs than the short-range positron emitters  $^{64}\text{Cu}$  and  $^{18}\text{F}$ , with  $^{44}\text{Sc}$  offering intermediate behaviour, independent of the reconstruction algorithm used. The greater RC of  $^{44}\text{Sc}$  was confirmed by Rosar et al. in their subsequent comparison of  $^{44}\text{Sc}$  and  $^{68}\text{Ga}$  on two different pre-clinical PET platforms (Rosar et al., 2020).

Measuring the effect of different radionuclides on standard imaging performance metrics using the NEMA NU 4-2008 protocol was first adapted by Disselhorst et al. (Disselhorst et al., 2010). While it has served as a useful standardized tool for radionuclide comparisons, the NEMA protocol's intended purpose was to establish a baseline of system performance that could be applied across different scanner configurations using the standard radionuclide  $^{18}\text{F}$ . To compare nuclides with more complex decay schemes, a dedicated procedure for quantifying radionuclide-dependent imaging performance should be identified. This would require adapting the procedure to study the differences brought about due to physical decay properties of the radionuclides, including half-life, positron emission energy and branching ratio, and prompt  $\gamma$ -rays. For example, measurements of SOR are unreliable in water for long range positron emitters for the current cavity diameters, as many counts collected in these regions are the result of positron annihilations rather than scatter. Further, Hallen et al. provide a thoughtful critique of the NEMA NU 4-2008 methodology, including the use of filtered backprojection (FBP) which can lead to artifacts in the reconstructed images (Hallen et al., 2020). While FBP is a standard image reconstruction algorithm that is implemented on many scanners, imaging studies often employ iterative reconstruction methods to obtain improved image quality. A phantom imaging procedure to compare these iterative algorithms on the same scanner would provide relevant information about image resolution and other relevant parameters obtained in imaging studies with different radionuclides.

Beyond phantom imaging, the work presented in Chapter 5 expands on the use of cyclotron produced  $^{44}\text{Sc}$  for radiotracer labelling and preclinical imaging. Radiolabelled peptides have demonstrated great utility in novel applications for theranostics (Baum et al., 2012; Chatalic et al., 2015). Expanding the radionuclides available for these studies is advantageous; for example, the longer half-life of  $^{44}\text{Sc}$  (3.97 h) as compared to  $^{68}\text{Ga}$  (68 min) allows for more complex radiolabelling procedures, and imaging at later timepoints post-injection. However, it is important to quantify changes in tracer properties and pharmacokinetics when they are bound to different radionuclides. For example biodistribution experiments with bombesin agonists decorated with  $^{177}\text{Lu}$  and  $^{90}\text{Y}$  demonstrated significant differences, while biodistribution was more comparable for the same tracer bound to  $^{68}\text{Ga}$  and  $^{44}\text{Sc}$  (Koumariou et

al., 2012, 2009). As such, this study builds on previous work to compare the properties of a novel metabolically stabilized bombesin analog when radiolabelled with either  $^{68}\text{Ga}$  or  $^{44}\text{Sc}$ . It was confirmed that the proton irradiation of metallic calcium targets and extraction via UTEVA resin is a simple production scheme that is adequate for providing high yields of  $^{44}\text{Sc}$  with sufficient radiochemical purity for preclinical research studies. The metabolically stabilized bombesin analog for targeting GRPR was radiolabelled in high yields and radiochemical purity with either  $^{44}\text{Sc}$  or  $^{68}\text{Ga}$ , the latter obtained from a radionuclide generator. *In vitro* studies demonstrated that the bound radiometal has no effect on lipophilicity of the resulting radiopeptide, while differences in the binding affinity with the GRPR were observed. *In vivo* imaging studies were performed in MCF7 and PC3 xenografts in mouse models, which are derived from breast cancer and prostate cancer cell lines, respectively. In the well studied PC3 cells, high tumor uptake and retention was observed, which was greater for the radiometal-labelled BBN2 derivatives as compared to  $^{18}\text{F}$ -labelled BBN2 derivatives previously reported (Richter et al., 2013). The previous finding from Koumarianou were confirmed as similar uptake between the  $^{68}\text{Ga}$ - and  $^{44}\text{Sc}$ -labelled bombesin derivatives was demonstrated (Koumarianou et al., 2012). While no measurable effect of radiometal on biodistribution was found in our studies, the similarities of the radiometal labelled tracers in this thesis demonstrate that radioscandium could be an interesting surrogate for therapies which currently employ  $^{68}\text{Ga}$  as a diagnostic nuclide for PET imaging studies. Future development of therapies incorporating  $^{47}\text{Sc}$  radiolabelled compounds would benefit from  $^{44}\text{Sc}$  imaging studies to predict absorbed doses and monitor patient response to therapy.

Many areas for future research with radioscandium isotopes remain. In their recent summary of advancements in the production, chemistry and imaging of radioscandium isotopes, Mikolajczak et al. emphasize the need for standardized procedures for evaluating the quality of the radionuclide precursor used for radiolabelling (Mikolajczak et al., 2021). The authors use the example from the European Pharmacopoeia monographs for  $^{177}\text{Lu}$ ,  $^{90}\text{Y}$ , and  $^{68}\text{Ga}$  to outline some potential quality specifications which could be proposed for radioscandium precursors. It is currently difficult to develop exact specifications due to the varied production routes currently being explored. However, the establishment of specific quality control procedures could help facilitate the transition for use of radioscandium into human studies.

While the research presented in this thesis is focused on the production and imaging of  $^{44}\text{Sc}$ ,  $^{43}\text{Sc}$  may ultimately be more a more desirable isotope for clinical translation because of both the absence of the high-energy co-emitted 1157 keV photon and the lower positron end-point energy. Together, these will

likely prove advantageous for patient dosimetry, radiation safety and image resolution (Domnanich et al., 2017a). However, the high-energy prompt  $\gamma$  enables  $^{44}\text{Sc}$  to have a unique role in emerging imaging applications for non-pure positron emitters, including  $\gamma$ -PET and multi-tracer PET (also known as dual-isotope PET (DIPET))(Conti and Eriksson, 2016; Kadrmas and Hoffman, 2013; Thirolf et al., 2015).

$\gamma$ -PET is a group of techniques that looks to improve PET imaging performance with  $\beta+\gamma$  emitter by using the additional information gained from the additional prompt gamma in the reconstruction procedure. For example, Grignon et al. proposed a technique to improve spatial resolution of PET by using a  $\beta+\gamma$  emitter, and demonstrated that a spatial resolution of 2.3 mm could be obtained by combining a micro-PET scanner with LSO crystals, which detect the annihilation photons, with a liquid xenon Compton telescope to detect the additional prompt gamma and its emission angle (Grignon et al., 2007). Lang et al. also studied the potential of the  $\gamma$ -PET technique using a Compton cone (Lang et al., 2014); this was done with simulations in Geant4 to look at the potential of this reconstruction strategy, which demonstrated the potential for submillimeter resolution. Beyond advantages in resolution, Thirolf et al. suggest that this technique can greatly reduce acquisition time by increasing sensitivity and lead to quasi-real time imaging (Thirolf et al., 2015). Furthermore, Yoshida et al. developed a prototype for  $\gamma$ -PET imaging, and demonstrated a resolution of 5mm for a scan with  $^{44}\text{Sc}$  with a PET detector ring diameter of 21.4 cm (Yoshida et al., 2020). With these promising results,  $^{44}\text{Sc}$  could be an ideal radionuclide to perform these imaging studies and further validate this technique.

On the other hand, multi-tracer imaging has been proposed as a method to simultaneously acquire two sets of data corresponding to co-injected tracers simultaneously imaging different processes. In their review summarizing developments of multi-tracer imaging in PET, Kadrmas and Hoffman outline several physiologic imaging targets and accompanying tracers: glucose metabolism ( $[^{11}\text{C}]$ glucose,  $[^{18}\text{F}]$ FDG), cellular proliferation ( $[^{11}\text{C}]$ thymidine,  $[^{18}\text{F}]$ fluorothymidine), blood flow and perfusion ( $[^{13}\text{N}]$ ammonia,  $[^{82}\text{Rb}]$ rubidium chloride) and hypoxia ( $[^{18}\text{F}]$ fluoromisonidazole) (Kadrmas and Hoffman, 2013).

Information gained from studies of different physiologic processes can provide additional information helpful in diagnosis; for example, it was found by Halter et al. that in the staging of bronchial carcinomas, imaging glucose metabolism with  $[^{18}\text{F}]$ FDG provided a higher sensitivity (95 %) but lower specificity (71 %) than imaging cellular proliferation with  $[^{18}\text{F}]$ FLT (86 % sensitive, 100 % specific) (Halter et al., 2004). As such,  $[^{18}\text{F}]$ FLT could help identify false-positive results on  $[^{18}\text{F}]$ FDG which often result from inflammation by providing complementary information about cellular proliferation.

In SPECT, multi-tracer imaging can be accomplished by radiolabelling tracers with radionuclides that emit photons at different energies; the counts originating from each tracer can be distinguished by employing different energy windows. For multi-tracer PET, energy discrimination would not be sufficient to differentiate tracers as all annihilation photons detected for the creation of the PET image have an energy of 511 keV. Initially, techniques for multi-tracer imaging relying on different radioactive half-lives of tracers were used, as well as multi-tracer compartment modelling and staggered injection techniques (Kadrmas and Hoffman, 2013). First proposed in 2011 by Andreyev et al., a novel technique paired radionuclides that decay by  $\beta^+$  decay and emit high-energy prompt  $\gamma$ -rays with pure positron emitters; the spatial extent of the  $\beta^+$   $\gamma$  emitter is deduced from the distribution of detected 511 keV photon pairs that are coincident with prompt gammas, which is scaled and subtracted from a larger dataset of all coincident annihilation photons to recover the spatial distribution of the pure positron emitter (Andreyev and Celler, 2011). This was first studied in GATE simulations and preclinical phantoms by pairing the pure positron emitter  $^{18}\text{F}$  with  $^{22}\text{Na}$  (1275 keV, 100 %) and  $^{60}\text{Cu}$  (1332 keV, 88 %), but  $^{44}\text{Sc}$  was identified as a potential radionuclide for use in multi-tracer imaging studies due to its high positron branching ratio (94 %) and high abundance prompt gammas (1157 keV, 99 %) (Andreyev et al., 2012; Miyaoka et al., 2011). This was further expanded on by Fukuchi et al, who used a similar subtraction technique to perform preclinical imaging of mice with  $^{18}\text{F}$ -FDG and  $^{44\text{m}}\text{Sc}$  to demonstrate the use of this technique *in vivo* (Fukuchi et al., 2021). The greater availability of  $^{44}\text{Sc}$  in coordination with basic scanner modifications could facilitate further research to incorporate the results and demonstrate the utility of the multi-tracer imaging paradigm.

Prompt gamma can facilitate  $\gamma$ -PET imaging and multi-tracer PET, but they also cause spurious coincidences contributing to noise in the reconstructed image (Conti and Eriksson, 2016; Martin et al., 1995). Many studies have investigated prompt gamma corrections (PGC) to account for spurious coincidences, however most of these concentrate on specific radionuclides, such as  $^{124}\text{I}$  (602 keV – 62.9%, 1691 keV – 11.2 %),  $^{82}\text{Rb}$  (777 keV – 15.1%),  $^{76}\text{Br}$  (559 keV – 74.0 %, 657 keV – 15.9 %), and  $^{86}\text{Y}$  (1077 keV – 82.5 %, 627 keV – 32.6 %). Many studies have explored quantification of these prompt gammas for specific radionuclides, as well as the removal of these using various strategies such as fitting the radial tail of sinograms, scaling the random coincidence estimate, convoluting the activity distribution with an attenuation-dependent kernel, and Monte Carlo simulations (Anizan et al., 2012; Beattie et al., 2003; Braad et al., 2015; Buchholz et al., 2003; Esteves et al., 2010; Hong et al., 2015; Laforest et al., 2002; Laforest and Liu, 2009; Lubberink et al., 2002; Lubberink and Herzog, 2011; Pentlow et al., 1996; Preylowski et al., 2013). Specific techniques for PGC based on sinogram tail fitting have been

patented and assigned to PET scanner manufacturers such as Siemens Medical Solutions USA Inc (Hayden, JR. et al., 2008). While these approaches have been diverse, further study is warranted for  $^{44}\text{Sc}$  as both the energy of the prompt gamma as well as the relative abundance compared to the positron branching ratio are different than the radionuclides that have been analyzed. In their study of  $^{44}\text{Sc}$  in a commercial PET scanner, Lima et al. determined that the available scatter correction and prompt-gamma correction were insufficient for obtaining recovery coefficients within the recommended range (Lima et al., 2020). A recent study by Rosar et al. investigating the impact of prompt gammas for quantification of  $^{44}\text{Sc}$  PET demonstrated that activity recovery was underestimated in PET systems by up to 27 % (Rosar et al., 2021). The authors suggest that quantitative accuracy could be recovered using a constant correction factor which must be determined individually for each PET scanner and reconstruction setting. Future research is warranted to determine the accuracy of this approach for varying imaging geometries and comparisons should be made with other PGCs.

A large body of evidence has been accumulated with the conclusion of the IAEA CRPs which has demonstrated the benefits and challenges for the development of radioscandium isotopes for use in diagnostic and therapeutic medicine (IAEA, 2021a, 2021b). While further *in vivo* imaging and dosimetry studies are required to build on this evidence, radioscandium isotopes already play an important role in exploring and establishing the theranostic paradigm, which holds great promise to improve future treatment options for the benefit of our patients.

## Bibliography

---

- Abel, E.P., Domnanich, K., Clause, H.K., Kalman, C., Walker, W., Shusterman, J.A., Greene, J., Gott, M., Severin, G.W., 2020. Production, Collection, and Purification of  $^{47}\text{Ca}$  for the Generation of  $^{47}\text{Sc}$  through Isotope Harvesting at the National Superconducting Cyclotron Laboratory. *ACS Omega* 5, 27864–27872. <https://doi.org/10.1021/acsomega.0c03020>
- Abiraj, K., Mansi, R., Tamma, M.-L., Forrer, F., Cescato, R., Reubi, J.C., Akyel, K.G., Maecke, H.R., 2010. Tetraamine-Derived Bifunctional Chelators for Technetium-99m Labelling: Synthesis, Bioconjugation and Evaluation as Targeted SPECT Imaging Probes for GRP-Receptor-Positive Tumours. *Chem. – Eur. J.* 16, 2115–2124. <https://doi.org/10.1002/chem.200902011>
- Afshar-Oromieh, A., Hetzheim, H., Kratochwil, C., Benesova, M., Eder, M., Neels, O.C., Eisenhut, M., Kübler, W., Holland-Letz, T., Giesel, F.L., Mier, W., Kopka, K., Haberkorn, U., 2015. The Theranostic PSMA Ligand PSMA-617 in the Diagnosis of Prostate Cancer by PET/CT: Biodistribution in Humans, Radiation Dosimetry, and First Evaluation of Tumor Lesions. *J. Nucl. Med.* 56, 1697–1705. <https://doi.org/10.2967/jnumed.115.161299>
- Agostinelli, S., Allison, J., Amako, K., Apostolakis, J., Araujo, H., Arce, P., Asai, M., Axen, D., Banerjee, S., Barrand, G., Behner, F., Bellagamba, L., Boudreau, J., Broglia, L., Brunengo, A., Burkhardt, H., Chauvie, S., Chuma, J., Chytracsek, R., Cooperman, G., Cosmo, G., Degtyarenko, P., Dell'Acqua, A., Depaola, G., Dietrich, D., Enami, R., Feliciello, A., Ferguson, C., Fesefeldt, H., Folger, G., Foppiano, F., Forti, A., Garelli, S., Giani, S., Giannitrapani, R., Gibin, D., Gómez Cadenas, J.J., González, I., Gracia Abril, G., Greeniaus, G., Greiner, W., Grichine, V., Grossheim, A., Guatelli, S., Gumplinger, P., Hamatsu, R., Hashimoto, K., Hasui, H., Heikkinen, A., Howard, A., Ivanchenko, V., Johnson, A., Jones, F.W., Kallenbach, J., Kanaya, N., Kawabata, M., Kawabata, Y., Kawaguti, M., Kelner, S., Kent, P., Kimura, A., Kodama, T., Kokoulin, R., Kossov, M., Kurashige, H., Lamanna, E., Lampén, T., Lara, V., Lefebvre, V., Lei, F., Liendl, M., Lockman, W., Longo, F., Magni, S., Maire, M., Medernach, E., Minamimoto, K., Mora de Freitas, P., Morita, Y., Murakami, K., Nagamatu, M., Nartallo, R., Nieminen, P., Nishimura, T., Ohtsubo, K., Okamura, M., O'Neale, S., Oohata, Y., Paech, K., Perl, J., Pfeiffer, A., Pia, M.G., Ranjard, F., Rybin, A., Sadilov, S., Di Salvo, E., Santin, G., Sasaki, T., Savvas, N., Sawada, Y., Scherer, S., Sei, S., Sirotenko, V., Smith, D., Starkov, N., Stoecker, H., Sulkimo, J., Takahata, M., Tanaka, S., Tcherniaev, E., Safai Tehrani, E., Tropeano, M., Truscott, P., Uno, H., Urban, L., Urban, P., Verderi, M., Walkden, A., Wander, W., Weber, H., Wellisch, J.P., Wenaus, T., Williams, D.C., Wright, D., Yamada, T., Yoshida, H., Zschesche, D.,

2003. Geant4—a simulation toolkit. *Nucl. Instrum. Methods Phys. Res. Sect. Accel. Spectrometers Detect. Assoc. Equip.* 506, 250–303. [https://doi.org/10.1016/S0168-9002\(03\)01368-8](https://doi.org/10.1016/S0168-9002(03)01368-8)
- Alliot, C., Kerdjoudj, R., Michel, N., Haddad, F., Huclier-Markai, S., 2015. Cyclotron production of high purity  $^{44}\text{m},^{44}\text{Sc}$  with deuterons from  $^{44}\text{CaCO}_3$  targets. *Nucl. Med. Biol.* 42, 524–529. <https://doi.org/10.1016/j.nucmedbio.2015.03.002>
- Alva-Sánchez, H., Quintana-Bautista, C., Martínez-Dávalos, A., Ávila-Rodríguez, M.A., Rodríguez-Villafuerte, M., 2016. Positron range in tissue-equivalent materials: experimental microPET studies. *Phys. Med. Biol.* 61, 6307. <https://doi.org/10.1088/0031-9155/61/17/6307>
- Amin, T., Infantino, A., Barlow, R., Hoehr, C., 2018. Validating production of PET radionuclides in solid and liquid targets: Comparing Geant4 predictions with FLUKA and measurements. *Appl. Radiat. Isot.* 133, 61–67. <https://doi.org/10.1016/j.apradiso.2017.12.009>
- Andreyev, A., Celler, A., 2011. Dual-isotope PET using positron-gamma emitters. *Phys. Med. Biol.* 56, 4539. <https://doi.org/10.1088/0031-9155/56/14/020>
- Andreyev, A., Sitek, A., Celler, A., 2012. EM reconstruction of Dual Isotope PET with staggered injections and prompt gamma positron emitters, in: 2012 IEEE Nuclear Science Symposium and Medical Imaging Conference Record (NSS/MIC). Presented at the 2012 IEEE Nuclear Science Symposium and Medical Imaging Conference Record (NSS/MIC), pp. 3701–3706. <https://doi.org/10.1109/NSSMIC.2012.6551850>
- Anizan, N., Carlier, T., Hindorf, C., Barbet, J., Bardiès, M., 2012. dAcquisition setting optimization and quantitative imaging for  $^{124}\text{I}$  studies with the Inveon microPET-CT system. *EJNMMI Res.* 2, 7. <https://doi.org/10.1186/2191-219X-2-7>
- Auger, M., Braccini, S., Carzaniga, T.S., Ereditato, A., Nesteruk, K.P., Scampoli, P., 2016. A detector based on silica fibers for ion beam monitoring in a wide current range. *J. Instrum.* 11, P03027–P03027. <https://doi.org/10.1088/1748-0221/11/03/P03027>
- Baratto, L., Duan, H., Mäcke, H., Iagaru, A., 2020. Imaging the Distribution of Gastrin-Releasing Peptide Receptors in Cancer. *J. Nucl. Med. Off. Publ. Soc. Nucl. Med.* 61, 792–798. <https://doi.org/10.2967/jnumed.119.234971>
- Bateman, H., 1910. The solution of a system of differential equations occurring in the theory of radioactive transformations, in: *Proc. Cambridge Philos. Soc.* pp. 423–427.

- Baum, R.P., Kulkarni, H.R., 2012. THERANOSTICS: From Molecular Imaging Using Ga-68 Labeled Tracers and PET/CT to Personalized Radionuclide Therapy - The Bad Berka Experience. *Theranostics* 2, 437–447. <https://doi.org/10.7150/thno.3645>
- Baum, R.P., Kulkarni, H.R., Carreras, C., 2012. Peptides and Receptors in Image-Guided Therapy: Theranostics for Neuroendocrine Neoplasms. *Semin. Nucl. Med., Theranostics* 42, 190–207. <https://doi.org/10.1053/j.semnuclmed.2012.01.002>
- Beattie, B.J., Finn, R.D., Rowland, D.J., Pentlow, K.S., 2003. Quantitative imaging of bromine-76 and yttrium-86 with PET: A method for the removal of spurious activity introduced by cascade gamma rays. *Med. Phys.* 30, 2410–2423. <https://doi.org/10.1118/1.1595599>
- Benoit, L., 2010. The National University Reactor shutdown and the future of medical isotopes production and research in Canada. Standing Committee on Natural Resources, Ottawa, Canada.
- Bensinger, S.J., Christofk, H.R., 2012. New aspects of the Warburg effect in cancer cell biology. *Semin. Cell Dev. Biol., Cancer Cell Metabolism & Notch Signaling* 23, 352–361. <https://doi.org/10.1016/j.semcdb.2012.02.003>
- Berger, M.J., Hubbell, J.H., Seltzer, S.M., Chang, J., Coursey, J.S., Sukumar, R., Zucker, D.S., Olsen, K., 2010. XCOM: Photon Cross Section Database (version 1.5) [WWW Document]. *Natl. Inst. Stand. Technol.* URL <http://physics.nist.gov/xcom> (accessed 6.23.21).
- Bethe, H., Heitler, W., Dirac, P.A.M., 1934. On the stopping of fast particles and on the creation of positive electrons. *Proc. R. Soc. Lond. Ser. Contain. Pap. Math. Phys. Character* 146, 83–112. <https://doi.org/10.1098/rspa.1934.0140>
- Bodei, L., Ferrari, M., Nunn, A., Llull, J., Cremonesi, M., Martano, L., Laurora, G., Scardino, E., Tiberini, S., Bufi, G., others, 2007. Lu-177-AMBA bombesin analogue in hormone refractory prostate cancer patients: a phase I escalation study with single-cycle administrations, in: *European Journal of Nuclear Medicine and Molecular Imaging*. SPRINGER 233 SPRING STREET, NEW YORK, NY 10013 USA, pp. S221–S221.
- Braad, P.E.N., Hansen, S.B., Thisgaard, H., Høilund-Carlsen, P.F., 2015. PET imaging with the non-pure positron emitters: 55 Co, 86 Y and 124 I. *Phys. Med. Biol.* 60, 3479. <https://doi.org/10.1088/0031-9155/60/9/3479>
- Buchholz, H.G., Herzog, H., Förster, G.J., Reber, H., Nickel, O., Rösch, F., Bartenstein, P., 2003. PET imaging with yttrium-86: comparison of phantom measurements acquired with different PET

- scanners before and after applying background subtraction. *Eur. J. Nucl. Med. Mol. Imaging* 30, 716–720. <https://doi.org/10.1007/s00259-002-1112-y>
- Bunka, M., Müller, C., Vermeulen, C., Haller, S., Türlér, A., Schibli, R., van der Meulen, N.P., 2016. Imaging quality of  $^{44}\text{Sc}$  in comparison with five other PET radionuclides using Derenzo phantoms and preclinical PET. *Appl. Radiat. Isot.* 110, 129–133. <https://doi.org/10.1016/j.apradiso.2016.01.006>
- C. High Performance Liquid Chromatography (HPLC), 2020. . Truro School in Cornwall.
- CADTH, 2021. The Canadian Medical Imaging Inventory, 2019–2020. *Canadian Journal of Health Technologies*.
- Cal-González, J., Herraiz, J.L., España, S., Corzo, P.M.G., Vaquero, J.J., Desco, M., Udias, J.M., 2013. Positron range estimations with PeneloPET. *Phys. Med. Biol.* 58, 5127. <https://doi.org/10.1088/0031-9155/58/15/5127>
- Carney, J.P.J., Townsend, D.W., Rappoport, V., Bendriem, B., 2006. Method for transforming CT images for attenuation correction in PET/CT imaging. *Med. Phys.* 33, 976–983. <https://doi.org/10.1118/1.2174132>
- Carroll, R.E., Matkowskyj, K.A., Tretiakova, M.S., Battey, J.F., Benya, R.V., 2000. Gastrin-releasing Peptide Is a Mitogen and a Morphogen in Murine Colon Cancer. *Cell Growth Differ.* 11, 385–393.
- Carzaniga, T.S., Auger, M., Braccini, S., Bunka, M., Ereditato, A., Nesteruk, K.P., Scampoli, P., Türlér, A., van der Meulen, N., 2017. Measurement of  $^{43}\text{Sc}$  and  $^{44}\text{Sc}$  production cross-section with an 18MeV medical PET cyclotron. *Appl. Radiat. Isot.* 129, 96–102. <https://doi.org/10.1016/j.apradiso.2017.08.013>
- Carzaniga, T.S., Braccini, S., 2019. Cross-section measurement of  $^{44\text{m}}\text{Sc}$ ,  $^{47}\text{Sc}$ ,  $^{48}\text{Sc}$  and  $^{47}\text{Ca}$  for an optimized  $^{47}\text{Sc}$  production with an 18 MeV medical PET cyclotron. *Appl. Radiat. Isot.* 143, 18–23. <https://doi.org/10.1016/j.apradiso.2018.10.015>
- Chakravarty, R., Goel, S., Valdovinos, H.F., Hernandez, R., Hong, H., Nickles, R.J., Cai, W., 2014. Matching the Decay Half-Life with the Biological Half-Life: ImmunoPET Imaging with  $^{44}\text{Sc}$ -Labeled Cetuximab Fab Fragment. *Bioconjug. Chem.* 25, 2197–2204. <https://doi.org/10.1021/bc500415x>
- Champion, C., Loirec, C.L., 2007. Positron follow-up in liquid water: II. Spatial and energetic study for the most important radioisotopes used in PET. *Phys. Med. Biol.* 52, 6605. <https://doi.org/10.1088/0031-9155/52/22/004>
- Champion, C., Loirec, C.L., 2006. Positron follow-up in liquid water: I. A new Monte Carlo track-structure code. *Phys. Med. Biol.* 51, 1707. <https://doi.org/10.1088/0031-9155/51/7/005>

- Champion, C., Quinto, M.A., Morgat, C., Zanotti-Fregonara, P., Hindié, E., 2016. Comparison between Three Promising  $\beta$ -emitting Radionuclides,  $^{67}\text{Cu}$ ,  $^{47}\text{Sc}$  and  $^{161}\text{Tb}$ , with Emphasis on Doses Delivered to Minimal Residual Disease. *Theranostics* 6, 1611–1618.  
<https://doi.org/10.7150/thno.15132>
- Chatalic, K.L.S., Kwekkeboom, D.J., Jong, M. de, 2015. Radiopeptides for Imaging and Therapy: A Radiant Future. *J. Nucl. Med.* 56, 1809–1812. <https://doi.org/10.2967/jnumed.115.161158>
- Chiappara, D., 2019. Preliminary modelling for the Proton Boron Capture Therapy (PBCT) [WWW Document]. URL <http://tesi.cab.unipd.it/62579/> (accessed 11.8.20).
- Cives, M., Strosberg, J., 2017. Radionuclide Therapy for Neuroendocrine Tumors. *Curr. Oncol. Rep.* 19, 9.  
<https://doi.org/10.1007/s11912-017-0567-8>
- Coenen, H.H., Gee, A.D., Adam, M., Antoni, G., Cutler, C.S., Fujibayashi, Y., Jeong, J.M., Mach, R.H., Mindt, T.L., Pike, V.W., Windhorst, A.D., 2017. Consensus nomenclature rules for radiopharmaceutical chemistry — Setting the record straight. *Nucl. Med. Biol.* 55, v–xi.  
<https://doi.org/10.1016/j.nucmedbio.2017.09.004>
- Conti, M., Eriksson, L., 2016. Physics of pure and non-pure positron emitters for PET: a review and a discussion. *EJNMMI Phys.* 3, 8. <https://doi.org/10.1186/s40658-016-0144-5>
- Dalm, S.U., Bakker, I.L., Blois, E. de, Doeswijk, G.N., Konijnenberg, M.W., Orlandi, F., Barbato, D., Tedesco, M., Maina, T., Nock, B.A., Jong, M. de, 2017.  $^{68}\text{Ga}/^{177}\text{Lu}$ -NeoBOMB1, a Novel Radiolabeled GRPR Antagonist for Theranostic Use in Oncology. *J. Nucl. Med.* 58, 293–299.  
<https://doi.org/10.2967/jnumed.116.176636>
- Dalm, S.U., Martens, J.W., Sieuwerts, A.M., Van, C.D., Koelewijn, S.J., De, E.B., Maina, T., Nock, B.A., Brunel, L., Fehrentz, J.A., Martinez, J., De, M.J., Melis, M., 2015. In vitro and in vivo application of radiolabeled gastrin-releasing peptide receptor ligands in breast cancer. *J. Nucl. Med. Off. Publ. Soc. Nucl. Med.* 56, 752–757. <https://doi.org/10.2967/jnumed.114.153023>
- deKemp, R.A., Klein, R., Beanlands, R.S.B., 2016.  $^{82}\text{Rb}$  PET imaging of myocardial blood flow—have we achieved the 4 “R”s to support routine use? *EJNMMI Res.* 6, 69.  
<https://doi.org/10.1186/s13550-016-0225-4>
- Disselhorst, J.A., Brom, M., Laverman, P., Slump, C.H., Boerman, O.C., Oyen, W.J.G., Gotthardt, M., Visser, E.P., 2010. Image-Quality Assessment for Several Positron Emitters Using the NEMA NU 4-2008 Standards in the Siemens Inveon Small-Animal PET Scanner. *J. Nucl. Med.* 51, 610–617.  
<https://doi.org/10.2967/jnumed.109.068858>

- Domnanich, K.A., Eichler, R., Müller, C., Jordi, S., Yakusheva, V., Braccini, S., Behe, M., Schibli, R., Türlér, A., van der Meulen, N.P., 2017a. Production and separation of  $^{43}\text{Sc}$  for radiopharmaceutical purposes. *EJNMMI Radiopharm. Chem.* 2, 14. <https://doi.org/10.1186/s41181-017-0033-9>
- Domnanich, K.A., Müller, C., Benešová, M., Dressler, R., Haller, S., Köster, U., Ponsard, B., Schibli, R., Türlér, A., van der Meulen, N.P., 2017b.  $^{47}\text{Sc}$  as useful  $\beta^-$ -emitter for the radiotheragnostic paradigm: a comparative study of feasible production routes. *EJNMMI Radiopharm. Chem.* 2, 5. <https://doi.org/10.1186/s41181-017-0024-x>
- Domnanich, K.A., Müller, C., Farkas, R., Schmid, R.M., Ponsard, B., Schibli, R., Türlér, A., van der Meulen, N.P., 2016.  $^{44}\text{Sc}$  for labeling of DOTA- and NODAGA-functionalized peptides: preclinical in vitro and in vivo investigations. *EJNMMI Radiopharm. Chem.* 1, 8. <https://doi.org/10.1186/s41181-016-0013-5>
- Eckerman, K., Endo, A., 2008. ICRP Publication 107. Nuclear decay data for dosimetric calculations. *Ann. ICRP* 38, 7–96. <https://doi.org/10.1016/j.icrp.2008.10.004>
- Eigner, S., Vera, D.R.B., Fellner, M., Loktionova, N.S., Piel, M., Lebeda, O., Rösch, F., Roß, T.L., Henke, K.E., 2013. Imaging of Protein Synthesis: In Vitro and In Vivo Evaluation of  $^{44}\text{Sc}$ -DOTA-Puromycin. *Mol. Imaging Biol.* 15, 79–86. <https://doi.org/10.1007/s11307-012-0561-3>
- Eppard, E., de la Fuente, A., Benešová, M., Khawar, A., Bundschuh, R.A., Gärtner, F.C., Kreppel, B., Kopka, K., Essler, M., Rösch, F., 2017. Clinical Translation and First In-Human Use of [ $^{44}\text{Sc}$ ]Sc-PSMA-617 for PET Imaging of Metastasized Castrate-Resistant Prostate Cancer. *Theranostics* 7, 4359–4369. <https://doi.org/10.7150/thno.20586>
- Esteves, F.P., Nye, J.A., Khan, A., Folks, R.D., Halkar, R.K., Garcia, E.V., Schuster, D.M., Lerakis, S., Raggi, P., Votaw, J.R., 2010. Prompt-gamma compensation in Rb-82 myocardial perfusion 3D PET/CT. *J. Nucl. Cardiol.* 17, 247–253. <https://doi.org/10.1007/s12350-009-9170-1>
- Fahey, F.H., 2002. Data Acquisition in PET Imaging. *J. Nucl. Med. Technol.* 30, 39–49.
- Fani, M., Maecke, H.R., Okarvi, S.M., 2012. Radiolabeled Peptides: Valuable Tools for the Detection and Treatment of Cancer. *Theranostics* 2, 481–501. <https://doi.org/10.7150/thno.4024>
- Fassbender, M., Arzumanov, A., Jamriska, D.J., Lyssukhin, S.N., Trelle, H., Waters, L.S., 2007. Proton beam simulation with MCNPX: Gallium metal activation estimates below 30MeV relevant to the bulk production of  $^{68}\text{Ge}$  and  $^{65}\text{Zn}$ . *Nucl. Instrum. Methods Phys. Res. Sect. B Beam Interact. Mater. At., The Application of Accelerators in Research and Industry* 261, 742–746. <https://doi.org/10.1016/j.nimb.2007.03.099>

- Ferguson, S., Jans, H.-S., Wuest, M., Riauka, T., Wuest, F., 2019. Comparison of scandium-44 g with other PET radionuclides in pre-clinical PET phantom imaging. *EJNMMI Phys.* 6, 23.  
<https://doi.org/10.1186/s40658-019-0260-0>
- Ferguson, S., Riauka, T., Jans, H., Gagnon, K., Engle, J.W., Barnhart, T.E., Nortier, F.M., O'Neil, J.P., Birnbaum, E.R., Gangon, K.M., 2017. Radionuclide production calculations: A GUI to determine irradiation conditions. *AIP Conf. Proc.* 1845, 020008. <https://doi.org/10.1063/1.4983539>
- Ferrero, V., Fiorina, E., Morrocchi, M., Pennazio, F., Baroni, G., Battistoni, G., Belcari, N., Camarlinghi, N., Ciocca, M., Del Guerra, A., Donetti, M., Giordanengo, S., Giraudo, G., Patera, V., Peroni, C., Rivetti, A., Rolo, M.D. da R., Rossi, S., Rosso, V., Sportelli, G., Tampellini, S., Valvo, F., Wheadon, R., Cerello, P., Bisogni, M.G., 2018. Online proton therapy monitoring: clinical test of a Silicon-photodetector-based in-beam PET. *Sci. Rep.* 8, 4100. <https://doi.org/10.1038/s41598-018-22325-6>
- Fukuchi, T., Shigeta, M., Haba, H., Mori, D., Yokokita, T., Komori, Y., Yamamoto, S., Watanabe, Y., 2021. Image reconstruction method for dual-isotope positron emission tomography. *J. Instrum.* 16, P01035–P01035. <https://doi.org/10.1088/1748-0221/16/01/P01035>
- Gagnon, K., Jensen, M., Thisgaard, H., Publicover, J., Lapi, S., McQuarrie, S.A., Ruth, T.J., 2011. A new and simple calibration-independent method for measuring the beam energy of a cyclotron. *Appl. Radiat. Isot.* 69, 247–253. <https://doi.org/10.1016/j.apradiso.2010.09.012>
- García Garayoa, E., Rüegg, D., Bläuenstein, P., Zwimpfer, M., Khan, I.U., Maes, V., Blanc, A., Beck-Sickinger, A.G., Tourwé, D.A., Schubiger, P.A., 2007. Chemical and biological characterization of new  $\text{Re}(\text{CO})_3/[^{99\text{m}}\text{Tc}](\text{CO})_3$  bombesin analogues. *Nucl. Med. Biol.* 34, 17–28.  
<https://doi.org/10.1016/j.nucmedbio.2006.10.004>
- Gnesin, S., Mitsakis, P., Cicone, F., Deshayes, E., Dunet, V., Gallino, A.F., Kosinski, M., Baechler, S., Buchegger, F., Viertl, D., Prior, J.O., 2017. First in-human radiation dosimetry of  $^{68}\text{Ga}$ -NODAGA-RGDyK. *EJNMMI Res.* 7, 43. <https://doi.org/10.1186/s13550-017-0288-x>
- Goertzen, A.L., Bao, Q., Bergeron, M., Blankemeyer, E., Blinder, S., Cañadas, M., Chatziioannou, A.F., Dinelle, K., Elhami, E., Jans, H.-S., Lage, E., Lecomte, R., Sossi, V., Surti, S., Tai, Y.-C., Vaquero, J.J., Vicente, E., Williams, D.A., Laforest, R., 2012. NEMA NU 4-2008 Comparison of Preclinical PET Imaging Systems. *J. Nucl. Med.* 53, 1300–1309. <https://doi.org/10.2967/jnumed.111.099382>
- Goertzen, A.L., Thiessen, J.D., 2017. PET instrumentation, in: *Physics of PET and SPECT Imaging*. CRC Press.

- Goodman, P.C., 1995. The new light: discovery and introduction of the X-ray. *Am. J. Roentgenol.* 165, 1041–1045. <https://doi.org/10.2214/ajr.165.5.7572473>
- Gracheva, N., Müller, C., Talip, Z., Heinitz, S., Köster, U., Zeevaart, J.R., Vögele, A., Schibli, R., van der Meulen, N.P., 2019. Production and characterization of no-carrier-added <sup>161</sup>Tb as an alternative to the clinically-applied <sup>177</sup>Lu for radionuclide therapy. *EJNMMI Radiopharm. Chem.* 4, 12. <https://doi.org/10.1186/s41181-019-0063-6>
- Grignon, C., Barbet, J., Bardiès, M., Carlier, T., Chatal, J.F., Couturier, O., Cussonneau, J.P., Faivre, A., Ferrer, L., Girault, S., Haruyama, T., Le Ray, P., Luquin, L., Lupone, S., Métivier, V., Morteau, E., Servagent, N., Thers, D., 2007. Nuclear medical imaging using  $\beta+\gamma$  coincidences from <sup>44</sup>Sc radionuclide with liquid xenon as detection medium. *Nucl. Instrum. Methods Phys. Res. Sect. Accel. Spectrometers Detect. Assoc. Equip., Proceedings of the 1st International Conference on Molecular Imaging Technology* 571, 142–145. <https://doi.org/10.1016/j.nima.2006.10.048>
- Gruber, L., Jiménez-Franco, L.D., Decristoforo, C., Uprimny, C., Glatting, G., Hohenberger, P., Schoenberg, S.O., Reindl, W., Orlandi, F., Mariani, M., Jaschke, W., Virgolini, I., 2020. MITIGATE-NeoBOMB1, a Phase I/IIa Study to Evaluate Safety, Pharmacokinetics, and Preliminary Imaging of <sup>68</sup>Ga-NeoBOMB1, a Gastrin-Releasing Peptide Receptor Antagonist, in GIST Patients. *J. Nucl. Med.* 61, 1749–1755. <https://doi.org/10.2967/jnumed.119.238808>
- Gugger, M., Reubi, J.C., 1999. Gastrin-Releasing Peptide Receptors in Non-Neoplastic and Neoplastic Human Breast. *Am. J. Pathol.* 155, 2067–2076. [https://doi.org/10.1016/S0002-9440\(10\)65525-3](https://doi.org/10.1016/S0002-9440(10)65525-3)
- Hallen, P., Schug, D., Schulz, V., 2020. Comments on the NEMA NU 4-2008 Standard on Performance Measurement of Small Animal Positron Emission Tomographs. *EJNMMI Phys.* 7, 12. <https://doi.org/10.1186/s40658-020-0279-2>
- Halter, G., Buck, A.K., Schirrmeister, H., Wurziger, I., Liewald, F., Glatting, G., Neumaier, B., Sunder-Plassmann, L., Reske, S.N., Hetzel, M., 2004. [<sup>18</sup>F] 3-deoxy-3'-fluorothymidine positron emission tomography: alternative or diagnostic adjunct to 2-[<sup>18</sup>F]-fluoro-2-deoxy-d-glucose positron emission tomography in the workup of suspicious central focal lesions? *J. Thorac. Cardiovasc. Surg.* 127, 1093–1099. <https://doi.org/10.1016/j.jtcvs.2003.09.003>
- Hayden, JR., C.H., Casey, M.E., Watson, C.C., 2008. Prompt gamma correction for non-standard isotopes in a pet scanner. US20080283758A1.
- Hernandez, R., Valdovinos, H.F., Yang, Y., Chakravarty, R., Hong, H., Barnhart, T.E., Cai, W., 2014. <sup>44</sup>Sc: An Attractive Isotope for Peptide-Based PET Imaging. *Mol. Pharm.* 11, 2954–2961. <https://doi.org/10.1021/mp500343j>

- Hoehr, C., Oehlke, E., Benard, F., Lee, C.J., Hou, X., Badesso, B., Ferguson, S., Miao, Q., Yang, H., Buckley, K., Hanemaayer, V., Zeisler, S., Ruth, T., Celler, A., Schaffer, P., 2014. 44gSc production using a water target on a 13 MeV cyclotron. *Nucl. Med. Biol.* 41, 401–406.  
<https://doi.org/10.1016/j.nucmedbio.2013.12.016>
- Hohla, F., Schally, A.V., 2010. Targeting gastrin releasing peptide receptors: New options for the therapy and diagnosis of cancer. *Cell Cycle* 9, 1738–1741. <https://doi.org/10.4161/cc.9.9.11347>
- Hong, I., Rothfuss, H., Fürst, S., Michel, C., Nekolla, S.G., Bendriem, B., Casey, M., 2015. Prompt Gamma Correction for Ga-68 PSMA PET studies, in: 2015 IEEE Nuclear Science Symposium and Medical Imaging Conference (NSS/MIC). Presented at the 2015 IEEE Nuclear Science Symposium and Medical Imaging Conference (NSS/MIC), pp. 1–2.  
<https://doi.org/10.1109/NSSMIC.2015.7582166>
- Hou, X., Vuckovic, M., Buckley, K., Bénard, F., Schaffer, P., Ruth, T., Celler, A., 2014. Graphical user interface for yield and dose estimations for cyclotron-produced technetium. *Phys. Med. Biol.* 59, 3337. <https://doi.org/10.1088/0031-9155/59/13/3337>
- Huclier-Markai, S., Alliot, C., Kerdjoudj, R., Mougin-Degraef, M., Chouin, N., Haddad, F., 2018. Promising Scandium Radionuclides for Nuclear Medicine: A Review on the Production and Chemistry up to *In Vivo* Proofs of Concept. *Cancer Biother. Radiopharm.* 33, 316–329.  
<https://doi.org/10.1089/cbr.2018.2485>
- Huclier-Markai, S., Kerdjoudj, R., Alliot, C., Bonraisin, A.C., Michel, N., Haddad, F., Barbet, J., 2014. Optimization of reaction conditions for the radiolabeling of DOTA and DOTA-peptide with 44m/44Sc and experimental evidence of the feasibility of an in vivo PET generator. *Nucl. Med. Biol.* 41, Supplement, e36–e43. <https://doi.org/10.1016/j.nucmedbio.2013.11.004>
- IAEA, 2021a. Production of Emerging Radionuclides towards Theranostic Applications: Copper-61, Scandium-43 and -44, and Yttrium-86, TECDOC Series. INTERNATIONAL ATOMIC ENERGY AGENCY, Vienna.
- IAEA, 2021b. Therapeutic Radiopharmaceuticals Labelled with Copper-67, Rhenium-186 and Scandium-47. INTL ATOMIC ENERGY AGENCY, S.I.
- IAEA, 2019. Gallium-68 Cyclotron Production. IAEA, Vienna.
- IAEA, 2001. Charged Particle Cross-Section Database for Medical Radioisotope Production: Diagnostic Radioisotopes and Monitor Reactions.
- IAEA, n.d. Cyclotrons used for Radionuclide Production [WWW Document]. IAEA Accel. Knowl. Portal. URL <https://nucleus.iaea.org/sites/accelerators> (accessed 6.1.21).

- Infantino, A., Cicoria, G., Pancaldi, D., Ciarmatori, A., Boschi, S., Fanti, S., Marengo, M., Mostacci, D., 2011. Prediction of  $^{89}\text{Zr}$  production using the Monte Carlo code FLUKA. *Appl. Radiat. Isot.*, Proceedings of the 6th CHERNE Workshop 69, 1134–1137.  
<https://doi.org/10.1016/j.apradiso.2010.11.027>
- Jammal, R., 2017. Safety and Security of Supply of Medical Isotope Production.
- Jødal, L., Loirec, C.L., Champion, C., 2012. Positron range in PET imaging: an alternative approach for assessing and correcting the blurring. *Phys. Med. Biol.* 57, 3931. <https://doi.org/10.1088/0031-9155/57/12/3931>
- Kadmas, D.J., Hoffman, J.M., 2013. Methodology for Quantitative Rapid Multi-Tracer PET Tumor Characterizations. *Theranostics* 3, 757–773. <https://doi.org/10.7150/thno.5201>
- Kassis, A.I., 2008. Therapeutic Radionuclides: Biophysical and Radiobiologic Principles. *Semin. Nucl. Med.* 38, 358–366. <https://doi.org/10.1053/j.semnuclmed.2008.05.002>
- Kelkar, S.S., Reineke, T.M., 2011. Theranostics: Combining Imaging and Therapy. *Bioconjug. Chem.* 22, 1879–1903. <https://doi.org/10.1021/bc200151q>
- Khawar, A., Eppard, E., Sinnes, J.P., Roesch, F., Ahmadzadehfar, H., Kürpig, S., Meisenheimer, M., Gaertner, F.C., Essler, M., Bundschuh, R.A., 2018a. [ $^{44}\text{Sc}$ ]Sc-PSMA-617 Biodistribution and Dosimetry in Patients With Metastatic Castration-Resistant Prostate Carcinoma. *Clin. Nucl. Med.* 43, 323–330. <https://doi.org/10.1097/RLU.0000000000002003>
- Khawar, A., Eppard, E., Sinnes, J.P., Roesch, F., Ahmadzadehfar, H., Kürpig, S., Meisenheimer, M., Gaertner, F.C., Essler, M., Bundschuh, R.A., 2018b. Prediction of Normal Organ Absorbed Doses for [ $^{177}\text{Lu}$ ]Lu-PSMA-617 Using [ $^{44}\text{Sc}$ ]Sc-PSMA-617 Pharmacokinetics in Patients With Metastatic Castration Resistant Prostate Carcinoma. *Clin. Nucl. Med.* 43, 486–491.  
<https://doi.org/10.1097/RLU.0000000000002102>
- Kinahan, P.E., Townsend, D.W., Beyer, T., Sashin, D., 1998. Attenuation correction for a combined 3D PET/CT scanner. *Med. Phys.* 25, 2046–2053. <https://doi.org/10.1118/1.598392>
- Klein, O., Nishina, Y., 1928. The Scattering of Light by Free Electrons according to Dirac's New Relativistic Dynamics. *Nature* 122, 398–399. <https://doi.org/10.1038/122398b0>
- Koning, A., Verpelli, M., 2020. The medical isotope browser. *Trends Radiopharm. ISTR-2019 Proc. Int. Symp. Programme Abstr.*
- Koning, A.J., Rochman, D., Sublet, J.-Ch., Dzysiuk, N., Fleming, M., van der Marck, S., 2019. TENDL: Complete Nuclear Data Library for Innovative Nuclear Science and Technology. *Nucl. Data*

- Sheets, Special Issue on Nuclear Reaction Data 155, 1–55.  
<https://doi.org/10.1016/j.nds.2019.01.002>
- Koumarianou, E., Loktionova, N.S., Fellner, M., Roesch, F., Thews, O., Pawlak, D., Archimandritis, S.C., Mikolajczak, R., 2012. 44Sc-DOTA-BN[2-14]NH<sub>2</sub> in comparison to 68Ga-DOTA-BN[2-14]NH<sub>2</sub> in pre-clinical investigation. Is 44Sc a potential radionuclide for PET? *Appl. Radiat. Isot.* 70, 2669–2676. <https://doi.org/10.1016/j.apradiso.2012.08.004>
- Koumarianou, E., Mikołajczak, R., Pawlak, D., Zikos, X., Bouziotis, P., Garnuszek, P., Karczmarczyk, U., Maurin, M., Archimandritis, S.C., 2009. Comparative study on DOTA-derivatized bombesin analog labeled with 90Y and 177Lu: in vitro and in vivo evaluation. *Nucl. Med. Biol.* 36, 591–603. <https://doi.org/10.1016/j.nucmedbio.2009.03.006>
- Kraan, A.C., Battistoni, G., Belcari, N., Camarlinghi, N., Ciocca, M., Ferrari, A., Ferretti, S., Mairani, A., Molinelli, S., Pullia, M., Sala, P., Sportelli, G., Del Guerra, A., Rosso, V., 2015. Online monitoring for proton therapy: A real-time procedure using a planar PET system. *Nucl. Instrum. Methods Phys. Res. Sect. Accel. Spectrometers Detect. Assoc. Equip.* 786, 120–126. <https://doi.org/10.1016/j.nima.2015.03.059>
- Krasnov, N.N., 1974. Thick target yield. *Int. J. Appl. Radiat. Isot.* 25, 223–227. [https://doi.org/10.1016/0020-708X\(74\)90031-3](https://doi.org/10.1016/0020-708X(74)90031-3)
- Kumar, K., 2020. The Current Status of the Production and Supply of Gallium-68. *Cancer Biother. Radiopharm.* 35, 163–166. <https://doi.org/10.1089/cbr.2019.3301>
- Laforest, R., Liu, X., 2009. Cascade removal and microPET imaging with 76 Br. *Phys. Med. Biol.* 54, 1503. <https://doi.org/10.1088/0031-9155/54/6/008>
- Laforest, R., Rowland, D.J., Welch, M.J., 2002. MicroPET imaging with nonconventional isotopes. *IEEE Trans. Nucl. Sci.* 49, 2119–2126. <https://doi.org/10.1109/TNS.2002.803685>
- Lampe, N., Karamitros, M., Breton, V., Brown, J.M.C., Kyriakou, I., Sakata, D., Sarramia, D., Incerti, S., 2018a. Mechanistic DNA damage simulations in Geant4-DNA part 1: A parameter study in a simplified geometry. *Phys. Med.* 48, 135–145. <https://doi.org/10.1016/j.ejmp.2018.02.011>
- Lampe, N., Karamitros, M., Breton, V., Brown, J.M.C., Sakata, D., Sarramia, D., Incerti, S., 2018b. Mechanistic DNA damage simulations in Geant4-DNA Part 2: Electron and proton damage in a bacterial cell. *Phys. Med.* 48, 146–155. <https://doi.org/10.1016/j.ejmp.2017.12.008>
- Lang, C., Habs, D., Parodi, K., Thirolf, P.G., 2014. Sub-millimeter nuclear medical imaging with high sensitivity in positron emission tomography using  $\beta^+\gamma$  coincidences. *J. Instrum.* 9, P01008–P01008. <https://doi.org/10.1088/1748-0221/9/01/P01008>

- Lecomte, R., 2009. Novel detector technology for clinical PET. *Eur. J. Nucl. Med. Mol. Imaging* 36, 69–85.  
<https://doi.org/10.1007/s00259-008-1054-0>
- Lehnert, W., Gregoire, M.-C., Reilhac, A., Meikle, S.R., 2011. Analytical positron range modelling in heterogeneous media for PET Monte Carlo simulation. *Phys. Med. Biol.* 56, 3313.  
<https://doi.org/10.1088/0031-9155/56/11/009>
- Levin, C.S., Hoffman, E.J., 1999. Calculation of positron range and its effect on the fundamental limit of positron emission tomography system spatial resolution. *Phys. Med. Biol.* 44, 781.  
<https://doi.org/10.1088/0031-9155/44/3/019>
- Levkovskij, V.N., Levkovskij, A., 1991. Activation cross section nuclides of average masses ( $A=40-100$ ) by protons and alpha-particles with average energies ( $E=10-50$  MeV). *Cs Protons Alphas Mosc.*
- Li, L., Jaraquemada-Peláez, M. de G., Aluicio-Sarduy, E., Wang, X., E. Barnhart, T., Cai, W., Radchenko, V., Schaffer, P., W. Engle, J., Orvig, C., 2020. Coordination chemistry of [Y(pypa)] – and comparison immuno-PET imaging of [  $^{44}\text{Sc}$  ]Sc- and [  $^{86}\text{Y}$  ]Y-pypa-phenyl-TRC105. *Dalton Trans.* 49, 5547–5562. <https://doi.org/10.1039/D0DT00437E>
- Lima, T.V.M., Gnesin, S., Nitzsche, E., Ortega, P.G., Müller, C., van der Meulen, N.P., 2020. First Phantom-Based Quantitative Assessment of Scandium-44 Using a Commercial PET Device. *Front. Phys.* 8.  
<https://doi.org/10.3389/fphy.2020.00241>
- Liolios, C., Buchmuller, B., Bauder-Wüst, U., Schäfer, M., Leotta, K., Haberkorn, U., Eder, M., Kopka, K., 2018. Monomeric and Dimeric  $^{68}\text{Ga}$ -Labeled Bombesin Analogues for Positron Emission Tomography (PET) Imaging of Tumors Expressing Gastrin-Releasing Peptide Receptors (GRPrs). *J. Med. Chem.* 61, 2062–2074. <https://doi.org/10.1021/acs.jmedchem.7b01856>
- Ljungberg, M., Strand, S.-E., King, M.A., 2012. *Monte Carlo Calculations in Nuclear Medicine, Second Edition: Applications in Diagnostic Imaging.* CRC Press.
- Lougheed, T., 2012. Uncertainties shroud medical isotope supply. *CMAJ Can. Med. Assoc. J.* 184, E567–E568. <https://doi.org/10.1503/cmaj.109-4217>
- Loveless, C.S., Lapi, S.E., 2020. Production of Therapeutic Radionuclides, in: *Handbook of Radiopharmaceuticals.* John Wiley & Sons, Ltd, pp. 89–105.  
<https://doi.org/10.1002/9781119500575.ch5>
- Loveless, C.S., Radford, L.L., Ferran, S.J., Queern, S.L., Shepherd, M.R., Lapi, S.E., 2019. Photonuclear production, chemistry, and in vitro evaluation of the theranostic radionuclide  $^{47}\text{Sc}$ . *EJNMMI Res.* 9, 42. <https://doi.org/10.1186/s13550-019-0515-8>

- Lubberink, M., Herzog, H., 2011. Quantitative imaging of  $^{124}\text{I}$  and  $^{86}\text{Y}$  with PET. *Eur. J. Nucl. Med. Mol. Imaging* 38, 10. <https://doi.org/10.1007/s00259-011-1768-2>
- Lubberink, M., Schneider, H., m, M.B., Lundqvist, H., 2002. Quantitative imaging and correction for cascade gamma radiation of  $^{76}\text{Br}$  with 2D and 3D PET. *Phys. Med. Biol.* 47, 3519–3534. <https://doi.org/10.1088/0031-9155/47/19/306>
- Maina, T., Bergsma, H., Kulkarni, H.R., Mueller, D., Charalambidis, D., Krenning, E.P., Nock, B.A., de Jong, M., Baum, R.P., 2016. Preclinical and first clinical experience with the gastrin-releasing peptide receptor-antagonist [ $^{68}\text{Ga}$ ]SB3 and PET/CT. *Eur. J. Nucl. Med. Mol. Imaging* 43, 964–973. <https://doi.org/10.1007/s00259-015-3232-1>
- Maisey, M.N., 2005. Positron Emission Tomography in Clinical Medicine, in: Bailey, D.L., Townsend, D.W., Valk, P.E., Maisey, M.N. (Eds.), *Positron Emission Tomography: Basic Sciences*. Springer, London, pp. 1–12. [https://doi.org/10.1007/1-84628-007-9\\_1](https://doi.org/10.1007/1-84628-007-9_1)
- Mamtimin, M., Harmon, F., Starovoitova, V.N., 2015. Sc-47 production from titanium targets using electron linacs. *Appl. Radiat. Isot.* 102, 1–4. <https://doi.org/10.1016/j.apradiso.2015.04.012>
- Marco, M., Antonella, C., Ettore, S., 2019. Peptide receptor radionuclide therapy after NETTER-1 clinical trial: what should not be left behind. *Clin. Transl. Imaging* 7, 155–157. <https://doi.org/10.1007/s40336-019-00327-2>
- Martin, C.C., Christian, B.T., Satter, M.R., Nickerson, L.D.H., Nickles, R.J., 1995. Quantitative PET with positron emitters that emit prompt gamma rays. *IEEE Trans. Med. Imaging* 14, 681–687. <https://doi.org/10.1109/42.476109>
- Martinuk, S., Meyer, T., 2013. The use of positron emission tomography (PET) for cancer care across Canada: Time for a national strategy. *J. Nucl. Med.* 54, 1302–1302.
- McQuade, P., McCarthy, D.W., Welch, M.J., 2005. Metal Radionuclides for PET Imaging, in: MACPSEM, D.L.B., ARCP (London), FIPEM, PD, D.W.T.Bs., FRACP, P.E.V.M., BS, FRCR, M.N.M.M., BSc, FRCP (Eds.), *Positron Emission Tomography*. Springer London, pp. 237–250. [https://doi.org/10.1007/1-84628-007-9\\_11](https://doi.org/10.1007/1-84628-007-9_11)
- Mikolajczak, R., Huclier-Markai, S., Alliot, C., Haddad, F., Szikra, D., Forgacs, V., Garnuszek, P., 2021. Production of scandium radionuclides for theranostic applications: towards standardization of quality requirements. *EJNMMI Radiopharm. Chem.* 6, 19. <https://doi.org/10.1186/s41181-021-00131-2>

- Minegishi, K., Nagatsu, K., Fukada, M., Suzuki, H., Ohya, T., Zhang, M.-R., 2016. Production of scandium-43 and -47 from a powdery calcium oxide target via the  $\text{nat}/^{44}\text{Ca}(\alpha, x)$ -channel. *Appl. Radiat. Isot.* 116, 8–12. <https://doi.org/10.1016/j.apradiso.2016.07.017>
- Misiak, R., Walczak, R., Wąs, B., Bartyzel, M., Mietelski, J.W., Bilewicz, A., 2017.  $^{47}\text{Sc}$  production development by cyclotron irradiation of  $^{48}\text{Ca}$ . *J. Radioanal. Nucl. Chem.* 313, 429–434. <https://doi.org/10.1007/s10967-017-5321-z>
- Miyaoka, R.S., Hunter, W.C.J., Andreyev, A., Pierce, L., Lewellen, T.K., Celler, A., Kinahan, P.E., 2011. Dual-radioisotope PET data acquisition and analysis, in: 2011 IEEE Nuclear Science Symposium Conference Record. Presented at the 2011 IEEE Nuclear Science Symposium Conference Record, pp. 3780–3783. <https://doi.org/10.1109/NSSMIC.2011.6153715>
- Morgat, C., MacGrogan, G., Brouste, V., Vélasco, V., Sévenet, N., Bonnefoi, H., Fernandez, P., Debled, M., Hindié, E., 2017. Expression of Gastrin-Releasing Peptide Receptor in Breast Cancer and Its Association with Pathologic, Biologic, and Clinical Parameters: A Study of 1,432 Primary Tumors. *J. Nucl. Med.* 58, 1401–1407. <https://doi.org/10.2967/jnumed.116.188011>
- Moses, W.W., 2011. Fundamental limits of spatial resolution in PET. *Nucl. Instrum. Methods Phys. Res. Sect. Accel. Spectrometers Detect. Assoc. Equip., NIMA\_4th International Conference on Imaging techniques in Subatomic Physics, Astrophysics, Medicine, Biology and Industry 648, Supplement 1, S236–S240.* <https://doi.org/10.1016/j.nima.2010.11.092>
- Müller, C., Bunka, M., Haller, S., Köster, U., Groehn, V., Bernhardt, P., Meulen, N. van der, Türler, A., Schibli, R., 2014a. Promising Prospects for  $^{44}\text{Sc}/^{47}\text{Sc}$ -Based Theragnostics: Application of  $^{47}\text{Sc}$  for Radionuclide Tumor Therapy in Mice. *J. Nucl. Med.* 55, 1658–1664. <https://doi.org/10.2967/jnumed.114.141614>
- Müller, C., Bunka, M., Haller, S., Köster, U., Groehn, V., Bernhardt, P., Meulen, N. van der, Türler, A., Schibli, R., 2014b. Promising Prospects for  $^{44}\text{Sc}/^{47}\text{Sc}$ -Based Theragnostics: Application of  $^{47}\text{Sc}$  for Radionuclide Tumor Therapy in Mice. *J. Nucl. Med.* 55, 1658–1664. <https://doi.org/10.2967/jnumed.114.141614>
- Müller, C., Bunka, M., Reber, J., Fischer, C., Zhernosekov, K., Türler, A., Schibli, R., 2013. Promises of Cyclotron-Produced  $^{44}\text{Sc}$  as a Diagnostic Match for Trivalent  $\beta^-$ -Emitters: In Vitro and In Vivo Study of a  $^{44}\text{Sc}$ -DOTA-Folate Conjugate. *J. Nucl. Med.* 54, 2168–2174. <https://doi.org/10.2967/jnumed.113.123810>

- Müller, C., Domnanich, K.A., Umbricht, C.A., van der Meulen, N.P., 2018. Scandium and terbium radionuclides for radiotheranostics: current state of development towards clinical application. *Br. J. Radiol.* 20180074. <https://doi.org/10.1259/bjr.20180074>
- Nagy, G., Dénes, N., Kis, A., Szabó, J.P., Berényi, E., Garai, I., Bai, P., Hajdu, I., Szikra, D., Trencsényi, G., 2017. Preclinical evaluation of melanocortin-1 receptor (MC1-R) specific <sup>68</sup>Ga- and <sup>44</sup>Sc-labeled DOTA-NAPamide in melanoma imaging. *Eur. J. Pharm. Sci.* 106, 336–344. <https://doi.org/10.1016/j.ejps.2017.06.026>
- Nardo, L.D., Pupillo, G., Mou, L., Furlanetto, D., Rosato, A., Esposito, J., Meléndez-Alafort, L., 2021. Preliminary dosimetric analysis of DOTA-folate radiopharmaceutical radiolabelled with <sup>47</sup>Sc produced through natV(p,x)<sup>47</sup>Sc cyclotron irradiation. *Phys. Med. Biol.* 66, 025003. <https://doi.org/10.1088/1361-6560/abc811>
- National Nuclear Data Center, n.d. Nudat 2 database v.2.8 [WWW Document]. URL <https://www.nndc.bnl.gov/nudat2/> (accessed 6.1.20a).
- National Nuclear Data Center, n.d. Medical Internal Radiation Dose (MIRD) Database [WWW Document]. URL <https://www.nndc.bnl.gov/nudat2/mird/index.jsp> (accessed 6.1.21b).
- Natural Resources Canada, 2013. Details on Transfer Payment Programs (Exceeding \$5 million during the reporting year) [WWW Document]. URL <https://www.nrcan.gc.ca/nrcan/transparency/reporting-accountability/plans-performance-reports/details-transfer-payment-programs-exceeding-5-million-during-reporting-year/11578> (accessed 6.1.21).
- NEMA, 2018. NEMA Standard Publication NU 2-2018: Performance measurements of positron emission tomographs (PET). Rosslyn, VA.
- NEMA, 2008. NEMA Standard Publication NU 4-2008: Performance Measurements of Small Animal Positron Emission Tomographs. National Electrical Manufacturers Association, Rosslyn, VA.
- Opalinska, M., Hubalewska-Dydejczyk, A., Sowa-Staszczak, A., 2017. Radiolabeled peptides: current and new perspectives. *Q. J. Nucl. Med. Mol. Imaging Off. Publ. Ital. Assoc. Nucl. Med. AIMN Int. Assoc. Radiopharmacol. IAR Sect. Soc. Of* 61, 153–167. <https://doi.org/10.23736/S1824-4785.17.02971-5>
- Otuka, N., Dupont, E., Semkova, V., Pritychenko, B., Blokhin, A.I., Aikawa, M., Babykina, S., Bossant, M., Chen, G., Dunaeva, S., Forrest, R.A., Fukahori, T., Furutachi, N., Ganesan, S., Ge, Z., Gritzay, O.O., Herman, M., Hlavač, S., Katō, K., Lalremruata, B., Lee, Y.O., Makinaga, A., Matsumoto, K., Mikhaylyukova, M., Pikulina, G., Pronyaev, V.G., Saxena, A., Schwerer, O., Simakov, S.P.,

- Soppera, N., Suzuki, R., Takács, S., Tao, X., Taova, S., Tárkányi, F., Varlamov, V.V., Wang, J., Yang, S.C., Zerkin, V., Zhuang, Y., 2014. Towards a More Complete and Accurate Experimental Nuclear Reaction Data Library (EXFOR): International Collaboration Between Nuclear Reaction Data Centres (NRDC). *Nucl. Data Sheets* 120, 272–276. <https://doi.org/10.1016/j.nds.2014.07.065>
- Otuka, N., Takács, S., 2015. Definitions of radioisotope thick target yields. *Radiochim. Acta* 103, 1–6. <https://doi.org/10.1515/ract-2013-2234>
- Paganetti, H., El Fakhri, G., 2015. Monitoring proton therapy with PET. *Br. J. Radiol.* 88, 20150173. <https://doi.org/10.1259/bjr.20150173>
- Parry, J.J., Andrews, R., Rogers, B.E., 2007. MicroPET Imaging of Breast Cancer Using Radiolabeled Bombesin Analogs Targeting the Gastrin-releasing Peptide Receptor. *Breast Cancer Res. Treat.* 101, 175–183. <https://doi.org/10.1007/s10549-006-9287-8>
- Patel, O., Shulkes, A., Baldwin, G.S., 2006. Gastrin-releasing peptide and cancer. *Biochim. Biophys. Acta BBA - Rev. Cancer* 1766, 23–41. <https://doi.org/10.1016/j.bbcan.2006.01.003>
- Pentlow, K.S., Graham, M.C., Lambrecht, R.M., Daghighian, F., Bacharach, S.L., Bendriem, B., Finn, R.D., Jordan, K., Kalaigian, H., Karp, J.S., Robeson, W.R., Larson, S.M., 1996. Quantitative Imaging of Iodine-124 with PET. *J. Nucl. Med.* 37, 1557–1562.
- Poignant, F., Penfold, S., Asp, J., Takhar, P., Jackson, P., 2016. GEANT4 simulation of cyclotron radioisotope production in a solid target. *Phys. Med.* 32, 728–734. <https://doi.org/10.1016/j.ejmp.2016.04.006>
- Preylowski, V., Schlögl, S., Schoenahl, F., Jörg, G., Samnick, S., Buck, A.K., Lassmann, M., 2013. Is the Image Quality of I-124-PET Impaired by an Automatic Correction of Prompt Gammas? *PLoS ONE* 8. <https://doi.org/10.1371/journal.pone.0071729>
- Pruszyński, M., Laktionova, N.S., Filosofov, D.V., Rösch, F., 2010. Post-elution processing of <sup>44</sup>Ti/<sup>44</sup>Sc generator-derived <sup>44</sup>Sc for clinical application. *Appl. Radiat. Isot.* 68, 1636–1641. <https://doi.org/10.1016/j.apradiso.2010.04.003>
- Pruszyński, M., Majkowska-Pilip, A., Laktionova, N.S., Eppard, E., Roesch, F., 2012. Radiolabeling of DOTATOC with the long-lived positron emitter <sup>44</sup>Sc. *Appl. Radiat. Isot.* 70, 974–979. <https://doi.org/10.1016/j.apradiso.2012.03.005>
- Pujatti, P.B., Massicano, A.V.F., Mengatti, J., de Araújo, E.B., 2012. Preparation of [<sup>111</sup>In]-labeled-DTPA-bombesin conjugates at high specific activity and stability: Evaluation of labeling parameters and potential stabilizers. *Appl. Radiat. Isot.* 70, 856–863. <https://doi.org/10.1016/j.apradiso.2012.02.064>

- Qi, J., Leahy, R.M., 2006. Iterative reconstruction techniques in emission computed tomography. *Phys. Med. Biol.* 51, R541–R578. <https://doi.org/10.1088/0031-9155/51/15/R01>
- Radchenko, V., Engle, J.W., Medvedev, D.G., Maassen, J.M., Naranjo, C.M., Unc, G.A., Meyer, C.A.L., Mastren, T., Brugh, M., Mausner, L., Cutler, C.S., Birnbaum, E.R., John, K.D., Nortier, F.M., Fassbender, M.E., 2017. Proton-induced production and radiochemical isolation of  $^{44}\text{Ti}$  from scandium metal targets for  $^{44}\text{Ti}/^{44}\text{Sc}$  generator development. *Nucl. Med. Biol.* 50, 25–32. <https://doi.org/10.1016/j.nucmedbio.2017.03.006>
- Rane, S., Harris, J.T., Starovoitova, V.N., 2015.  $^{47}\text{Ca}$  production for  $^{47}\text{Ca}/^{47}\text{Sc}$  generator system using electron linacs. *Appl. Radiat. Isot.* 97, 188–192. <https://doi.org/10.1016/j.apradiso.2014.12.020>
- Rang, H.P., 2006. The receptor concept: pharmacology's big idea. *Br. J. Pharmacol.* 147, S9–S16. <https://doi.org/10.1038/sj.bjp.0706457>
- Ratcliffe, N., Barlow, R., Bungau, A., Bungau, C., Cywinski, R., 2013. GEANT4 Target Simulations for Low Energy Medical Applications, in: *Proceedings of the 4th International Particle Accelerator Conference*. JACoW, Shanghai, China, pp. 3717–3719.
- Ratcliffe, N., Edgecock, T.R., 2017. A Study of Potential Accelerator Production of Radioisotopes for Both Diagnostics and Therapy 3.
- Reubi, J., Gugger, M., Waser, B., 2002. Co-expressed peptide receptors in breast cancer as a molecular basis for in vivo multireceptor tumour targeting. *Eur. J. Nucl. Med. Mol. Imaging* 29, 855–862. <https://doi.org/10.1007/s00259-002-0794-5>
- Richter, S., Wuest, M., Bergman, C.N., Krieger, S., Rogers, B.E., Wuest, F., 2016. Metabolically Stabilized  $^{68}\text{Ga}$ -NOTA-Bombesin for PET Imaging of Prostate Cancer and Influence of Protease Inhibitor Phosphoramidon. *Mol. Pharm.* 13, 1347–1357. <https://doi.org/10.1021/acs.molpharmaceut.5b00970>
- Richter, S., Wuest, M., Krieger, S.S., Rogers, B.E., Friebe, M., Bergmann, R., Wuest, F., 2013. Synthesis and radiopharmacological evaluation of a high-affinity and metabolically stabilized  $^{18}\text{F}$ -labeled bombesin analogue for molecular imaging of gastrin-releasing peptide receptor-expressing prostate cancer. *Nucl. Med. Biol.* 40, 1025–1034. <https://doi.org/10.1016/j.nucmedbio.2013.07.005>
- Robinson, S., Julyan, P.J., Hastings, D.L., Zweit, J., 2004. Performance of a block detector PET scanner in imaging non-pure positron emitters—modelling and experimental validation with  $^{124}\text{I}$ . *Phys. Med. Biol.* 49, 5505. <https://doi.org/10.1088/0031-9155/49/24/008>

- Roesch, F., 2012. Scandium-44: Benefits of a Long-Lived PET Radionuclide Available from the  $^{44}\text{Ti}/^{44}\text{Sc}$  Generator System. *Curr. Radiopharm.* 5, 187–201.
- Rogers, B.E., Bigott, H.M., McCarthy, D.W., Manna, D.D., Kim, J., Sharp, T.L., Welch, M.J., 2003. MicroPET Imaging of a Gastrin-Releasing Peptide Receptor-Positive Tumor in a Mouse Model of Human Prostate Cancer Using a  $^{64}\text{Cu}$ -Labeled Bombesin Analogue. *Bioconjug. Chem.* 14, 756–763. <https://doi.org/10.1021/bc034018l>
- Rogers, D.W.O., 2006. Fifty years of Monte Carlo simulations for medical physics\*. *Phys. Med. Biol.* 51, R287. <https://doi.org/10.1088/0031-9155/51/13/R17>
- Rosar, F., Bohnenberger, H., Moon, E.S., Rösch, F., Denig, A., Vincenz-Zörner, D., Hoffmann, M.A., Khreish, F., Ezziddin, S., Schreckenberger, M., Buchholz, H.-G., Schaefer-Schuler, A., 2021. Impact of prompt gamma emission of  $^{44}\text{Sc}$  on quantification in preclinical and clinical PET systems. *Appl. Radiat. Isot.* 170, 109599. <https://doi.org/10.1016/j.apradiso.2021.109599>
- Rosar, F., Buchholz, H.-G., Michels, S., Hoffmann, M.A., Piel, M., Waldmann, C.M., Rösch, F., Reuss, S., Schreckenberger, M., 2020. Image quality analysis of  $^{44}\text{Sc}$  on two preclinical PET scanners: a comparison to  $^{68}\text{Ga}$ . *EJNMMI Phys.* 7, 16. <https://doi.org/10.1186/s40658-020-0286-3>
- Rotsch, D.A., Brown, M.A., Nolen, J.A., Brossard, T., Henning, W.F., Chemerisov, S.D., Gromov, R.G., Greene, J., 2018. Electron linear accelerator production and purification of scandium-47 from titanium dioxide targets. *Appl. Radiat. Isot.* 131, 77–82. <https://doi.org/10.1016/j.apradiso.2017.11.007>
- Rutkowska, E., Pajak, K., Jóźwiak, K., 2013. Lipophilicity--methods of determination and its role in medicinal chemistry. *Acta Pol. Pharm.* 70, 3–18.
- Schlyer, D.J., 2002. Production of Radionuclides in Accelerators, in: *Handbook of Radiopharmaceuticals*. John Wiley & Sons, Ltd, pp. 1–70. <https://doi.org/10.1002/0470846380.ch1>
- Schroeder, R.P.J., van Weerden, W.M., Krenning, E.P., Bangma, C.H., Berndsen, S., Grievink-de Ligt, C.H., Groen, H.C., Reneman, S., de Blois, E., Breeman, W.A.P., de Jong, M., 2011. Gastrin-releasing peptide receptor-based targeting using bombesin analogues is superior to metabolism-based targeting using choline for in vivo imaging of human prostate cancer xenografts. *Eur. J. Nucl. Med. Mol. Imaging* 38, 1257–1266. <https://doi.org/10.1007/s00259-011-1775-3>
- Schueller, M.J., Mulnix, T.L., Christian, B.T., Jensen, M., Holm, S., Oakes, T.R., Roberts, A.D., Dick, D.W., Martin, C.C., Nickles, R.J., 2003. Addressing the third gamma problem in PET. *IEEE Trans. Nucl. Sci.* 50, 50–52. <https://doi.org/10.1109/TNS.2002.807868>

- Schuhmacher, J., Zhang, H., Doll, J., Mäcke, H.R., Matys, R., Hauser, H., Henze, M., Haberkorn, U., Eisenhut, M., 2005. GRP Receptor-Targeted PET of a Rat Pancreas Carcinoma Xenograft in Nude Mice with a  $^{68}\text{Ga}$ -Labeled Bombesin(6–14) Analog. *J. Nucl. Med.* 46, 691–699.
- Seco, J., Verhaegen, F., 2013. Monte Carlo Techniques in Radiation Therapy. CRC Press.
- Severin, G.W., Engle, J.W., Valdovinos, H.F., Barnhart, T.E., Nickles, R.J., 2012. Cyclotron produced  $^{44}\text{Sc}$  from natural calcium. *Appl. Radiat. Isot.* 70, 1526–1530.  
<https://doi.org/10.1016/j.apradiso.2012.04.030>
- Singh, A., van der Meulen, N.P., Müller, C., Klette, I., Kulkarni, H.R., Türler, A., Schibli, R., Baum, R.P., 2017. First-in-Human PET/CT Imaging of Metastatic Neuroendocrine Neoplasms with Cyclotron-Produced  $^{44}\text{Sc}$ -DOTATOC: A Proof-of-Concept Study. *Cancer Biother. Radiopharm.* 32, 124–132.  
<https://doi.org/10.1089/cbr.2016.2173>
- Sitarz, M., 2019. Research on production of new medical radioisotopes with cyclotron.
- Sitarz, M., Nigrón, E., Guertin, A., Haddad, F., Matulewicz, T., 2019. New Cross-Sections for  $\text{natMo}(\alpha, x)$  Reactions and Medical  $^{97}\text{Ru}$  Production Estimations with Radionuclide Yield Calculator. *Instruments* 3, 7. <https://doi.org/10.3390/instruments3010007>
- Sitarz, M., Szkliniarz, K., Jastrzębski, J., Choiński, J., Guertin, A., Haddad, F., Jakubowski, A., Kapinos, K., Kisieliński, M., Majkowska, A., Nigrón, E., Rostampour, M., Stolarz, A., Trzcińska, A., Walczak, R., Wojtkowska, J., Zipper, W., Bilewicz, A., 2018. Production of Sc medical radioisotopes with proton and deuteron beams. *Appl. Radiat. Isot.* 142, 104–112.  
<https://doi.org/10.1016/j.apradiso.2018.09.025>
- Siwowska, K., Guzik, P., Domnanich, K.A., Rodríguez, J.M.M., Bernhardt, P., Ponsard, B., Hasler, R., Borgna, F., Schibli, R., Köster, U., Meulen, N.P. van der, Müller, C., 2019. Therapeutic Potential of  $^{47}\text{Sc}$  in Comparison to  $^{177}\text{Lu}$  and  $^{90}\text{Y}$ : Preclinical Investigations. *Pharmaceutics* 11.  
<https://doi.org/10.3390/pharmaceutics11080424>
- Smith, N.A., Bowers, D.L., Ehst, D.A., 2012. The production, separation, and use of  $^{67}\text{Cu}$  for radioimmunotherapy: A review. *Appl. Radiat. Isot.* 70, 2377–2383.  
<https://doi.org/10.1016/j.apradiso.2012.07.009>
- Snyder, D.L., Miller, M.I., Thomas, L.J., Politte, D.G., 1987. Noise and Edge Artifacts in Maximum-Likelihood Reconstructions for Emission Tomography. *IEEE Trans. Med. Imaging* 6, 228–238.  
<https://doi.org/10.1109/TMI.1987.4307831>
- Soderlund, A.T., Chaal, J., Tjio, G., Totman, J.J., Conti, M., Townsend, D.W., 2015. Beyond  $^{18}\text{F}$ -FDG: Characterization of PET/CT and PET/MR Scanners for a Comprehensive Set of Positron Emitters

- of Growing Application—<sup>18</sup>F, <sup>11</sup>C, <sup>89</sup>Zr, <sup>124</sup>I, <sup>68</sup>Ga, and <sup>90</sup>Y. *J. Nucl. Med.* 56, 1285–1291.  
<https://doi.org/10.2967/jnumed.115.156711>
- Starovoitova, V.N., Cole, P.L., Grimm, T.L., 2015. Accelerator-based photoproduction of promising beta-emitters <sup>67</sup>Cu and <sup>47</sup>Sc. *J. Radioanal. Nucl. Chem.* 305, 127–132.  
<https://doi.org/10.1007/s10967-015-4039-z>
- Strosberg, J., El-Haddad, G., Wolin, E., Hendifar, A., Yao, J., Chasen, B., Mitra, E., Kunz, P.L., Kulke, M.H., Jacene, H., Bushnell, D., O’Dorisio, T.M., Baum, R.P., Kulkarni, H.R., Caplin, M., Lebtahi, R., Hobday, T., Delpassand, E., Van Cutsem, E., Benson, A., Srirajaskanthan, R., Pavel, M., Mora, J., Berlin, J., Grande, E., Reed, N., Seregini, E., Öberg, K., Lopera Sierra, M., Santoro, P., Thevenet, T., Erion, J.L., Ruzsniowski, P., Kwekkeboom, D., Krenning, E., 2017. Phase 3 Trial of <sup>177</sup>Lu-Dotatate for Midgut Neuroendocrine Tumors. *N. Engl. J. Med.* 376, 125–135.  
<https://doi.org/10.1056/NEJMoa1607427>
- Synowiecki, M.A., Perk, L.R., Nijssen, J.F.W., 2018. Production of novel diagnostic radionuclides in small medical cyclotrons. *EJNMMI Radiopharm. Chem.* 3, 3. <https://doi.org/10.1186/s41181-018-0038-z>
- Szkliniarz, K., Sitarz, M., Walczak, R., Jastrzębski, J., Bilewicz, A., Choiński, J., Jakubowski, A., Majkowska, A., Stolarz, A., Trzcińska, A., Zipper, W., 2016. Production of medical Sc radioisotopes with an alpha particle beam. *Appl. Radiat. Isot.* 118, 182–189.  
<https://doi.org/10.1016/j.apradiso.2016.07.001>
- Thin Layer Chromatography, 2019.
- Thirolf, P.G., Lang, C., Parodi, K., 2015. Perspectives for Highly-Sensitive PET-Based Medical Imaging Using  $\beta^+$   $\gamma$  Coincidences. *Acta Phys. Pol. A* 127, 1441–1444.  
<https://doi.org/10.12693/APhysPolA.127.1441>
- Thomas, R., Chen, J., Roudier, M.M., Vessella, R.L., Lantry, L.E., Nunn, A.D., 2008. In vitro binding evaluation of <sup>177</sup>Lu-AMBA, a novel <sup>177</sup>Lu-labeled GRP-R agonist for systemic radiotherapy in human tissues. *Clin. Exp. Metastasis* 26, 105. <https://doi.org/10.1007/s10585-008-9220-0>
- Tornesello, A.L., Tornesello, M.L., Buonaguro, F.M., 2017. An Overview of Bioactive Peptides for in vivo Imaging and Therapy in Human Diseases. *Mini Rev. Med. Chem.* 17, 758–770.  
<https://doi.org/10.2174/1389557517666170120151739>
- Umbricht, C.A., Benešová, M., Schmid, R.M., Türlér, A., Schibli, R., van der Meulen, N.P., Müller, C., 2017. <sup>44</sup>Sc-PSMA-617 for radiotheragnostics in tandem with <sup>177</sup>Lu-PSMA-617—preclinical

- investigations in comparison with  $^{68}\text{Ga}$ -PSMA-11 and  $^{68}\text{Ga}$ -PSMA-617. *EJNMMI Res.* 7, 9. <https://doi.org/10.1186/s13550-017-0257-4>
- Valdovinos, H.F., Hernandez, R., Barnhart, T.E., Graves, S., Cai, W., Nickles, R.J., 2015. Separation of cyclotron-produced  $^{44}\text{Sc}$  from a natural calcium target using a dipentyl pentylphosphonate functionalized extraction resin. *Appl. Radiat. Isot.* 95, 23–29. <https://doi.org/10.1016/j.apradiso.2014.09.020>
- van der Meulen, N.P., Bunka, M., Domnanich, K.A., Müller, C., Haller, S., Vermeulen, C., Türler, A., Schibli, R., 2015. Cyclotron production of  $^{44}\text{Sc}$ : From bench to bedside. *Nucl. Med. Biol.* 42, 745–751. <https://doi.org/10.1016/j.nucmedbio.2015.05.005>
- Von Neumann, J., 1963. Various techniques used in connection with random digits. *John Von Neumann Collect. Works* 5, 768–770.
- Walczak, R., Krajewski, S., Szkliniarz, K., Sitarz, M., Abbas, K., Choiński, J., Jakubowski, A., Jastrzębski, J., Majkowska, A., Simonelli, F., Stolarz, A., Trzcińska, A., Zipper, W., Bilewicz, A., 2015. Cyclotron production of  $^{43}\text{Sc}$  for PET imaging. *EJNMMI Phys.* 2, 33. <https://doi.org/10.1186/s40658-015-0136-x>
- Walrand, S., Jamar, F., Mathieu, I., Camps, J.D., Lonneux, M., Sibomana, M., Labar, D., Michel, C., Pauwels, S., 2003. Quantitation in PET using isotopes emitting prompt single gammas: application to yttrium-86. *Eur. J. Nucl. Med. Mol. Imaging* 30, 354–361. <https://doi.org/10.1007/s00259-002-1068-y>
- Wang, M., Huang, W.J., Kondev, F.G., Audi, G., Naimi, S., 2021. The AME 2020 atomic mass evaluation (II). Tables, graphs and references\*. *Chin. Phys. C* 45, 030003. <https://doi.org/10.1088/1674-1137/abddaf>
- Williams, H.A., Robinson, S., Julyan, P., Zweit, J., Hastings, D., 2005. A comparison of PET imaging characteristics of various copper radioisotopes. *Eur. J. Nucl. Med. Mol. Imaging* 32, 1473–1480. <https://doi.org/10.1007/s00259-005-1906-9>
- Wilson, A.A., Jin, L., Garcia, A., DaSilva, J.N., Houle, S., 2001. An admonition when measuring the lipophilicity of radiotracers using counting techniques. *Appl. Radiat. Isot.* 54, 203–208. [https://doi.org/10.1016/S0969-8043\(00\)00269-4](https://doi.org/10.1016/S0969-8043(00)00269-4)
- W. Price, E., Orvig, C., 2014. Matching chelators to radiometals for radiopharmaceuticals. *Chem. Soc. Rev.* 43, 260–290. <https://doi.org/10.1039/C3CS60304K>

- W. Price, T., Greenman, J., J. Stasiuk, G., 2016. Current advances in ligand design for inorganic positron emission tomography tracers  $^{68}\text{Ga}$ ,  $^{64}\text{Cu}$ ,  $^{89}\text{Zr}$  and  $^{44}\text{Sc}$ . *Dalton Trans.* 45, 15702–15724. <https://doi.org/10.1039/C5DT04706D>
- Yagi, M., Kondo, K., 1977. Preparation of carrier-free  $^{47}\text{Sc}$  by the  $^{48}\text{Ti}(\gamma, p)$  reaction. *Int. J. Appl. Radiat. Isot.* 28, 463–468. [https://doi.org/10.1016/0020-708X\(77\)90178-8](https://doi.org/10.1016/0020-708X(77)90178-8)
- Yang, Y.-S., Zhang, X., Xiong, Z., Chen, X., 2006. Comparative in vitro and in vivo evaluation of two  $^{64}\text{Cu}$ -labeled bombesin analogs in a mouse model of human prostate adenocarcinoma. *Nucl. Med. Biol.* 33, 371–380. <https://doi.org/10.1016/j.nucmedbio.2005.12.011>
- Yoshida, E., Tashima, H., Nagatsu, K., Tsuji, A.B., Kamada, K., Parodi, K., Yamaya, T., 2020. Whole gamma imaging: a new concept of PET combined with Compton imaging. *Phys. Med. Biol.* 65, 125013. <https://doi.org/10.1088/1361-6560/ab8e89>
- Zhang, J., Niu, G., Fan, X., Lang, L., Hou, G., Chen, L., Wu, H., Zhu, Z., Li, F., Chen, X., 2018. PET Using a GRPR Antagonist  $^{68}\text{Ga}$ -RM26 in Healthy Volunteers and Prostate Cancer Patients. *J. Nucl. Med.* 59, 922–928. <https://doi.org/10.2967/jnumed.117.198929>
- Ziegler, J., Littmark, U., Biersack, J., 2008. Calculation using the stopping and range of ions in matter (SRIM) code.
- Ziegler, J.F., Ziegler, M.D., Biersack, J.P., 2010. SRIM – The stopping and range of ions in matter (2010). *Nucl. Instrum. Methods Phys. Res. Sect. B Beam Interact. Mater. At.*, 19th International Conference on Ion Beam Analysis 268, 1818–1823. <https://doi.org/10.1016/j.nimb.2010.02.091>

## Appendix A

# Radionuclide Production Calculations: A GUI to Determine Irradiation Conditions

---

---

### A.1 Introduction

There are a wide variety of potential radionuclides being explored, each with diverse strategies for production; comparing these production methods requires many time intensive calculations to survey the various irradiation parameters. There is therefore a need to facilitate production calculations to determine the most efficient method of producing these radionuclides. Theoretical yield calculations can often be complicated by the use of multi-isotopic targets and the diverse possible reaction channels. The yield of the radionuclide of interest must be calculated as well as that of contaminants which could, in turn, affect radionuclidic purity and patient dosimetry.

In this work, a graphical user interface (GUI) has been developed to facilitate this calculation process. The GUI includes the ability for comparing reaction cross-sections, determining target thicknesses, and calculating thick target yields. This is a general purpose GUI which can facilitate calculations for the production of various radionuclides from a variety of charged particle beams (e.g. proton, deuteron, alpha particles) given the appropriate input data. It is divided into 3 tabs, “Cross Sections”, “Targets”, and “Yield”. On one hand, these tabs work independently to visualize the inputs. On the other, the parameters of these tabs are coupled together to calculate radionuclide yields and radioactivities. The functionality of these tabs is described in further detail below, and, as an example, the production of scandium-44 from proton irradiation of natural calcium is used in this conference proceeding to exemplify the GUI. Scandium-44 is a positron emitter of interest for PET imaging with a 3.96h half-life and 94% positron branching ratio.

### A.2 The “cross sections” tab

The cross-section tab allows the user to import tabulated cross-section data as displayed in Figure 0.1. At present it is able to import a folder of TENDL files, and parse the data to determine target nuclide,

reaction channel, product nuclide, isomeric state (ground or metastable), reaction Q-value and threshold energy, as well as the energy dependent cross-sections.

In this example, the TENDL-2014 library files served as the input for the theoretical excitation functions. The TENDL files have the advantage of being easy to automatically parse and represent an excitation function which spans a large energy range for an extensive array of reaction pathways. The GUI can also import experimental cross-sections as input for comparisons; however, this process is not as robust due to the varying quality of the data and, in general, non-uniform/fixed energy steps between samples. At this time, any imported non-TENDL data must be corrected and formatted manually.

The imported reaction channels are summarized in a table and the user can individually select which cross-sections to plot and compare. Additionally, the cross-sections can be plotted in groups based on a target nuclide, reaction channel, production nuclide, threshold energy, and/or by type.

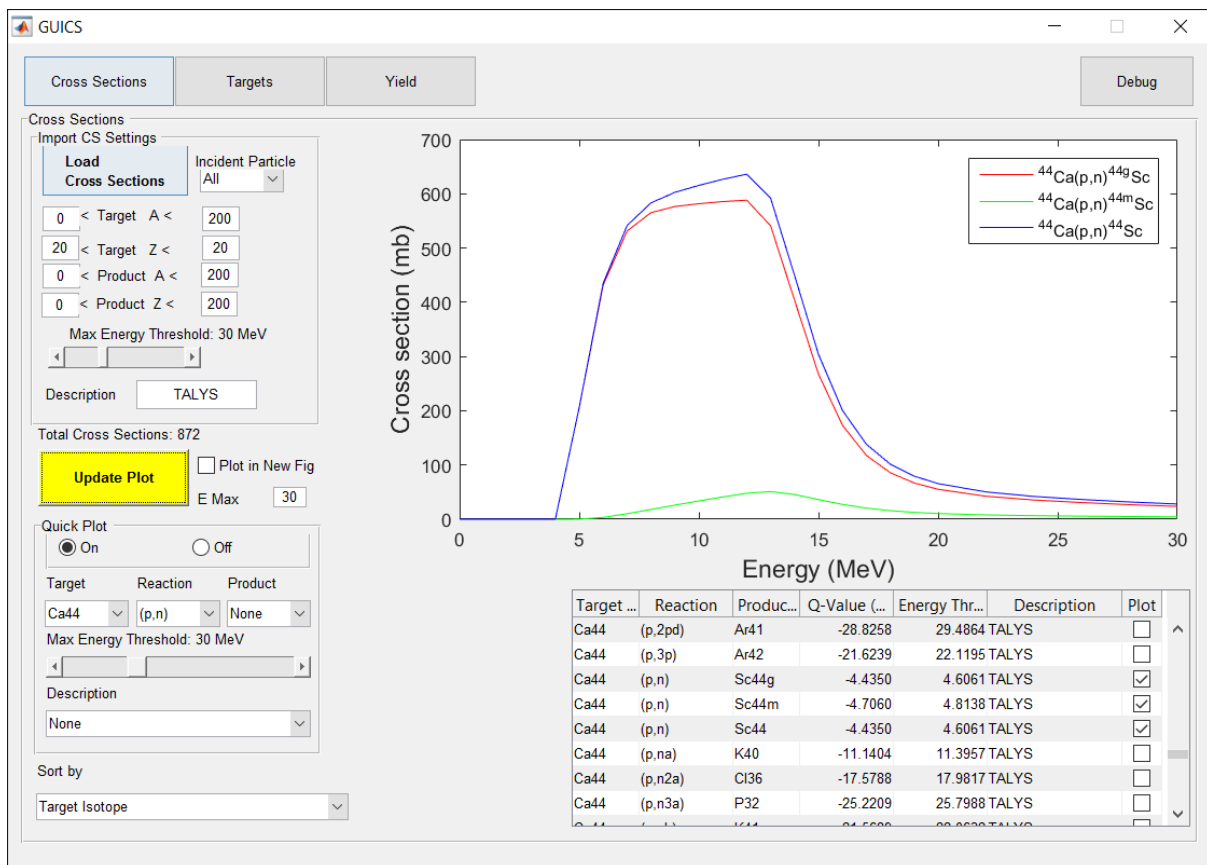


Figure 0.1 The cross-section tab allows the user to selectively import cross-sections and includes a table which summarizes all imported reaction channels which can be used to plot and compare various cross-sections.

In the example of the proton irradiation of natural calcium, the reaction channels of interest in the production of scandium are the (p,xn) reactions. In Figure 0.2, the relevant (p,xn) excitation functions from TENDL-2014 are plotted. The main production channel of interest in producing scandium-44 is  $^{44}\text{Ca}(p,n)^{44}\text{Sc}$ ; however, there are many other radioisotopes that may be co-produced during irradiation. These contaminants will affect the radioisotopic purity of the resulting product.

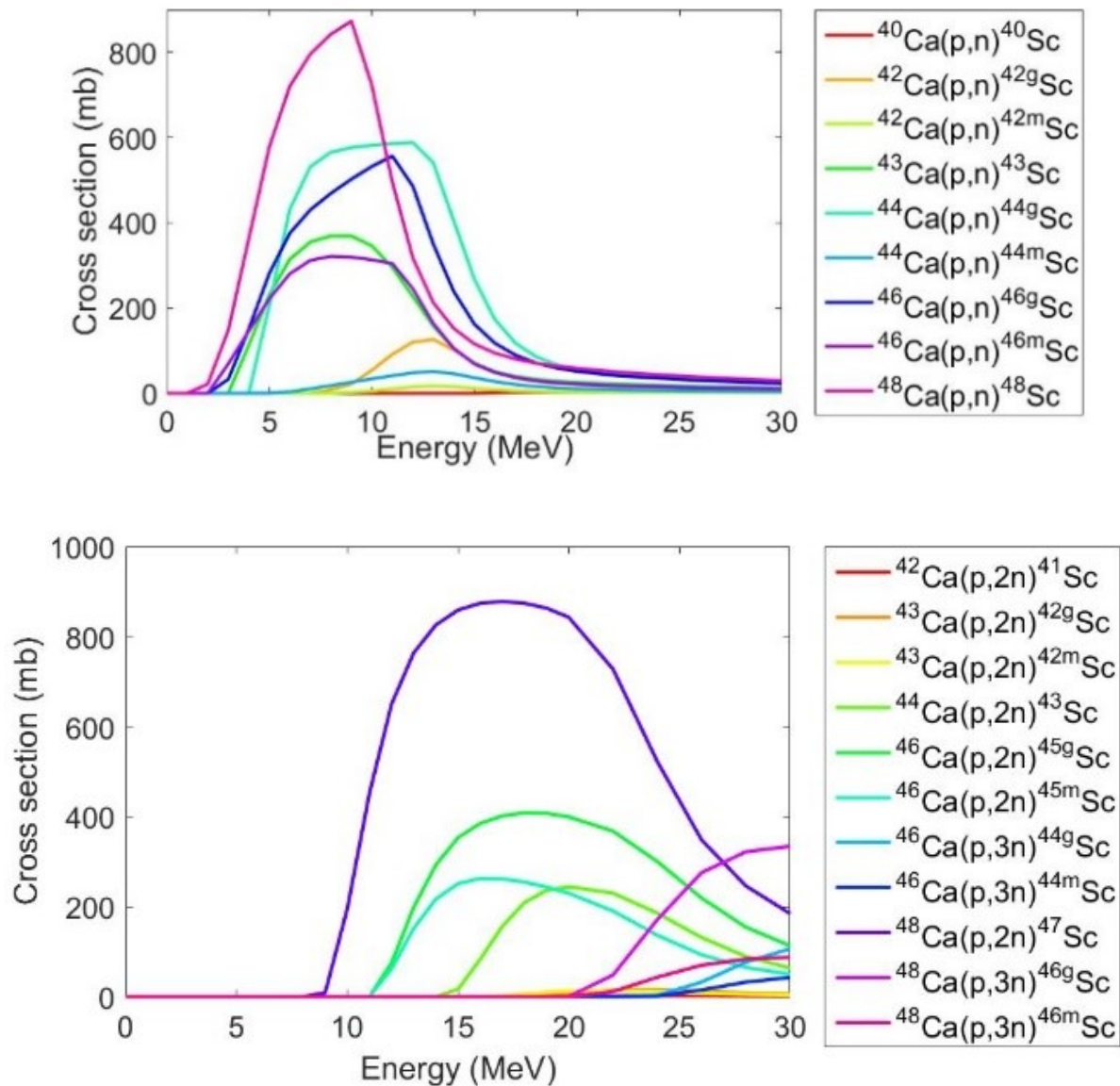


Figure 0.2: Comparison of relevant (p,xn) reaction channels on naturally occurring isotopes of calcium from TENDL-2014.

### A.3 The “targets” tab

The target tab demonstrated in Figure 0.3 allows the user to create new targets as well as import and save existing targets. The user must specify a target density and its isotopic composition as well as the stopping power output file calculated in SRIM (Ziegler et al., 2010). The stopping power must be specified for each charged particle of interest in the target material.

The user can plot the stopping power for a given incident particle as a function of energy, as well as the target thickness (assuming full density) required to degrade the incident beam energy to the outgoing energy of interest. By defining the isotopic compositions of the targets, the user can later repeat yield calculations for various enriched target materials and compare the advantages of enriched materials and/or compositions, and decide if the increase in yields and/or possible change in radionuclidic purity offset the cost.

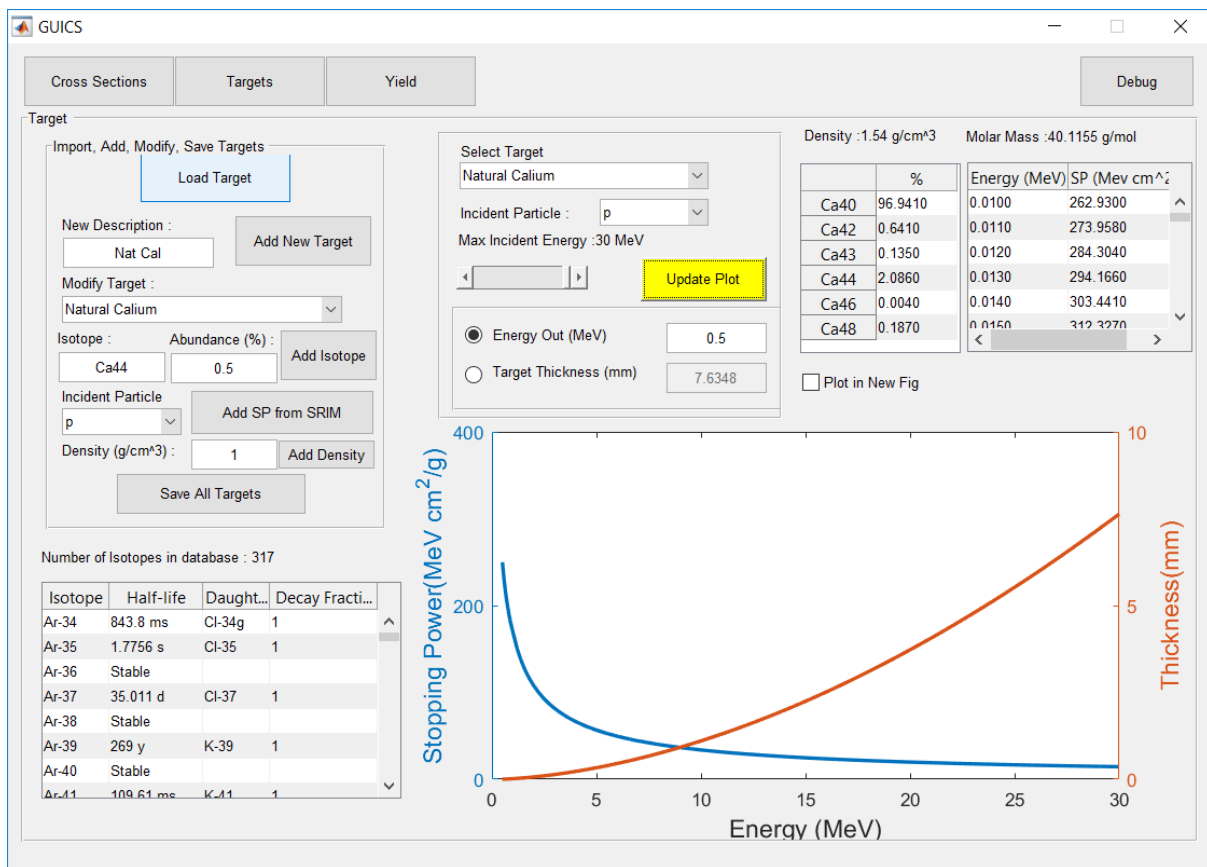


Figure 0.3: The target tab allows the user to import, add, modify, and save targets. It displays the target properties, including isotopic composition, density and molar mass. The stopping power of incident charged particles can be plotted along with the thickness of the target which will degrade an incident charged particle beam to the selected outgoing energy.

Returning to the example of the proton irradiation of natural calcium, the stopping power of protons in natural calcium is shown in Figure 0.4. The thickness required, assuming full density, to degrade an incident proton energy to the  $^{44}\text{Ca}(p,n)^{44}\text{Sc}$  reaction threshold of 4.5 MeV is plotted concurrently. From this, one sees that natural calcium targets require thickness of 2.3 and 3.5 mm, respectively, to degrade incident proton energies of 16 and 20 MeV down to 4.5 MeV.

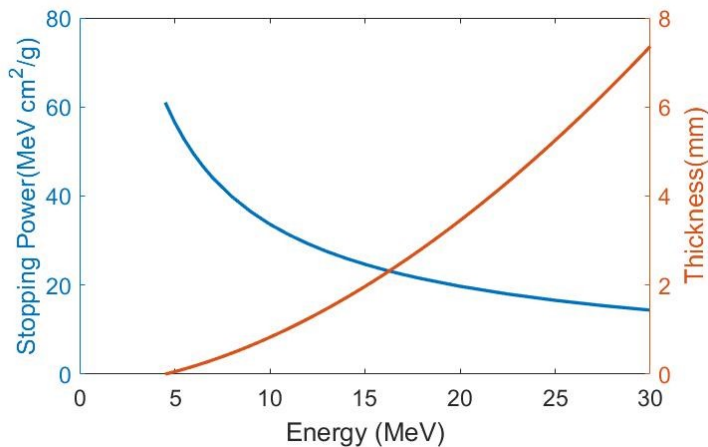


Figure 0.4: Stopping power and thickness, assuming full density, of an incident proton beam degraded to 4.5 MeV in a natural

#### A.4 The “yield” tab

For a given target, the GUI will calculate the saturated yields of the radionuclides in the library for all imported cross-sections with threshold energies below the maximum beam energy specified. The saturated yield can then be plotted directly, or used to calculate the activity of all radionuclides using the generalized Bateman equation. The activity of each radionuclide can be plotted and the user can vary irradiation time, time after end of beam, and incident and outgoing beam energy. The corresponding radioactivities are plotted as a function of beam energy (incident beam energy vs. outgoing beam energy at a given time) or time (for a given incident & outgoing beam energy). The radioactivities can be displayed in absolute or relative units (i.e. MBq/ $\mu\text{A}$  or %), and are also presented in tabular format, as seen in Figure 0.5.

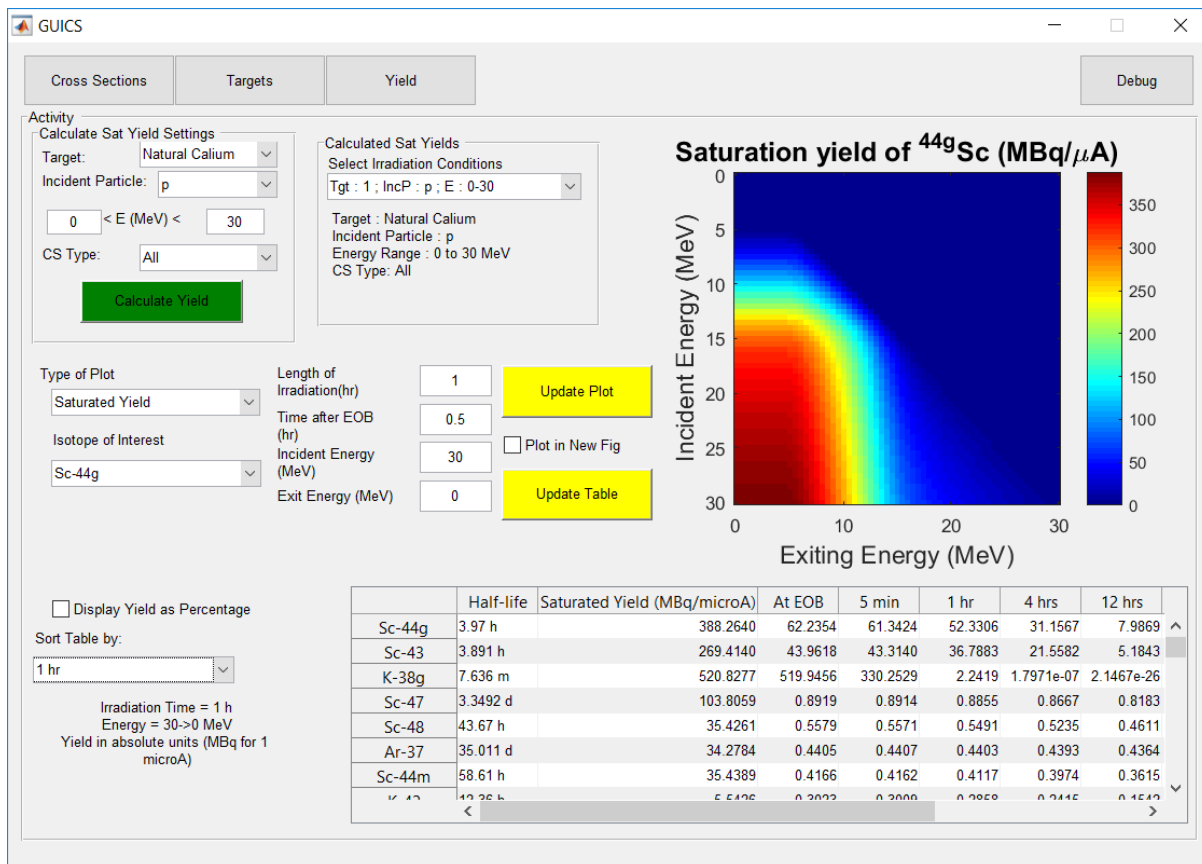


Figure 0.5: The yield tab includes a summary of the parameters used to calculate the saturated yields, including selected target and range of incident particle energies. The saturated yield can be used to calculate and plot activities as a function of time or beam energy, and these can be displayed for any radionuclide. The activity of the radionuclides is also compared in tabular format as a function of time.

Importantly, knowing the radioactivity fraction of nuclides as a function of beam energy is interesting because it is an indicator of optimal incident beam energy and target thickness. In continuing with scandium-44 production as an example, by looking at Figure 0.6a, we can see that increasing the incident proton energy will lead to an increase in yield; however, as demonstrated in Figure 0.6b this will correspondingly lead to a decrease in radionuclidic purity. Therefore, by limiting the incident proton energy to 16 MeV for a 1hr irradiation, 94% of the resulting activity at 30 minutes after end of beam can be expected to be scandium-44. Thus, the calculations from the GUI based on the TENDL cross-sections suggest it is possible to produce scandium-44 of reasonably high purity from natural calcium targets with the appropriate irradiation conditions. This is in alignment with the observations by Severin et al, who found that the radionuclidic purity of scandium-44 is greater than 95% for irradiations up to 7 hours at 16 MeV (Severin et al., 2012).

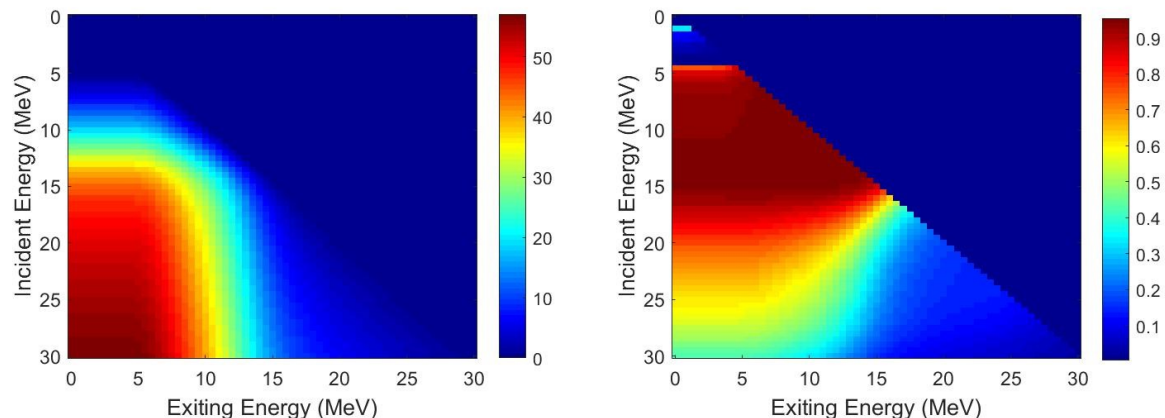


Figure 0.6: (a) Activity of scandium-44g per  $\mu\text{A}$  of beam current for a 1-hour irradiation, as observed 30 min after end of beam in MBq. (b) Radioactivity fraction of scandium-44 at 30min after a 1-hour irradiation as a function of incident and exiting proton energy. The activity fraction is greatest for incident beam energies lower than 16 MeV as at higher energies, competing reaction channels begin to dominate.

## A.5 Conclusions

This GUI simplifies the process of exploring different production methods. By importing all available reaction channels from the TENDL, the GUI can determine the corresponding radionuclides that will be produced and provides an estimate of their yields for various target compositions and irradiation conditions. If available, corresponding experimental cross-sections can be imported for comparisons. The GUI allows the users to easily determine the irradiation parameters and target compositions that are adequate for their purposes within the limitations of the input parameters. To date, downloading version 1.00 of the GUI includes all TENDL-2014 files necessary for proton-based production of  $^{44}\text{Sc}$ ,  $^{99\text{m}}\text{Tc}$ , and  $^{89}\text{Zr}$ , along with SRIM outputs to 100 MeV. While the user can incorporate the files needed for other applications, packaging of other isotopes is currently in progress and is expected to be released with future versions. In the future, gamma and particle emissions data will be included in order to facilitate radiation handling and shielding calculations as well as patient dosimetry.

## A.6 References

- A. J. Koning, D. Rochman, S. C. Van Der Marck, et al. TALYS Evaluated Nuclear Data Library (TENDL-2014) (Nuclear Research and Consultancy Group (NRG), Petten, The Netherlands, 2014)
- G. W. Severin, J. W. Engle, H. F. Valdovinos, T. E. Barnhart, R. J. Nickles Cyclotron produced 44g Sc from natural calcium. Applied Radiation and Isotopes vol. 70, no 8, 1526-1530 (2012)

J. F. Ziegler, M. D. Ziegler, J. P. Biersack. SRIM – The stopping and range of ions in matter. Nuclear Instruments and Methods in Physics Research Section B: Beam Interactions with Materials and Atoms vol. 26, no 11, 1818-1823 (2010)